NORTHWESTERN UNIVERSITY

Measurement of the W Plus N Inclusive Jets Cross-section at CDF Run II

A DISSERTATION

SUBMITTED TO THE GRADUATE SCHOOL

IN PARTIAL FULFILLMENT OF THE REQUIREMENTS

for the degree

DOCTOR OF PHILOSOPHY

Field of Physics and Astronomy

By

Dale Stentz

EVANSTON, ILLINOIS

March 2012

ABSTRACT

Measurement of the W Plus N Inclusive Jets Cross-section at CDF Run II

Dale Stentz

In this thesis we present the study of the production of the W boson in association with hadronic jets at the Collider Detector at Fermilab (CDF). Along with the electroweak properties the W boson, we examine jet kinematic variables with the aim of studying predictions of perturbative quantum chromodynamics. We derive several differential cross-sections as a function of the inclusive jet multiplicity and the transverse momenta of each jet. In this analysis, we are using 2.8 fb^{-1} of data and consider both the electron and muon lepton final states for the W boson decay.

Table of Contents

8

List of Tables

is divided in to three respective parts: statistical, total systematic
which is without the final luminosity systematic, and the luminosity
systematic itself. This is a table version of plot 9.10 on page 426.   472

.12   CDF Run II Preliminary. The third leading jet p_T cross-section
differential for $W \to e\nu+ \geq 3$ inclusive jets. The W cross-section is
restricted to $|\eta^e| < 1.1$, $p_T^e > 20$ GeV/c, and $M_T^W > 40$ GeV/c^2 while
jets are defined with $p_T^{jet} > 20$ GeV/c and $|\eta^{jet}| < 2.0$. The error
is divided in to three respective parts: statistical, total systematic
which is without the final luminosity systematic, and the luminosity
systematic itself. This is a table version of plot 9.11 on page 427.   473

.13   CDF Run II Preliminary. The fourth leading jet p_T cross-section for
$W \to e\nu+ \geq 4$ inclusive jets. The W cross-section is restricted to $|\eta^e| <$
1.1, $p_T^e > 20$ GeV/c, and $M_T^W > 40$ GeV/c^2 while jets are defined
with $p_T^{jet} > 20$ GeV/c and $|\eta^{jet}| < 2.0$. The error is divided in to three
respective parts: statistical, total systematic which is without the final
luminosity systematic, and the luminosity systematic itself. This is a
table version of plot 9.12 on page 427.   473

.14   CDF Run II Preliminary. The leading jet p_T cross-section for
$W \to \mu\nu+ \geq 1$ inclusive jet. The W cross-section is restricted to $|\eta^\mu| <$
1.1, $p_T^\mu > 20$ GeV/c, and $M_T^W > 30$ GeV/c^2 while jets are defined
with $p_T^{jet} > 20$ GeV/c and $|\eta^{jet}| < 2.0$. The error is divided in to three
respective parts: statistical, total systematic which is without the final

multiplicity cross-section. The W cross-section is restricted to $|\eta^e| <$ 1.1, $p_T^e > 20$ GeV/c, and $M_T^W > 40$ GeV/c^2 while jets are defined with $p_T^{jet} > 20$ GeV/c and $|\eta^{jet}| < 2.0$. The error is divided in to a statistical and total systematic uncertainty, respectively. This is a table version of plot 9.20 on page 432. 479

.41   CDF Run II Preliminary. Dijet separation (R_{jj}) cross-section normalized to the inclusive 2 jets cross-section for $W \to \mu\nu + \geq 2$ jets. The W cross-section is restricted to $|\eta^\mu| < 1.1$, $p_T^\mu > 20$ GeV/c, and $M_T^W > 30$ GeV/c^2 while jets are defined with $p_T^{jet} > 20$ GeV/c and $|\eta^{jet}| < 2.0$. The error is divided in to a statistical and total systematic uncertainty, respectively. This is a table version of plot 9.40 on page 445.   496

.42   CDF Run II Preliminary. Closest $\Delta\eta$ cross-section for $W \to e\nu + \geq 2$ jets. The W cross-section is restricted to $|\eta^e| < 1.1$, $p_T^e > 20$ GeV/c, and $M_T^W > 40$ GeV/c^2 while jets are defined with $p_T^{jet} > 20$ GeV/c and $|\eta^{jet}| < 2.0$. The error is divided in to three respective parts: statistical, total systematic which is without the final luminosity systematic, and the luminosity systematic itself. This is a table version of plot 9.43 on page 448.   497

.43   CDF Run II Preliminary. Closest $\Delta\eta$ cross-section for $W \to e\nu + \geq 3$ jets. The W cross-section is restricted to $|\eta^e| < 1.1$, $p_T^e > 20$ GeV/c, and $M_T^W > 40$ GeV/c^2 while jets are defined with $p_T^{jet} > 20$ GeV/c and $|\eta^{jet}| < 2.0$. The error is divided in to three respective parts: statistical, total systematic which is without the final luminosity systematic, and the luminosity systematic itself. This is a table version of plot 9.47 on page 450.   498

.44   CDF Run II Preliminary. Closest $\Delta\eta$ cross-section normalized to the inclusive 2 jet cross-section for $W \to e\nu + \geq 2$ jets. The W cross-section

is restricted to $|\eta^e| < 1.1$, $p_T^e > 20$ GeV/c, and $M_T^W > 40$ GeV/c^2 while jets are defined with $p_T^{jet} > 20$ GeV/c and $|\eta^{jet}| < 2.0$. The error is divided in to a statistical and total systematic uncertainty, respectively. This is a table version of plot 9.45 on page 449.

CDF Run II Preliminary. Closest $\Delta\eta$ cross-section normalized to the inclusive 3 jet cross-section for $W \to e\nu+ \geq 3$ jets. The W cross-section is restricted to $|\eta^e| < 1.1$, $p_T^e > 20$ GeV/c, and $M_T^W > 40$ GeV/c^2 while jets are defined with $p_T^{jet} > 20$ GeV/c and $|\eta^{jet}| < 2.0$. The error is divided in to a statistical and total systematic uncertainty, respectively. This is a table version of plot 9.49 on page 451.

CDF Run II Preliminary. Closest $\Delta\eta$ cross-section for $W \to \mu\nu+ \geq 2$ jets. The W cross-section is restricted to $|\eta^\mu| < 1.1$, $p_T^\mu > 20$ GeV/c, and $M_T^W > 30$ GeV/c^2 while jets are defined with $p_T^{jet} > 20$ GeV/c and $|\eta^{jet}| < 2.0$. The error is divided in to three respective parts: statistical, total systematic which is without the final luminosity systematic, and the luminosity systematic itself. This is a table version of plot 9.44 on page 449.

CDF Run II Preliminary. Closest $\Delta\eta$ cross-section for $W \to \mu\nu+ \geq 3$ jets. The W cross-section is restricted to $|\eta^\mu| < 1.1$, $p_T^\mu > 20$ GeV/c, and $M_T^W > 30$ GeV/c^2 while jets are defined with $p_T^{jet} > 20$ GeV/c and $|\eta^{jet}| < 2.0$. The error is divided in to three respective parts: statistical, total systematic which is without the final luminosity systematic, and

30 GeV/c^2 while jets are defined with $p_T^{jet} > 20$ GeV/c and $|\eta^{jet}| < 2.0$. The error is divided in to a statistical and total systematic uncertainty, respectively. This is a table version of plot 9.52 on page 453.

List of Figures

CHAPTER 1

Introduction

In this chapter, we provide an introduction to this thesis. We have divided this chapter into four sections. First, we give a basic physics motivation of this analysis as well as a brief physics background of the relevant material. Secondly, we highlight previous results; notably, a previous result from CDF Run II in section 1.2. Next, section 1.3, we will introduce, by way of comparison and contrast of previous measurements, our basic analysis goals and expectations of this thesis work. Finally, in section 1.4 we will provide an outline of the rest of the content of this thesis.

1.1. Physics Introduction and Motivation

Matter interacts through the gravitational, electromagnetic, weak nuclear, and strong nuclear interactions [1][2][3]. Colloquially these are sometimes refereed to as the four fundamental forces. The kind of interaction depends on the properties of matter. For example, particles with electric charge interact electromagnetically. One of the goals of physicists is to unify these interactions by describing them in a unique consistent way as a result of a set of proscribed properties of matter. Ideally at the very high energies all interactions were reduced to one and the breakdown into four interactions was the result of symmetries broken at lower energies. Currently, only the electromagnetic and weak interactions have been unified to an electroweak interaction. Electromagnetism (EM) is mediated by the massless boson known as the photon (γ) which is sometimes simply

refereed to as the "force carrier" or mediator for EM [2][3]. The weak nuclear interaction is meditated by the $W^{\mp}$ and Z bosons which are massive due to electroweak symmetry breaking [1][6].

The theory concerning the current view in particle physics of the electromagnetic, weak, and strong nuclear interactions together with the collection of known elementary particles (i.e. leptons, quarks, and force mediators) is called as the Standard Model (SM) [2][4]. Figure 1.1 shows a visible representation of the Standard Model of elementary particles which is not unlike the Periodic table of elements. Effectively the Standard Model of particle physics is the union of two extant theories: quantum electroweak and quantum chromodynamics which will be discussed further below.

Collectively the electroweak interactions are described with perturbative quantum field theory (QFT) [7][8] which is a relativistically invariant of quantum mechanics. An example of a particular quantum field theory with respect to electromagnetism is quantum electrodynamics (QED) [9]. The calculation of cross-sections is given as a sum of a series of terms that are proportional to increasing power of the coupling of the particles to the gauge boson. In principle, the series converges when the couplings are smaller then unity which is the case, for example, in QED.

Like QED, the strong nuclear interactions are likewise described by a quantum field theory; namely, quantum chromodynamics (QCD) [10]. Rather than electric charge or left-handedness, QCD accounts for the three types of color charge for quarks via the eight mediating gauge bosons (gluons). Also by comparison to the fine structure constant in QED (α), the strong coupling constant (α_S) is larger and thus perturbative calculations are potentially problematic. Theoretical calculation schemes fall under the general rubric

of perturbative QCD (pQCD). QCD is remarkable in a few other regards. First, asymptotic freedom is a property of QCD that posits that interactions (via color charge) become weak at high energies (small interaction distance scales). Another feature of QCD is confinement (pedantically, *color charge* confinement). As will be noted later, confinement is where color charged particles cannot be isolated (e.g. no "free quarks") due to the strength of the strong interaction at large distances.

Figure 1.1. Standard model of elementary particles: the 12 fundamental fermions and 4 fundamental bosons [5].

In particle physics, a jet is a collimated stream of hadrons and is a by-product of hadronization [11]. In QCD, confinement causes quarks and gluons (collectively referred to as partons in this context) to hadronize. The actual process of hadronization is called fragmentation (e.g. fragmentation model). This fragmentation of color charged particles can be identified by gathering particles observed in a narrow cone and classified as a jet with kinematic properties within some jet defining scheme/algorithm.

In this analysis, we wish to study a known process in the Standard Model of jets production in association with the charged $W^{\mp}$ boson (simply W hereafter) decays into either an electron/positron ($e^{\mp}$) or a muon ($\mu^{\mp}$). We do not directly consider tau (τ) decays although we do incorporate this as a background to be subtracted from our candidate selection. In this thesis, we will denote the two lower mass charged leptons via a single title (e.g. "electron" for electron or positron) and likewise to the W, not explicitly noting the charge (i.e. e and μ for $e^{\mp}$ and $\mu^{\mp}$, respectively). Also for convenience, we will not directly reference the neutrino flavor and, as with the charged leptons, will omit whether it is matter or anti-matter. Thus, all neutrinos in this analysis will be represented by ν. In addition, we will incorporate ℓ to represent both leptons ($\ell \, \epsilon \, \{e, \mu\}$). Schematically, $W \to \ell\nu$ will represent our W signal production which will signify a high momentum transfer.

The physics motivation for this analysis is to study different jets kinematic observables and measure a set of differential cross-sections. These experimental measurements can then be compared to theoretical measurements via pQCD.

1.2. Previous Results

In this section we highlight a previous measurement of W+jets at CDF [12][13][14][15] which provides a good benchmark for the discussion. However, first we note that this section necessarily draws upon the explanations and details of the later chapters. To begin with, as will become clear in our discussion in sections 7.4 and 9.1 and our jet definition provided in section 5.1, these results are not by the letter of the law directly comparable to the results finally present in chapter 9. We incorporate a different jet definition and construction algorithm and our W acceptance is slightly different. Nevertheless, this previous work offered a relatively mature analysis to briefly discuss.

The previous cited analysis looked for events where a high momentum electron and missing energy signature of the neutrino implied a W event. From this sample, jets were constructed and measured. The analysis utilized 320 pb^{-1} of data. As noted in detail in [12] and [14], this analysis pioneered a method for constructing a QCD/fakes sample and then using this sample along with the Monte Carlo predictions for other backgrounds to get a proper background measurement independent of event weighting assumptions on the background. This background fitting method will be incorporated in this analysis with some minor improvements. As noted in the previous section, we also plan to measure the muon channel in addition to the electrons and thus have to construct a QCD/fakes sample from scratch for this channel. Details on this thesis work with respect to backgrounds and QCD/fakes sample are explained in detail in sections 4.2, 4.4, and 6.4.

The previous analysis uses the CDF default JetClu jet algorithm with a lower transverse jet energy selection cut. We explain these differences in some detail in section 5.1. Beyond the normal jet energy corrections that are performed in a CDF Run II analysis,

the final measure cross-sections were corrected back to the hadron level and thus removing the detector signature. We follow suit and also perform this full jet correction as noted in section 5.8.

We present their results from [15][17] in figures 1.2-1.4. As we will note in the next section, one of the flagship cross-sections to measure is the differential transverse jet energy or rather in our analysis the transverse jet momentum which is preferred given our choice jet algorithm. This $d\sigma/dE_T$ differential cross-section is shown in figure 1.2. It shows the jet transverse energy for $\geq$1-4 jets on a single plot. This and the other plots give the W kinematic phase-space restriction cuts as well as the jet definition on the plot. It is compared to a prediction from the Alpgen+Pythia Monte Carlo sample that has been normalized to the data. Like our analysis this comparison to Monte Carlo serves as a basic bench mark in lieu of better (i.e. NLO) theoretical predictions. Unlike our analysis, the previous analysis makes comparisons to individual $W+\#$ partons samples rather than summing all Monte Carlo predictions together. Section 3.5 provides greater detail on this analysis refinement.

The next two differential cross-section measurements involve events with at least two jets (dijet events) using the two highest energy (in E_T) jets. The first (figure 1.3) is the dijet mass (M_{jj}) while the second (figure 1.4) is the angular separation (ΔR). In both of these distributions have discrepancies with the theoretical comparison (i.e. LO Alpgen+PYTHIA). In the case of the dijet mass, the theory shape (it is normalized to the data) overestimates in the lowest mass bins but then underestimates around mass = 50 GeV/c^2. The jet pair separation also has a section where the data is under represented around ΔR of π.
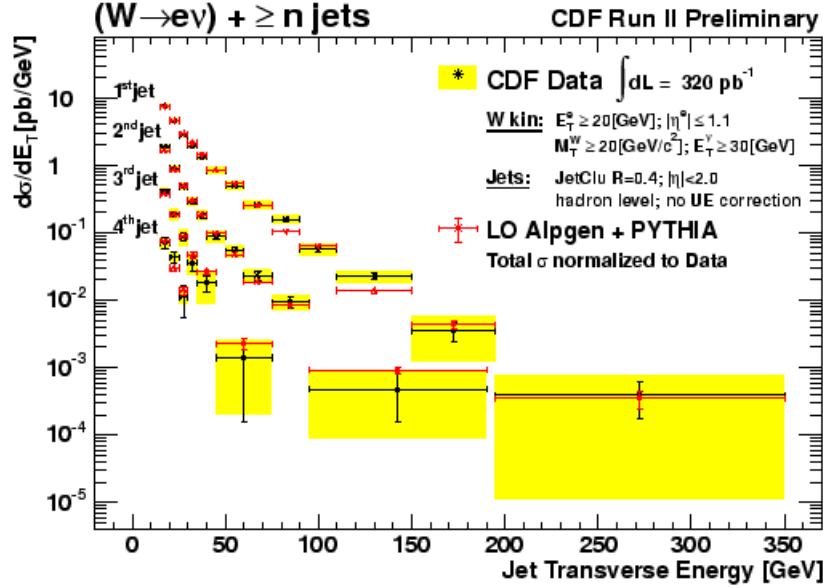
Figure 1.2. "The differential cross sections for the leading jet in ≥ 1 jet events, second jet in ≥ 2 jets events, third jet in ≥ 3 jets events, and fourth jet in ≥ 4 jets events [for jet transverse energy]. The W(ev) + 1p LO Alpgen(v2)+PYTHIA theoretical prediction is compared to the leading jet, $W(e\nu)$ + 2p to the second jet, and so on." [**17**]

1.3. Analysis Goals

The end goal of this analysis is to measure a wide array of cross-sections and cross-section ratios (literally observables formed by the quotient of two measured cross-sections) as a function of kinematic properties of jets produced in association with W bosons. We will briefly describe and motivate these final analysis observables (the full details of which will be reserved for chapter 9 when we present our results in full) but will first outline our expectations and preliminary analysis-oriented goals.

Unlike the previous CDF results and results at the Tevatron, we will present both the electron and muon channels which occupy roughly the same geometric acceptance. In both channels we will utilize the central part of the detector (favoring object transverse to
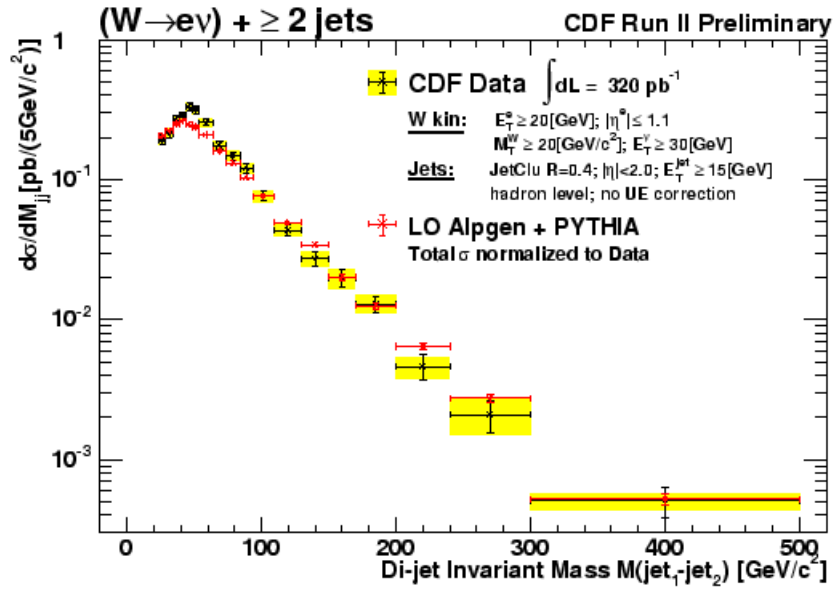
Figure 1.3. "The first-second jets invariant mass differential cross section for $W + \geq 2$ jets, where both jets have a minimum jet E_T of 15 GeV." [**17**]
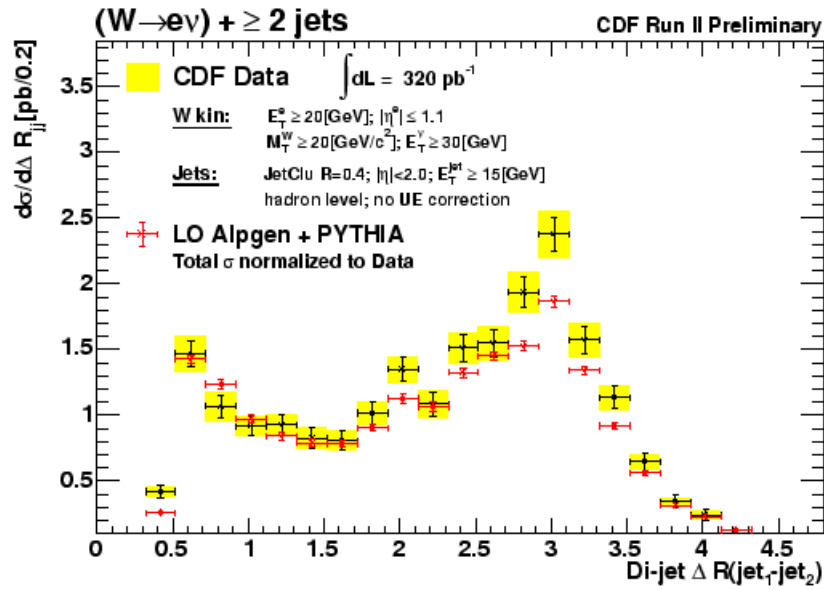
Figure 1.4. "The first-second jets ΔR differential cross section for $W + \geq 2$ jets, where both jets have a minimum jet E_T of 15 GeV." [**17**]

the beam direction) which happens to be the best understood area of the CDF detector. Another goal of this work was to incorporate improved $W/Z+m$ parton Monte Carlo ($m = 0 - 4$) that removed a possible bias in over (or under) counting the jet kinematic phase space. This problem plagued previous analysis work at CDF in both the internal QCD and Top Quark groups.

It is worth noting that this analysis does not focus on W+jets production where some number of the jets are tagged as heavy flavor (examples of these complimentary measurements at CDF are noted in [**16**]). As a result, our analysis focus on total jet production which is expected to favor jets associated gluon and light-flavor quark parton hadronization.

Additional preliminary and incremental goals include a full accounting of the W acceptance for each jet multiplicity which is independent of any parton sample cross-section weight or *a priori* assumptions. We also needed a systematic way to deal with the reality of additional reconstructed jets that are not originating from our primary event vertex associated with W production. This effect promotes the respective events to a higher jet multiplicity (we call this effect "promotion"). As a final issue to address is not only a full accounting of our individual systematic uncertainties but how and to what degree these uncertainties correlate with each other.

Once we have dealt with a multitude of intermediate goals, we form various differential cross-sections based upon jet kinematics for jet inclusive multiplicities 1 through 4. Most of the cross-sections of [**15**] are repeated. Our final measurements are present in chapter 9. We begin by focusing on the jet transverse momentum for each jet multiplicity. In each event, we can order the jets (by jet p_T) and construct a differential cross-section based on

the nth leading jet for $\geq n$ jets. Of course, from this we can immediately calculate the W cross-section for each jet multiplicity. As already noted (see previous section), this was the central measurement of the previous analysis. Likewise, we also measure the two dijet distributions formed by looking at the two leading jets in an event with at least two jets. First is the dijet mass and second is the dijet separation. We also look at two additional jet separation schemes based on the difference in pseudo-rapidity. With these results we also form the respective variable differential cross-sections.

One additional avenue of discovery open to us is to take the above quantities and construct various normalized shapes and cross-section ratios. From the point of view of theoretical predictions, comparing to absolute cross-sections is ideal but, on the other hand, dividing by the total cross-section gives a shape or relative measurement. The advantage as explained in chapter 8 is that many systematics are expected to cancel or be reduce and thus giving better constrained cross-section shape. We also consider for similar reasons taking quotients of our cross-section results.

1.4. Outline of Thesis

The main body of this thesis is divided into nine chapters including this introduction chapter. The next chapter deals with an overview of the Tevatron and accelerator complex at the Fermi National Laboratory (FNAL). Also in chapter 2, we discuss the CDF detector in general and the relevant sub-detectors needed for this thesis in particular. While the detector and accelerator discussion is obviously crucial to our final measurements, none of the details will be ground breaking as these have been dealt with *ad nauseam* in a multitude of previous papers and results.

Chapter 3 (page 105) deals with the details of our data and Monte Carlo samples. Many of the details of this chapter deal with technical matters related to the actual conduction of the analysis via the mature CDF run II software. Also for discussion is a breakdown of the total luminosity and the application of scale factors and weighting of the Monte Carlo samples.

The analysis proper begins in chapter 4 (page 116) where we discuss our selection of W candidates both in data and simultaneously in our signal and background Monte Carlo. This gives a detailed accounting of our selection cuts for both the electron and muon channels. The W selection chapter also describes our parallel construction of our QCD/fake background sample.

The W selection discussion of chapter 4 only gives us a sample of events likely to have high-momentum transfer (large Q^2) and relatively standard multi-jet production at the Tevatron. The next step is to analyze these events using our jet definition. This crucial discussion of our jet definition is executed in chapter 5 (page 135). In addition, this chapter presents our jet corrections in the form of detector level corrections (jet energy scale correction) as well as our correction to the hadron level (hadron unfolding correction).

Once we have constructed our final sample of selected events with our jet classification via our outlined procedure of the previous two chapters, we discuss our treatment of our expected backgrounds to our W+jets signal in chapter 6 (page 221). Our background estimation treatment involves a fitting procedure designed to remove any *a priori* bias assumptions on the W+jets and Z+jets cross-section and simultaneously scale our QCD/fake background estimation constructed from the data. Chapter 6 also details our

handling of promotion via an additional event selection criteria (the number of vertices) and scaling correction to the Monte Carlo simulation.

After the discussion of our background estimation, we present an experimental observable in the form of the number of W+jets candidates in data after removing the background. As our final goal is a cross-section or acceptance-corrected observable, we need to discuss our detector acceptance for W+jets events and our various selection efficiencies. This is achieved in chapter 7 (page 7). We also introduce the concept of a "constrained acceptance" or "reduced acceptance" as a way to make our final observables more palatable to theoretical predictions and to preclude any bias in our generated Monte Carlo samples in the kinematic regions excluded by our W selection.

With the details of our acceptance and efficiency chapter (combined with our discussion of the luminosity in chapter 3) we know have the ingredients necessary to construct our final cross-section based results. However, such measurements are effectively useless without an understanding of the various uncertainties (random errors and the more problematic systematic errors) associated with the measurement. Chapter 8 (page 362) deals with our systematic and Poisson errors.

The penultimate chapter, deals with our final results as a series of cross-sections and cross-section ratios for $W+ \geq n$ (n=1-4) jets. We provide our signal Monte Carlo as a baseline theoretical comparison and describe the basic requirements for future theoretical predictions of these results. In addition to a presentation of the CDF Run II preliminary results plots, chapter 9 (page 414) includes a general discussion of results and comments on any interesting features. The results obtained here are presented painstakingly in table form in Appendix A (page 465).

Finally, in chapter 10 (page 454) we provide the bookend to this thesis with a summary of analysis as a whole. We comment on the improvement of the analysis with respect to previous work and its general importance as an experimental measurement of QCD.

CHAPTER 2

The Tevatron and CDF Detector

The Fermi National Accelerator Laboratory (FNAL), also known as Fermilab, is a Department of Energy (DoE) national laboratory. Most of the work at FNAL deals with high energy physics. In particular, Fermilab is home of the Tevatron which is a proton/anti-proton ($p\bar{p}$) synchrotron with beam energies of 980 GeV (about a TeV). As of this writing, the Tevatron is now the second highest energy collider having been surpassed by the Large Hadron Collider (LHC) at CERN. It will cease collisions in October 2011.

There are two primary interaction point experiments on the Tevatron main ring which are named CDF and DØ. The latter is a collaboration named after the interaction point and is not directly relevant to the work presented in this thesis. The Collider Detector at Fermilab (hereafter, CDF) collaboration is a group of institutions (laboratories and universities) that conduct high energy particle research using the CDF Run II detector. The name of the collaboration and detector are often used interchangeably when the context is otherwise clear. The work presented here is made possible by the collisions produced by the Tevatron, the hard work of the members of CDF, and the data collected by the detector.

This chapter gives an overview of the main details surrounding the accelerator and detector. The next section of this chapter describes the Tevatron accelerator. In section 2.2 we describe the CDF Run II detector. We focus on the hardware and the various sub-detector systems that make up the full CDF detector. The details of both the accelerator

and main detector sections are crucial but likewise have been discussed *ad nauseam* elsewhere as Run II at the Tevatron is 10 years old and none of the discussion here presents new or ground breaking information. In section 2.3 we describe the physical objects we need to conduct our analysis and link this to the reconstruction of these objects via the detector. These objects include the measurement and identification of electrons and muons, the inference of the respective neutrinos, and the classification and measurement of jets. Additional details concerning the actual selection of these objects in presented in chapters 4 (W boson selection) and 5 (Jets definition and selection).

2.1. Tevatron Accelerator

The Tevatron itself is the 2.0 km diameter main ring whose above ground outline is prominently noticed in any aerial photograph such as figure 2.1. However, in order to get final proton/anti-proton beam energies at 980 GeV there are several stages of acceleration which includes the production of anti-protons ($\bar{p}$ or "p-bars"). Figure 2.2 is a schematic of the Fermilab/Tevatron accelerator complex and shows the various accelerator components.

Proton production begins with a hydrogen (gas) ion source (H^-) via Cockcroft-Walton. The negative hydrogen ions are accelerated to 750 keV. The Cockcroft-Walton is not shown in figure 2.2 but it is located at the start of the Linac. The aptly named Linac (linac: linear particle accelerator) accelerates the ions further to 400 MeV. The Linac then injects the beam into the Booster but not before a stripper foil removes the electrons from the hydrogen. The Booster is a synchrotron that accelerates the protons up to 8 GeV.

At this stage protons can be move to the Main Injector which serves a variety of functions. First, the Main Injector can accelerate protons up to 120 GeV to transfer

Figure 2.1. An aerial view of the Fermi National Lab (FNAL). The lower oval outline houses the main injector and recycler. The upper circle outline is the 2.0 km diameter Tevatron which includes both the CDF and DØ experiments.

to a Nickle (Ni) target for anti-proton production. Anti-protons are then debunched and cooled via the Debuncher. These anti-protons are then accumulated and stored via the Accumulator. Both the Debuncher and Accumulator are 8 GeV accelerators and are housed in the same "round-triangle" ring (see figure 2.2). From the Accumulator, anti-protons can then be moved to the Main Injector.

In addition to the Accumulator, Fermilab also makes use of the 8 GeV Recycler ring (housed with the Main Injector) which can store anti-protons. The Recycler indirectly helps to increase the anti-proton stacking (accumulation) rate as the stacking rate highest for an empty (or low stack) Accumulator. Anti-protons can then be injected back to the Main Injector.
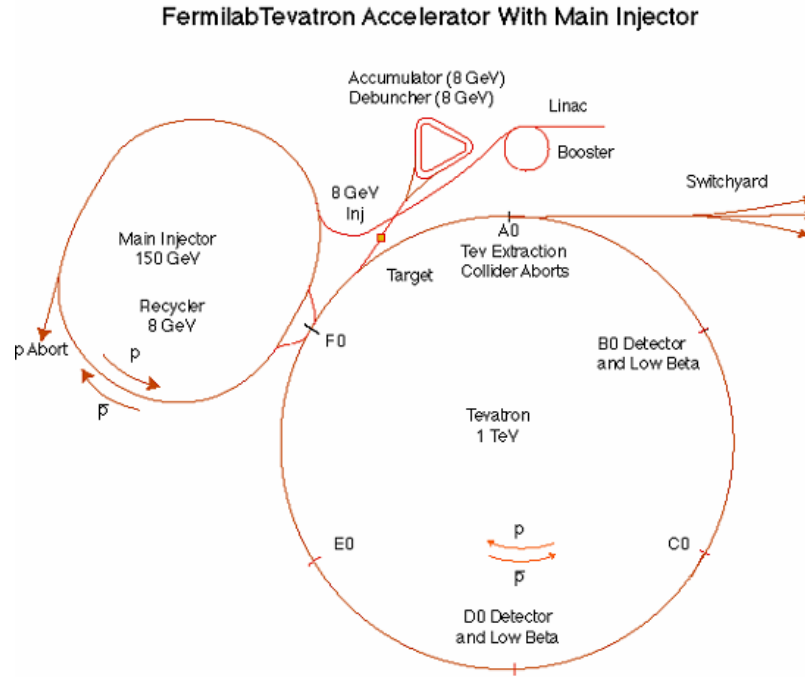
Figure 2.2. Schematic of the Tevatron Accelerator complex at Fermilab.

In the Main Injector protons or anti-protons can be accelerated (from 8 GeV) up to 150 GeV and be injected into the Tevatron. The Tevatron is a synchrotron that ramps up the beam energy (protons and anti-protons travel in the same beam pipe) from 150 to 980 GeV. The Tevatron houses two experiments at the two interaction points (low β). These two points (refer to figure 2.2) are named BØand DØ. As noted before, one of the experiments takes its name from the Tevatron nomenclature while the experiment at BØis CDF.

2.2. CDF Run II Detector Overview

For this analysis, we exclusively use data collected at the CDF Run II detector. For brevity, we will use the more colloquial name "the CDF detector" as this work was

undertaken during Run II at the Tevatron as part of the CDF collaboration. Modulo a few sub-detector upgrades or extensions (the details of which are not central to this thesis), the CDF detector has been operational since 2001. Previous descriptions of the CDF detector during earlier runs (circa 1987-1996) are described in [26]. The CDF detector was designed as an azimuthally and forward-backward symmetric detector structure designed to study $p\bar{p}$ collisions with center of mass energies approaching 2 TeV[18].

With respect to the CDF detector and this thesis analysis, we use a cylindrical coordinate system (r, ϕ, z) where the z-axis is along the proton (p) direction. Additionally, we use cylindrical angle system in which angles are measured with θ (ϕ) as the polar (azimuthal) angle. We define η (the pseudo-rapidity) as

$$(2.1) \qquad\qquad\qquad \eta \equiv -\ln(\tan(\theta/2))$$

where $\eta=0$ corresponds to a perpendicular axis with respect to the beam line. In CDF nomenclature the region around $|\eta| <1.0$ is the central region while $|\eta| >1.0$ is the forward region in the detector. In this thesis we also will use notation to describe transverse quantities. For example, the transverse momentum (i.e. p_T) is the momentum component on the $\eta=0$ axis and thus transverse to the beam direction. We also will use this notation for the transverse energy (E_T) such that

$$(2.2) \qquad\qquad\qquad E_T = E \sin(\theta)$$

and likewise for other quantities.

The CDF detector can be summarized as a general purpose solenoidal detector which combines precision charged particle tracking with fast projective calorimetry and fine
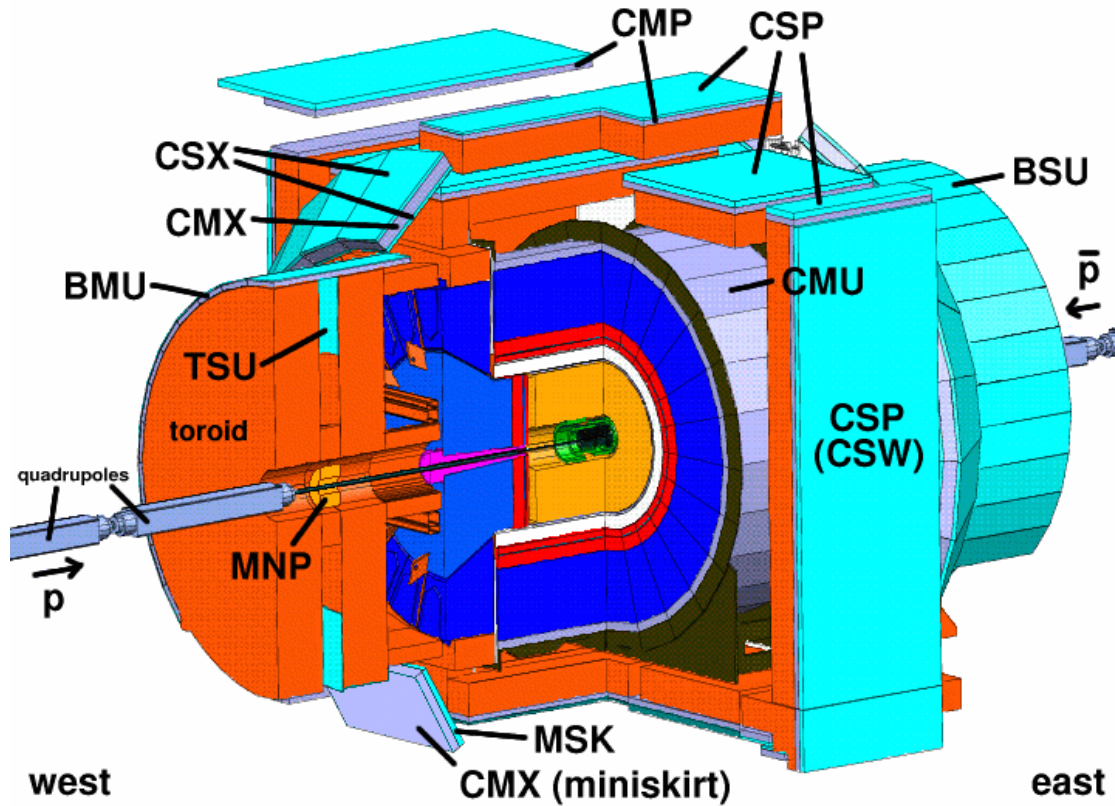
Figure 2.3. A cutaway model of the CDF Run II detector with the approximate placement of each sub-detector and its label (acronym). The inner details of the detector are shown in figure 2.4.

grained muon detection. The detector is general purpose in the sense that it can identify and measure multiple particle signatures and hence is open to a wide variety of high energy physics measurements. A color coated cutaway model is shown in figures 2.3 (overview) and 2.4 (inner details). The figures present a cornucopia of acronyms for the various sub-detectors. We will directly reference the relevant pieces of the detector needed in this thesis work in this section.

The basic of design of the detector is to have multiple layers of individual sub-detectors that measure individual physical components of each event and from these infer type of
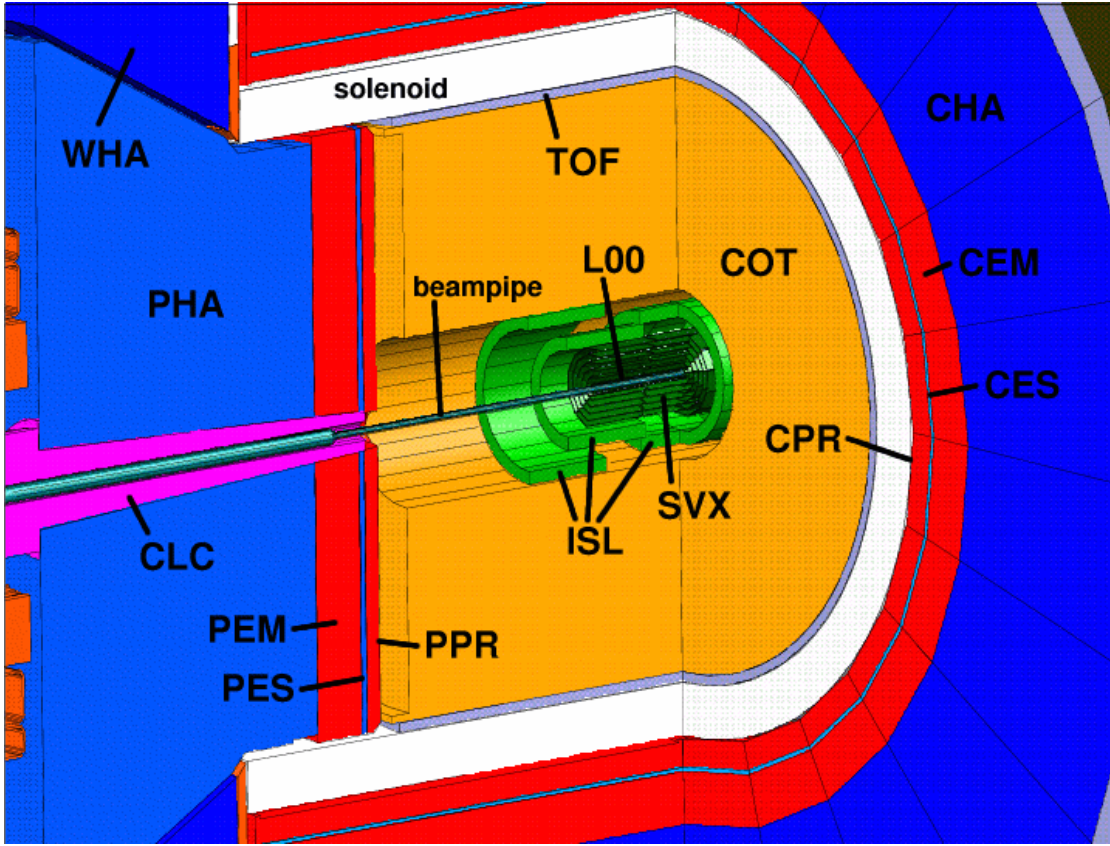
Figure 2.4. A cutaway model of the CDF Run II detector with the approximate placement of each sub-detector and its label (acronym). This is a zoomed in version of figure 2.3.

particle and its kinematics. Tracking systems are contained in a superconducting solenoid, 1.5 m in radius and 4.8 m in length. This generates a 1.4 T magnetic field parallel to the beam axis. Calorimetry and muon systems are all outside the solenoid. The description of how to use the detector as a whole to construct our data sample and primary physical objects is described in the next section.

The tracking system consists of a silicon microstrip system (silicon detector) [19] which surrounds of an open-cell wire drift chamber, the Central Outer Tracker (COT)[20]. The silicon microstrip detector consists of seven layers in the central region (an eighth layer is

available for $1.0 < |\eta| < 2.0$) in a barrel geometry that extends from a radius of r 1.5 cm from the beam line to $r = 28$ cm. The layer closest to the beam pipe is a radiation-hard single sided detector called Layer 00 (L00). This enables signal-to-noise performance even after extreme radiation doses. The remaining seven layers are radiation-hard double sided detectors. The first five layers outside of L00 comprise the Silicon Vertex (SVX) system and the two outer layers comprise the Intermediate Silicon Layers (ISL) system. These three systems (L00, SVX, and ISL) form the silicon detector which is the green region seen in figure (see figure 2.4). The silicon detector provides track reconstruction in three dimensions. The impact parameter resolution of the combination of SVX and ISL is 40 μm or 30 μm if including the contribution from the beamline. The z resolution for these two systems together is 70 μm.

The COT is a 3.1 m long cylidircal drift chamber that covers the radial range from 40 to 137 cm and provides 96 measurement layers organized into alternating axial and ± 2°stereo superlayers (eight combined in total)[20]. The COT provides coverage for $\eta < 1.0$. The hit position resolution is approximately 140 μm and the momentum resolution (curvature) resolution is $\Delta(p_T)/p_T^2 = 0.0015$ (c/GeV). A few centimeters outside the COT but inside the solenoid is a Time of Flight detector (TOF) based on plastic scintillators and fine meshed photomultipliers [21]. The TOF resolution is around 100 ps and it provides at least two standard deviation separation to distinguish between $K^\pm$ and $\pi^\pm$ for momenta (p) less than 1.6 GeV/c.

Segmented electromagnetic and hadronic calorimeters surround the tracking system and measure the energy of interacting particles in the range $|\eta| < 3.64$. The central calorimeters cover the range $|\eta| < 1.1$. The Central ElectroMagnetic calorimeter (CEM)

uses lead sheets interspersed with polystyrene scintillator as the active medium and employs photo-multiplier readout. Its energy resolution is $13.5\%/\sqrt{E_T} + 2\%$ [22]. The Central HAdronic colorimeter (CHA) uses steel absorber interspersed with acrylic scintillator as the active medium. Its energy resolution is $75\%/\sqrt{E_T} + 3\%$ [23]. The plug caloimeters cover the region $1.1 < |\eta| < 3.64$. The energy resolution of the Plug Electro-Magnetic (PEM) calorimeter is $16\%/\sqrt{E_T} + 1\%$ [24]. Resolution of the Plug HAdronic (PHA) calorimeter is $74\%/\sqrt{E_T} + 4\%$ [24]. Figure 2.4 displays the electromagetic (EM) calorimeters in red and hadronic (HAD) calorimeters in blue. The EM calorimeters (CEM and PEM) also contain a set of Shower-MaX (SMX) systems. These system are designed and positioned to be about 6 interaction lengths deep which is approximately the electron shower maximum (hence the name, shower-max). The Central Electromagnetic Shower-max (CES) and Plug Electromagnetic Shower-max (PES) are stripped detectors that provide position resolution of 2 mm at 50 GeV and are used for particle identification.

The muon system is the outermost system of detectors. Just outside the central calorimetry, four layers of planar drift chambers are positioned to detect muons with $p_T > 1.4$ GeV/c which penetrate the five absorption lengths of calorimeter steel. This inner central muon system is the Central MUon (CMU) detector. An additional four layers of planar drift chambers instrument 60 cm of steel outside the magnet return yoke and detect muons with $p_T > 2.0$ GeV/c. This detector was added as an upgrade to the CMU and is called the Central Muon uPgrade (CMP) detector. The CMU and CMP chambers each provide coverage in the range $|\eta| < 0.6$ although their physical geometries are quite different as highlighted by figure 2.3. Muon coverage is extended ($0.6 < |\eta| < 1.0$) with the Central Muon eXtension (CMX) detector. The CMX has eight (2×4) layers

of planar drift chambers that provide coverage in 87.5% of ϕ. Both the CMP and CMX are complimented by attached scintillation counters. The former by a single outside layer and the latter by both a outer and inner scintillator layer relative to the detector. The Central Scintillator uPgrade (CSP) and Central Scintillator eXtension (CSX) systems provide timing information good to 3 ns and are used to cut out-of-time background at the trigger. Note that figure 2.3 displays the muon drift chambers systems (CMU, CMP, and CMX) as purple while scintillator components (CSP and CSX) are shown in teal.

Crucial to many measurements including the cross-sections presented later in this analysis is the detector system for measuring beam luminosity. We achieve this by using gas Cherenkov counters located in the $3.7 < |\eta| < 4.7$ region. The Cherenkov Luminosity Counters (CLC) measures the average number of inelastic $p\bar{p}$ collisions per bunch crossing [25]. The CLC is displayed in magenta in figure 2.4.

The trigger and data acquisition systems are designed to accommodate the high rates and large data volume of Run II. The trigger system is designed to discriminate against events that do not pass basic selection criteria (e.g. high momentum quality track). There are three layers or levels of filter. The first is Level 1 (L1) which is a hardware trigger designed to process events in the 132 ns clock cycle between crossings. L1 takes an input rate on the order of MHz and reduces it of order 10 kHz. The second trigger level is Level 2 (L2) which is a dual hardware and quick software trigger which includes additional event information such as silicon detector tracking information. Processing time is of the order of 30 ms and L2 drops the event rate to hundreds of Hz. Finally Level 3 (L3) is a software trigger calculated via a PC farm. L3 reduces the rate to an manageable on the order of tens of Hz (max rate is about 75 Hz). The output from the trigger is written to tape

and eventually processed in order to reconstruct higher level physics objects (electrons, muons, etc.).

2.3. Detector Functionality

The previous section laid out the basic details of the CDF detector. However, once the raw data from the detector is process, there is still the work of using this information to form the needed physics objects. In this section, we will discuss how the results of various detector components are used in order to describe the physical process we are interested in (W+jets).

The main physical objects that we need to detect in order to reconstruct the leptonic decay of the W bosons are electrons, muons, and neutrinos. As noted in section 1.1, we do not consider $W \to \tau\nu$ in this analysis and thus do not directly concern ourselves tau leptons except as a possible fake to our signal. Ultimately, the objects of our affection are jets which will also be reconstructed using our detector results and with our jet definition. We now consider each of these objects one-by-one.

- Detection of electrons:

    The momentum unit vector of the electron is determined using the COT or the full tracking system of the COT and silicon detector. Since the electrons are completely absorbed in the calorimeters, its energy is thus the energy deposited in the calorimeters. The actual magnitude of the momentum of electrons is taken to be equal to their energy although in the CDF nomenclature, we explicitly cite the transverse energy (E_T, see equation 2.2) rather than transverse momentum (p_T) to avoid confusion with momenta measured via tracking. The calorimeter

energy describes more accurately the original energy of the electron because of potential almost co-linear photon-radiation in-flight by the electron. The energy of these photons will be measured by the same calorimeter wedges, so using the calorimeter instead of the tracker gives us the original energy of the electron. Almost all of the energy of the electrons is deposited in the EM calorimeter. In order to identify an electron candidate, its track is matched to the stripped detector (CES) situated at the location of the maximum shower of the electronin the calorimeter. Our electron selection is described further in section 4.1 (page 117).

- Detection of muons:

    Muons being minimally ionizing particles with interact weakly with the calorimeters and thus their momentum unit vector as well as it is magnitude is determined using only the COT or the full tracking system. At the same time, only muons as well as some hadronic punch-throughs are able to penetrate the entire CDF hadron calorimeter and steel to reach the muon detector system. As a result, a muon candidate has to have its track measured in the central tracking volume matched to a track segment inside the muon chambers (muon stub). Additionally, the high p_T muons we desire will, for the same reason, are expected to leave relatively little (a few GeV) in both the EM and HAD colorimeters. Our muon selection is described further in section 4.3 (page 120).

- Detection of neutrinos:

    Neutrinos are detected through their absence. They interact very weakly with the detector material (e.g. they have no electric charge) and effectively

leaving no trace of the presence. The solution is to infer the momentum of the neutrino via the additive inverse of the vector energy sum (i.e. the "missing energy" of the event assuming the conservation of 4-momentum). However, there is a complication which constrains this analysis and generally any measurement involving missing energy. The CDF detector has an instrumented volume due to the beam pipe which penetrates through it. As a result, the particles that are produced along or close to the z-axis are not fully reconstructed. Under such a configuration, missing energy along the beam direction is natural and no indication of a missing particle and its longitudinal momentum. On the other hand, all the energy deposited in the transverse plane can be recorded. We can thus associate any missing energy in the transverse plan as an indication of a production of a neutrino. From this, we can make an indirect measurement of the energy or momentum of neutrino via the conservation of transverse momentum-energy. We define this quantity as the missing transverse energy ($\not{E}_T$). Our calculation and basic corrections to the missing transverse energy is given in section 4.6. This transverse limitation does also force us to construct a transverse mass of the W which is discussed further in section 4.7.

- Detection of jets:

  Jets being a collimated stream of hadrons will deposit their energy in the electromagnetic and hadronic calorimeters. In this respect, jets are actually easy to reconstruct as there are no identification cuts and are selected based on their (transverse) momentum and pseudorapidity. What makes jets complicated is that there are a multitude of jet algorithms (jet reconstruction models) with

different advantages, weaknesses, and definitional parameters. In this analysis, jets are reconstructed using the Midpoint algorithm which is a seed based cone algorithm. The details of this algorithm and our jet definition are given in section 5.1.

Details of our actual selection cuts and other considerations are explained in detail in chapters 4 and 5 (pages 116 and 135, respectively).

CHAPTER 3

Data and MC Samples

This chapter deals with the basic description of the data and MC samples. We first describe several technical details with respect to the basic software analysis and data file format. In section 3.2 we discuss our data sample with respect to trigger requirements, run periods, and integrated luminosity. We note the use of the good run list (GRL) is section 3.3 which is used to skip runs where the detector was not optimal or consistent to be used in our analysis. Section 3.4 deals with the Joint Physics scale factor class and its use in our analysis. This is followed by two section on our Monte Carlo (MC) samples. The first (section 3.5) gives a description of each of the MC samples that is used while the last section deals with applying an event-by-event weight to the MC based on its generator or theoretical cross-section.

3.1. Software and File Format

This analysis uses topNtuples in collaboration with the Top Group. The samples and basic details can be found on various Top Group pages [27]. MC samples as well as data samples are inclusive samples in the sense that they are not filtered by any selection criteria. The topNtuple uses an electron-jet reclustering algorithm which is explained in section 5.2. In addition, we used a modified "top tarball" [29] to rerun over the initially generated W MC samples in order to perform a hadron level correction to our final cross-sections the details of this procedure are given in section 5.8 starting on page 165).

From the topNtuple we derive a reduced ntuple version which has the relevant and largely self-explanatory branches: `evt`, `lum`, `met`, `zvtxs`, `hepg`, `electron`, `muon`, `track`, and `jet`. We never filter our W MC since we use these samples in their entirety for our acceptance calculation. However, if a data or background sample event fails a basic selection criteria we skip the event. For example there has to be at least one lepton with E_T $(p_T) > 20$ GeV(/c) that passes basic track and fiducial requirements. However, we do not simply look for tight central lepton as our QCD background requires us to allow several identification (ID) or lepton quality variables to fail. There are secondary concerns as well like accounting for stubless muons in our missing energy correction which are discussed in section 4.6.

Our simplified ntuple allows us to run our analysis code locally to produce the necessary histograms by loading the ntuples and making the necessary event-by-event cuts. Once the basic selection stage of the analysis is over we then run over our histograms with the goal producing a final cross-section. Necessarily the analysis involves several components that have to be run in parallel (acceptance calculation, pdf and $t\bar{t}$ systematics) or separately (jet energy and hadron level systematics). Some components, most notably the reweighting of the MC via our vertex fitting (see section 6.6 on page 280) require rerunning the analysis as an iterative procedure and in conjunction with our background fitting procedure of section 6.4.

Our analysis code is produced via `CDFsoft2 6.1.4(.m)` and is run via complied ROOT code. The associated version of ROOT is 4.00/08 which is recognized as a relatively archaic version [**30**].

3.2. Data

In this analysis we concentrate on both the high p_T muon triggered data and also study corresponding trigger for the electrons. The electron trigger is via `HIGH_PT_ELECTRON` and the muon is via `HIGH_PT_MUON`.

We use data up to and including period 17 which are represented by 13 different run segments. Most of these segments directly correspond to a single run period or in the case of the first few segments a couple of periods taken together. These segments are defined in table 3.1 by the (inclusive) beginning and ending run numbers. Hereafter, we will refer to the integrated luminosity, L, as just the (total) luminosity. Technically this is just the summation of the individual luminosities (L_i) of each (i^{th}) segment:

$$(3.1) \qquad\qquad L = \sum_{\forall i} L_i$$

where i represents the different run periods. The actual luminsoity is derived via the measurement of the instantaneous luminosity, $\mathcal{L}$, which can be symbolically written as

$$(3.2) \qquad\qquad L = \int \mathcal{L}\mathrm{dt}$$

In table 3.2 we breakdown each run segment with their respective integrated luminosities for both CEM electrons and CMUP muons as well as CMX (arch and miniskirt) muons.

Run Period	Beginning Run #	Ending Run #
0d	138425	186598
0h	190697	203799
5-7	203819	212133
8	217990	222426
9	222529	228596
10	228664	233111
11	233133	237795
12	237845	241664
13	241665	246231
14	252836	254683
15	254800	256824
16	256840	258787
17	258880	261005

Table 3.1. Beginning and ending run numbers (inclusive) for each defined run segment and the corresponding CDF run period(s).

3.3. Good Run List

We are using good run list version 26 which includes runs up to and including period 17. We use the '(1, 0, 1, 1)' criteria which signifies the good detectors for CEM, CMUP, and CMX but no explicit SVX requirement [**31**].

3.4. Joint Physics Scale Factors

Details on the Joint Physics scale factor procedure are noted on the Joint Physics SF Spreadsheet/Class page [**32**]. The relevant results from which it is derived from are taken from the PerfIDia page [**33**]. Our discussion of the various lepton efficiencies that are needed for our cross-section measurements are described in section 7.6 on page 353. We apply the scale factor in part to address disagreement between MC (with full detector simulation) and data.

Run Period	CEM & CMUP Luminosity (pb^{-1})	CMX-Arch & Mini Luminosity (pb^{-1})
0d	360.1	340.1
0h	399.4	395.9
5-7	269.0	269.0
8	172.7	172.7
9	167.2	162.5
10	257.5	257.8
11	242.5	237.2
12	165.1	157.3
13	305.6	290.5
14	35.1	33.3
15	163.6	157.6
16	103.7	102.6
17	184.4	183.8
Total	2826.	2760.

Table 3.2. Luminosity (L) for CEM/CMUP events and CMX-Arch/CMX-Mini events for each run segment/period. The total integrated luminosity is given at the bottom. We latter assign a 6% systematic uncertainty due to our knowledge of the CLC (see section 7.7).

3.5. Monte Carlo (MC) Samples

Our analysis uses various *Monte Carlo* simulations (hereafter MC) to extract our background estimations and to compare with our expected signal. All of our main MC samples used in this analysis come from the Top Group's MC generation. With the exception of the special hadron level jet reconstruction samples described in section 5.8, we used the inclusive TopNtuples files [34]. Table 3.3 gives the CDF specific sample name and its corresponding process. The only special consideration of note in terms of specific parameters used in generations is for our $t\bar{t}$ production (data set: ytkt72) where we use a top mass of 172.5 GeV/c^2.

The Alpgen+Pythia MC references Alpgen (v2) with Pythia added to hadronize the W or $Z + n$ parton generation. The Alpgen generator is described in [35]. Although n partons (via CDF and the top groups generation [36]) generally correlates to final state with n (exclusive) jets this is not always the case. For example, Pythia can produce additional jets. This combined with jet detector acceptance allows for both promotion and demotion of the number of detector level jets relative to the number of generator level partons.

There is a real and potential concern for Alpgen with Pythia to "double count" events especially if one is interested in combining the various $W+\#$p samples together as a description for $W+ \geq n$ jets. Indeed this was an issue with a previous version of Alpgen (v1.3) which did not fully account for the potential for the overlapping phase space if the samples were naively added together with respect to potential non-physical bias between generator level "jets" and hadron level jets. However, this is no longer an issue as the current version incorporates MLM matching [35] between both levels during generation and thus avoids the potential to over count. The end result is that n partons (np) is matched at generator level to n jets (or ≥ 4 jets for 4p).

3.6. MC weighting to data

As will be explain in greater detail in chapter 6 we want to avoid biasing our background estimation with predictions from the MC. In particular this is a concern for our overall background estimation method when we want to account for our QCD (e.g. multijet) background which we derive from data and for which MC estimation is particularly

poorly suited. We formally tackle this concerns in chapter 6 but this section provides the baseline weighting of the MC for the analysis.

In order to get the relative cross-sections correct for W+jets and Z+jets production and in order to directly estimate the contributions for WW, WZ, $W\gamma^*$, and $t\bar{t}$, we scale the MC by weighting each event by w given by

$$(3.3) \qquad\qquad w = \frac{L_{\text{data}}}{L_{\text{eff}}}$$

with L_{eff} being the effective luminosity defined as

$$(3.4) \qquad\qquad L_{\text{eff}} = \frac{N(\text{Generated})}{\sigma(\text{MC})}$$

where L_{data} is the total luminosity (2826. pb^{-1}; see section 3.2), $N(\text{Generated})$ is the number of events generated in the MC sample, and $\sigma(\text{MC})$ is the MC or theory based cross-section. Obviously, this procedure does not effect the data which is not weighted ($w \equiv 1$). The theoretical cross-section values for WW, WZ, and $W\gamma^*$ are taken from [37] while we derive the $t\bar{t}$ cross-section from [38]. Section 6.1 (page 222) will elaborate on the details of our actual diboson and $t\bar{t}$ background estimation.

As explained in the previous section, we do not have samples that directly correspond to $\geq n$ jets for W+jets and Z+jets rather we have samples MLM matched for 0-4 partons at the generator level of Alpgen+Phythia. In this case, we present the a priori weighting based on equation 3.3 but the overall scale will be reweighted based off our template fitting method described in section 6.4. Thus only the relative cross-section for each parton sample will matter. The MC generator level cross-section for the W+#p and Z+#p partons comes from the top MC generation page [34].

Table 3.4 shows the event weight (w) for each MC sample along with the appropriate cross-section ($\sigma(\mathrm{MC})$), and number of events generated ($N(\mathrm{Generated})$). Note that the $W\gamma^*$ cross-section is effectively doubled (from 19.3 pb) to account for both $W \to e\nu$ and $W \to \mu\nu$. The number of events in each $W\gamma^*$ sample is 661901 and 688901 for the electron and muon channels, respectively.

Dataset	MC Sample	Generator
ptop0w	$W \to e\nu$+0p	Alpgen
ptop1w	$W \to e\nu$+1p	Alpgen
ptop2w	$W \to e\nu$+2p	Alpgen
ptop3w	$W \to e\nu$+3p	Alpgen
ptop4w	$W \to e\nu$+4p	Alpgen
ptop5w	$W \to \mu\nu$+0p	Alpgen
ptop6w	$W \to \mu\nu$+1p	Alpgen
ptop7w	$W \to \mu\nu$+2p	Alpgen
ptop8w	$W \to \mu\nu$+3p	Alpgen
ptop9w	$W \to \mu\nu$+4p	Alpgen
utop0w	$W \to \tau\nu$+0p	Alpgen
utop1w	$W \to \tau\nu$+1p	Alpgen
utop2w	$W \to \tau\nu$+2p	Alpgen
utop3w	$W \to \tau\nu$+3p	Alpgen
utop4w	$W \to \tau\nu$+4p	Alpgen
ztop0p	$Z \to ee$+0p	Alpgen
ztop1p	$Z \to ee$+1p	Alpgen
ztop2p	$Z \to ee$+2p	Alpgen
ztop3p	$Z \to ee$+3p	Alpgen
ztop4p	$Z \to ee$+4p	Alpgen
ztop5p	$Z \to \mu\mu$+0p	Alpgen
ztop6p	$Z \to \mu\mu$+1p	Alpgen
ztop7p	$Z \to \mu\mu$+2p	Alpgen
ztop8p	$Z \to \mu\mu$+3p	Alpgen
ztop9p	$Z \to \mu\mu$+4p	Alpgen
ztopt0	$Z \to \tau\tau$+0p	Alpgen
ytkt72	$t\bar{t}$	Pythia
itopww	WW	Pythia
itopwz	WZ	Pythia
rewk28	$W(\to e\nu)\gamma^*$	Baur
rewk29	$W(\to \mu\nu)\gamma^*$	Baur

Table 3.3. The table gives the dataset name of MC samples used, their generator, and their corresponding physical processes. All samples are inclusive (no special filtering) and come from the Top MC page [**34**]. Standalone Pythia samples come from version 6.216 while Alpgen samples come from v2.10. In addition, the Alpgen generator also includes Pythia (v6.325) for showering and is often denoted by "Alpgen+Pythia". The number of events as well as the appropriate theoretical or MC generator based cross-section for weighting is given in table 3.4 and described in section 3.6. The ytkt72 ($t\bar{t}$) sample was generated using a top mass of 172.5 GeV/c^2.

Segment #	MC Sample	σ(MC/Theory) (pb)	N(Generated)	weight (w)
1	$W \to e\nu$+0p	1800	997474	5.100
2	$W \to e\nu$+1p	225	1013373	0.627
3	$W \to e\nu$+2p	35.4	1003193	0.100
4	$W \to e\nu$+3p	5.6	1003040	0.016
5	$W \to e\nu$+4p	1.03	989607	0.003
6	$W \to \mu\nu$+0p	1800	1013373	5.020
7	$W \to \mu\nu$+1p	225	1013373	0.627
8	$W \to \mu\nu$+2p	35.4	1002804	0.100
9	$W \to \mu\nu$+3p	5.6	1013373	0.016
10	$W \to \mu\nu$+4p	1.03	988545	0.003
11	$W \to \tau\nu$+0p	1800	952876	5.338
12	$W \to \tau\nu$+1p	225	965219	0.659
13	$W \to \tau\nu$+2p	35.4	923989	0.108
14	$W \to \tau\nu$+3p	5.6	1008221	0.016
15	$W \to \tau\nu$+4p	1.03	986494	0.003
16	$Z \to ee$+0p	158	513779	0.869
17	$Z \to ee$+1p	21.6	536159	0.114
18	$Z \to ee$+2p	3.47	536159	0.018
19	$Z \to ee$+3p	0.55	528491	0.003
20	$Z \to ee$+4p	0.0992	525065	0.001
21	$Z \to \mu\mu$+0p	158	536159	0.833
22	$Z \to \mu\mu$+1p	21.6	536159	0.114
23	$Z \to \mu\mu$+2p	3.47	530843	0.018
24	$Z \to \mu\mu$+3p	0.55	536159	0.003
25	$Z \to \mu\mu$+4p	0.0992	536159	0.001
26	$Z \to \tau\tau$+0p	158	1170084	0.382
27	$t\bar{t}$	7.5	1186128	0.018
28	WW	12.4	2284862	0.015
29	WZ	3.96	2340145	0.005
30	$W\gamma^*$	38.6	1350802	0.081

Table 3.4. Default MC weighting for each MC sample

Which MC segment

Which MC segment - normal fill
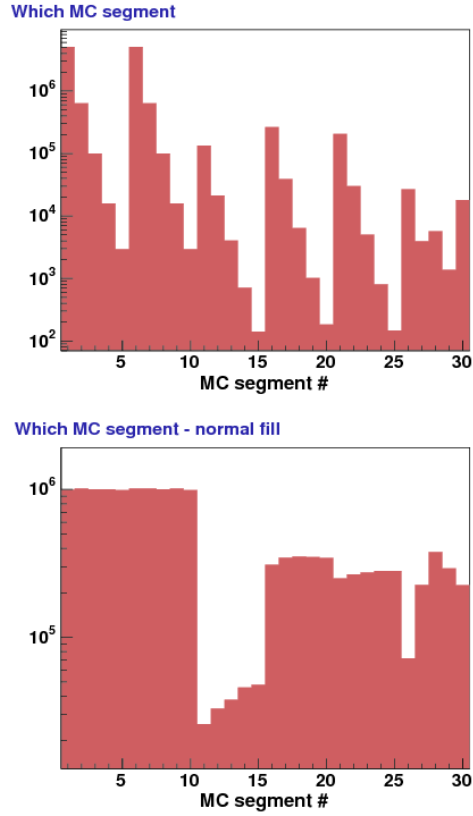
Figure 3.1. The bottom plot gives the number of events in each MC sample while the top gives the number of events relative to the luminosity via the weighting scheme given in equation 3.3. Note that for segments above 10 (non-signal MC) a simple filter has been applied to remove events that will clearly our selection (e.g. having a lepton with $p_T > 10$ GeV/c. MC Segment # is given in table 3.4.

CHAPTER 4

W selection

The selection of the W boson candidate events is straight forward. We select high momentum electrons and muons which pass the standard "tight" central lepton cuts along with some additional analysis specific requirements. Using the transverse energy or momentum of the selected lepton (electron E_T and muon p_T, respectively) and the missing transverse energy ($\not{E}_T$) of the event (representing the energy lost from the non-interacting neutrino), we reconstruct the W transverse mass (M_T) which we use as our final selection cut. In the next chapter, we define our jet selection and this will end up putting further constraints on our final W selection as will be explained in detail there.

The next section of this chapter deals with the electron selection while section 4.3 gives the selection criteria for the muons. Following each respective section we present the requirements of a sample that will be used to estimate our QCD background (from multi-jet fakes, etc.). This sample is defined by inverting certain selection cuts and will be denoted as our *anti-selected* lepton requirements. Sections 4.2 and 4.4 deal with our anti-selected electron and muon selection, respectively.

Our selection procedure produces events where we may have multiple candidates. Section 4.5 deals with event level veto on events with dileptons or otherwise characteristic of Z-like production. As a preamble to our W selection, we define our missing energy procedure in section 4.6. In the final section, we describe our W selection (for both electrons and muons) based off of our reconstructed W transverse mass.

4.1. Electron selection

Electron candidate events are selected based on a high E_T requirement for central electro-magnetic (CEM) object along with a series of quality and identification (ID) cuts in addition to basic fiducial and tracking constraints. In the CDF nomenclature these will be "tight electrons" [**40**] with a few additions mentioned below. Unlike the muons, there is only one equivalent (sub-)detector classification for electrons; namely the central calorimeter. We do not use more forward electrons (plug-electrons) in this analysis. We will simply refer to electron related quantities (for their acceptance, efficiencies, etc.) as CEM. Table 4.1 summaries our tight selection cuts.

Selection Cut	Notes and Details
Fiducial CEM electron $|\eta| \leq 1.1$	
$|z_0| \leq 60.$ cm $|z_0 - z_{vtx}| \leq 2.0$ cm $1 \leq \#$ vertices ≤ 3	z_{vtx} closest vertex quality 12 vertices with $p_T > 10$ GeV/c
Conversion Veto	**not** a conversion
$E_T \geq 20$ GeV $p_T \geq 10$ GeV/c	calorimeter based E_T track based p_T
$(E_{HAD}/E_{EM}) \leq 0.055 + 0.00045E$ $L_{\text{shr}} \leq 0.2$ $E/p \leq 2.0$ **or** $p_T \geq 50$ GeV/c	$E = E_{EM} + E_{HAD}$
$-3.0 \leq q\Delta x \leq 1.5$ cm $|\Delta z| \leq 3.0$ cm $\chi^2_{\text{strip}} \leq 10.$	$q =$ electron charge
$\#$ COT Axial Segments ≥ 3 $\#$ COT Stereo Segments ≥ 2	with ≥ 5 hits/segment with ≥ 5 hits/segment
(Relative) Isolation ≤ 0.1	isolation with $R = 0.4$

Table 4.1. Electron selection requirements

The first non-standard lepton selection cut is our $|\Delta z_{vtx}| < 2.0$ cm requirement. The motivation for this cut is to veto events where the lepton's vertex information was not

well understood. The form the cut takes is similar to the $|z_+ - z_-| < 4.0$ cm constraint on (opposite-sign) dileptons such as the $Z \to \ell^+\ell^-$ production. We define Δz_{vtx} as the separation between the leptons vertex position (z_0) and the closest (best) quality 12 vertex with $\sum p_T^{vtx} > 10$ GeV/c or

$$\Delta z_{vtx} \equiv |z_0 - z_{vtx}|$$
(4.1)

Functionally, we loop over the `zvtxs` collection with the standard vertex quality check along with a sum vertex (track) momentum cut. At the level our implementation, this cut enforces our lower side # vertices ≥ 1 cut which is simply a check that the lepton vertex information matches to a good vertex. Section 6.6 on page 280 deals with our vertex definition and related particulars as it applies to our reweight of the number of vertices in the MC. We give the full motivation for our # vertices ≤ 3 cut there but the basic concept is to reduce the number of additional interactions in the event to control for promotion. As will be noted in full in our acceptance chapter, the acceptance is about 95% and does not show a dependence on jet multiplicity. In addition to using this Δz_{vtx} cut for electrons we apply it to muons as noted in section 4.3. We show the distribution (using the muon channel) in figure 4.1.

4.2. Anti-selected Electrons

In this section we introduce a separate set of cut requirements that will allow us to build a sample that will be used to estimate our QCD/fake background. We call this sample our "anti-selected electrons" as they are comprised of events from our same high p_T trigger data sample that necessarily were not selected in the analysis but are informative

of the behavior of non-W events. The sample will be composed of potential electron candidates which pass our basic kinematic/acceptance requirements but are likely fakes due to failing some of our identification requirements. This anti-selection electron sample becomes the bases for our QCD template explained in section 6.3 on page 226.

The previous version of this analysis was the vanguard of this procedure where the nomenclature of these candidates were called "anti-electrons" [12]. We note that several of our plots will make reference to this older and somewhat imprecise descriptor for convenience. This is more of an issue on our anti-selected muons (see section 4.4) where "anti-muon" could be confusing.

The selection criteria for our anti-selected electrons mirrors the selection requirements of the previous section. The difference is that several of the electron quality/identification cuts are allowed to be inverted. We require two or more of the cuts in table 4.2 to fail our normal selection cut. In other words, these anti-selected candidates must pass two (or more) of our *inverted* selection requirements. Consistent with finding of the previous analysis, we do not use the calorimeter based isolation requirement nor the E/p ratio to minimize potential bias in measuring our final jet kinematics.

Inverted Selection Cut	Notes and Details
$|z_0 - z_{vtx}| > 2.0$ cm	z_{vtx} closest vertex
$(E_{HAD}/E_{EM}) > 0.055 + 0.00045E$	$E = E_{EM} + E_{HAD}$
$L_{\text{shr}} > 0.2$	
$\chi^2_{\text{strip}} > 10.$	
$q\Delta x < $ -3.0 **or** $q\Delta x > 1.5$ cm	CES Δx, $q = $ charge
$|\Delta z| > 3.0$ cm	CES Δz

Table 4.2. Anti-selection electron candidates must pass two of the listed "inverted" cuts.

Events which pass our anti-selection cuts are subject to the same constraints as our normal W candidate events. As such, they undergo the same Z-veto procedure of section 4.5 as well as the transverse mass cutting scheme of section 4.7. They will also need to pass the same lepton-jet requirements but with several important caveats (e.g. section 5.3). We present the composition of our anti-selected sample ($M_T > 20$ GeV/c^2) in table 4.3. We have approximately 358k events in the total inclusive ≥ 0 jet bin and 600 in the inclusive ≥ 4 jet bin.

Inverted Cut Variable	# of events (in data)	Relative Fraction (%)
HAD/EM	196582	54.9
CES Δx	100149	28.0
CES Δz	106938	29.9
L_{shr}	213848	59.7
χ^2_{strip}	281185	78.5
Δz_{vtx}	16360	4.5
Total	358204	100.

Table 4.3. The composition of anti-selection electron candidates with $M_T > 20$ GeV/c^2. Anti-selection electrons must fail two (or more) cuts of table 4.2 but pass the remaining lepton and W selection criteria modulo additional constraints due to jet selection. The relative fraction is the fraction of events that pass the inverted cut (i.e. fail the nominal lepton candidate selection cut).

4.3. Muon selection

Our muon selection proceeds as follows. We select events by requiring a high transverse momentum track matched to a muon stub in the central muon detectors. These muon candidate events then have to pass additional tracking requirements and have their own set of identification cuts. The latter are based on the amount of energy (absolute and relative) deposited in the calorimeter which is expected to be small for minimally ionizing

particles (i.e. muons). Like our electron selection, our final muon selection is a "tight muon" [41] with a couple of additional constraints.

Whereas our candidate electrons are constructed via a universal selection of the central calorimeter (CEM), central muons are divided up into three sub-detectors which we will denote as CMUP, CMX-Arch, and CMX-Mini. A CMUP muon is formed using the stub information for both the CMU (Central MUon) and CMP (Central Muon uPgrade) detectors [42]. We do not use the exclusive CMU or CMP muon definitions in this analysis. However, some cuts (notably the stub minus tracking location in local x, Δx) require specific detector. The detector coverage for CMU/CMP and therefore the range of our selected CMUP muons is approximately $|\eta| < 0.6$ representing the central most selection of our muon sample.

The CMX (Central Muon eXtension) detector [42] is further sub-divided into the CMX *arches*, *keystone*, and *miniskirts*. The difference between the CMX divisions is primarily due to their coverage as well as historical details about their commissioning. A historical note giving details on using CMX muons is given in [43]. In our analysis CMX-Arch or simply Arches will represent the CMX arches and keystone while CMX-Mini will signify CMX miniskirt muons. In many cases, such as the selection cuts presented in this section, a CMX muon will represent the obvious union between CMX-Arch and CMX-Mini. True to its name, the CMX extends coverage out to approximately $0.6 < |\eta| < 1.0$ although the azimuthal angle (ϕ) coverage is not complete (300°east and 330°west).

For our purposes here we note that for many considerations of the analysis we will have to deal with each sub-detector individually. For example, our acceptance and efficiencies calculations require this sub-dividing while our selected muon events from data and MC

(after their respective detector dependent cuts) are simply pooled together as candidate muon events. Table 4.4 presents our selection requirements for CMUP and CMX muons. As needed, the type of muon cut required (CMUP and CMX) will be noted in the second (Notes and Details) column.

Selection Cut	Notes and Details
Cosmic Veto	COT out of time veto
Muon Fiducial to CMU	for CMUP muons
Muon Fiducial to CMP	for CMUP muons
Muon Fiducial to CMX	for CMX muons
$\rho(\eta, z_0) \leq 140$ cm	COT exit radius cut for CMX muons
$\|z_0\| < 60.$ cm	
$\|z_0 - z_{vtx}\| < 2.0$ cm	z_{vtx} closest vertex
$1 \leq \#$ vertices ≤ 3	quality 12 vertices with $p_T > 10$ GeV/c
$p_T \geq 20$ GeV/c	track based p_T
$\|\Delta x_{CMU}\| < 7.0$ cm	CMU stub/track match
$\|\Delta x_{CMP}\| < 5.0$ cm	CMP stub/track match
$\|\Delta x_{CMX}\| < 6.0$ cm	CMX stub/track match
# COT Axial Segments ≥ 3	with ≥ 5 hits/segment
# COT Stereo Segments ≥ 2	with ≥ 5 hits/segment
$\|d_0\| \leq 0.20$	no silicon hits
$\|d_0\| \leq 0.02$	with silicon hits
$\chi^2_{\text{COT}} < 2.75$	for run # ≤ 186598 (*data only*)
$\chi^2_{\text{COT}} < 2.30$	for run # > 186598 (*data only*)
$E_{EM} \leq \text{MAX}[2, 2+0.0115 \times (p - 100)]$	track based p
$E_{HAD} \leq \text{MAX}[6, 6+0.0280 \times (p - 100)]$	track based p
(Relative) Isolation < 0.1	isolation with $R = 0.4$

Table 4.4. CMUP and CMX Muon selection requirements

The muon COT exit radius (ρ) requirement is taken with the COT length (z_{COT}) from the origin as 155 cm [44]. The formula for ρ is given by

$$(4.2) \qquad \rho_{\eta \gtrless 0} \equiv \frac{\pm(z_{\text{COT}} \mp z_0)}{\tan\left(\frac{\pi}{2} - \theta\right)}$$

where θ is the zenith angle of the muon in radians and the plus or minus signs correspond, respectively, for $\eta \gtrless 0$.

The $\Delta z = |z_0 - z_{vtx}|$ requirement is the same as described in our electron section. We also apply the same vertex requirements as noted in the table. Its discrimination power in data for muons is a bit stronger due to the nature of potential fakes and is 98% efficient on signal with no significant correlation with jet multiplicity.

The χ^2_{COT} is an additional lepton requirement for our muon selection beyond the normal tight muon cuts. It is a track based cut representing the reduced goodness of fit measure via the COT tracking information. This cut was suggested by colleagues and used in several analysises at CDF [45][46][47]. The discussion of this cut and its efficiency for intermediate ($5 < p_T < 20$ GeV/c) muons in [48] was also instructive. We note that the reduced COT χ^2 cut is run dependent and is applied only to the data consistent with [45][46]. Although this is likely an artifact of our tracking simulation and/or the details of the χ^2_{COT} calculation, the cut, if applied to our signal MC, would be fully efficient. The χ^2_{COT} distribution after the basic selection criteria given here but without our final W selection of section 4.7 is shown in figure 4.2.

4.4. Anti-selected Muons

As was the case with our electron sample we mirror our muon channel W selection with an anti-selected muon sample described here. The basic kinematic selection criteria is the same but we look for events that pass at least two of the inverted cuts as noted in table 4.5 with additional details to follow. The relative composition of our anti-selected muon pre-template is given in table 4.6.
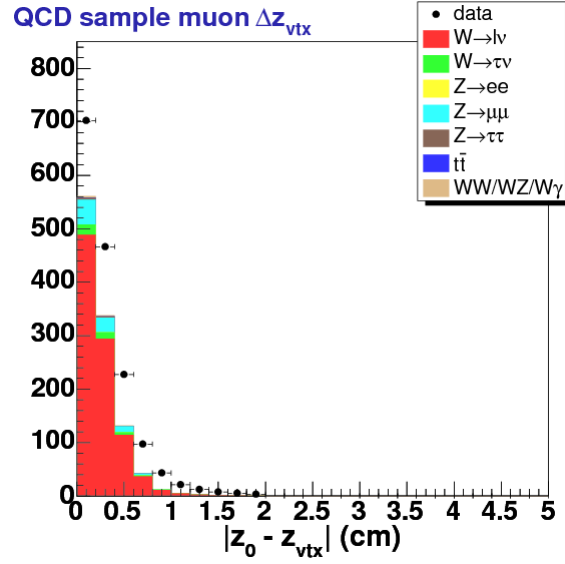
Figure 4.1. Δz_{vtx} (as defined in equation 4.1) used in our lepton selection (muon channel results shown). The cut at 2.0 cm is highly efficient with our signal MC and rejects potential fakes where Δz_{vtx} becomes flat in the data pass our cut.
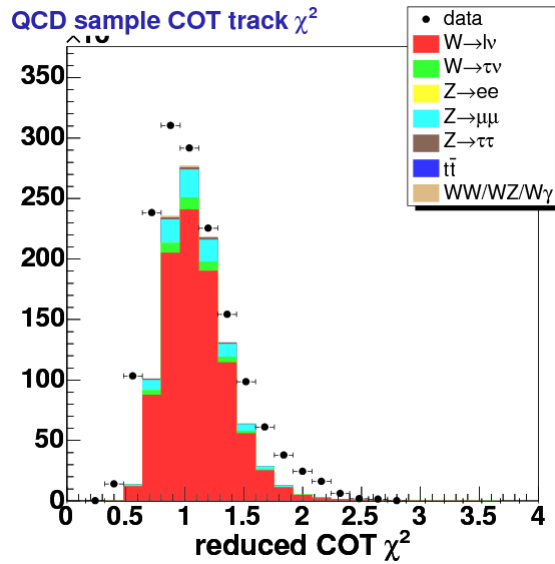
Figure 4.2. χ^2_{COT} is the per-degree-freedom χ^2 (COT) tracking quality of fit variable with our basic muon sample selection.

It is instructive to divide the 6 quality/ID cuts into two classifications. First there are calorimeter/energy base cuts which include the isolation (ISO), EM, and HAD variables. These are the equivalent of the majority of the anti-selection electron quality/ID cuts and are characteristic of our multi-jet background as well as punch-throughs. The second triplet of cuts are track/stub/vertex based using the χ^2_{COT}, Δz_{vtx}, and Δx variables. The latter set of inverted cuts is particularly descriptive of decays in flight as well as semi-leptonic decays. Note that the anti-selection muon candidates here form a single QCD template as noted in section 6.3. In other words, like our anti-selection electron sample we combine all the cuts together and do not try to separately account for different types of fakes.

Inverted Selection Cut	Notes and Details
$|z_0 - z_{vtx}| > 2.0$ cm	z_{vtx} closest vertex
$7.0 < \Delta x_{\mathrm{CMU}} < 14.0$ cm $5.0 < \Delta x_{\mathrm{CMP}} < 13.0$ cm $6.0 < \Delta x_{\mathrm{CMX}} < 12.0$ cm	
$\chi^2_{\mathrm{COT}} > 2.75$ $\chi^2_{\mathrm{COT}} > 2.30$	for run # ≤ 186598 for run # > 186598
$2 < E_{EM} < 20$ GeV	
$6 < E_{HAD} < 60$ GeV	
$0.1 < \text{Isolation} < 0.67$	isolation with $R = 0.4$

Table 4.5. Anti-selection muon candidates must pass two of the listed "inverted" cuts.

With our Δx cuts we decided to look at the shape of MC simulation and a sample of muon candidates without the stub-track cut in addition to our prospective anti-selection sample. We found these distributions (pass their respective nominal detector based Δx cut) were composed of a flat distribution that extended pass twice the normal cut and a tail consistent with our MC and quality data sample. Our upper bound anti-selection cut

(as given in table 4.5) represent the cut off when the natural tail events where the stub and track were in all likely hood actually linked was dominated by the flat (random/uniform) Δx component.

The Δx cut for a CMUP muon counts as a single inverted cut. In our normal CMUP muon selection we require both the CMU and CMP Δx cuts to pass so when we invert it we only need one cut to fail the CMUP Δx criteria (i.e. we follow De Morgan's law). We originally had a much tighter CMU cut (3 cm verses 7 cm) but loosening the cut had no effect on the anti-selected muon sample size but effectively increased our signal acceptance and efficiency [49].

The energy based variables (E_{EM}, E_{HAD}, and isolation) as well as our Δx have upper bounds on their inverted cuts. The former triplet is based on scaling the nominal (inverted) bound by a factor of 5. The basic feature of these observables is that they have long tails (see for example figures 4.3 and 4.4) for potential muon fakes. As one would expect cutting on isolation immediately limits the EM and HAD observables (they are efficient cuts given isolation).

Like our anti-selection electrons, events which pass our anti-selection muon cuts are subject to the same constraints as our normal W candidate events. As such, they undergo the same Z-veto procedure of section 4.5 as well as the transverse mass cutting scheme of section 4.7. They will also need to pass the same lepton-jet requirements but with several important caveats (e.g. section 5.3). We present the composition of our anti-selected sample ($M_T > 20$ GeV/c^2) in table 4.6. We have approximately 438k events in the total inclusive ≥ 0 jet bin and about 3200 in the inclusive ≥ 4 jet bin.
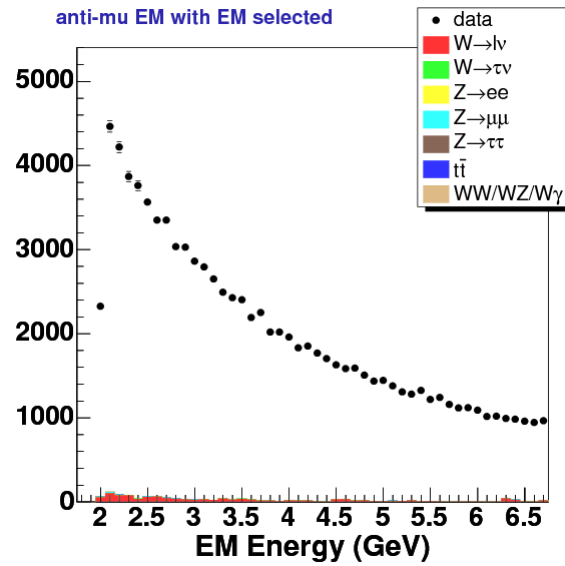
Figure 4.3. EM energy (E_{EM}) associated with the linked calorimeter towers for an anti-selected muon sample with $E_{EM} > 2.0$ GeV.
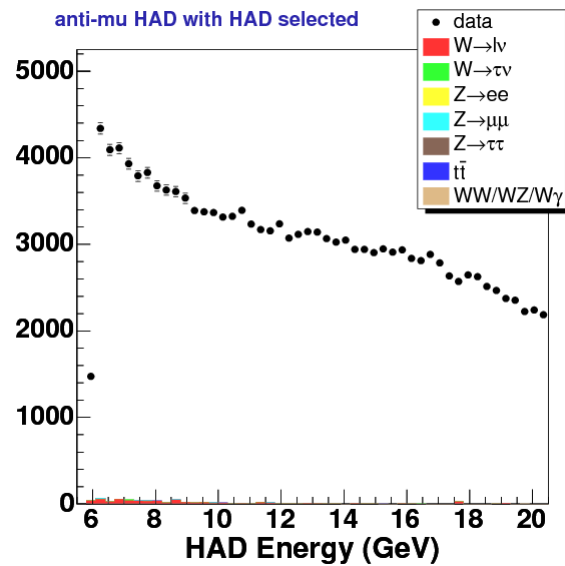
Figure 4.4. HAD energy (E_{HAD}) associated with the linked calorimeter towers for an anti-selected muon sample with $E_{HAD} > 6.0$ GeV.

Inverted Cut Variable	# of events (in data)	Relative Fraction (%)
Δx	31318	7.2
Δz_{vtx}	64346	14.7
χ^2_{COT}	102289	23.3
E_{EM}	161756	37.0
E_{HAD}	259853	59.4
Isolation	397882	90.9
Total	437605	100.

Table 4.6. The composition of anti-selection muon candidates with $M_T >$ 20 GeV/c^2. Anti-selection muon must fail two (or more) cuts of table 4.5 but pass the remaining lepton and W selection criteria modulo additional constraints due to jet selection. The relative fraction is the fraction of events that pass the inverted cut (i.e. fail the nominal lepton candidate selection cut).

4.5. Z Veto

Events which have two or more selected leptons are vetoed as these are clearly not representative of our expected W signal. This is done regardless of the charge, dilepton mass, or electron/muon combination. The same procedure is carried out in our anti-selected lepton events with the equivalent motivation to produce representative W *fakes*. This procedure alone vetoes some 87k multi-lepton events most of which are likely Z decays as confirmed from our Z MC. The veto also removes obvious diboson candidates.

In addition, we look for Z production in the mass window of $m_Z = $ 76-106 GeV/c^2 via two additional selection methods. First we look as lose lepton requirements as defined in table 4.7. The second method involves looking at the track collection and performing a similar simple selection as outlined in table 4.8. Once we have a selected (or anti-selected) lepton we loop through the other potential candidates in our lepton and track collections. If a opposite signed candidate spotted passing the prerequisite cuts and inside our mass

window, we veto the event. There are over 123k events vetoed in this way with 80%
coming from our additional lepton selection verses the 20% acquired via our track based
veto method.

Electron	Muon
$E_T > 10$ GeV	$p_T > 10$ GeV/c
HAD/EM < 0.12	EM < 3 GeV
	HAD < 9 GeV
Isolation < 0.15	Isolation < 0.15

Table 4.7. Summary of lepton cuts use to veto potential Z and other non-single W decays. If an additional opposite signed lepton if found that passes the above cuts and has dilepton mass between 76 and 106 GeV/c^2 the event is vetoed.

Track Requirement	Notes and details
# COT Axial Segments ≥ 3	with ≥ 5 hits/segment
# COT Stereo Segments ≥ 2	with ≥ 5 hits/segment
$p_T > 10$ GeV/c	beam constrained track p_T
$|z_0 - z_{\text{trk}}| $ ¡ 10 cm	lepton vs. track z
Absolute Isolation < 4 GeV	$p_T \times$ Isolation

Table 4.8. Summary of track based cuts use to veto potential Z and other non-single W decays. If an additional opposite signed track if found that passes the above cuts and has dilepton mass between 76 and 106 GeV/c^2 the event is vetoed.

4.6. Missing Energy Corrections (muons)

The procedure for calculating the missing transverse momentum ($\not{E}_T$) begins by calculating a vector sum over all calorimeter towers. Let $\vec{E}_{\text{EM}}^{\,\eta,\phi}$ and $\vec{E}_{\text{HAD}}^{\,\eta,\phi}$ be the respective transverse EM and HAD energy associated with a calorimeter tower denoted by its η-ϕ

location. The equation for the raw missing energy $(\vec{\not{E}}_T^{\text{raw}})$ is given by

$$(4.3) \qquad \vec{\not{E}}_T^{\text{raw}} \equiv - \sum_{\forall \text{ towers}} \left(\vec{E}_{\text{EM}}^{\,\eta,\phi} + \vec{E}_{\text{HAD}}^{\,\eta,\phi} \right)$$

which is simply the sum negation of the EM and HAD vector sum. However, equation 4.3 does not account for the transverse energies associated with minimum ionizing particles that can have a high (track-based) transverse momentum that leave little energy in the calorimeter (e.g. muons). As a result, we need to correct for the effect of muons. The initial correction is just to subtract the vector transverse momentum of the muon $(\vec{p}_T^{\,\mu})$. This is correct but since muons do leave some energy in the calorimeter and this feature will need to be addressed. To this end, let $\vec{E}_{\text{EM}}^{\,\mu}$ and $\vec{E}_{\text{HAD}}^{\,\mu}$ be the transverse EM and HAD energy in the tower(s) associated with the muon's calorimeter flight path. We effectively need to add back in the calorimeter based energy associated with the muon. Thus the muon corrected $\not{E}_T$ is given by

$$(4.4) \qquad \vec{\not{E}}_T = \vec{\not{E}}_T^{\text{raw}} - \left(\vec{p}_T^{\,\mu} - \vec{E}_{\text{EM}}^{\,\mu} - \vec{E}_{\text{HAD}}^{\,\mu} \right)$$

From equation 4.4 we have the $\hat{\text{x}}$ and $\hat{\text{y}}$ components of the missing energy. Trivially we can derive $\not{E}_T = |\vec{\not{E}}_T|$ and note the corresponding ϕ variable. For convenience, the direction of the $\not{E}_T$ can be noted by the neutrino symbol (ν). For example, $\Delta\phi(\mu, \nu)$ is the difference in azimuthal angles for the muon and the missing energy.

There are a few additional details to this procedure. The $\not{E}_T$ is corrected for all detector (fiducial) defined muons (e.g. CMUP, CMX, BMU, etc.) as well as stubless muons (CMIOs) [50]. No additional constraint is applied to detector muons; if they are

in the collection they will contribute to the event's $\not{E}_T$. Stubless muons need to pass three cuts[51] in order to contribute to the corrected missing energy:

- $p_T > 10$ GeV/c

- EM < 3 GeV

- HAD < 9 GeV

We can naturally extend equation 4.4 to multiple muons:

$$\vec{\not{E}}_T = \vec{\not{E}}_T^{\text{raw}} - \sum_{\forall\ \mu} \left(\vec{p}_T^{\ \mu} - \vec{E}_{\text{EM}}^{\ \mu} - \vec{E}_{\text{HAD}}^{\ \mu} \right) \tag{4.5}$$

Note that we will need to modify our missing transverse energy a final time when we account for our jet energy scale corrections (section 5.7).

4.7. W identification

Our final formal selection cut is to combine our selected lepton (electron/muon) with our missing energy (representative of the escaped neutrino) to form the mass of candidate W. With this we can require this to be large enough to reject a significant fraction of the background while accepting the signal. However, due to the limitations of measuring the missing energy we cannot fully reconstruct the mass and instead calculate the transverse mass, M_T, by effectively ignoring the z information in our momentum as well as our energy measurement. Via the equivalent "3-vector" calculation M_T is given by

$$M_T = 2\sqrt{\left(p_T^\ell\ \not{E}_T \right)} \sin\left(\frac{\Delta\phi(\ell, \nu)}{2} \right) \tag{4.6}$$

where $\Delta\phi(\ell, \nu)$ is the difference in the respective azimuth angles of the charged lepton (ℓ) and $\not{E}_T$ (ν) and p_T^ℓ is the E_T of the electron or the p_T of the muon. We note that both

p_T^ℓ and $\not{E}_T$ peak around 39 GeV in signal $W \to \ell\nu$ MC which suggests (for a back-to-back decay) a transverse mass around 76 GeV/c^2.

We have an additional goal and function for our transverse mass cut; we want to select a set of events with a looser requirement to aid in our background estimation. The full details of our background estimation will be dealt with in chapter 6. For now we note that this selection will be referred to as our pre-W sample. We will allow in larger fractions of Zs and QCD backgrounds at the lower values of M_T and then use this sample to fit for our (jet multiplicity dependent) backgrounds where we do not have an *a priori* cross-section knowledge.

For our pre-W sample we apply a $M_T > 20$ GeV/c^2 cut to both electron and muon samples. For clarity we will explicitly note this pre-final selection sample via "$W \to \ell\nu$ with $M_T > 20$ GeV/c^2" when presenting results (i.e. tables and figures). Our final selection cut for our proper W candidate sample is $M_T \geq 40$ GeV/c^2 for the electron sample and $M_T \geq 30$ GeV/c^2 for the muon sample. The harder cut is required for the electrons due to the QCD background being larger whereas we gain a bit more acceptance with the cleaner muon sample. We present the M_T distribution for $W \to \ell\nu+ \geq 1$ jets with $M_T > 20$ GeV/c^2 in figures 4.5 (electrons) and 4.6 (muons). Both of these figures are presented without undergoing our formal background estimation procedure of section 6.4 (page 233) and as such do not have a formal QCD estimation nor are the W and Z MC modified away from our default weighting scheme of section 3.6.

The other lepton/W related selection cuts relate to our jet selection. Section 5.4 (page 142) deals with our separation veto which is enforced to remove potential bias for our final jet observables. In section 5.5 (page 143) we deal with an additional cut designed
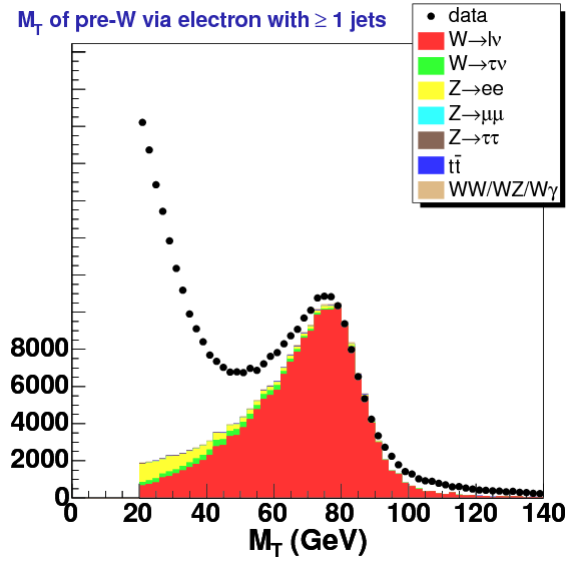
Figure 4.5. Transverse Mass (M_T) for $W \to e\nu + \geq 1$ jets with $M_T > 20$ GeV/c^2. We are applying the raw MC weights for our $W \to \ell\nu$ and $Z \to \ell\ell$ MC and have not introduced our QCD estimation.
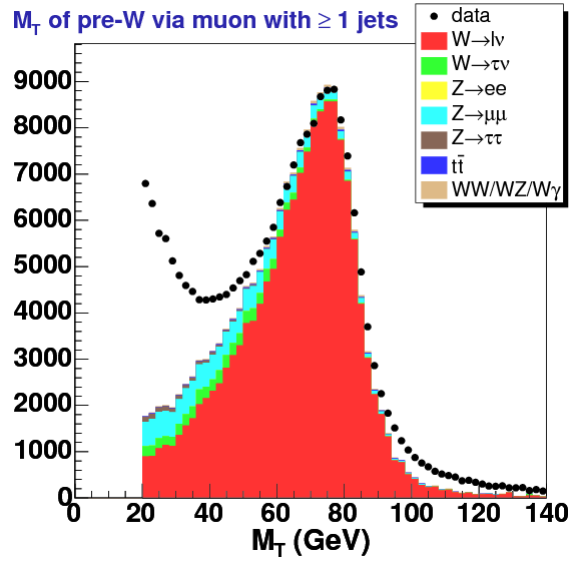
Figure 4.6. Transverse Mass (M_T) for $W \to \mu\nu + \geq 1$ jets with $M_T > 20$ GeV/c^2. We are applying the raw MC weights for our $W \to \ell\nu$ and $Z \to \ell\ell$ MC and have not introduced our QCD estimation.

to reduce our QCD and improve overall background agreement. Formally in the analysis we assign these additional jet related requirements to our analysis before preceding to form our pre-W and final W samples via the final, respective, M_T selection cut.

CHAPTER 5

Jet definition and selection

The previous chapter dealt with our W selection procedure but this is only gets us halfway to the various observables we wish to finally measure. Now that we have preferentially selected events with high momentum transfer, we discuss our classification, corrections, and concerns with respect to jets. We present our definition of jets in the next section. In section 5.2 we quickly note the electron-jet removal procedure which leads into our general prescription for identify and removing lepton-jets which is required for our anti-selected leptons. This procedure and its motivation are described in section 5.3. We then explain our lepton-jet separation veto in section 5.4. In the case of our electron sample, we also apply an additional cut based off of the $\Delta\phi$ between the electron and the vector jet momentum sum as explained in section 5.5. Next we discuss our general detector level jet energy corrections in section 5.6. Finally we explain our correction procedure to unfold our cross-section to the hadron level from our detector level measurement via the MC in section 5.8 and give the our results of said procedure in the last section, 5.9.

This chapter makes heavy use of $\Delta R(a, b)$ which is a separation variable in terms of pseudo-rapidity (η) and the azimuthal angle (ϕ) between objects a and b. For convenience, this will sometimes be denoted as simply as R_{ab} for cases like the dijet separation variable (R_{jj}) where there is an established meaning. More generally, R can be used the η-ϕ

angular area such as describing the jet cone radius. For object a let η_a be its pseudo-rapidity and ϕ_a be its azimuthal angle and likewise for object b then

$$\Delta R(a,b) \equiv \sqrt{(\phi_a - \phi_b)^2 + (\eta_a - \eta_b)^2} \tag{5.1}$$

or

$$\Delta R(a,b) = \sqrt{(\Delta\phi(a,b))^2 + (\Delta\eta(a,b))^2}$$

where $\Delta\phi(a,b)$ is always taken to be in the $[0, \pi)$ domain.

5.1. Jet definition

Jets are selected using the cone-based Midpoint algorithm using an η-ϕ radius of 0.4 ($R = 0.4$) [52]. The Midpoint jet definition was preferred above the use of JetClu which is more typical in other CDF analyses (e.g. all major top analyses).

Both JetClu and Midpoint are seed based cone algorithms. As such, they are not infrared or collinear safe to all orders in pQCD. However, Midpoint is thought as an improvement as it places additional seeds at the mid-point between tower seeds and the center of groups of seeds [52]. Thus, theoretical concerns like infrared radiation via soft gluon emission are better handled. Seedless jet algorithms are generally too CPU intensive while Midpoint only adds the addition of the midpoint seeds verses the relatively fast JetClu.

In the TopNtuple the jet collection from which we derive our data/MC samples is called: `MyTop_MIDPOINT0.4_LJ_ReclusterJetColl` and was jet collection type 6 up to and included period 17. Note that it is no longer in the jet list for the topNtuple for periods above 17.

In the analysis jets are defined with two cuts:

- $p_T > 20$ GeV/c

- $|\eta| < 2.0$

The pseudo-rapidity cut was chosen based on the understanding of the detector and the reliability of describing jet energy corrections at forward rapidity. The p_T cut was also similarly selected with the additional advantage being that a higher momentum jet definition selects against the effect of additional interactions (see our discussion in section 6.6 with respect to this potential "promotion" background). We note that the jet transverse momentum cut, in addition to the other jet observables we reference, is always on the corrected jet energy variable as detailed in section 5.6.

To get a scale of the numbers we load in over 30 million jets via our jet collection in our high lepton p_T data samples. We end up accepting (passing our base cuts) more than 18 million. Note that jet acceptance is not directly used in our acceptance calculation (section 7.2); rather, the jet multiplicity (i.e. the inclusive number of jets in an event) tautologically defines our acceptance for each jet multiplicity.

5.2. Electron-Jet Reclustering/Removal

Physics level objects such as electrons and jets overlap in their definitions with respect to being a calorimeter based measurement. As such it is possible for an electron to fake a jet and vice versa. There are several electron identification (ID) variables which does a relatively efficient job of removing jets faking electrons though these are still the source of much of our QCD background via multi-jets. There are also handles on distinguishing reconstructed jet objects that are electrons (such as the EM fraction shown in figure 5.1)

but these are not directly used in our jet selection. We define an *electron-jet* as a jet object that matches a selected electron. Clearly, we must formally deal with electron-jets in order to get a proper measurement.

In the process of forming the `jet` (i.e. jet objects) and `electron` (i.e. electron objects) collections in the topNtuple an algorithm is used to remove and correct for cases where a jet is matched to a tight electron (as defined in section 4.1). The algorithm removes the energy associated with the electron and then allows for jets to be reconstructed normally via the desired cone algorithm [**14**]. We did not directly investigate the electron-jet algorithm as this is a standard analysis tool but did look at cases where there where we had a high E_T electron that passes most of our selection cuts. Unsurprisingly we find the algorithm highly effective. For example, figure 5.2 shows the η-ϕ separation (denoted as $\Delta R(e, j)$) between the electron (which has passed most of the standard electron requirements including isolation less than 0.10) and the nearest jet. The bottom plot of the figure also shows the behavior for muons which (not being calorimeter based) has no equivalent tight muon-jet removal process. A follow up plot of the same $\Delta R(e, j)$ variable in figure 5.3 shows the performance of a straightforward electron-jet removal algorithm. The muon version of this plot just shows our lepton-jet separation cut/veto which is dealt with in section 5.4.

The electron-jet removal process (as apposed to the jet reclustering/removal scheme automatically done at the level of topNtuple production) is not formally needed when running our normal W selection analysis procedure on our data and MC samples. However, an additional procedure will be needed for a special sample comprised of potential electron as well as muon channel fakes. These anti-selected leptons that need to be removed

from the jet collection are discussed in the next section (5.3). This lepton-jet removal procedure will also be applied when discussing our hadron level corrections in section 5.8.
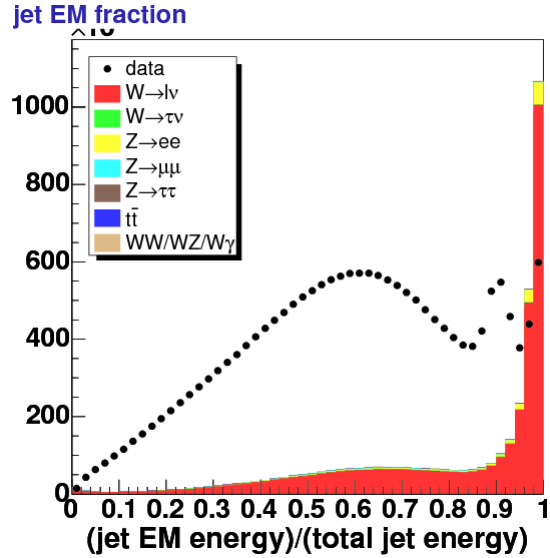
Figure 5.1. Jet EM fraction (defined as the fraction of EM calorimeter energy to the total energy) for all jets in all events. A component of the signal MC ($W \rightarrow \ell\nu$) rapidly starts to peak starting at 0.9 with the maximum at the final bin. The vast majority of these "jets" are electrons that fail one or more of our tight electron cuts and are not de facto removed via the procedure of section 5.2.

5.3. Anti-selected Lepton-Jet removal

The previous section introduced the necessary complication in the electron channel that electrons and jets are expected to populate and potentially adversely effect each others collections. However, the tight electron removal and reclustering algorithm solves this problem. In this section, we turn to our anti-selected lepton samples which will serve as the basis for our QCD estimation as explained in chapter 6. We will need to

manually remove the associated jets with our candidate electrons as well as the anti-selected muons. We begin by investigating cases where the anti-selected lepton is close to a jet before applying an additional lepton/jet separation veto which is the subject of the next section.

Figure 5.6 presents the $\Delta R(\ell, j)$ between the anti-selected lepton and the nearest jet. It is analogous with the previous figure for candidate selected leptons (see figure 5.2) with the upper and lower plots representing the electron and muon channels, respectively. We given an additional pair of zoomed in plots of these distributions in figures 5.4 ($\Delta R(e, j)$) and 5.5 ($\Delta R(\mu, j)$) where the range goes from ΔR=0.00-0.24. Unlike in the previous section, the electron-jet is clearly not removed which is consistent with the electron necessarily failing at least two identification cuts (see section 4.2). Interestingly our anti-selected muon sample *also* shows the same tell-tale signature of a jet being very close to the muon object. Note that the events at low ΔR (centered around 0.03) are completely dominated by events which pass our inverted energy (calorimeter variables) based cuts (see section 4.4). When we compare channels we notice that the muons tend to have a wider separation and tail in $\Delta R(\ell, j)$ due to the nature of electron and muon reconstruction. The latter is track-stub based (calorimeter based ID variables are accounted for later) while the former is calorimeter based which is why we naturally expect `jet` objects to be in the `electron` collection and vice versa.

Originally our treatment for the (anti-selected) muons was to directly apply separation veto of the next section and this had the expected effect of eliminating many potential anti-selected candidates and actually producing a somewhat biased phase space for our W and jet related observables. However, the separation veto is designed to distance the

effects of our defined jets with our lepton object. Given that our anti-selected muon sample allows and selects for the equivalent style multi-jet fakes in the electron channel due to its effective calorimeter dependence, we allow for this behavior and thus apply the same lepton-jet removal procedure for both anti-selected leptons samples.

The general procedure for removing a lepton-jet to search through the `jet` collection for the closest jet that satisfies $\Delta R(\ell, j) < 0.40$. While a tighter matching requirement (e.g. $\Delta R(\ell, j) < 0.24$) is nearly fully efficient we take a full jet cone radius since this is the normative cutoff between reconstructing jets. Note that the separation veto (next section) is designed to separate the falling tail end of lepton-jets with the natural rise in reconstructing a near by jet. This is seen in the $\Delta R(\ell, j)$ between 0.40-0.50 in figure 5.7 where we have followed through and removed our candidate anti-selection lepton-jets of figure 5.6. Figure 5.7 is analogous to figure 5.3 of the previous section.

Originally, when optimizing our electron-jet matching we opted for a jet EM fraction requirement in addition to a tighter separation. However, this additional requirement did not add anything when looking at high quality (i.e. tight) electrons where EM fraction greater than 0.8 (see figure 5.1) were nearly 100% by construction. Simply looking for the closest jet to the electron was enough. In the case of anti-selected electrons we are naturally looking for a fake in the `electron` collection that will necessarily fail a pair of ID cuts (e.g. HAD/EM) so this would not have been beneficial either. (For completeness, figures 5.8 and 5.9 show the jet EM fraction of anti-selected electron-jets and muon-jets, respectively.) In the case of our W selected muons there is are no observed muon-jets (as seen in data and MC) and thus geometrically matching anti-selected muons to the nearest jet is the natural procedure. Ultimately we find it unnecessary to add any additional

requirements to our jet matching anti-selected lepton procedure. This has the benefit of keeping our jet selection and matching simple and consistent for both leptons yet fully efficient.

At the level of the analysis, matching and removing a lepton-jet literally means skipping said object in the `jet` collection as if it had failed our jet selection requirements. This is a natural procedure for the electrons but somewhat avant-garde for muons. As we will see in section 5.8, a similar procedure will be needed when reconstructing jets at the hadron level. It is also worth noting that this removal scheme is consistent with our later treatment of our calorimeter (detector based) jets. All said jets go through jet energy scale corrections (section 5.6), but we do not correct the $\not{E}_T$ (section 5.7) with the removed lepton-jet.

5.4. Lepton/Jet separation

In our analysis we want to avoid potential lepton/jet overlap bias that comes from these objects being too close. Part of the motivation is to remove semi-leptonic decay events and other signatures were the charged lepton is colinear with a jet. Another issue is that our analysis does not directly account for out-of-cone effects whereas applying an excluded buffer region between our leptons and the nearest selected jet removes this concern.

The approach for selected electrons effectively clears out a cone of $R{=}0.4$ due to the electron-jet removal/reclustering procedure and both electrons and muons enforce explicit isolation requirements such as isolation less than 0.1 (which itself is a $R{=}0.4$ cone base measurement). However, even when we switch to our anti-selected sample (potential

QCD events from fakes and multijets) there is a motivation to keep the activity around the candidate anti-selected lepton separate from the normal jet activity outside of it cone of influence such that we can measure various jet observables independently.

In our analysis after having selected (or "anti-selected") a lepton passing our basic requirements we apply a $\Delta R(\ell, j) < 0.52$ cut with j being the closest selected jet. The numerical value of 0.52 is based off (1) the historical use of this value as 1.3×0.4 [12][84] and (2) our own analysis of the separation behavior in particular the previous section's description of anti-selected lepton-jets.

This is the second-to-last acceptance selection cut before our final acceptance selection cut (the subject of the next section). We give our full acceptance procedure description in section 7.1 (page 339) as well as our basic "raw" acceptance results via our signal MC there (see tables ??-7.7). Here we present these acceptance results for our $\Delta R(\ell, j)$ cut in table 5.1 for each exclusive ($= n$) number of jets. We give the trivial exclusive 0 jet case for completeness and transparency. Our electron results (acceptance of $\Delta R(e, j) < 0.52$) is given as CEM while we segment our muon results based on their fiducial sub-detector description. The muon results are internally consistent and the electron results show the obvious artifact of the efficient electron-jet removal/reclustering scheme. In the latter case, the acceptance is effectively lost in our basic electron geometric (detector fiducially requirement) and kinematic (E_T and p_T cuts) acceptance cuts.

5.5. $\Delta\phi(\ell, \wp)$ cut

As noted in the previous chapter there is an additional analysis wide cut we make as part of our final selection. The motivation was to find a variable that would help us

n jets	CEM	CMUP	CMX-Arch	CMX-Mini
0	1.000	1.000	1.000	1.000
1	0.997	0.959	0.960	0.961
2	0.992	0.915	0.919	0.916
3	0.985	0.865	0.876	0.867
4	0.979	0.786	0.799	0.802

Table 5.1. Acceptance Results for $\Delta R(\ell, j) < 0.52$ for electrons (CEM) and muons (CMUP, CMX-Arch, and CMX-Mini) for exclusive n jets. This partial acceptance result is calculated from events already passing our geometric and kinematic cuts of section 7.1.

understand our QCD backgrounds that could be correlated with a direct understand of our jet kinematics. Given that our expected background is made up a multi-jet where one jet fakes as a lepton to mask as our signal. One such handle, to consider dijet events specifically, would be to look at the $\Delta\phi$ between lepton and a normally reconstructed jet. One would expect via conservation of momentum that potential fakes be back-to-back while real leptons would ideally be flat in $\Delta\phi$. Realistically the latter situation where we select for tight lepton would be biased against colinear lepton/jets but would still have a linear dependence for signal while dijet fakes would exponentially favor high values of $\Delta\phi$.

As it turns out such a procedure has actually been used along with the relative isolation of the lepton to estimate the QCD background [53]. This was also cited as a possible improvement in estimating the QCD without resorting to the so called "iso vs. MET" method [54]. We investigated this early on in the analysis and made a obvious improvement. In cases where we record 2 or more jets (with the expected background coming from tri-jets, etc.) this procedure will not work as stated. The solution is to form a vector sum of jet energies and then compare this to the lepton or rather compare their

directions with $\Delta\phi$. We represent this vector jet quantity with the variable $\wp$ and define it as follows,

$$(5.2) \qquad \wp \equiv \sum_{\forall \text{ jets}} \left(E_x \hat{\mathrm{x}} + E_y \hat{\mathrm{y}} + E_z \hat{\mathrm{z}} \right)$$

with E_x, etc., the jet energy components.

Although we do not use $\wp$ directly to select for a QCD rich sample it is instructive to show that its behavior is as advertised. We will then compare the behavior of $\Delta\phi(\ell, \wp)$ between data, signal and background MC, and our preliminary QCD estimation. We begin with plots where we have found a lepton passing our basic selection but where we have not enforced a tight triggered lepton requirement nor made a W transverse mass cut. Figures 5.10 (for $W \rightarrow e\nu + \geq 1$ jet) and 5.11 (for $W \rightarrow \mu\nu + \geq 1$ jet) show the missing transverse energy ($\not{E}_T$) after partition events into two plots using $\Delta\phi(\ell, \wp) \gtrless 120°$. These plots show that data for events in the highest 60°are dominated by an undescribed background which favors $\not{E}_T$ unlike our signal. This same shape can be seen in the lower 120°but the signal and other backgrounds from the MC are relatively distinct.

For completeness we can flip around the nature of these plots and show $\Delta\phi(\ell, \wp)$ where we partition with the missing energy. Figure 5.12 shows the $\Delta\phi(e, \wp)$ with $\not{E}_T \gtrless$ 30 GeV for the electron channel while figure 5.13 showcases $\Delta\phi(\mu, \wp)$ with $\not{E}_T \gtrless 20$ GeV. Events in the low $\not{E}_T$ region which are necessarily poorly populated by signal MC events, show a very strong turn on of $\Delta\phi(\ell, \wp)$ in the data which is maximal where the lepton is approximately back-to-back to the sum vector jet energy. Meanwhile the higher $\not{E}_T$ region we can clearly see the data being made up of the behavior of lower region along with the behavior of our signal and background estimations from MC.

Consistent with our motivation to study the QCD by exploiting the behavior of multi-jet events, figures 5.10-5.13 suggest an obvious correlation with the undescribed QCD background and $\Delta\phi(\ell, \wp)$ via our definition of $\wp$. We can then use this distribution as a good bench-mark and quality check for anti-selected leptons which forms our QCD estimation as explained in detail in the next chapter. We now plot $\Delta\phi(\ell, \wp)$ for each inclusive jet multiplicity (1-4) after applying our formal background estimation procedure in figures 5.14 ($\Delta\phi(e, \wp)$) and 5.15 ($\Delta\phi(\mu, \wp)$). Both of these plots represent our final W selection modulo the lower requirement of $M_T > 20$ GeV/c^2 rather than our final 40 (30) GeV/c^2 cut for $W \to e\nu$ ($W \to \mu\nu$). We note the basic good agreement and that the behavior of the backgrounds and the data are independent of jet multiplicity. In the electron channel (figure 5.14) we initially overestimate the QCD fraction of events with $\Delta\phi(e, \wp) > 2.95$ in the data. We interpret this as our QCD shape being too multi-jet fake-like. In other words, candidate events in data contain events will less purity than our unmodified QCD estimation from our anti-selected electrons. In the case of the muon channel (figure 5.15) there is similar but smaller excess is seen for $\Delta\phi(\mu, \wp) > 2.95$. We also observe that the agreement is actually quite good for the higher jet multiplicities in comparison to the electrons.

From the $\Delta\phi(\ell, \wp)$ results we will apply $\Delta\phi(e, \wp) < 2.95$ cut in just the electron channel. We originally had the same $\Delta\phi(\ell, \wp)$ cut on the muons as well but this hypothetical selection cut would drop the ≥ 1 jet acceptance but about 10% without improving the quality of any W or jet kinematic observable. As a result, we have eliminated this cut from our muon selection in favor of better acceptance. As noted later in our chapter of acceptance (chapter 7) this cut reduces our full acceptance for events with at least one jet

by about 5% for electrons and 10% for muons. Updated version of these $\Delta\phi(\ell, \wp)$ plots with our final W transverse mass selection cut are given in the next chapter as part of a general survey as to the quality of our background estimation. They can be seen in figures 6.48 (page 273) and 6.60 (page 279).
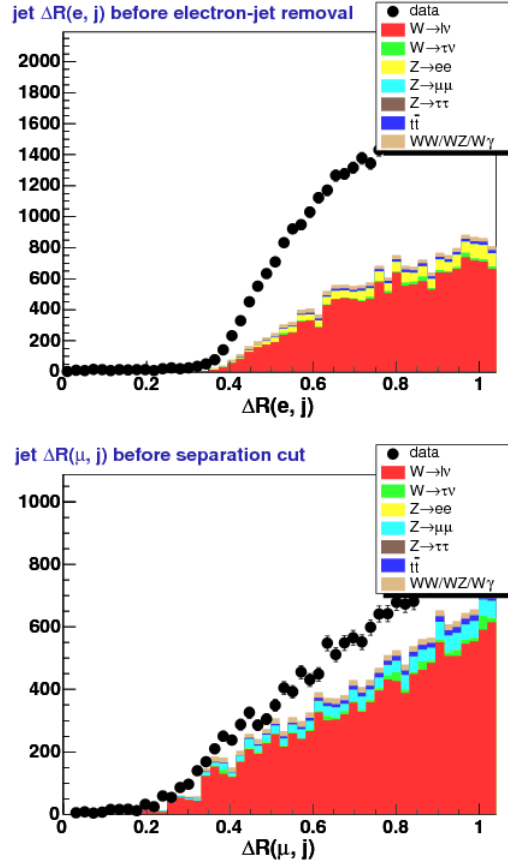
Figure 5.2. η-ϕ separation $(\Delta R(\ell, j))$ between candidate lepton and closest jet. The top plot is for electrons while the bottom is reserved for muons. Leptons pass most of the standard W selection cuts and thus are negatively biased against colinear lepton/jet events. The electrons have the tight electron reculustering scheme applied which further reduces events within $0.0 < \Delta R < 0.4$. Muons have no such reclustering scheme.
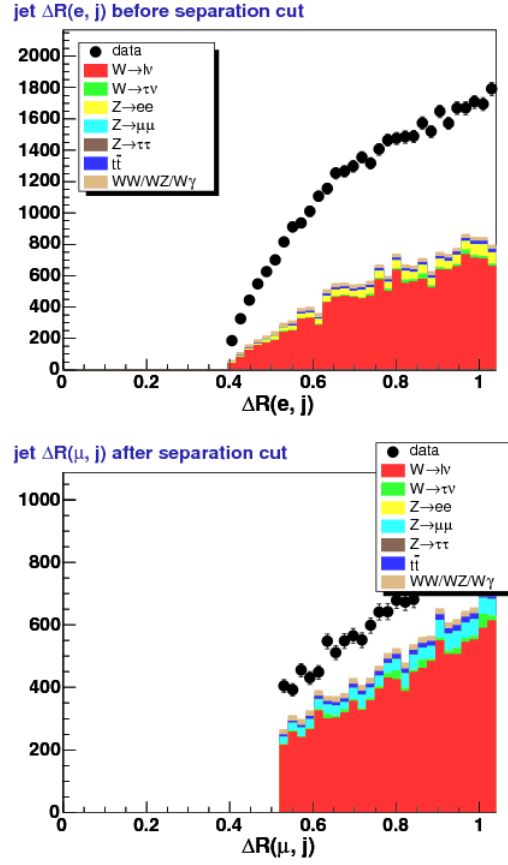
149

Figure 5.3. η-ϕ separation $(\Delta R(\ell, j))$ between candidate lepton and closest jet. The top plot is for electrons while the bottom is reserved for muons. The lepton selection is the same as figure 5.2 but we skip jets that have been matched to the electron. The track based muons in the bottom plot simply have a $\Delta R(\mu, j) < 0.52$ cut applied as per our discussion in section 5.4.
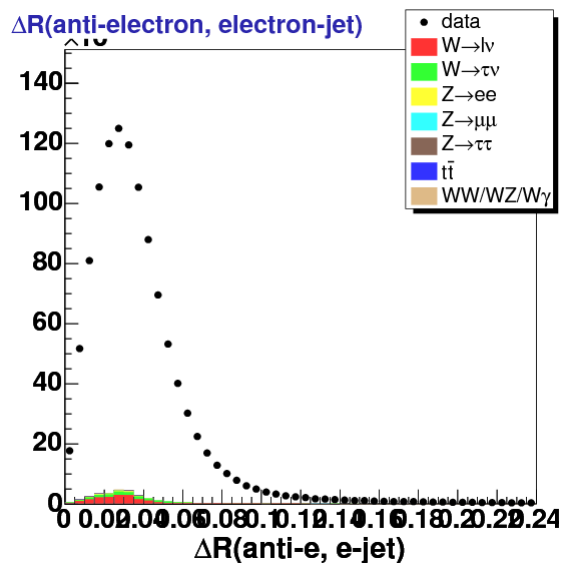
Figure 5.4. The η-ϕ separation (ΔR(anti-e,jet)) for anti-selected muons and the closest jet. There is some signal contamination from the MC which is small and shows the same behavior. We identify the jet as the anti-selection electron-jet. This plot is effectively the zoomed in version of figure 5.6 with the range set from ΔR=0.00 to 0.24.
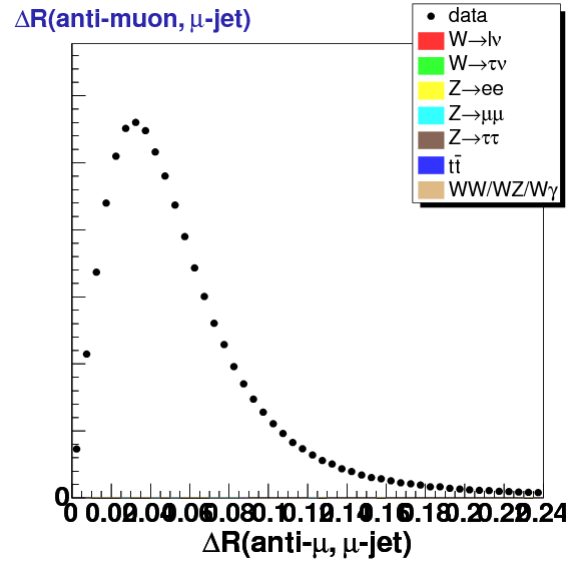
Figure 5.5. The η-ϕ separation (ΔR(anti-μ,jet)) for anti-selected muons and the closest jet. There is virtually no contamination from our MC signal or other backgrounds as these poorly fake our anti-selection requirements. We identify the jet as the anti-selection muon-jet. This plot is effectively the zoomed in version of figure 5.6 with the range set from ΔR=0.00 to 0.24. Several of our inverted selection cuts are based off of the calorimeter with the result being a similar behavior as seen in the anti-selected electrons (see figure 5.4).
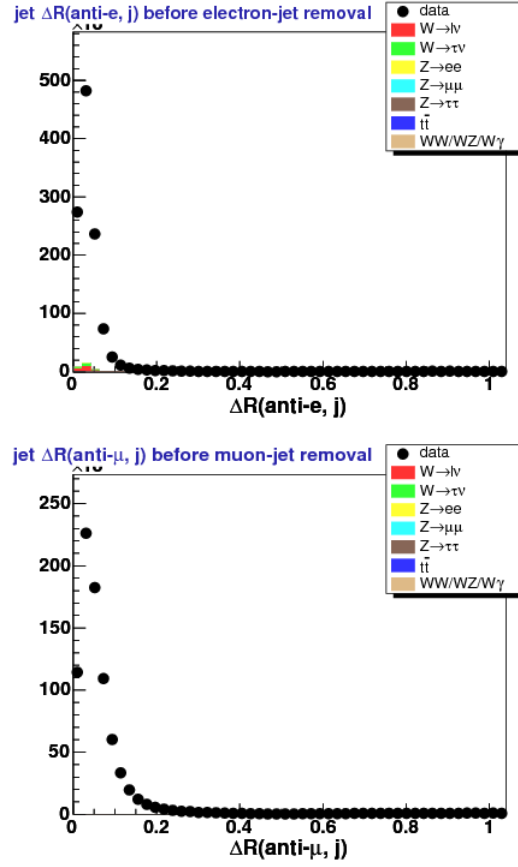
Figure 5.6. η-ϕ separation $(\Delta R(\ell, j))$ between candidate anti-selected lepton and the closest jet. This is before our separation veto and before any lepton-jet removal procedure is applied. The top plot is for anti-selected electrons while the bottom is reserved for anti-selected muons. Unlike figure 5.2 there is no automatic removal for electrons and both leptons show the presence of overlapping jets. We identify these jets as the anti-selection lepton-jets. Figure 5.7 shows $\Delta R(\ell, j)$ after these jets are removed.
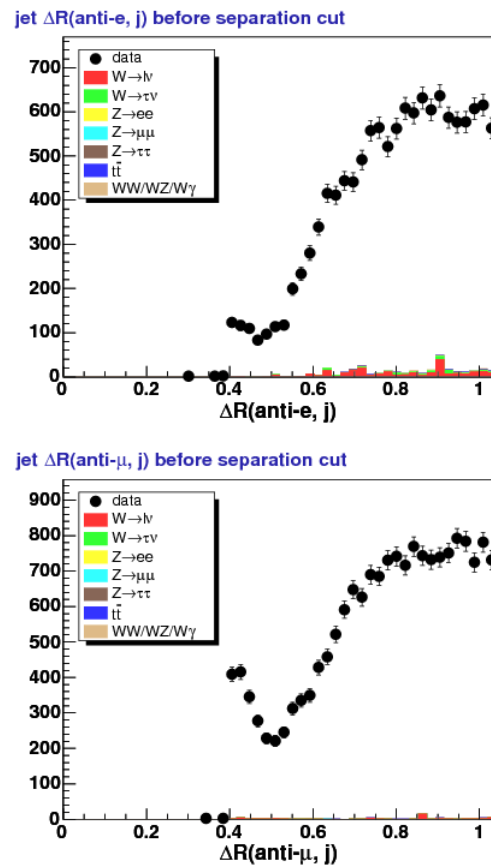
Figure 5.7. η-ϕ separation $(\Delta R(\ell, j))$ between candidate anti-selected lepton and the closest jet. This is just before our separation veto but after we removed the (anti-selected) lepton-jet. There is a slight tail effect of candidate lepton-jets between ΔR0.40-0.50 but The top plot is for anti-selected electrons while the bottom is reserved for anti-selected muons.
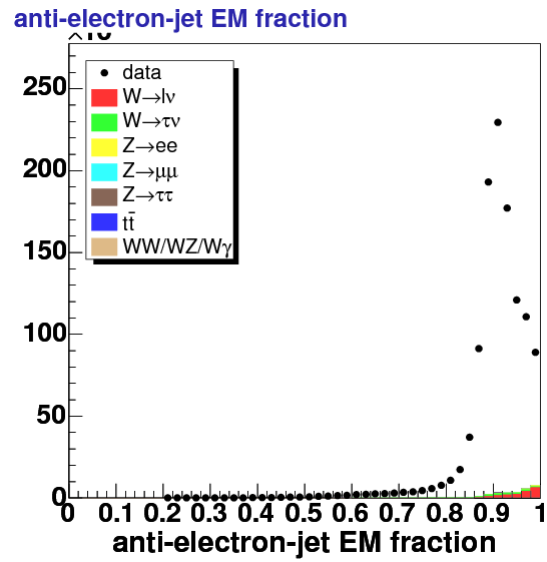
Figure 5.8. Jet EM fraction of jets matched to an anti-selected electron (anti-electron-jet).
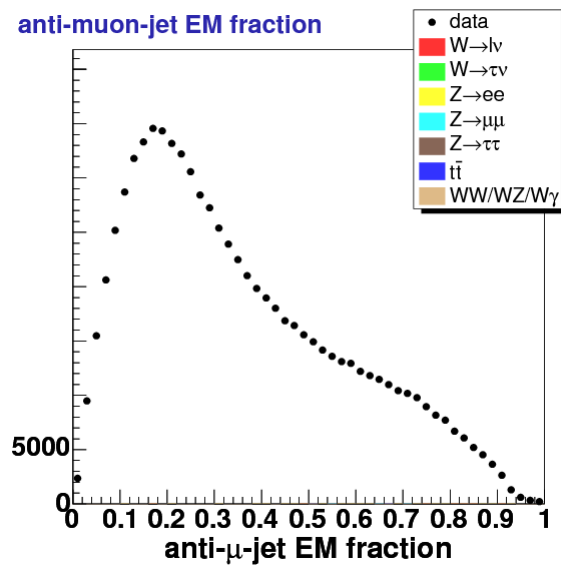
Figure 5.9. Jet EM fraction for all jets in events with an anti-selected muon (anti-muon-jet).

5.6. Jet Energy Scale Corrections

The details for the jet energy corrections are explained on the *Jet Energy and Resolution Group* page [**55**]. A full description of the procedure with and additional detector level and jet definition specific information is given elsewhere [**56**]. We use the corrections based up to our last run period/number (see table 3.1) which corresponds to `jetCorr17`. The correction is applied in a straightforward way via the instructions for generation 6 CDF code [**57**]. This amounts to loading corrections for each event based on the number of quality 12 vertices in addition to the run number and the types or level of jet corrections to apply. There is also the option to systematically vary the procedure by the derived uncertainties ($\pm\sigma_{\mathrm{JES}}$) in order to obtain a systematic uncertainty. Our full discussion of the jet energy scale systematic on our cross-section is given in section 8.7.

In the CDF nomenclature we use a level 5 jet energy correction which is comprised of a relative, multiple interaction, and absolute corrections as described below. This is in addition to the CDF basic calibration of the calorimeter energy scale [**58**]. This baseline (level 0) detector-level correction is automatically applied in our reconstructed objects in our `jet` collection. For brevity, we will call these our "raw" or uncorrected jets which are corrected via the following procedures.

- Relative correction: This jet η dependent correction is designed to make the jet energy response uniform in η relative to the behavior of jets in the $0.2 < |\eta| < 0.6$ region which is fiducial to our best understood part of our detector. This is accomplished by measuring dijet events where one expects the transverse energy for each jet to be equal and back-to-back. The correction is applied to the raw jet energies as measured in the calorimeter. [**60**]

- Multiple interaction correction: This correction accounts for additional $p\bar{p}$ interactions in the same bunch crossing producing additional energy that can fall inside a candidate jet cluster. Using minimum bias data, an averaged energy contribution is calculated along with the number of vertices in the event which is highly correlated with the effect of multiple interactions. The correction takes the form of a subtracted averaged contribution due to multiple interactions parameterized based on the number of vertices. [59]

- Absolute correction: The final type of correction deals with non-linearity in the calorimeter response as well as the effect of energy loss in the non-instrumented regions of the calorimeter. Here MC is added to better improve the description between simulation and data. The jet energy is corrected to the $\sum p_T$ of the particles within a cone of R=0.4 centered on a generated parton (p) matched ($\Delta R_{\mathrm{p},j}$ <0.4) to a calorimeter jet (j). [61].

The comparison of γ+jet events is instructive here as a cross-check as the photon can be well measured and compared back-to-back to the response of the jet [65]. We do not append additional (higher level) corrections like underlying event [62] or out-of-cone effects [63][64]. However, an additional global correction is made to correct the data to the hadron level to remove the (corrected) detector dependence, and this is the subject on the next section.

Once the jet corrections are setup, we loop through the jet collection and derive a jet energy scale factor based on the uncorrected p_T, η, and EM fraction of the jet. Typically this correction is between 1.05-1.75. We then apply this scale factor (s_{JES}) as appropriate to our energy based jet observables. Equation 5.3 provides an obvious and important

example of this correction in action for the raw (uncorrected) jet transverse momentum (p_T^{raw}) in becoming our nominal (corrected) jet transverse momentum (p_T^{corr}).

$$(5.3) \qquad\qquad\qquad p_T^{\text{corr}} = s_{\text{JES}}\left(p_T^{\text{raw}}\right)$$

We note that all jet variables referenced and used in this analysis are the corrected variables (e.g. $p_T = p_T^{\text{corr}}$) unless explicitly stated otherwise.

As would be expected, jet corrections do "promote" jets that would have failed our jet p_T cut if left uncorrected. Of the 18.5 million passed jets some 3.8 million were promoted. We never observe the converse: a jet demoted by corrections that would have passed if left uncorrected. Figures 5.16-5.19 give the basic flavor of the jet energy scale factor (s_{JES}) dependence. The former pair (figures 5.16 and 5.17) is the dependence on jet p_T for electrons and muons, respectively, via a 2-dimensional plot. The latter pair (figures 5.18 and 5.19) likewise show the constructed dependence via jet η.

5.7. Missing Energy Corrections (jets)

Section 4.6 gave an overview of our $\not{E}_T$ definition and how we handle additions due to our track based muons. In this section, we note an additional correction based on the jet energy corrections of the previous section. The procedure is straightforward: adjust the missing energy by the difference in the energy (specifically the vector transverse momentum) between corrected and uncorrected jets. Let the default (level 0) jet transverse momentum be given by $\vec{p}_T^{\text{raw}}$ while $\vec{p}_T^{\text{corr}}$ is the level 5 jet energy corrected variable consistent with our notation in equation 5.3. Via our $\not{E}_T$ as defined in equation 4.4 (page

130) we derive our corrected missing energy ($\not{E}_T{}^{\mathrm{corr}}$) as

$$(5.4) \qquad\qquad \vec{\not{E}}_T{}^{\mathrm{corr}} = \vec{\not{E}}_T - \sum_{\forall\text{ jets}} \left(\vec{p}_T{}^{\mathrm{corr}} - \vec{p}_T{}^{\mathrm{base}} \right)$$

The order of operations is important so to be clear:

- All raw candidate jets are corrected to level 5 (section 5.6)

- Candidates identified as (anti-)lepton-jets are skipped (section 5.3)

- Analysis level jets pass our selection/definition cuts (section 5.1)

- $\not{E}_T$ is corrected via equation 5.4 based off selected jets (this section)

- The corrected $\not{E}_T$ is always used in our M_T cuts for our W selection (section 4.7)

- Events that fail our lepton-jet separation cut are vetoed (section 5.4)

To get a sense of overall effect of our jet energy scale correction to the missing energy correction, we plot the ratio between the corrected and uncorrected $\not{E}_T$ values. The former is unoriginally called "Corrected $\not{E}_T$" while the latter is noted as "Raw $\not{E}_T$" which is actually the $|\vec{\not{E}}_T|$ of equation 5.4. Figure 5.20 is the $W \to e\nu + \geq n$ jets version of $|\vec{\not{E}}_T{}^{\mathrm{corr}}|/|\vec{\not{E}}_T|$ while figure 5.21 is likewise the muon channel version. We plot n=1-4 as the total inclusive (≥ 0 jets) case is completely dominated by the bin at unity.
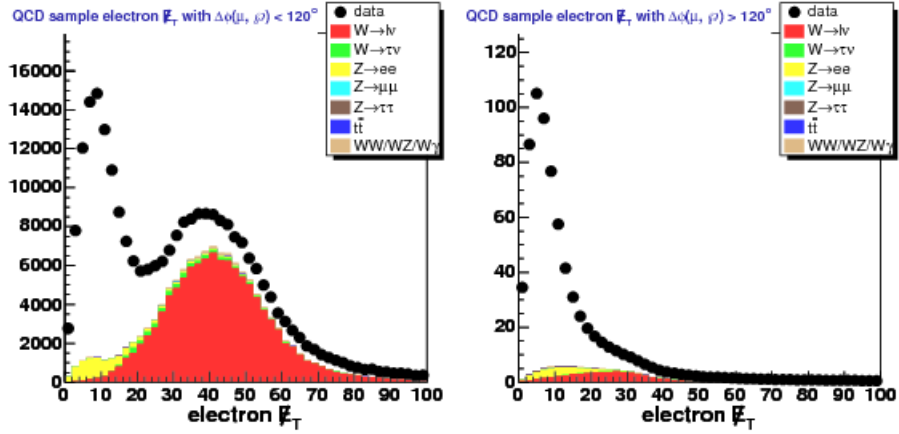
Figure 5.10. The $\not{E}_T$ for $W \rightarrow e\nu+ \geq 1$ jet where the left plot represents events with $\Delta\phi(e, \wp) < 120°$ while the right plot shows $\Delta\phi(e, \wp) > 120°$. The latter (right) plot is dominated by non-signal non-MC background events.
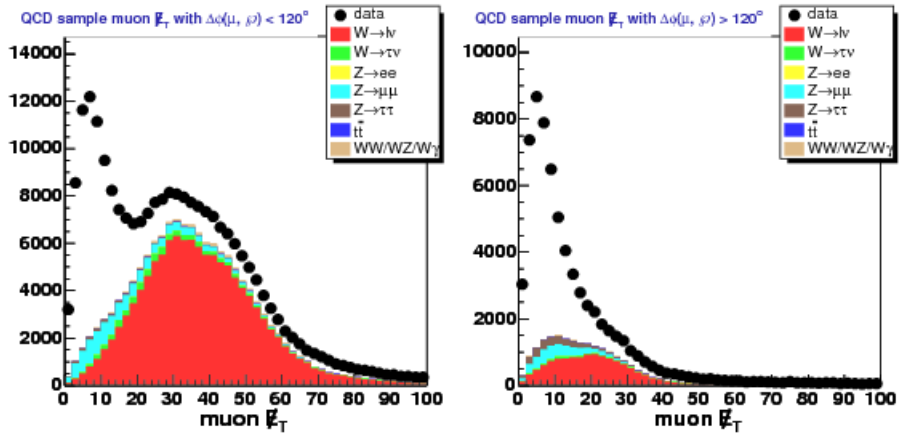
Figure 5.11. The $\not{E}_T$ for $W \rightarrow \mu\nu+ \geq 1$ jet where the left plot represents events with $\Delta\phi(\mu, \wp) < 120°$ while the right plot shows $\Delta\phi(\mu, \wp) > 120°$. The latter (right) plot is dominated by non-signal non-MC background events.

160
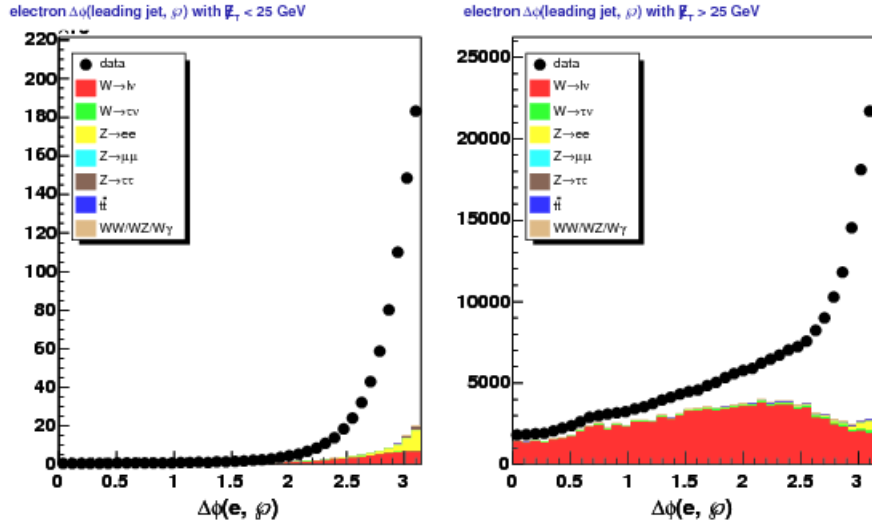
Figure 5.12. The $\Delta\phi(e,\wp)$ for $W \to e\nu + \geq 1$ jet where the left plot represents events with $\not{E}_T > 30$ GeV while the right plot shows $\not{E}_T < 30$ GeV. Note that the in-plot titles incorrectly imply that the $\not{E}_T$ cut is at 25 GeV. The former (left) plot shows Jacobian turn on for back-to-back events with low $\not{E}_T$
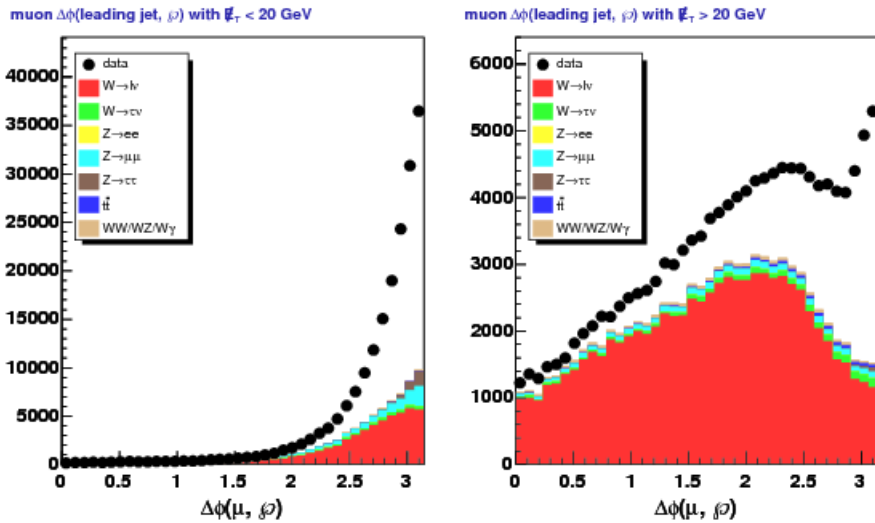
Figure 5.13. The $\Delta\phi(\mu,\wp)$ for $W \to \mu\nu + \geq 1$ jet where the left plot represents events with $\not{E}_T > 20$ GeV while the right plot shows $\not{E}_T < 20$ GeV. The former (left) plot shows Jacobian turn on for back-to-back events with low $\not{E}_T$.

161
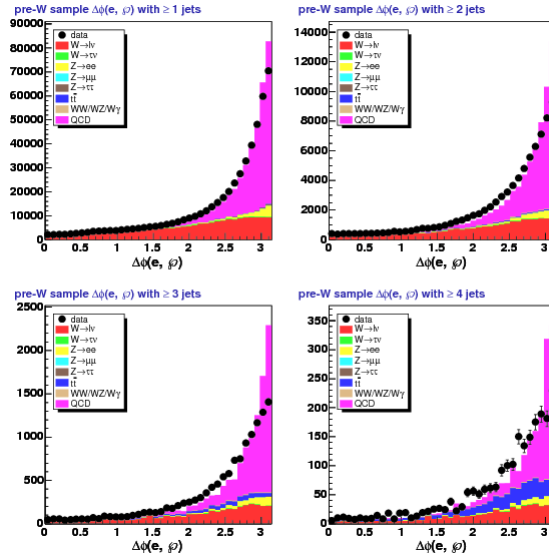
Figure 5.14. The $\Delta\phi$ between the muon and the jet vector sum, $\wp$ (see equation 5.2) for $W \to e\nu+ \geq n$ jets with $M_T > 20$ GeV/c. (The full W selection requires $M_T > 40$ GeV/c; see figure 6.48.) Upper-left plot is for ≥ 1 jets, upper-right for ≥ 2, lower-left for ≥ 3, and lower-right for ≥ 4.
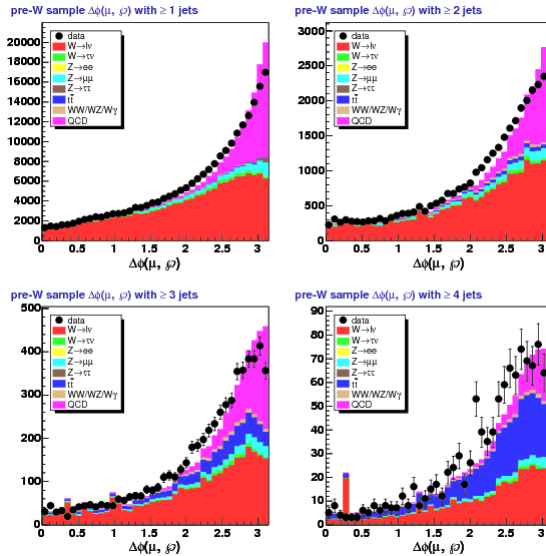
Figure 5.15. The $\Delta\phi$ between the muon and the jet vector sum, $\wp$ (see equation 5.2) for $W \to \mu\nu+ \geq n$ jets with $M_T > 20$ GeV/c. (The full W selection requires $M_T > 30$ GeV/c; see figure 6.60.) Upper-left plot is for ≥ 1 jets, upper-right for ≥ 2, lower-left for ≥ 3, and lower-right for ≥ 4.
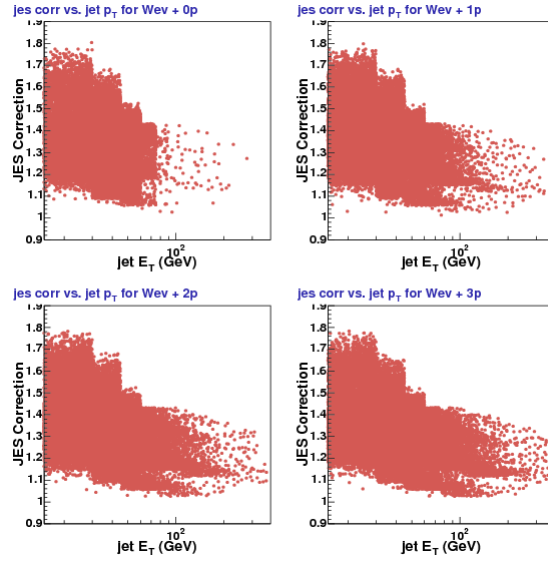
Figure 5.16. 2D histogram of the jet energy scale (JES) correction verses corrected jet p_T for all jets with $|\eta| < 2.0$ and $p_T > 20.$ GeV/c in Alpgen+Pythia $W \to e\nu + n$p MC. Each plot represents n patron sample with 4p omitted.
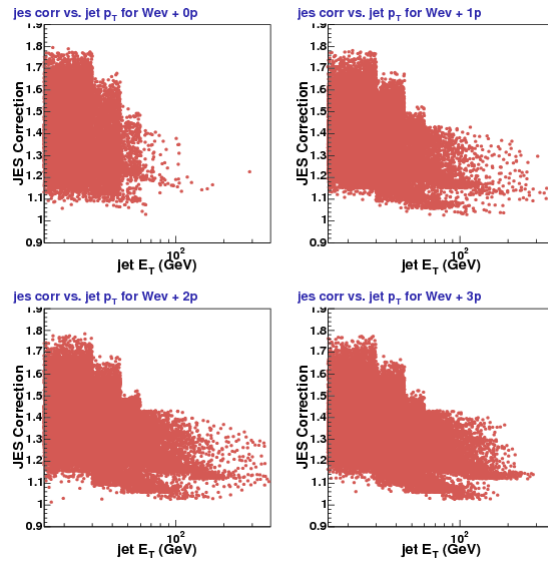
Figure 5.17. 2D histogram of the jet energy scale (JES) correction verses corrected jet p_T for all jets with $|\eta| < 2.0$ and $p_T > 20.$ GeV/c in Alpgen+Pythia $W \to \mu\nu + n$p MC. Each plot represents n patron sample with 4p omitted.
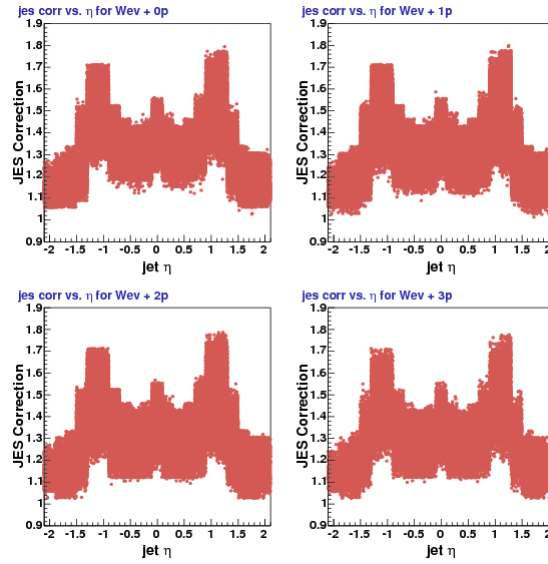
Figure 5.18. 2D histogram of the jet energy scale (JES) correction verses jet η for all jets with $|\eta| < 2.0$ and $p_T > 20.$ GeV/c in Alpgen+Pythia $W \to e\nu + n$p MC. Each plot represents n patron sample with 4p omitted.
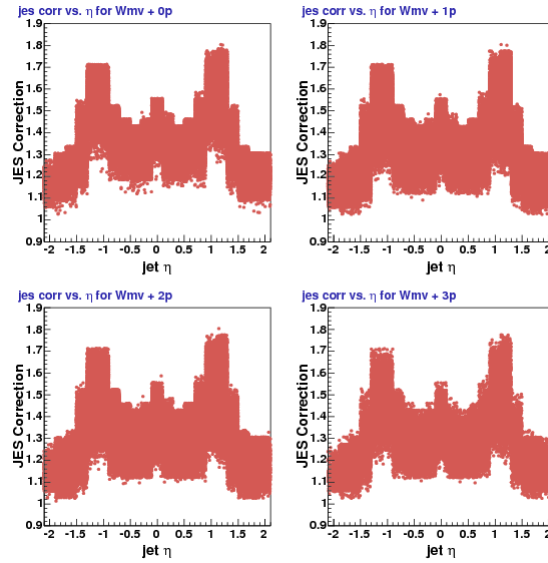
Figure 5.19. 2D histogram of the jet energy scale (JES) correction verses jet η for all jets with $|\eta| < 2.0$ and $p_T > 20.$ GeV/c in Alpgen+Pythia $W \to \mu\nu + n$p MC. Each plot represents n patron sample with 4p omitted.
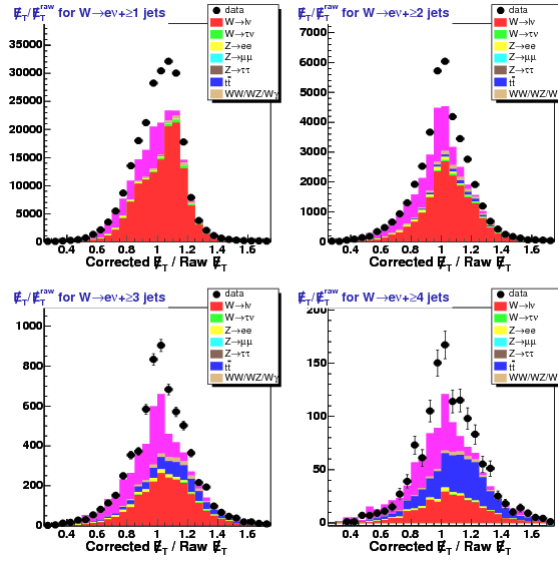
Figure 5.20. Ratio of the jet energy scale (JES) corrected $\not{E}_T$ with the non-JES $\not{E}_T$ as defined in equation 5.4 for $W \to e\nu+ \geq n$ jets. Upper-left plot is for ≥ 1 jets, upper-right for ≥ 2, lower-left for ≥ 3, and lower-right for ≥ 4.
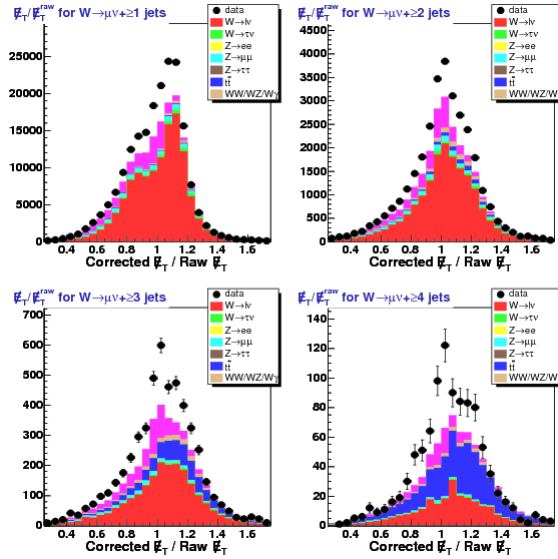
Figure 5.21. Ratio of the jet energy scale (JES) corrected $\not{E}_T$ with the non-JES corrected $\not{E}_T$ as defined in equation 5.4 for $W \to \mu\nu+ \geq n$ jets. In this plot, the Raw $\not{E}_T$ refers to the already μ correct $\not{E}_T$ of equation 4.4 (130). Upper-left plot is for ≥ 1 jets, upper-right for ≥ 2, lower-left for ≥ 3, and lower-right for ≥ 4.

5.8. Hadron Level Correction Procedure

Section 5.6 dealt with detector level jet corrections. However, for our final cross-section we wish to effectively apply an additional correction that maps our jet related observables to the hadron rather than the calorimeter level. We do this by studying the signal W MC and tracking its response to the default CDF detector simulated calorimeter jets and to jets reconstructed using the same midpoint (R=0.4) algorithm but applied to the (post-shower) pre-CDF simulation. For simplicity, we denote the normal CDF simulation level calorimeter jets, whether from signal MC or via the data, by CAL while the signal MC sample that has been run for hadron level jets will be referred by HAD. The final goal is to effectively measure the cross-section from each sample (HAD and CAL) and then correct the data, bin-by-bin as necessary, given the response. We describe this correction process as an *unfolding* of the data to the hadron level.

We construct a pseudo-cross-section with both MC samples by applying the same W selection criteria as described in chapter 4. In particular, we use the same (detector-simulation based) lepton and missing energy objects such that the acceptance is defined in a consistent way so that our final correction factor is a simple quotient of the number of weighted events. Section 7.2 deals with our acceptance definition and the results follow in section 7.3. For our purposes here, the acceptance is calculated with respect to the jet multiplicity (the number of inclusive jets in an event) for CAL jets to be consistent with what we measure in data. The motivation is not to have the hadron level correction linked to the W selection criteria but rather to focus on the unfolding the corrected CAL jets to the behavior of HAD jets by looking at the spectrum of jet kinematic observables. This procedure is therefore invariant with respect to our acceptance and systematics

considerations. The acceptance differs between jet multiplicity bins by only a couple of percent maximum and we account for potential correlations in our systematics between acceptance and both jet corrections as well as between jet energy corrections and the hadron level corrections described in this section. Our systematic treatment for our unfolding will be addressed in section 8.8.

The default topNtuple does not have hadron level jets (midpoint or otherwise) in the default jet collection. Thus we reproduced the topNtuples for our W signal MC (the first 10 samples of table 3.3 on page 113) by running the hadron level midpoint (R=0.4) algorithm over raw CDF MC samples via a modified top group "tarball"[28] from `tarball_614_1invfb.tar` [29] which was commonly used in the MC samples used in this analysis. Like most things in CDF software (i.e. AC++), the needed modification was straightforward once one knew where to look [66].

Modification to the code included changing `TopAlgorithms.cc` such that it would recognize an additional jet algorithm label (`jetAlgorithm="MPHAD"`). After including `JetMods/MidPointModule.hh` to go along with the existing `JetMods/JetCluModule.hh` in `TopFind.cc`, we then modified `topevent_SAM.tcl` to replace the last two jet collections (`JetCluModule-cone0.4H1` and `JetCluModule-cone0.7H1`) via the "jetList add" command. The new jet list included `MidPointModule-had-cone0.4` as well as the sister JetClu method, `JetCluModule-hadCone0.4`, which was left unused in this analysis. Per the instructions of Ben Kilminster, we also modified `CollectionAndViewTypeFinder.hh` such that the jet types were 10 and 11 for Midpoint and JetClu, respectively.

While making the new topNtuples with the HAD jet modifications we discovered that some of the original MC files had been overwritten and thus some of the samples have

fewer "generated" events. This is most dramatic in $W \to e\nu$+4p sample which has 40%

of number of events that are in the default topNtuples. Table 5.2 shows the number of

events as well as the relative weight calculated via equation 3.3 assuming the CEM/CMUP

luminosity of table 3.2. For brevity we do not include the separate weights for CMX

muons as this follows from the cited procedure in section 3.6. As is the case in general in

this analysis we do not assume the theoretical (MC generator) cross-section, σ(MC), is

absolutely correct but that it gets the relative weight between samples correct. The one

advantage to this consistency is that we can cross check basic distributions (lepton p_T,

missing energy, ϕ and η coverage, etc.) between the nominal samples presented in section

3.5. Near total agreement is found with only minor differences due to sample composition.

MC Sample	N(GEN)	σ(MC) (pb)	weight (w)
$W \to e\nu$+0p	939749	1800	5.4129
$W \to e\nu$+1p	1012254	225	0.6282
$W \to e\nu$+2p	776802	35.4	0.1288
$W \to e\nu$+3p	783415	5.6	0.0202
$W \to e\nu$+4p	397543	1.03	0.0073
$W \to \mu\nu$+0p	981752	1800	5.1813
$W \to \mu\nu$+1p	962243	225	0.6608
$W \to \mu\nu$+2p	867378	35.4	0.1153
$W \to \mu\nu$+3p	817043	5.6	0.0194
$W \to \mu\nu$+4p	906274	1.03	0.0032

Table 5.2. MC samples reconstructed using midpoint calorimeter and hadron level jets with the number of events and the event weight. The weight (w) is calculated via equation 3.3 using 2826. pb^{-1} for the total luminosity in the data.

This part of the analysis first selects for a W before applying any lepton/jet seperation

veto. Then we consider the number of jets in the event and compute our desired set of

observables (e.g. n^{th} leading jet p_T, etc.) independently in both samples and treat these as pseudo-cross-sections. Selecting HAD jets mirrors our CAL jets based cuts:

- $p_T > 20$ GeV/c

- $|\eta| < 2.0$

We mirror the procedure and concern of section 5.4 by vetoing events where the electron or muon is too close to the nearest jet in η-ϕ such that we effectively require $R_{\ell j} < 0.52$.

The HAD jet collection does have some unique considerations that needed to be addressed. Normally for a tight electron, it is removed from the jet list and is reclustered (see section 5.2) but the HAD jet algorithm does not automatically do this. In addition, the muon as well as the respective neutrinos also make it into the jet collection. We call these objects lepton-HAD-jets. In once sense the problem is minimal as there are no towers to be reclustered, etc. and cases where the lepton would be near ($R_{\ell j} < 0.52$) the closest jet are vetoed anyway. However, we have to first find the leptons in our HAD jet collection and remove them from consideration. This follows from our basic lepton-jet removal procedure explained in section 5.3 modulo some additional details that we have via working with the MC.

First we identify the leptons from the W decay via the `hepg` information bank. We loop through the jet collection (skipping jets that fail selection criteria) and match the leptons (ℓ and then ν) to the closest jet within $R < 0.40$. The jet cone radius is chosen as our matching criteria to be consistent with our normal (detector based) lepton-jet removal procedure. Even more so than our anti-selected lepton-jets this is largely overkill but matching with $R < 0.40$ removes a potential overlap bias on the rising edge of $R_{\ell j}$ after apply our separation veto. In cases where there are only 2 HAD jet objects and the

`hepg` information on the leptons satisfies our equivalent kinematic and geometric jet level cuts, our matching algorithm is over 99.9% effective for $R < 0.20$. The efficiency drops to about 98% if the matching requirement is relaxed to $R < 0.15$.

As a graphical check of our matching lepton-HAD-jet algorithm and more generally of our hadron level objects via the midpoint algorithm definition from the MC, we present a fully "reconstructed" W mass plots using the equivalent 4-vector information from the HAD jet collection. No additional cuts besides our baseline jet selection are used. Figures 5.22 and 5.23 show the results for $W \rightarrow e\nu + \geq n$ jets while figures 5.24 and 5.25 show the equivalent results for $W \rightarrow \mu\nu + \geq n$ jets.

For completeness we checked some basic variables to compare the HAD and CAL results directly at the event-by-event level. In particular, we were interested in how often jets (whether by jet multiplicity, momentum, and rapidity) were matched in both collections. In general the agreement is good and we see the type of spread that one expects when effectively changing the jet definition from detector based to being independent of the calorimeter. Figures 5.26 and 5.27 show the even-by-event difference in the number of HAD and CAL jets for electrons and muon, respectively. Additionally, we made the same plot but looked at the events that failed our W selection cuts which can be seen in figures 5.28 and 5.29. The motivation for looking at non-accepted events will be discussed below but the basic idea for these was to confirm that there was no W acceptance dependence. For now, we observe that there is no obvious dependence on the number of exclusive jets with regard to the HAD and CAL jets.

Continuing our basic investigation of HAD to CAL jets, we looked at various ratio plots of basic jet kinematic variables. Our final goal will be to compare the overall distributions
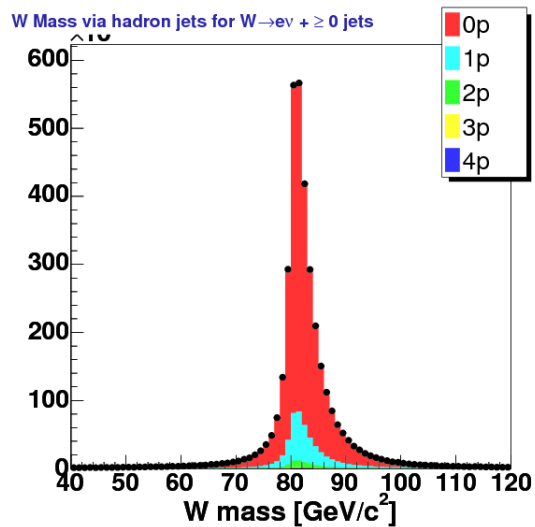
Figure 5.22. W mass constructed with hadron level jets for $W \to e\nu+ \geq 0$ jets in the post-shower/pre-cdf-detector-sim Alpgen+Pythia MC. The stacked histogram shows the contributions from each of the 5 parton samples ($W \to e\nu+$0-4p).
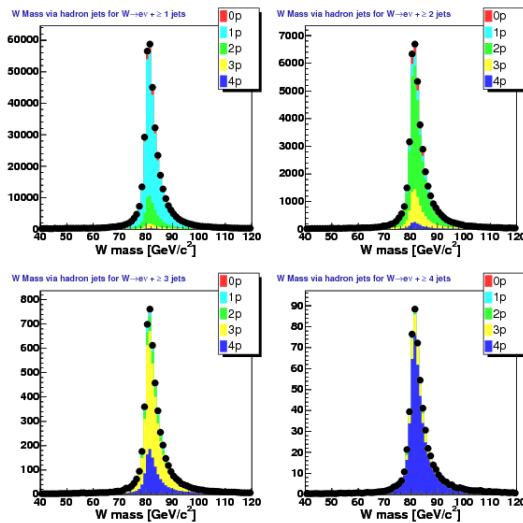
Figure 5.23. W mass constructed with hadron level jets for $W \to e\nu+ \geq 1$-4 jets in the post-shower/pre-cdf-detector-sim Alpgen+Pythia MC. The stacked histogram shows the contributions from each of the 5 parton samples ($W \to e\nu+$0-4p). The four plot represent each inclusive jet multiplicity: ≥ 1 for upper-left, ≥ 2 for upper-right, ≥ 3 for lower-left, and ≥ 4 for lower-right.
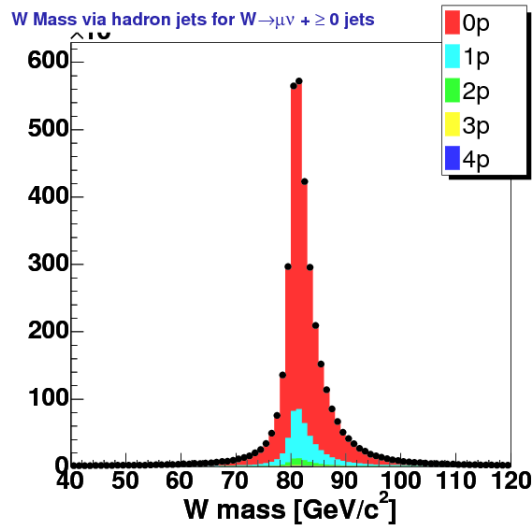
Figure 5.24. W mass constructed with hadron level jets for $W \to \mu\nu + \geq 0$ jets in the post-shower/pre-cdf-detector-sim Alpgen+Pythia MC. The stacked histogram shows the contributions from each of the 5 parton samples ($W \to \mu\nu$+0-4p).
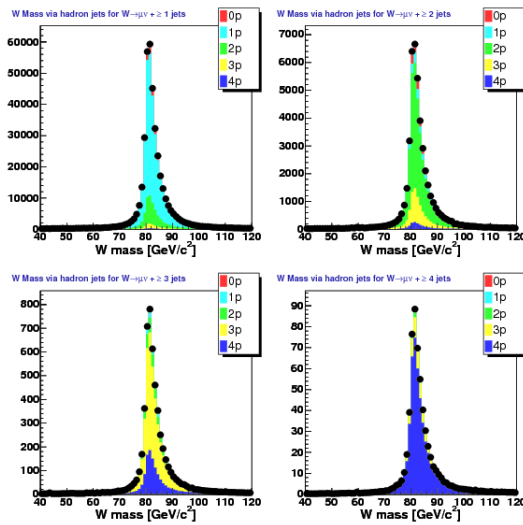
Figure 5.25. W mass constructed with hadron level jets for $W \to \mu\nu + \geq 1$-4 jets in the post-shower/pre-cdf-detector-sim Alpgen+Pythia MC. The stacked histogram shows the contributions from each of the 5 parton samples ($W \to \mu\nu$+0-4p). The four plot represent each inclusive jet multiplicity: ≥ 1 for upper-left, ≥ 2 for upper-right, ≥ 3 for lower-left, and ≥ 4 for lower-right.

of HAD and CAL jets and this will intrinsically allow for a jet in one collection to have no corresponding jet in the others collection. This also allows for corresponding jets in both collections to shift their relative rank in jet p_T which we colloquially refer to as "jockeying for position". For example, the 1st leading CAL jet might occupy the same η-ϕ as the 2nd leading HAD jet. However, it is instructive to look at cases where we can match our default calorimeter based jets to our hadron level jets. Operationally we loop through the CAL jets and match them (independent of their energy or p_T rank) by a simple $R_{j^{CAL}j^{HAD}} < 0.4$ algorithm. We chose the jet cone size ($R = 0.4$) as this as the effective minimum separation between jets in both collections. For our investigation here, the jet transverse momentum rank (i.e. n^{th} leading jet) is always with respect to the CAL based jet. Obviously, this procedure does not allow for comparisons of unmatched jets in either collection.

First we looked at the event-by-event ratio of the nth leading jet p_T (p_T^{HAD}/p_T^{CAL}) as well as the corresponding jet η ratio (η^{HAD}/η^{CAL}). The former is plotted in figures 5.30 and 5.31 for the electron and muon channel, respectively. Likewise the jet η ratio is shown in figures 5.32 and 5.33. In both sets of plots it is clear that jets often match up and favor a ratio around unity as would be expected. The jet pseudo-rapidity is considerably narrower relative to the jet transverse momentum and this is consistent in general with the relative spread in these variables with respect to jet energy correction and the general bias we introduced in our matching procedure. As a final check we looked at two dijet distributions: m_{jj} (jet-jet mass) and R_{jj} (the η-ϕ separation) between the leading two CAL jets and their matching corespondents in the HAD collection. The dijet mass HAD/CAL ratio is presented in figures 5.34 and 5.35 for the electron and muon

channel, respectively. Similarly, the dijet separation plots are given in figures 5.36 and 5.37. These dijet plots mirror the basic features of the nth leading jet p_T and η plots with m_{jj} being relatively smeared while R_{jj} is very narrow.
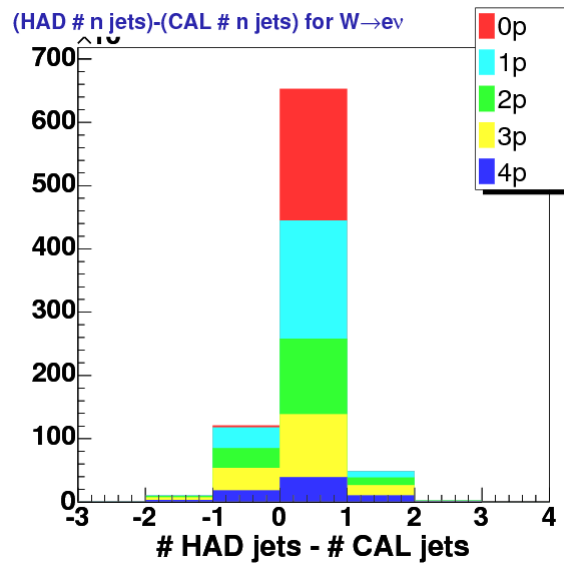
Figure 5.26. The difference in the number of exclusive HAD jets to CAL jets for $W \to e\nu + \geq 0$ jets from Alpgen+Pythia MC. This is an event-by-event distribution that passes all our W selection cuts. The stacked histogram shows the contributions from each of the 5 parton samples ($W \to e\nu$+0-4p).
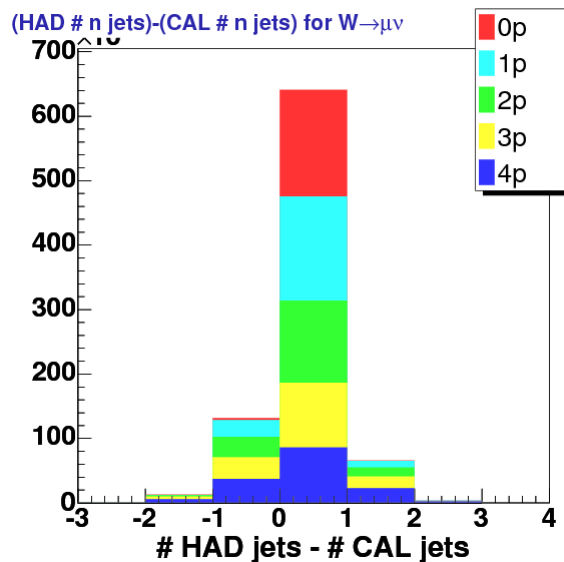
Figure 5.27. The difference in the number of exclusive HAD jets to CAL jets for $W \to \mu\nu + \geq 0$ jets from Alpgen+Pythia MC. This is an event-by-event distribution that passes all our W selection cuts. The stacked histogram shows the contributions from each of the 5 parton samples ($W \to \mu\nu$+0-4p).
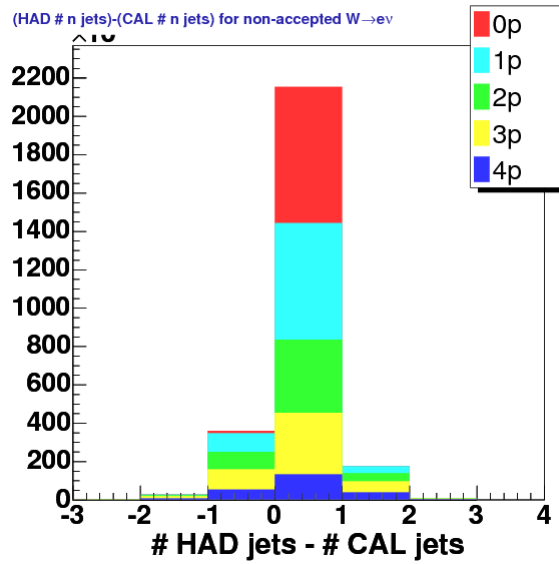
Figure 5.28. The difference in the number of exclusive HAD jets to CAL jets for non-accepted $W \to e\nu + \geq 0$ jets from Alpgen+Pythia MC. This is an event-by-event distribution that *fails* our W selection criteria. The stacked histogram shows the contributions from each of the 5 parton samples ($W \to e\nu$+0-4p).
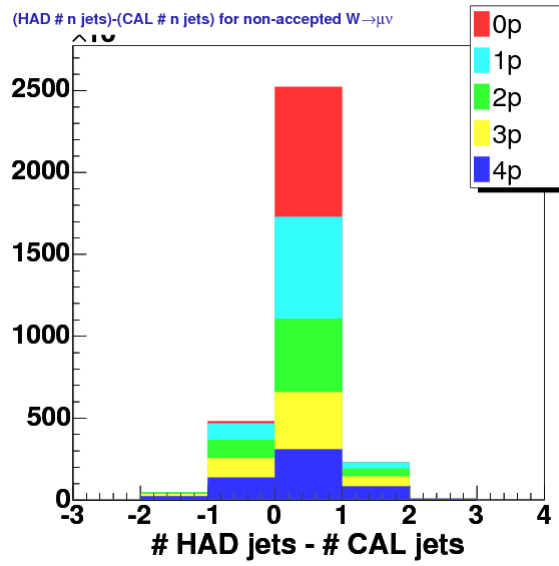
Figure 5.29. The difference in the number of exclusive HAD jets to CAL jets for non-accepted $W \to \mu\nu+ \geq 0$ jets from Alpgen+Pythia MC. This is an event-by-event distribution that *fails* our W selection criteria. The stacked histogram shows the contributions from each of the 5 parton samples ($W \to \mu\nu$+0-4p).
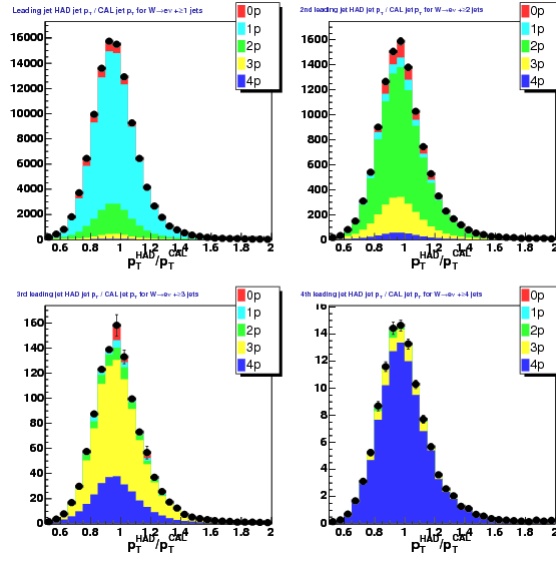
Figure 5.30. The nth leading jet p_T ratio between HAD and CAL jets for $W \rightarrow e\nu + \geq n$ jets from Alpgen+Pythia MC. This is an event-by-event distribution of p_T^{HAD}/p_T^{CAL}. The stacked histogram shows the contributions from each of the 5 parton samples ($W \rightarrow e\nu+$0-4p). The four plot represent each inclusive jet multiplicity: ≥ 1 for upper-left, ≥ 2 for upper-right, ≥ 3 for lower-left, and ≥ 4 for lower-right.
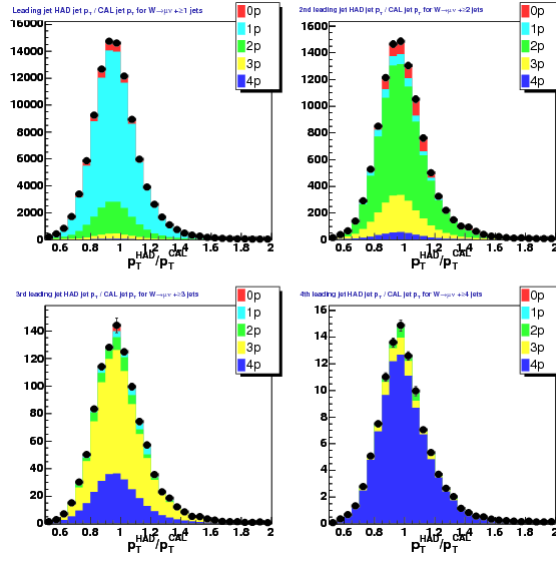
Figure 5.31. The nth leading jet p_T ratio between HAD and CAL jets for $W \rightarrow \mu\nu + \geq n$ jets from Alpgen+Pythia MC. This is an event-by-event distribution of p_T^{HAD}/p_T^{CAL}. The stacked histogram shows the contributions from each of the 5 parton samples ($W \rightarrow \mu\nu$+0-4p). The four plot represent each inclusive jet multiplicity: ≥ 1 for upper-left, ≥ 2 for upper-right, ≥ 3 for lower-left, and ≥ 4 for lower-right.
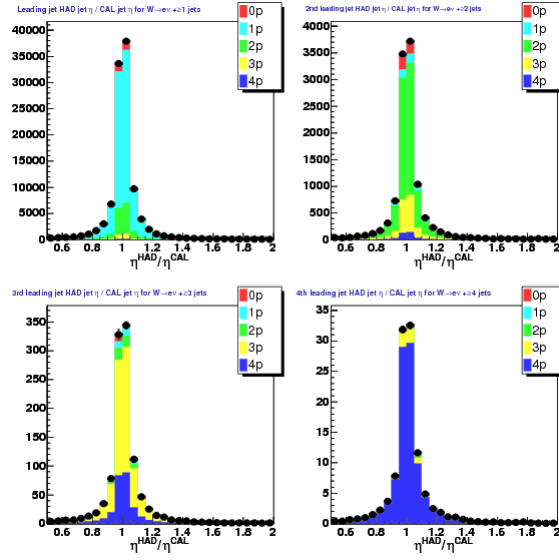
Figure 5.32. The nth leading jet η ratio between HAD and CAL jets for $W \to e\nu+ \geq n$ jets from Alpgen+Pythia MC. This is an event-by-event distribution of η^{HAD}/η^{CAL}. The stacked histogram shows the contributions from each of the 5 parton samples ($W \to e\nu$+0-4p). The four plot represent each inclusive jet multiplicity: ≥ 1 for upper-left, ≥ 2 for upper-right, ≥ 3 for lower-left, and ≥ 4 for lower-right.
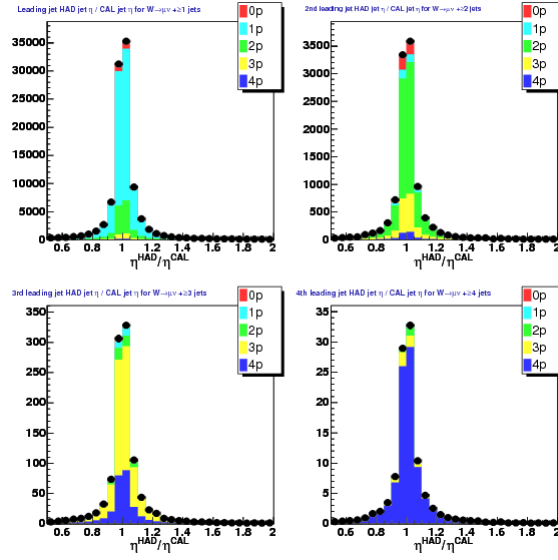
Figure 5.33. The nth leading jet η ratio between HAD and CAL jets for $W \to \mu\nu+ \geq n$ jets from Alpgen+Pythia MC. This is an event-by-event distribution of η^{HAD}/η^{CAL}. The stacked histogram shows the contributions from each of the 5 parton samples ($W \to \mu\nu$+0-4p). The four plot represent each inclusive jet multiplicity: ≥ 1 for upper-left, ≥ 2 for upper-right, ≥ 3 for lower-left, and ≥ 4 for lower-right.

At this stage, we have dealt with several potential pitfalls such as dealing with lepton-HAD-jets and have a basic handle on understanding our hadron level jets with respect to our nominal detector derived calorimeter jets. Now we turn to the process of deriving an unfolding factor that will correct our calorimeter jet based cross-sections to a detector independent hadron level cross-section. We proceed by forming distributions using both HAD and CAL jets using our normal W selection criteria and also accounting for additional global analysis factors like our vertex reweighting (full details in section 6.6). The goal is to from a ratio between our HAD results and CAL results; this literally takes the form of dividing the HAD based distribution (histogram) by the CAL distribution. Since the relative weighting of events is completely consistent and acceptance/efficiency terms are by definition the same this ratio is identical to a full cross-section measurement.

Let $\sigma_{CAL}(\text{data})$ be a CAL jet based cross-section (for example the nth leading jet differential cross-section, $\mathrm{d}\sigma/\mathrm{d}p_T^{n^{\text{th}}}$) based on the data minus background estimates divided by the product of luminosity, acceptance, and efficiency (see section 9.1 for details on our cross-section definition). Let $\sigma_{HAD}(\text{MC})$ and $\sigma_{CAL}(\text{MC})$ be W MC based distributions based, respectively, on the hadron level jet collection and the post-CDF simulation based calorimeter jets. We define our unfolding factor, u, as

$$(5.5) \qquad u \equiv \left(\frac{\sigma_{HAD}(\text{MC})}{\sigma_{CAL}(\text{MC})} \right)$$

As we desire to correct the data to the hadron level with this unfolding factor, we have $\sigma_{HAD}(\text{data}) = u(\sigma_{CAL}(\text{data}))$ or

$$(5.6) \qquad \sigma_{HAD}(\text{data}) = \left(\frac{\sigma_{HAD}(\text{MC})}{\sigma_{CAL}(\text{MC})} \right) \sigma_{CAL}(\text{data})$$

The uncertainty in u which we call Δu we take as the standard error propagation (equation 5.7) from quotient of the HAD and CAL statistical (Poisson) uncertainty; $\Delta\sigma_{HAD}$ and $\Delta\sigma_{CAL}$, respectively. Note that we take these errors as uncorrelated as they represent two independent statements about our MC sample.

$$\text{(5.7)} \qquad\qquad \Delta u = u\sqrt{\left(\frac{\Delta\sigma_{HAD}}{\sigma_{HAD}}\right)^2 + \left(\frac{\Delta\sigma_{CAL}}{\sigma_{CAL}}\right)^2}$$

A full example of this procedure is given in the next section along with our full hadron level correction (unfolding) results. The use of this unfolding scale factor is later mentioned in our cross-section definition (equation 9.2) on page 416 in section 9.1. Our systematic treatment for the unfolding is given in section 8.8.

5.9. Hadron Level Correction (Unfolding) Results

As a general test of this procedure in action and to double check our basic HAD results we consider a trivial distribution that should be independent of jet collection/level. The example which follows involves an idealized case where the sample is artificially confined to have $\geq n$ jets matched between HAD and CAL jets. This same sampling process was use to produce our HAD/CAL event-by-event ratios of figures 5.30-5.37. Let $\Delta R_{\ell j}$ be the η-ϕ separation between the charged lepton ($\ell = e$ or μ) and the nth leading jet (j). This distribution is expected to largely be independent of jet multiplicity as well as lepton channel and should not have an dependence HAD or CAL jets modulo the handling of jets very close to the lepton. Figures 5.38 and 5.39 shows the HAD and CAL results, respectively, for ΔR_{ej}. In the same fashion, figures 5.40 and 5.41 gives the results for

$\Delta R_{\mu j}$. Our bin-by-bin unfolding factors are given in figures 5.42 and 5.43 for ΔR_{ej} and $\Delta R_{\mu j}$, respectively.

As advertised, there is broad agreement in the distributions across jet multiplicity, lepton channel, and between HAD and CAL jets. The unfolding factor distribution $(\sigma_{HAD}/\sigma_{CAL})$ is consistent unity. Only the first bin which starts at $\Delta R_{\ell j}$=0.4 and only has content for $\Delta R_{\ell j} > 0.52$ deviates. Since the effect is seen in both electrons and muons (and the latter is indifferent to the response in the calorimeter) we take this as an indication that our lepton-jet veto is overly efficient. In any event, if we were constructing a cross-section based off of $\Delta R_{\ell j}$ we would be able to correct to the hadron level by multiplying bin-by-bin by our unfolding factor. As already noted, in this case we could safely declare the unfolding factor as globally consistent with unity and derive an uncertainty based on the spread which would ultimately be negligible relative to the basic jet energy scale systematic.

As an additional test, we also looked at the unfolding of the nth leading jet η using the same matched sample as our $\Delta R_{\ell j}$ example. This variable is of interest as we know our jet energy corrections have an obvious η dependence due to the composition of calorimeter (for example see figures 5.18 and 5.19). Looking at the response without the (simulated) detector via our hadron level jet η compared to the (corrected) detector response at the calorimeter level is useful as we expect our relative jet energy corrections combined with rigidity of the pseudo-rapidity variable for jets that are in both jet collections to produce a relatively flat unfolding. First we show the HAD results for the nth leading jet η in figures 5.44 (electrons) and 5.46 (muons). Likewise our CAL results are given in figures

5.45 and 5.47. We present the respective electron and muon unfolding in figures 5.48 and 5.49.

In cases where the unfolding is flat or where we want explicitly estimate the overall unfolding fraction for each inclusive jet multiplicity (as indeed we must for the jet multiplicity cross-section itself) we calculate the unfolding factor with its associated uncertainty directly using our jet multiplicity pseudo-cross-sections with our HAD and CAL jet collections. This procedure is straightforward as it follows for our prescription of equations 5.5 and 5.7 and is consistent with the bin-by-bin approach outlined in our previous two examples. Our original approach of averaging over each unfolding spectrum gave a consistent result but was overly complicated and potentially statistically problematic [**67**].

The jet multiplicity unfolding factor (u) for both lepton channels is given in table 5.3. Not surprisingly, distributions with η and ϕ are more uniform and flat and thus an overall unfolding factor and its error can with the universal factor presented in the table. For example, we apply the ≥ 2 jet unfolding factor for our dijet separation (R_{jj}) differential cross-section.

$\geq n$ jets	$W \to e\nu$ u	$W \to e\nu$ Δu	$W \to \mu\nu$ u	$W \to \mu\nu$ Δu
0	1.0000	0.0028	1.0000	0.0029
1	0.7557	0.0031	0.7793	0.0032
2	0.6445	0.0061	0.6771	0.0064
3	0.5759	0.0103	0.6069	0.0101
4	0.5410	0.0134	0.5822	0.0186

Table 5.3. Jet multiplicity unfolding factor and its associated error for $W \to \ell\nu$ Alpgen MC. Calculated directly via equations 5.5 and 5.7. This unfolding factor can be applied to results where the bin-by-bin unfolding factor for a differential cross-section is flat and relatively uniform (e.g. R_{jj}). The total inclusive unfolding factor is effectively unity by construction as the inclusive W acceptance is invariant to jet definition/algorithm.

Our unfolding results for our jet kinematic variables follows is a straight forward way. The definition of most of these plots will be formally introduced in chapter 9. We will generally omit the individual HAD and CAL plots and go straight to their quotient represented on the y-axis as $\sigma_{HAD}/\sigma_{CAL}$. The error is statistical and follows via the naive error propagation of dividing the two histograms (see equation 5.7). Kinematic observables with momentum, mass, energy, etc. by in large have features that make bin-by-bin corrections a necessity and as such do not use the universal unfolding factor of table 5.3.

We begin by presenting the unfolding factor for the nth leading jet p_T for $W \rightarrow \ell\nu+ \geq n$ jets. Figure 5.50 presents the results for 1-4 jets in the electron channel; likewise the muon channel results are given in figure 5.51. The jet p_T is very much central to this analysis and is directly effected by this hadron level correction procedure. As a result, we also have several follow up plots that check various factors. For example, figure 5.52 shows the first and second jet p_T for inclusive 3 jets for both electron and muon channels. This was done to check the unfolding factor at higher jet multiplicities (the nth leading jet p_T is dominated by the exclusive n number of jets). We repeated this style of plot for the first, second, and third leading jet p_T for ≥ 4 jets. The electron channel is shown in figure 5.53 while the muon channel is given in figure 5.54.

Continuing with our additional set of unfolding plots for jet p_T we present results where we modified our procedure to directly match (event-by-event) hadron level jets to their calorimeter simulated counterparts. Figures 5.57 and 5.58 correspond to the electron and muon results, respectively, of figures 5.50 and 5.51. Although we do not use this results directly, they are useful as a check on our default (unmatched) scheme

described previously. This "true matching" scheme is effectively the same make up sample wise with our ratio plots present in the previous section (e.g. figures 5.30-5.37 and our $\Delta R_{\ell,j}$ example). The strict matching requirement requires each jet in the CAL sample to have a corresponding jet in the HAD sample and vise versa. Hadron level jets are allowed to jockey for position relative to being matched with the calorimeter jet ordering. The unfolding factor is still calculated as a proper quotient between pseudo cross-sections for HAD and CAL. The advantage to this procedure is that the acceptance is literally equal between both qualities (the jet multiplicity is identical for HAD and CAL event-by-event).
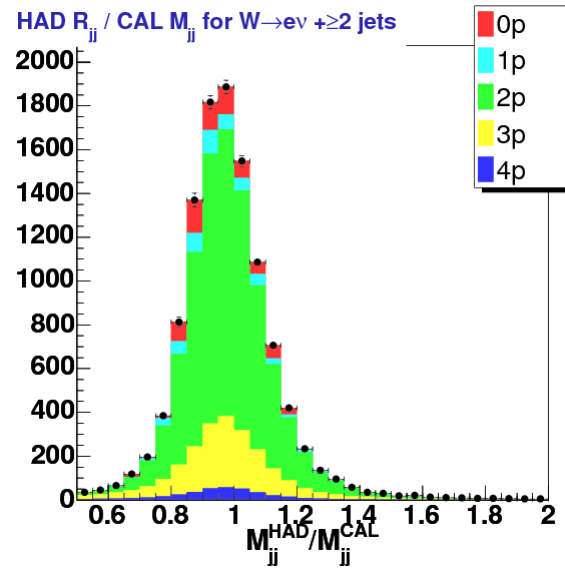
Figure 5.34. The dijet mass ratio for HAD and CAL jets for $W \to e\nu+ \geq 2$ jets from Alpgen+Pythia MC. This is an event-by-event distribution of $M_{jj}^{HAD}/M_{jj}^{CAL}$. The stacked histogram shows the contributions from each of the 5 parton samples ($W \to e\nu+$0-4p).
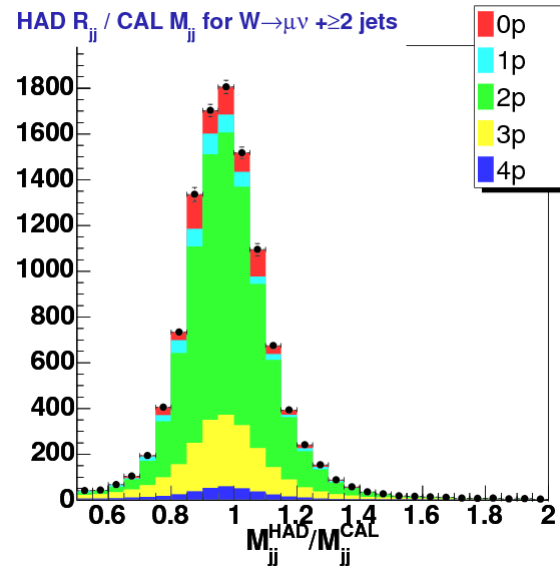
Figure 5.35. The dijet mass ratio for HAD and CAL jets for $W \to \mu\nu+ \geq 2$ jets from Alpgen+Pythia MC. This is an event-by-event distribution of $M_{jj}^{HAD}/M_{jj}^{CAL}$. The stacked histogram shows the contributions from each of the 5 parton samples ($W \to \mu\nu$+0-4p).
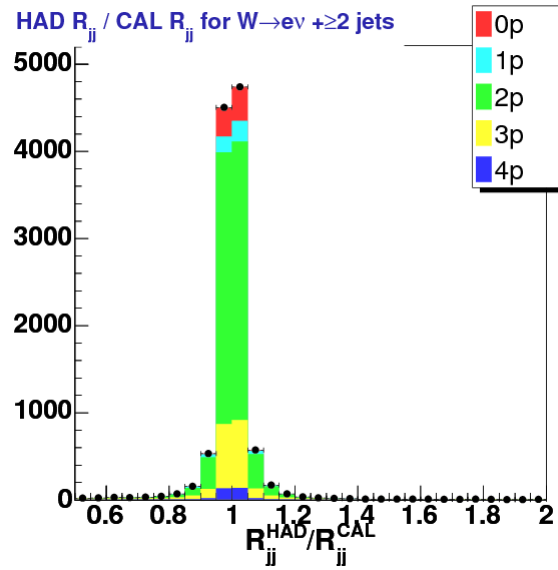
Figure 5.36. The dijet separation ratio for HAD and CAL jets for $W \rightarrow e\nu+ \geq 2$ jets from Alpgen+Pythia MC. This is an event-by-event distribution of $R_{jj}^{HAD}/R_{jj}^{CAL}$. The stacked histogram shows the contributions from each of the 5 parton samples ($W \rightarrow e\nu$+0-4p).
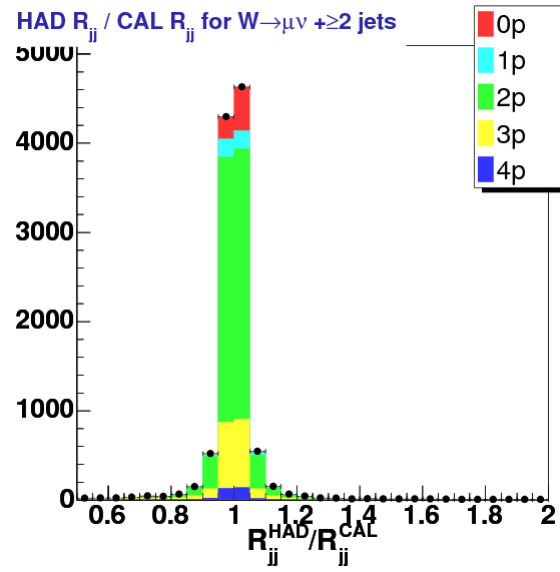
Figure 5.37. The dijet separation ratio for HAD and CAL jets for $W \rightarrow \mu\nu + \geq 2$ jets from Alpgen+Pythia MC. This is an event-by-event distribution of $R_{jj}^{HAD}/R_{jj}^{CAL}$. The stacked histogram shows the contributions from each of the 5 parton samples ($W \rightarrow \mu\nu$+0-4p).
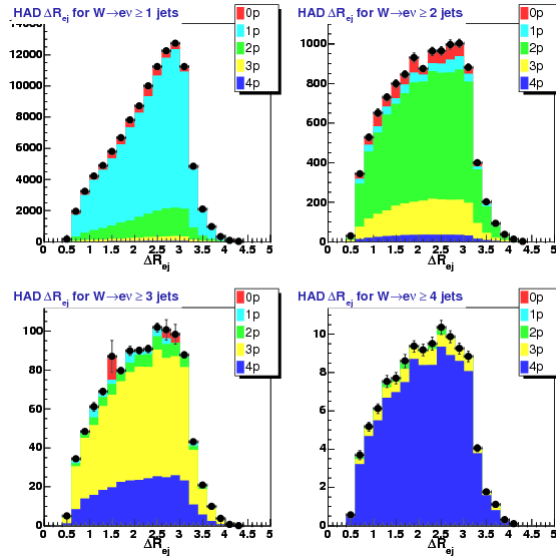
Figure 5.38. The electron and n^{th} leading jet separation (ΔR_{ej}) for hadron level jets for $W \rightarrow e\nu+ \geq n$ jets from Alpgen+Pythia MC. The stacked histogram shows the contributions from each of the 5 parton samples ($W \rightarrow e\nu$+0-4p). The four plot represent each inclusive jet multiplicity: ≥ 1 for upper-left, ≥ 2 for upper-right, ≥ 3 for lower-left, and ≥ 4 for lower-right.
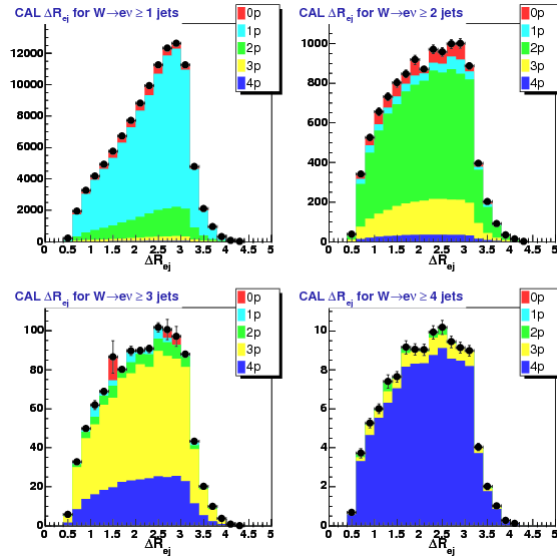
Figure 5.39. The electron and n^{th} leading jet separation (ΔR_{ej}) for calorimeter (detector simulation) level jets for $W \rightarrow e\nu+ \geq n$ jets from Alpgen+Pythia MC. The stacked histogram shows the contributions from each of the 5 parton samples $(W \rightarrow e\nu+0\text{-}4\text{p})$. The four plot represent each inclusive jet multiplicity: ≥ 1 for upper-left, ≥ 2 for upper-right, ≥ 3 for lower-left, and ≥ 4 for lower-right.
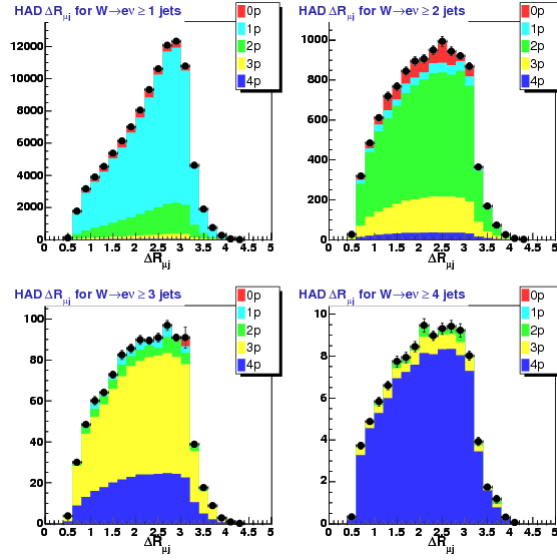
Figure 5.40. The muon and n^{th} leading jet separation $(\Delta R_{\mu j})$ for hadron level jets for $W \to \mu\nu+ \geq n$ jets from Alpgen+Pythia MC. The stacked histogram shows the contributions from each of the 5 parton samples $(W \to e\nu+$0-4p$)$. The four plot represent each inclusive jet multiplicity: ≥ 1 for upper-left, ≥ 2 for upper-right, ≥ 3 for lower-left, and ≥ 4 for lower-right.
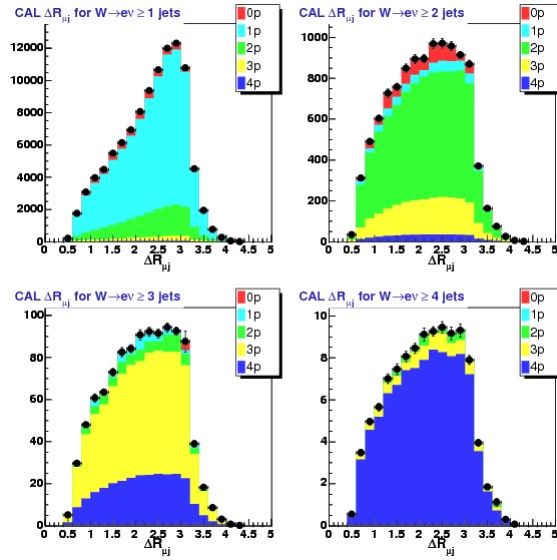
Figure 5.41. The muon and n^{th} leading jet separation $(\Delta R_{\mu j})$ for calorime-
ter (detector simulation) level jets for $W \rightarrow \mu\nu+ \geq n$ jets from Alp-
gen+Pythia MC. The stacked histogram shows the contributions from each
of the 5 parton samples $(W \rightarrow \mu\nu+\text{0-4p})$. The four plot represent each
inclusive jet multiplicity: ≥ 1 for upper-left, ≥ 2 for upper-right, ≥ 3 for
lower-left, and ≥ 4 for lower-right.

195
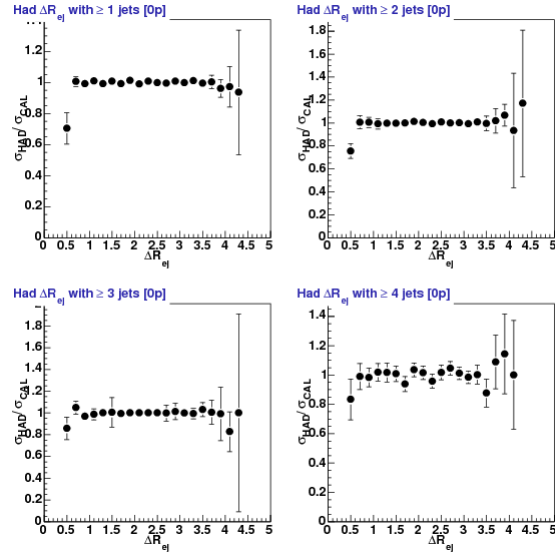
Figure 5.42. Unfolding factor ($u = \sigma(HAD)/\sigma(CAL)$, see equation 5.5 on page 181) for ΔR_{ej} for $W \rightarrow e\nu + \geq n$ jets from Alpgen+Pythia MC. The title for each plot should be ignored to avoid confusion with its content. The four plot represent each inclusive jet multiplicity: ≥ 1 for upper-left, ≥ 2 for upper-right, ≥ 3 for lower-left, and ≥ 4 for lower-right.
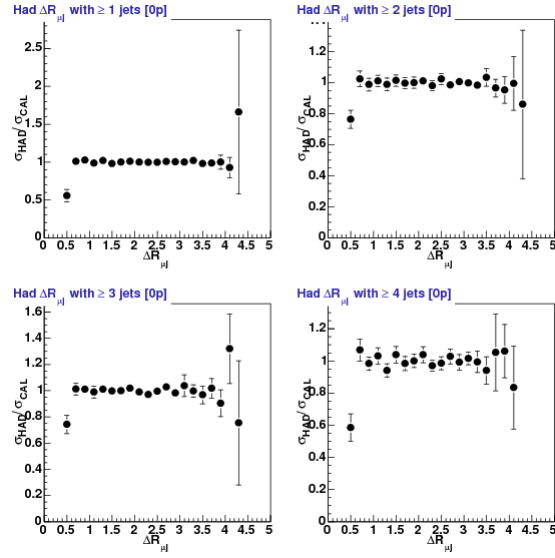
Figure 5.43. Unfolding factor ($u = \sigma(HAD)/\sigma(CAL)$, see equation 5.5 on page 181) for $\Delta R_{\mu j}$ for $W \to \mu\nu+ \geq n$ jets from Alpgen+Pythia MC. The title for each plot should be ignored to avoid confusion with its content. The four plot represent each inclusive jet multiplicity: ≥ 1 for upper-left, ≥ 2 for upper-right, ≥ 3 for lower-left, and ≥ 4 for lower-right.
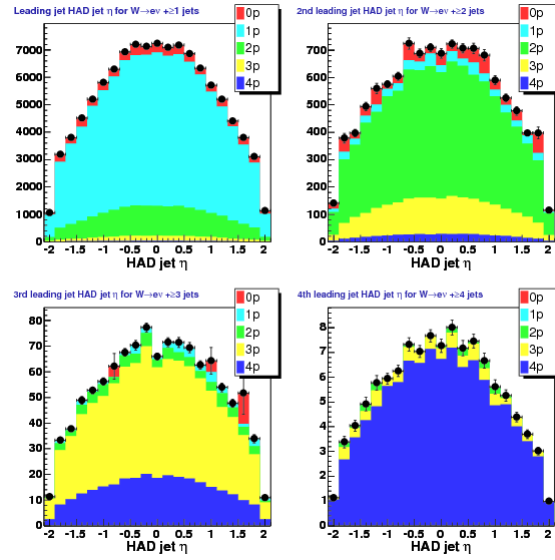
Figure 5.44. n^{th} leading jet η of hadron level jets for $W \to e\nu+ \geq n$ jets from Alpgen+Pythia MC. The stacked histogram shows the contributions from each of the 5 parton samples ($W \to e\nu+$0-4p). The four plot represent each inclusive jet multiplicity: ≥ 1 for upper-left, ≥ 2 for upper-right, ≥ 3 for lower-left, and ≥ 4 for lower-right.
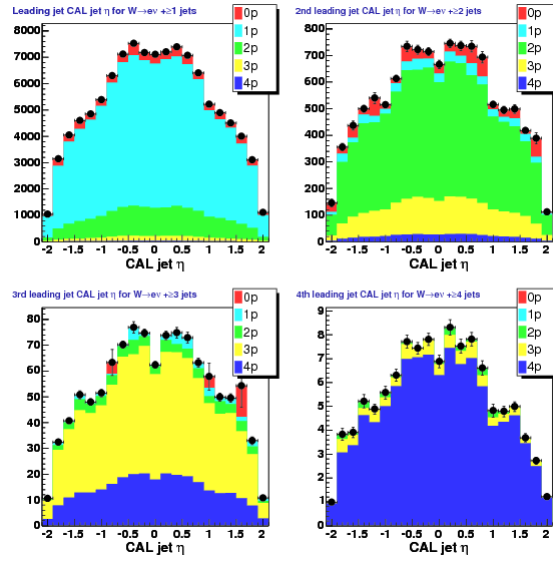
Figure 5.45. n^{th} leading jet η of calorimeter (detector simulation) level jets for $W \to e\nu + \geq n$ jets from Alpgen+Pythia MC. The stacked histogram shows the contributions from each of the 5 parton samples ($W \to e\nu$+0-4p). The four plot represent each inclusive jet multiplicity: ≥ 1 for upper-left, ≥ 2 for upper-right, ≥ 3 for lower-left, and ≥ 4 for lower-right.

199
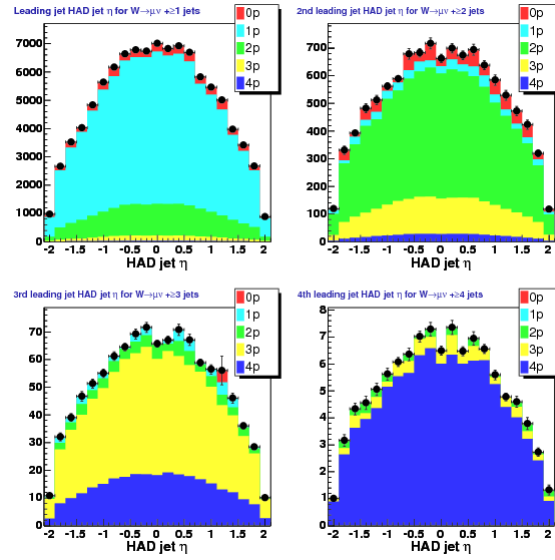
Figure 5.46. n^{th} leading jet η of hadron level jets for $W \rightarrow \mu\nu+ \geq n$ jets from Alpgen+Pythia MC. The stacked histogram shows the contributions from each of the 5 parton samples ($W \rightarrow \mu\nu$+0-4p). The four plot represent each inclusive jet multiplicity: $\geq$1 for upper-left, $\geq$2 for upper-right, $\geq$3 for lower-left, and $\geq$4 for lower-right.
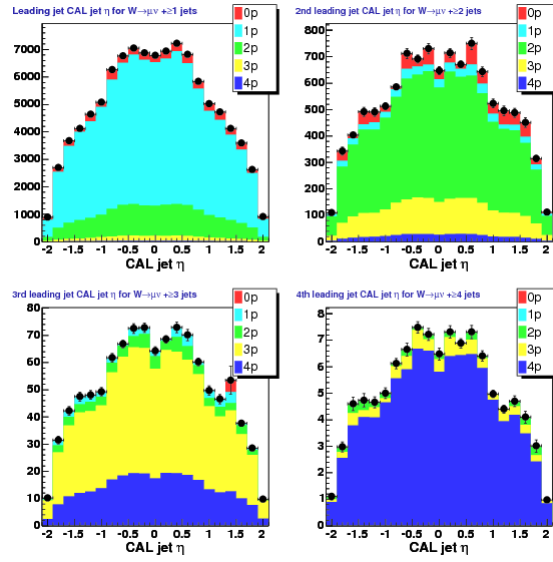
Figure 5.47. n^{th} leading jet η of calorimeter (detector simulation) level jets for $W \to \mu\nu+ \geq n$ jets from Alpgen+Pythia MC. The stacked histogram shows the contributions from each of the 5 parton samples ($W \to \mu\nu$+0-4p). The four plot represent each inclusive jet multiplicity: ≥ 1 for upper-left, ≥ 2 for upper-right, ≥ 3 for lower-left, and ≥ 4 for lower-right.
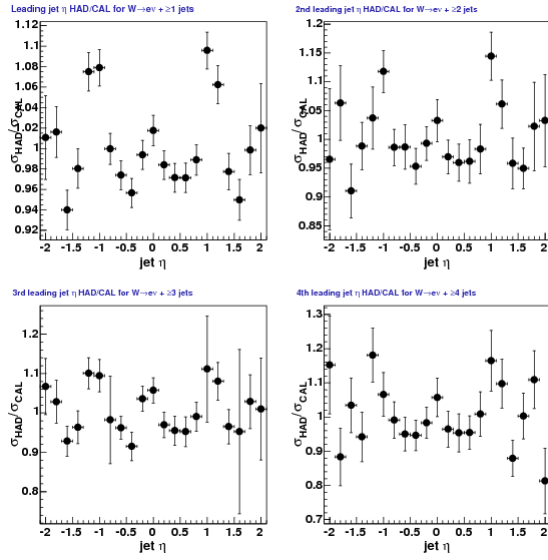
Figure 5.48. Unfolding factor $(\sigma(HAD)/\sigma(CAL))$ of the nth leading jet η for $W \to e\nu + \geq n$ jets from Alpgen+Pythia MC. The four plot represent each inclusive jet multiplicity: ≥ 1 for upper-left, ≥ 2 for upper-right, ≥ 3 for lower-left, and ≥ 4 for lower-right.
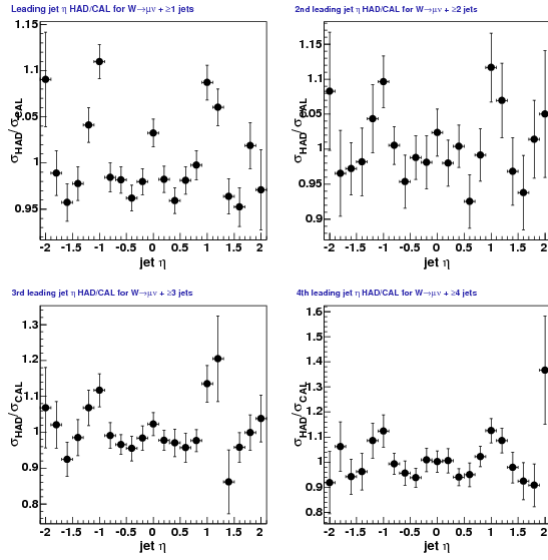
Figure 5.49. Unfolding factor $(\sigma(HAD)/\sigma(CAL))$ of the nth leading jet η for $W \rightarrow \mu\nu+ \geq n$ jets from Alpgen+Pythia MC. The four plot represent each inclusive jet multiplicity: ≥ 1 for upper-left, ≥ 2 for upper-right, ≥ 3 for lower-left, and ≥ 4 for lower-right.
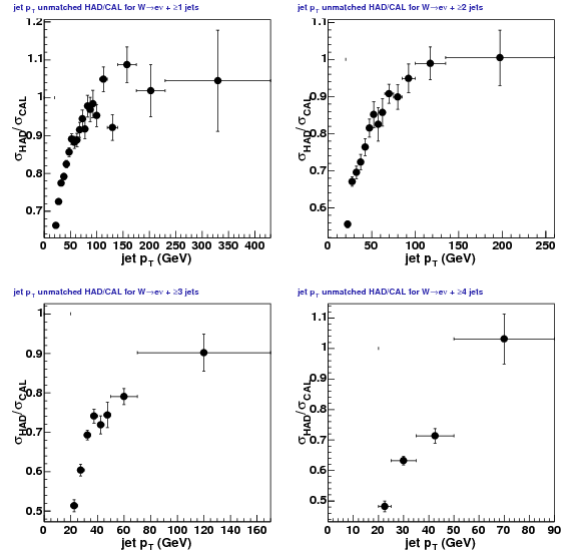
Figure 5.50. Unfolding factor $(\sigma(HAD)/\sigma(CAL))$ of the nth leading jet p_T for $W \to e\nu+ \geq n$ jets from Alpgen+Pythia MC. The four plot represent each inclusive jet multiplicity: ≥ 1 for upper-left, ≥ 2 for upper-right, ≥ 3 for lower-left, and ≥ 4 for lower-right.
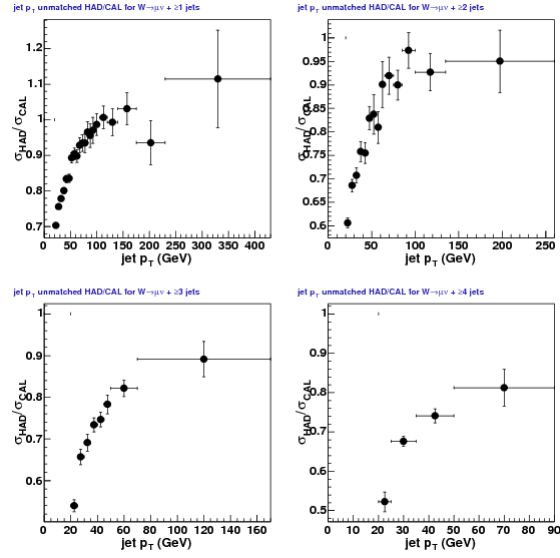
Figure 5.51. Unfolding factor $(\sigma(HAD)/\sigma(CAL))$ of the nth leading jet p_T for $W \to \mu\nu + \geq n$ jets from Alpgen+Pythia MC. The four plot represent each inclusive jet multiplicity: ≥ 1 for upper-left, ≥ 2 for upper-right, ≥ 3 for lower-left, and ≥ 4 for lower-right.
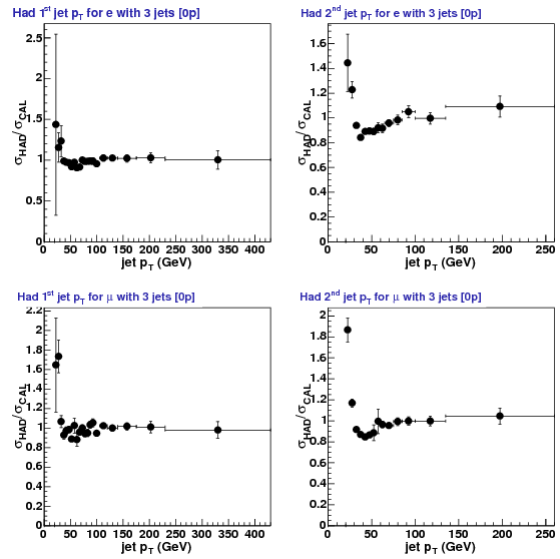
Figure 5.52. Unfolding factor $(\sigma(HAD)/\sigma(CAL))$ of the first (left side) and second (right side) leading jet p_T for $W \to \ell\nu + \geq 3$ jets from Alpgen+Pythia MC. The top plots are for the electron channel while the bottom ones are for the muon channel.

205
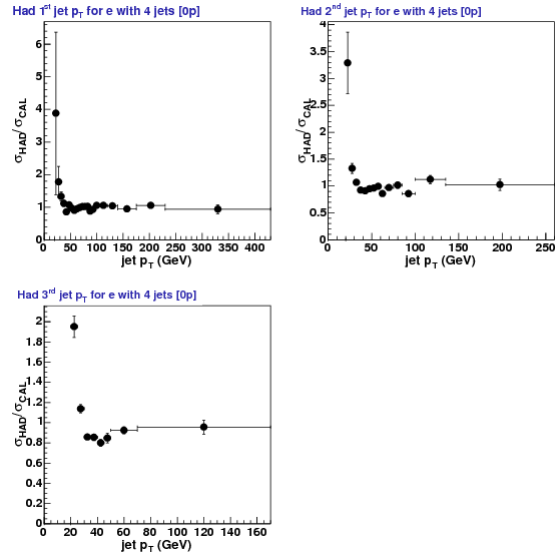
Figure 5.53. Unfolding factor $(\sigma(HAD)/\sigma(CAL))$ of the first (upper-left side), second (upper-right side), and third leading jet (lower-left side) leading jet p_T for $W \rightarrow e\nu+ \geq 3$ jets from Alpgen+Pythia MC.
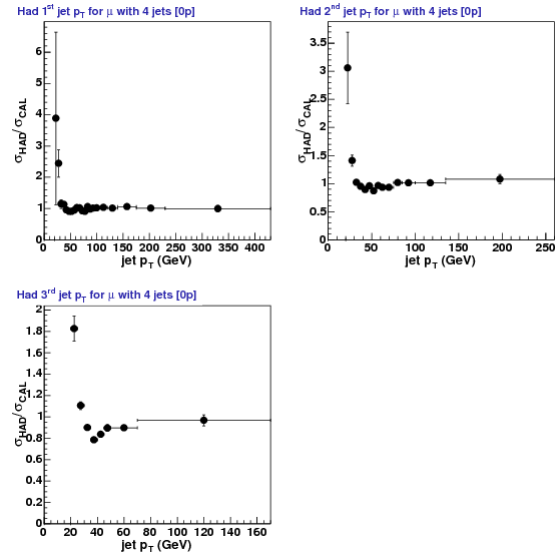
Figure 5.54. Unfolding factor $(\sigma(HAD)/\sigma(CAL))$ of the first (upper-left side), second (upper-right side), and third leading jet (lower-left side) leading jet p_T for $W \rightarrow \mu\nu+ \geq 3$ jets from Alpgen+Pythia MC.
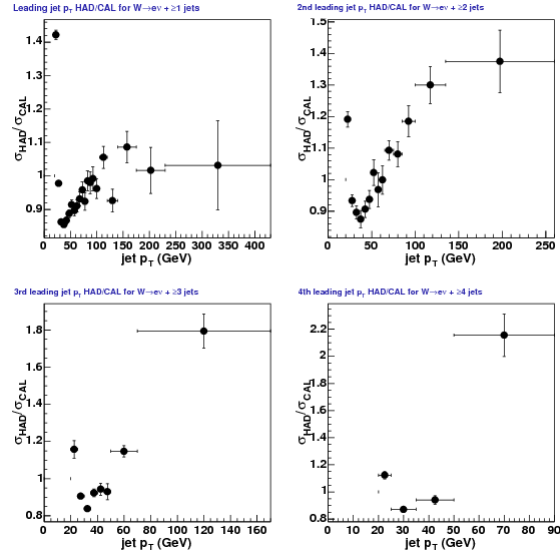
Figure 5.55. Unfolding factor $(\sigma(HAD)/\sigma(CAL))$ of the nth leading jet p_T for $W \to e\nu + \geq n$ jets from Alpgen+Pythia MC. These results require that n jets be matched although the number and order are not required to be the same. The four plot represent each inclusive jet multiplicity: ≥ 1 for upper-left, ≥ 2 for upper-right, ≥ 3 for lower-left, and ≥ 4 for lower-right.
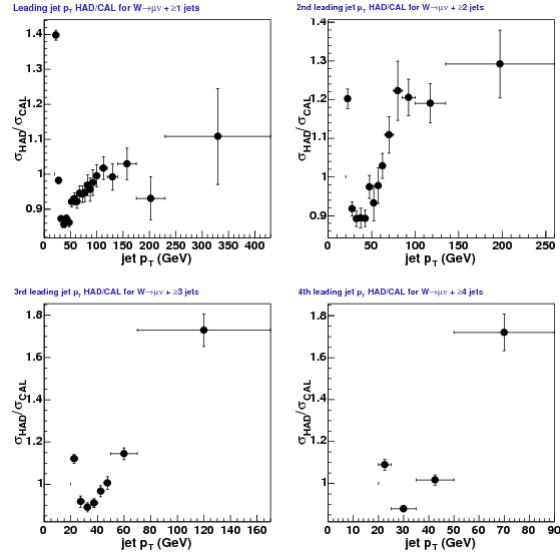
Figure 5.56. Unfolding factor $(\sigma(HAD)/\sigma(CAL))$ of the nth leading jet p_T for $W \rightarrow \mu\nu + \geq n$ jets from Alpgen+Pythia MC. These results require that n jets be matched although the number and order are not required to be the same. The four plot represent each inclusive jet multiplicity: ≥ 1 for upper-left, ≥ 2 for upper-right, ≥ 3 for lower-left, and ≥ 4 for lower-right.
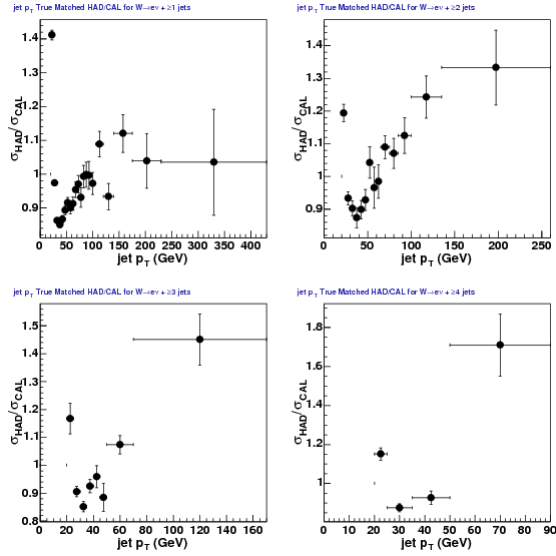
Figure 5.57. Unfolding factor $(\sigma(HAD)/\sigma(CAL))$ of the nth leading jet p_T for $W \to e\nu + \geq n$ jets from Alpgen+Pythia MC where both pseudo-cross-sections have been constructed via a sample where every calorimeter jet is matched ("true matched") to its hadron level counterpart. While biased toward the calorimeter jet definition jet p_T ordering, it has the virtue of having explicitly equal number of events in both HAD and CAL samples. The four plot represent each inclusive jet multiplicity: ≥ 1 for upper-left, ≥ 2 for upper-right, ≥ 3 for lower-left, and ≥ 4 for lower-right.
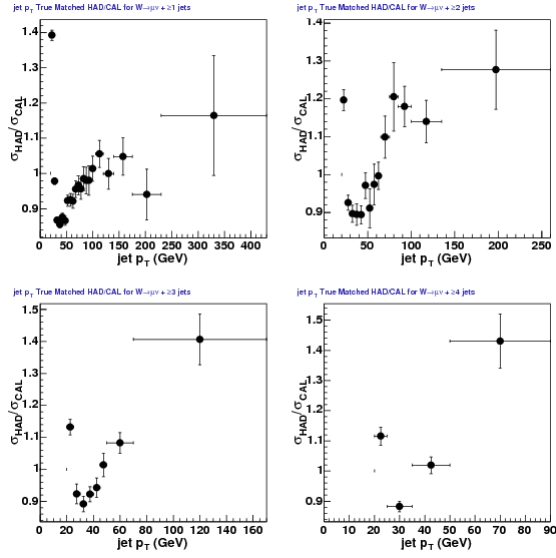
Figure 5.58. Unfolding factor $(\sigma(HAD)/\sigma(CAL))$ of the nth leading jet p_T for $W \to \mu\nu+ \geq n$ jets from Alpgen+Pythia MC where both pseudo-cross-sections have been constructed via a sample where every calorimeter jet is matched ("true matched") to its hadron level counterpart. While biased toward the calorimeter jet definition jet p_T ordering, it has the virtue of having explicitly equal number of events in both HAD and CAL samples. The four plot represent each inclusive jet multiplicity: ≥ 1 for upper-left, ≥ 2 for upper-right, ≥ 3 for lower-left, and ≥ 4 for lower-right.
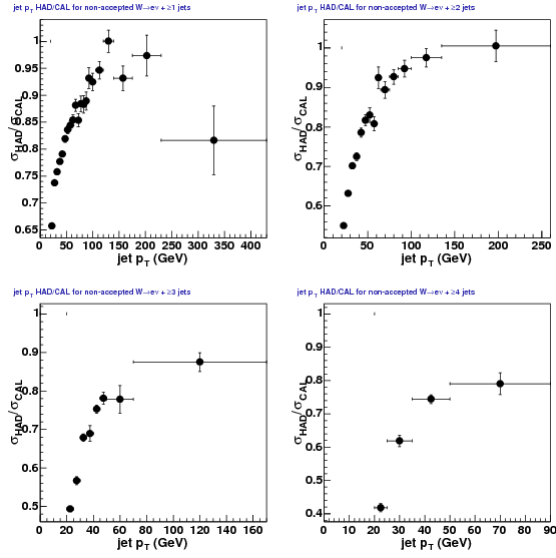
Figure 5.59. Unfolding factor $(\sigma(HAD)/\sigma(CAL))$ of the nth leading jet p_T for $W \to e\nu + \geq n$ jets from Alpgen+Pythia MC for events where it failed W selection (i.e. was not accepted). The four plot represent each inclusive jet multiplicity: ≥ 1 for upper-left, ≥ 2 for upper-right, ≥ 3 for lower-left, and ≥ 4 for lower-right.
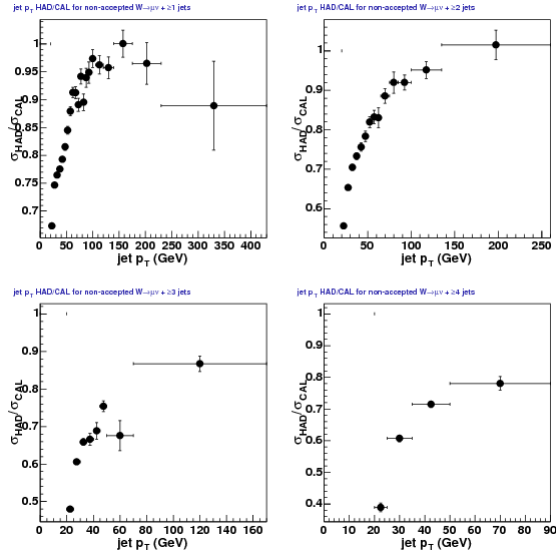
Figure 5.60. Unfolding factor $(\sigma(HAD)/\sigma(CAL))$ of the nth leading jet p_T for $W \rightarrow \mu\nu+ \geq n$ jets from Alpgen+Pythia MC for events where it failed W selection (i.e. was not accepted). The four plot represent each inclusive jet multiplicity: ≥ 1 for upper-left, ≥ 2 for upper-right, ≥ 3 for lower-left, and ≥ 4 for lower-right.
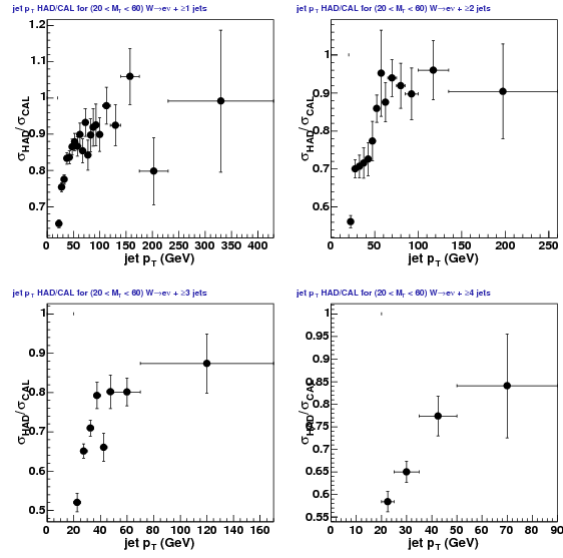
Figure 5.61. Unfolding factor $(\sigma(HAD)/\sigma(CAL))$ of the nth leading jet p_T for $W \to e\nu+ \geq n$ jets for events with the W transverse mass limited to $20 < M_T < 60$ from Alpgen+Pythia MC. The four plot represent each inclusive jet multiplicity: ≥ 1 for upper-left, ≥ 2 for upper-right, ≥ 3 for lower-left, and ≥ 4 for lower-right.

213
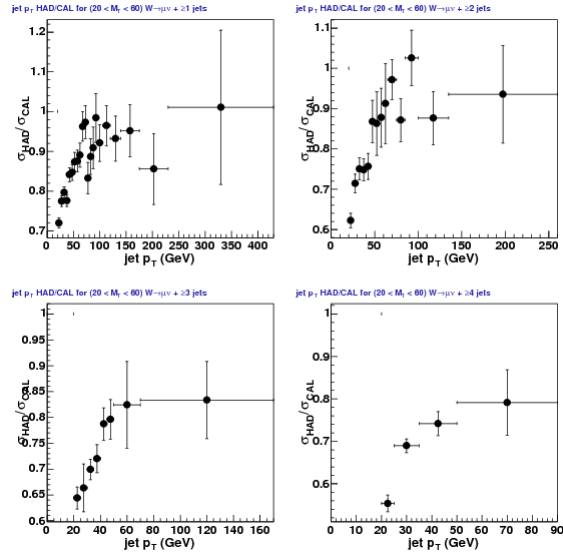
Figure 5.62. Unfolding factor $(\sigma(HAD)/\sigma(CAL))$ of the nth leading jet p_T for $W \rightarrow \mu\nu+ \geq n$ jets for events with the W transverse mass limited to $20 < M_T < 60$ from Alpgen+Pythia MC. The four plot represent each inclusive jet multiplicity: ≥ 1 for upper-left, ≥ 2 for upper-right, ≥ 3 for lower-left, and ≥ 4 for lower-right.
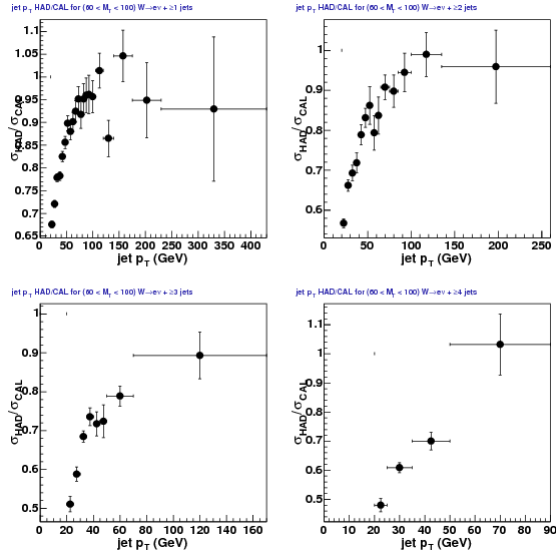
Figure 5.63. Unfolding factor $(\sigma(HAD)/\sigma(CAL))$ of the nth leading jet p_T for $W \rightarrow e\nu + \geq n$ jets for events with the W transverse mass limited to $60 < M_T < 100$ from Alpgen+Pythia MC. The four plot represent each inclusive jet multiplicity: ≥ 1 for upper-left, ≥ 2 for upper-right, ≥ 3 for lower-left, and ≥ 4 for lower-right.
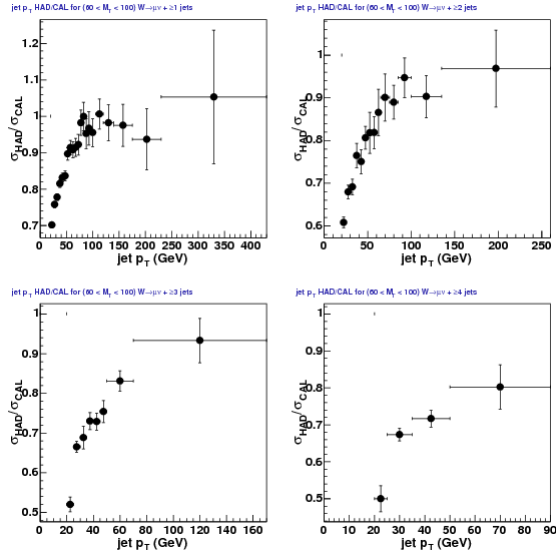
Figure 5.64. Unfolding factor $(\sigma(HAD)/\sigma(CAL))$ of the nth leading jet p_T for $W \to \mu\nu + \geq n$ jets for events with the W transverse mass limited to $60 < M_T < 100$ from Alpgen+Pythia MC. The four plot represent each inclusive jet multiplicity: ≥ 1 for upper-left, ≥ 2 for upper-right, ≥ 3 for lower-left, and ≥ 4 for lower-right.
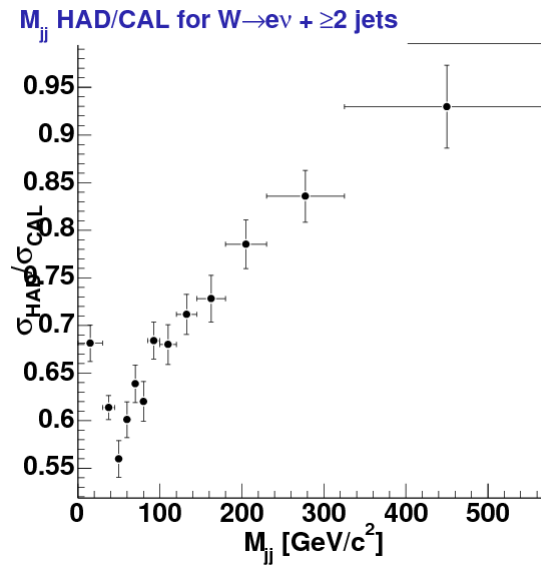
Figure 5.65. Unfolding factor $(\sigma(HAD)/\sigma(CAL))$ of the dijet mass (m_{jj}) as defined in section 9.7 (page 437) for $W \to e\nu+ \geq 2$ jets from Alpgen+Pythia MC.
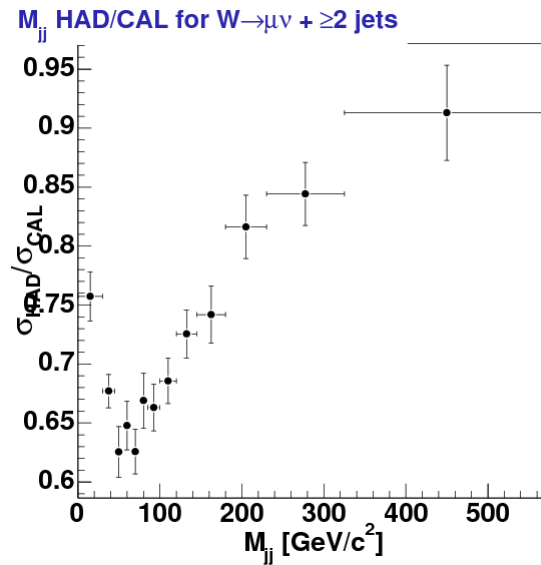
Figure 5.66. Unfolding factor $(\sigma(HAD)/\sigma(CAL))$ of the dijet mass (m_{jj}) as defined in section 9.7 (page 437) for $W \to \mu\nu+ \geq 2$ jets from Alpgen+Pythia MC.

R$_{jj}$ HAD/CAL for W→eν + ≥2 jets
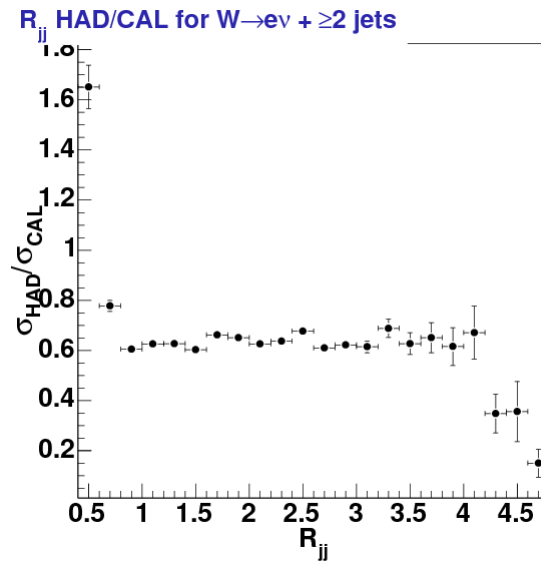
Figure 5.67. Unfolding factor $(\sigma(HAD)/\sigma(CAL))$ of the dijet separation (R_{jj}) as defined in section 9.8 (page 442) for $W \rightarrow e\nu+ \geq2$ jets from Alpgen+Pythia MC.

R$_{jj}$ HAD/CAL for W→μν + ≥2 jets
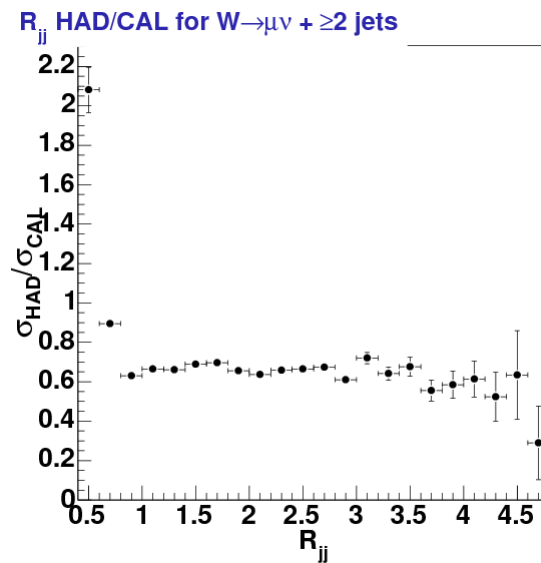
Figure 5.68. Unfolding factor $(\sigma(HAD)/\sigma(CAL))$ of the dijet separation (R_{jj}) as defined in section 9.8 (page 442) for $W \rightarrow \mu\nu+ \geq2$ jets from Alpgen+Pythia MC.

218
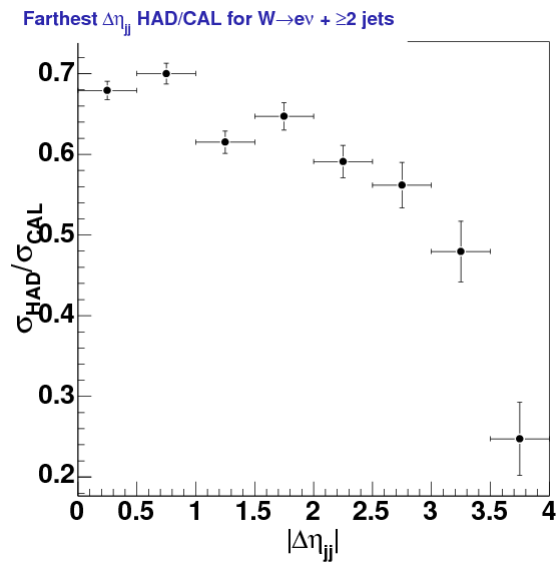
Figure 5.69. Unfolding factor $(\sigma(HAD)/\sigma(CAL))$ for $\Delta\eta_{jj}$ between the closest jet pair (defined in section 9.9 on page 446) for $W \rightarrow e\nu+ \geq 2$ jets from Alpgen+Pythia MC.
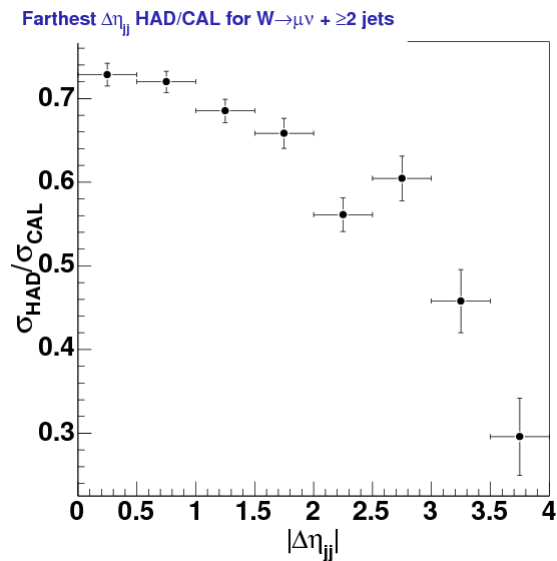
Figure 5.70. Unfolding factor $(\sigma(HAD)/\sigma(CAL))$ for $\Delta\eta_{jj}$ between the closest jet pair (defined in section 9.9 on page 446) for $W \rightarrow \mu\nu+ \geq 2$ jets from Alpgen+Pythia MC.
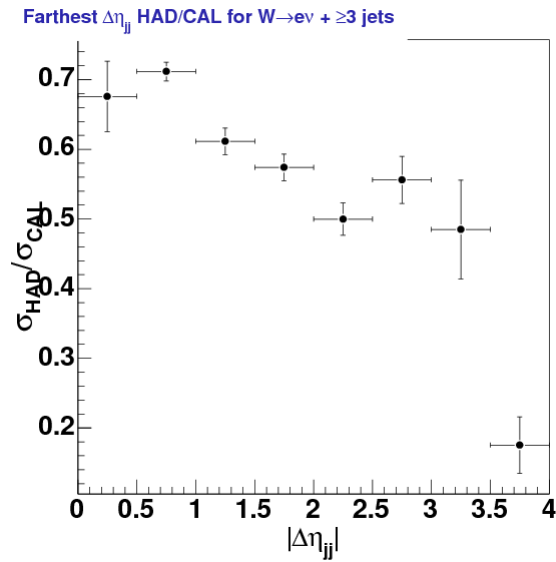
Figure 5.71. Unfolding factor $(\sigma(HAD)/\sigma(CAL))$ for $\Delta\eta_{jj}$ between the closest jet pair (defined in section 9.9 on page 446) for $W \rightarrow e\nu+ \geq 3$ jets from Alpgen+Pythia MC.
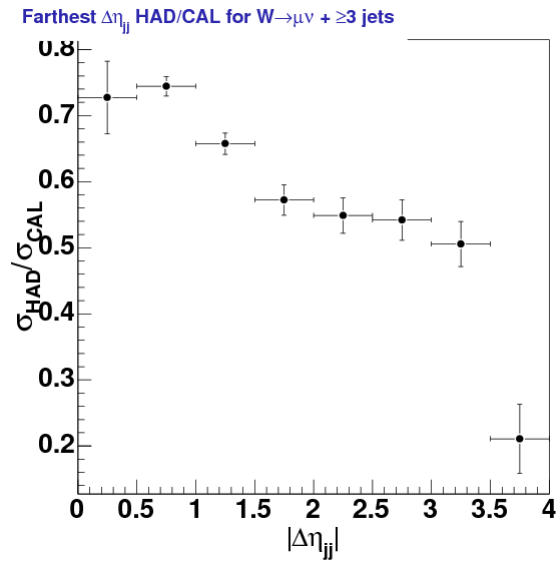
Figure 5.72. Unfolding factor $(\sigma(HAD)/\sigma(CAL))$ for $\Delta\eta_{jj}$ between the closest jet pair (defined in section 9.9 on page 446) for $W \rightarrow \mu\nu+ \geq 3$ jets from Alpgen+Pythia MC.

η* HAD/CAL for W→eν + ≥3 jets with |Δη$_{jj}$| > 2
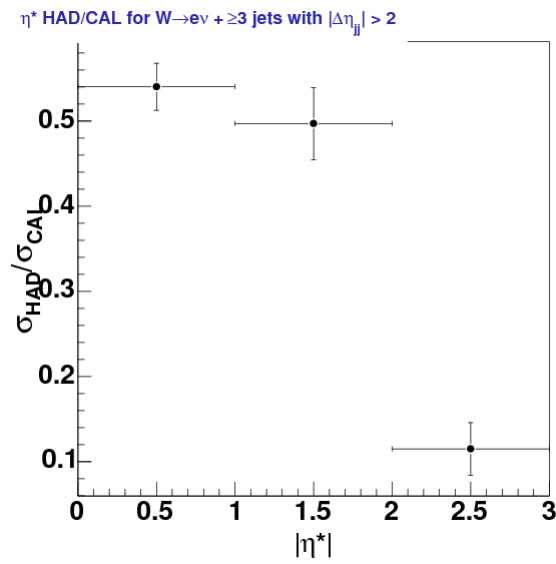
Figure 5.73. Unfolding factor $(\sigma(HAD)/\sigma(CAL))$ for η^* as defined in section 9.9 (page 446) for $W \rightarrow e\nu + \geq 3$ jets from Alpgen+Pythia MC.

η* HAD/CAL for W→μν + ≥3 jets with |Δη$_{jj}$| > 2
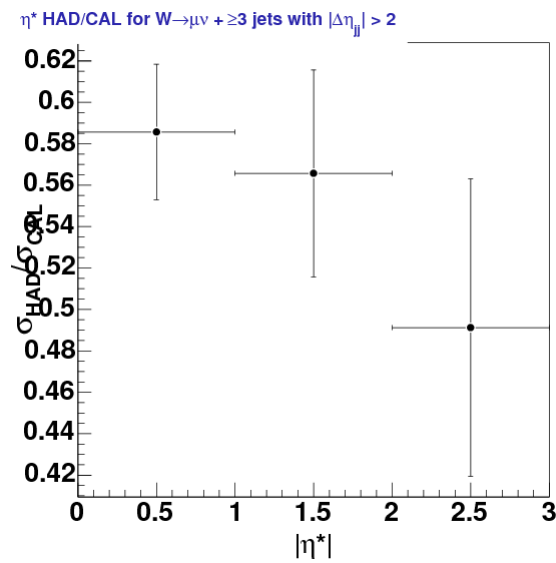
Figure 5.74. Unfolding factor $(\sigma(HAD)/\sigma(CAL))$ for η^* as defined in section 9.9 (page 446) for $W \rightarrow \mu\nu + \geq 3$ jets from Alpgen+Pythia MC.

CHAPTER 6

Background Estimation

In order to measure various jet kinematic cross-sections for W+jets we must first understand the various backgrounds that either have the same final state or that can otherwise mimic or fake our signal. This chapter deals with our background estimation in addition to a basic goal of understanding our signal MC. We classify our backgrounds into three different categories: electro-weak (EWK) backgrounds from $W \rightarrow \tau\nu$+jets and $Z \rightarrow \ell\ell$+jets, quantum chromodynamics (QCD) background fakes from multi-jets and semi-leptonic decays as well as punch-throughs, and "fixed" contributions including diboson (defined here as WW, WZ, and $W\gamma^*$) and t$\bar{\text{t}}$ production. We describe the latter estimation of our fixed contributions in a straightforward manner in section 6.1.

In the case of our EWK background the goal is to get estimations that do not depend upon theoretical predictions for $W \rightarrow \tau\nu$ and $Z \rightarrow \ell\ell$ with n inclusive jets. Similarly, it is difficult to obtain an appropriate and inclusive fake rate for our non-W QCD background and to be able to comfortably apply a rate that is not jet multiplicity dependent. Our solution to these separate issues is to form two templates based on the shape of various lepton variables via our MC samples (EWK) and a special anti-selection lepton sample from the data (QCD). In particular, we look at the transverse mass shapes (before our final W selection cut via the transverse mass) for each template and fit this to the observed distribution in data minus our contributions from our previously mentioned dibosons and t$\bar{\text{t}}$ estimation. Based on our fitted scalings we then apply this scale to each of template

samples (with the final W selection cut on the transverse mass) to arrive at our final background estimation.

Our EWK template is explained in section 6.2. The construction and details of our QCD sample and template are given in 6.3 which follows from the modified selection criteria of sections 4.2 (anti-selected electrons) and 4.4 (anti-selected muons). The theory and formal procedure for fitting our templates to the data is described in section 6.4. This is followed by our fitting results from which we derive our final background estimations. Additionally section 6.5 showcases numerous quality check plots which demonstrate good agreement across a spectrum of W and lepton observables. Based on this agreement and understanding we can then subtract our background estimation across an array of jet kinematic observables which serves as the basses for the W+jets cross-sections we present in chapter 9.

6.1. Diboson + $\mathrm{t\bar{t}}$ Background Estimation

We use the WW, WZ, $W\gamma^*$, and $\mathrm{t\bar{t}}$ MC samples outlined in section 3.5 and our normal W selection criteria (see chapter 4). Unlike in our estimation of the other processes where we wish to have a data-driven method that is independent of theoretical cross-section, we directly estimate the number of expected events via the theoretical cross-section, the number of events in each MC sample, and the luminosity of the data. We present the theoretical cross-sections used and their associated errors in table 6.1.

The diboson (defined here as WW, WZ, and $W\gamma^*$) theoretical cross-sections are taken from [37]. Note that the $W\gamma^*$ cross-section production is for a single lepton channel and we consider both the electron and muon channel but neglect the tau channel. For

Background Process	Cross-section σ(theory) (pb)	Error $\Delta\sigma$(theory) (pb)
$t\bar{t}$	7.50	0.48
WW	12.4	0.8
WZ	3.96	0.3
$W\gamma^*$	19.3	1.4

Table 6.1. Experimental $t\bar{t}$ cross-section and theoretical cross-sections for WW, WZ, $W\gamma^*$. See references cited in [37] (dibosons) and [38] ($t\bar{t}$) for the theoretical cross-sections while the experimental (CDF) $t\bar{t}$ cross-section comes from [39]. Tables 3.3 and 3.4 provide the MC sample and generator information as well as the # of events in each sample.

simplicity we will present the diboson contributions summed together as these never rise above 4% of the expected signal+background. We have investigated the background from ZZ production which is already negligible relative to the smallest included diboson contribution.

The largest "fixed" theoretical (actually experimental) cross-section background estimation contribution comes from $t\bar{t}$ production [38]. This becomes a significant background for three or more jets. In addition, the jet kinematics for $t\bar{t}$ (notably the jet p_T shape) are generally very different from the other backgrounds and the signal. The theoretical cross-section is 7.27 ± 0.87 pb which is the extrapolated (Run II tevatron) cross-section for a top mass of 172.5 GeV/c^2. The actual cited and used value of 7.5 ± 0.48 pb is the CDF experimental result assuming a top mass of 172.5 GeV/c^2 [39].

6.2. EWK Signal and Background Template

In order to estimate the electro-weak backgrounds we combine both our signal and background W+jets and Z+jets MC into a common electro-weak (EWK) sample. Our W selection follows from our procedure in chapter 4. However, in order to derive a theory

independent estimation of the electro-weak backgrounds we form a template with the W transverse mass (M_T) shape with a relaxed $M_T > 20$ GeV/c^2 requirement. We normalize this template for each inclusive jet multiplicity (0-4) to the respective number of events in data (minus the "fixed" diboson and $t\bar{t}$ backgrounds of the previous section) in the range of $20 < M_T < 120$ GeV/c^2. We define n_{EWK} to be the multiplicative scale factor needed to normalize the unscaled EWK sample to the data via our relaxed transverse mass samples. We give the normalization scale factors in table 6.2. This normalization of the templates (we do this for the QCD template as well) is just an artifact of our fitting which gives us a percentage of each template best describes the data. This "fitting fraction" will eventually be combined with our normalization scale factor and applied to our final electron (muon) EWK background sample with $M_T > 40$ (30) GeV/c^2 based on the fitting described in section 6.4.

$\geq n$ jets	n_{EWK} for Electrons	n_{EWK} for Muons
0	1.723	1.290
1	2.284	1.395
2	2.604	1.507
3	2.957	1.760
4	3.539	1.948

Table 6.2. EWK template normalization scale factors (n_{EWK}) for each inclusive jet multiplicity (0-4). The electron results will be used for our $W \rightarrow e\nu + \geq n$ jets EWK background while the muons will be used for $W \rightarrow \mu\nu + \geq n$ jets.

The results of table 6.2 are relatively trivial to understand in relation to the dependence on the size and background composition of our W candidates in data. For example, the electrons universally have a higher normalization as we expect more QCD/fakes background events in our data sample compared to the muons. Likewise, the inclusive ($\geq$) 0

jet multiplicity bin which is dominated by exclusive (=) 0 jet by construction filters the potential QCD background present and results in a smaller normalization. In the case of our electron channel, this is exacerbated due to electrons and jets both sharing being reconstructed (in part, in the former case) by the calorimeter.

Note that unlike the case for the QCD template construction (see the following section) the sample construction is straightforward as we apply the same selection cuts as we do in the data. The samples we use are given in section 3.5 and include the various W (electron and muon for signal with tau as a background) and Z (all lepton channels) samples with 0-4 partons MLM matched and the relative weighting of the MC described in section 3.6. Although this is implicit in the handling of our Z background and W signal samples, we want to make it explicit that we are not applying a post hoc W/Z cross-section ratio to scale the background to the signal (or vice-versa). Rather we make the assumption that the underlining electro-weak physics is correct and consistent for each 0-4 parton sample. We then observe that the ratio of the W and Z cross-sections ($R_{W/Z} = \sigma_W/\sigma_Z$) using Alpgen MC is consistant with the CDF measurements in data [68]. We also trivially note that we observe lepton universality ($\sigma(W \rightarrow e\nu) = \sigma(W \rightarrow \mu\nu)$) in the Alpgen MC as well.

Figures 6.1 (electron channel) and 6.2 (muon channel) show our EWK templates from $\geq$ 1-4 jets using the W transverse mass spectrum after it has after its normalization to the data. As expected, the signal W MC is the dominate contribution peaking just before a M_T of 80 GeV/c^2. The same figures also show QCD template which is the subject of the next section. Later in section 6.5 we will show the templates for the inclusive 1

jet as an example case and how a linear combination of the templates replicates the M_T distribution of the data.

6.3. QCD template

The final piece to our background puzzle is our non-W background that we cannot directly extract from any MC: QCD. We use QCD as a catch-all term that specifies actual quantum chromodynamics processes like dijet and multi-jet production as well as other potential fakes to our W signal such as punch throughs, decays-in-flights, semi-leptonic meson decay, etc. We have attempted to track some of these contributions separately (e.g. decays-in-flights for our muon sample) but find an inclusive approach (modulo refinements and additions to our default selection criteria) sufficient to explain this encompassing background.

The objective is to use a data based method to calculate this important background. This template is constructed in parallel to our normal W selection via our anti-selection lepton criteria as described in sections 4.2 and 4.4 for the electron and muon channels, respectively. Recall that these samples use the same basic kinematic and geometric requirements (including a mirrored W selection of section 4.7) but must fail two or more of our normal quality/identification cuts.

Like the EWK template of the previous section, we normalize these samples to the size of the data (minus the "fixed" diboson and $t\bar{t}$ backgrounds of section 6.1) in the range of $20 < M_T < 120$ GeV/c^2. We define n_{QCD} to be the multiplicative scale factor needed to normalize the unscaled QCD sample to the data via our relaxed transverse mass samples. We give the normalization scale factors in table 6.3. Like the basic behavior of our EWK

227
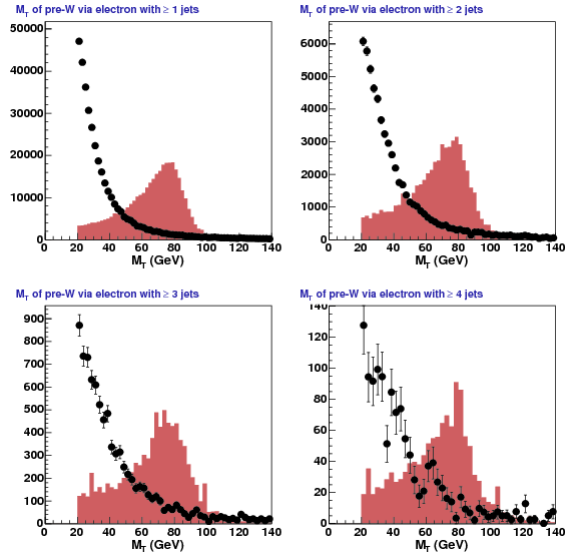
Figure 6.1. Transverse Mass (M_T) for the EWK (maroon histogram) and QCD (data points) templates for $W \rightarrow e\nu + \geq n$ jets with $M_T > 20$ GeV/c^2 for $n =$1-4. Both templates have been normalized to the number of events in the same distribution in data after $t\bar{t}$ and diboson estimation removal.
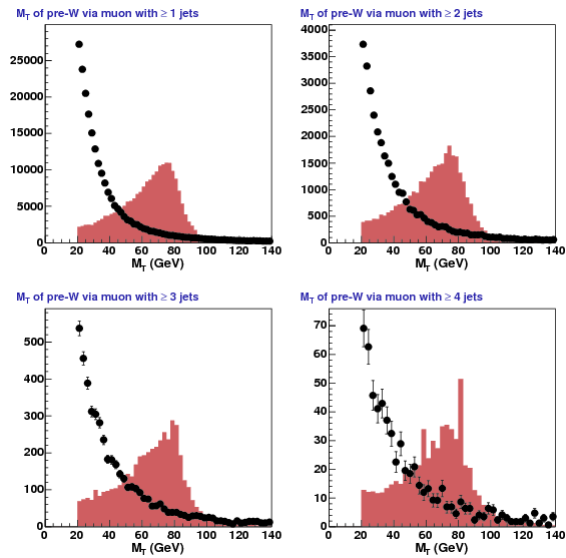
Figure 6.2. Transverse Mass (M_T) for the EWK (maroon histogram) and QCD (data points) templates for $W \rightarrow \mu\nu + \geq n$ jets with $M_T > 20$ GeV/c^2 for $n =$1-4. Both templates have been normalized to the number of events in the same distribution in data after $t\bar{t}$ and diboson estimation removal.

normalization (table 6.2) the jet multiplicity and lepton differences are simply an artifact of our selection criteria on the composition of the data.

$\geq n$ jets	n_{QCD} for Electrons	n_{QCD} for Muons
0	7.671	3.338
1	3.468	0.8914
2	2.998	0.4959
3	2.685	0.3057
4	2.734	0.2011

Table 6.3. QCD template normalization scale factors (n_{QCD}) for each inclusive jet multiplicity (0-4)

Unlike the EWK template, our QCD template has the additional complication of *contamination* from other backgrounds and even the signal that satisfy our anti-selection criteria. Clearly, we intend to use the data (detector based) sample to form a template but we first need to subtract the contributions from already accounted for by the other backgrounds. The contamination is roughly 5% in the electron channel and less than 0.5% in the muon. While contamination removal has virtually no effect on our muon channel results care is taken to make sure the contamination is properly removed from both the electron and muon channels.

Removing the diboson and $t\bar{t}$ contributions is done by a literal subtraction. In the case of our EWK signal ($W \rightarrow \ell\nu$) and backgrounds ($W \rightarrow \tau\nu + Z$) we have to remove the contamination by using the fitting procedure and their results of the next two sections. We preform this iterative procedure until we reach a steady convergence. This is readily achieved after a single refitting due to the default weighting being relatively close to the data to begin with. Note that this background subtraction procedure is also carried out anytime we reevaluate our backgrounds/fittings. For example, we assign a systematic

M$_T$ of pre-W via electron with $\geq$ 1 jets
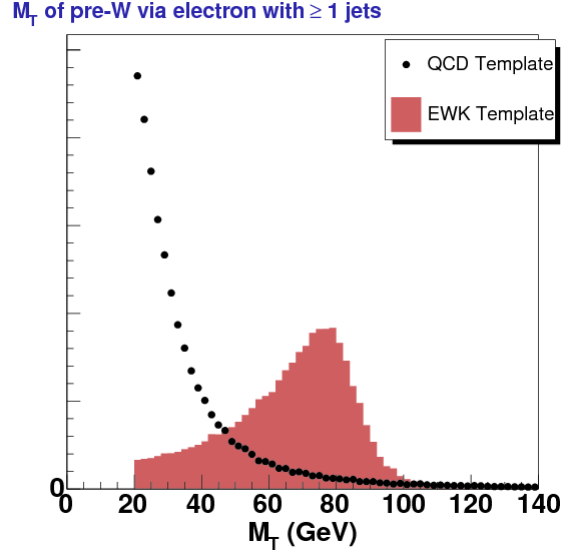
Figure 6.3. Transverse Mass (M_T) for the EWK (histogram) and QCD (data points) templates for $W \to e\nu+ \geq 1$ jets with $M_T > 20$ GeV/c^2. Both templates have been normalized to the number of events in the same distribution in data after $t\bar{t}$ and diboson estimation removal.

on our $t\bar{t}$ background estimation (see section 8.6) and that separate background fitting procedure requires us to remove our EWK signal and background contamination to our QCD template.

Example plots of the QCD template (along with the EWK template of the previous section) normalized to the data for the M_T distribution were given in figures 6.1 and 6.2 for the electron and muon channel, respectively. The QCD template shows the expected exponential like decay of the W transverse mass spectrum which dominates the EWK spectrum for $M_T < 50$ GeV/c^2.
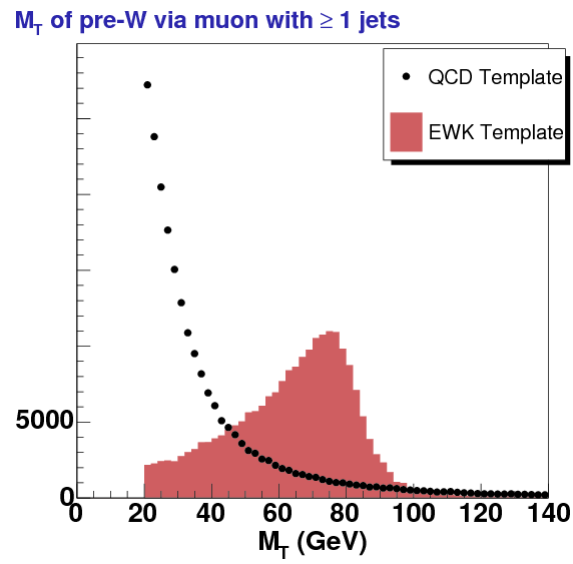
Figure 6.4. Transverse Mass (M_T) for the EWK (histogram) and QCD (data points) templates for $W \to \mu\nu+ \geq 1$ jets with $M_T > 20$ GeV/c^2. Both templates have been normalized to the number of events in the same distribution in data after $t\bar{t}$ and diboson estimation removal.

231
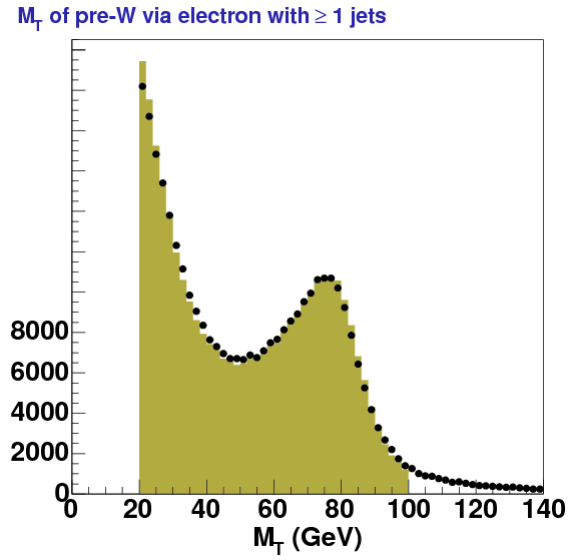
Figure 6.5. Transverse Mass (M_T) for the combined EWK+QCD templates fit (histogram) and data (data points) after $t\bar{t}$ and diboson estimation removal for $W \to e\nu+ \geq 1$ jets with $M_T > 20$ GeV/c^2. The fitting is done using `TFractionFitter` [69]. To arrive at our final W background estimation and samples (across the scaled EWK+QCD templates and in the data) we take $M_T > 40$ GeV/c^2.
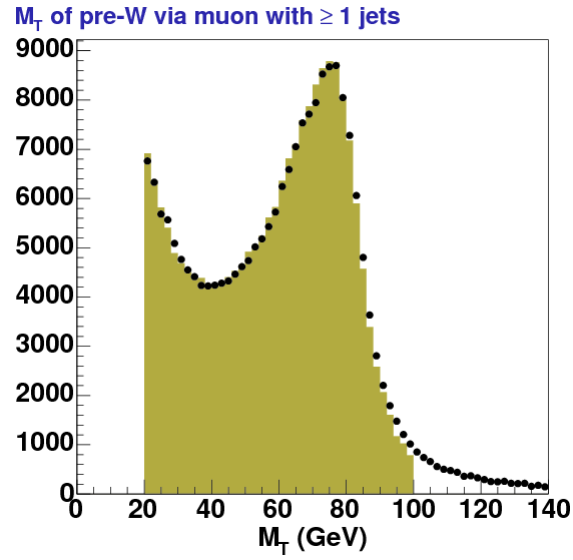
Figure 6.6. Transverse Mass (M_T) for the combined EWK+QCD templates fit (histogram) and data (data points) after $t\bar{t}$ and diboson estimation removal for $W \rightarrow \mu\nu+$ $\geq$1 jets with $M_T > 20$ GeV/c^2. The fitting is done using `TFractionFitter` [69]. To arrive at our final W background estimation and samples (across the scaled EWK+QCD templates and in the data) we take $M_T > 30$ GeV/c^2.

6.4. Background Fitting Procedure and Results

The background fitting procedure is designed to circumvent the need for a direct jet multiplicity dependent theoretical cross-section for our $W \to \tau\nu + Z$ backgrounds which come from the MC via our normal W selection process in addition to providing the relative scale for our QCD/fake estimation. The former is important since directly assigning a theoretical cross-section would be circular; we would be assuming the thing we wish to measure. The latter case with our catch-all QCD template via our anti-selection sample is even more problematic as the sample relies on the inefficiency of our quality/identification variables via our anti-selection sample and, in any event, there does not exist a single representative process from which to apply a jet dependent cross-section.

Our goal here is to take our EWK and QCD templates and fit them to shape of the W transverse mass distribution for each jet multiplicity and for both electron and muon channels. In this way, we can calculate the relative fraction of each template which will give us a linear combination that when taken together should provide a bin-by-bin background estimation of the data not only for distributions like M_T and $\not{E}_T$ but for several important kinematic variables based on our lepton and jet selection. Unlike the previous version of this analysis [12], we use the transverse mass distribution instead of the missing transverse energy ($\not{E}_T$) as is has slightly better separation power between our W signal and our non-W backgrounds. This was also the reason for using the M_T as our final kinematic variable (as noted in section 4.7) as it has better signal-to-background ratio for a given W acceptance. Note however that we do use the $\not{E}_T$ shape as a cross-check to our method and as a potential systematic for our background estimation procedure. The fitting procedure for the $\not{E}_T$ is the same as outlined here although we normalize over the

entire range of the histogram (0-100 GeV). The results given as the relative difference in the electron channel were no more than 1.1% and within our given uncertainties. The same relative differences in M_T and $\not{E}_T$ for the muon channel was as high as 2.6%.

Recall that in section 6.1 we applied our knowledge of the theoretical cross-sections for our diboson and $t\bar{t}$ (via Pythia MC) background estimations. Therefore, for the purpose of our procedure here, we subtract these accounted for background estimates from our raw data shape in the M_T distribution. We use the number of events in this corrected data distribution between $20 < M_T < 120$ GeV/c^2 to normalize to our EWK and QCD templates as noted in the previous sections (see tables 6.2 and 6.3). We then setup `TFractionFitter` which is one of the general histogram tools in `ROOT` [**69**]. The basic details of the original (Fortran) algorithm are described in [**70**]. The `TFractionFitter` method takes the templates and perform a likelihood fit to the modified data. The virtue of this fitting method

> is that it takes into account both data and Monte Carlo statistical uncertainties. The way in which this is done is through a standard likelihood fit using Poisson statistics; however, the template (MC) predictions are also varied within statistics, leading to additional contributions to the overall likelihood. [**69**]

The fitting is done for each lepton channel and for each inclusive jet multiplicity. We set the fitting range over the same normalization range of 20-120 GeV/c^2. By default, the fitting fraction starts at 0.5 for both templates. The `TFractionFitter` method also allows for us to directly output the combined likelihood fit histogram which we now give an example of along with our basic templates prior to fitting. Figures 6.3 and 6.4 show

the QCD and EWK and templates normalized to the data (minus the fixed background components) for $W \to \ell\nu+\ \geq 1$ jets for the electron and muon channel, respectively. The final "fitted" results are shown in figures 6.5 and 6.6 which shows the output via `TFractionFitter` with the data for the same jet multiplicity. The basic template behavior and fit results are typical for the higher jet multiplicities.

The output of the fit is the relative fitting fractions for each template (k_{EWK} for EWK and k_{QCD} for QCD) along with an uncertainty in the parameter (Δk_{EWK} and Δk_{QCD}, respectively). Note that due to the normalization of each template to the data there is actually only one degree of freedom:

$$(6.1) \qquad\qquad k_{EWK} + k_{QCD} \;=\; 1$$

$$(6.2) \qquad\qquad k_{QCD} \;=\; 1 - k_{EWK}$$

In order to apply these results to all of our distributions we need to account for the normalization factors (n_{EWK} and n_{QCD}) of the previous section. We then apply the product of these two factors ($k_{EWK} \times n_{EWK}$ and $k_{QCD} \times n_{QCD}$) to our EWK and QCD histograms, respectively, finally giving us a full bin-by-bin background estimation for all distributions. Note that the histograms of interest to us include our final W transverse mass cut and thus the absolute number of background events need not be precisely equal to the number of W candidate events in the data. As a result, we expect the jet multiplicity in data to be close but not exactly equal to the number of events predicted in our signal+background estimation.

As noted in the previous section, the QCD template deals with contamination that comes from our MC based estimates also "passing" our inverted cut scheme for our anti-selection samples. Technically, this includes our diboson and $t\bar{t}$ samples but these are simply subtracted from the data before hand and thus are not effected by the iterative method outlined here. We deal with this by scaling the EWK contamination by the result of the previous fit (k_{EWK}) and then subtracting it as normal from the data (minus the diboson and $t\bar{t}$ contribution) to form QCD template. We normalize to our pre-candidate W data sample as normal and refit. As suggested, the effect on the electron channel is small (0.5%). On a second pass the fit changes by only 1 part in 10,000. The effect is trivial in the muon channel where there was less contamination to begin with. As a result, the change in our fit fractions was only a few parts in 10,000 after the first iteration.

Finally, we present tables 6.4 and 6.5 which give fit values from `TFractionFitter` and their uncertainty. The fit fractions (k_{EWK} and k_{QCD}) when combined with the normalization fractions (via tables 6.2 and 6.3) give us a scale factor (not presented) to apply to each template for each jet multiplicity.

$\geq n$ jets	k_{EWK}	Δk_{EWK}	k_{QCD}	Δk_{QCD}
0	0.7701	0.0008	0.2299	0.0004
1	0.5746	0.0020	0.4254	0.0017
2	0.5048	0.0048	0.4952	0.0048
3	0.4770	0.0134	0.5230	0.0138
4	0.5008	0.0355	0.4991	0.0353

Table 6.4. The EWK and QCD template fitting fractions (k_{EWK} and k_{QCD}) and their errors for $W \rightarrow e\nu + \geq n$ jets

$\geq n$ jets	k_{EWK}	Δk_{EWK}	k_{QCD}	Δk_{QCD}
0	0.9010	0.0012	0.0990	0.0005
1	0.8404	0.0033	0.1596	0.0018
2	0.8090	0.0086	0.1910	0.0055
3	0.7823	0.0237	0.2177	0.0167
4	0.7581	0.0707	0.2419	0.0555

Table 6.5. The EWK and QCD template fitting fractions (k_{EWK} and k_{QCD}) and their errors for $W \rightarrow \mu\nu + \geq n$ jets

6.5. Background Estimation Results

In order to highlight the effectiveness of our background fitting method and as an overview of our basic analysis results, we present an array of plots giving a breakdown of the various background contributions of the expected number of events for different variables. Some will serve as a quality check of our final results, while others are the actual observables that we will use to form our final cross-sections. All of these plots unless otherwise noted come from our final W selection including the final transverse mass cut.

Before diving into these results we want to present a basic table with the number of candidate W events for each jet multiplicity as well as a breakdown into the fraction of events from each background process. Table 6.6 gives the electron channel results while table 6.7 shows the muon channel results. Keeping with section 6.1, the diboson contributions are taken together as a single column. The final column in these tables is our measured W fraction taken by summing all background processes and subtracting this from unity.

Figures 6.7 and 6.22 shows the jet multiplicity (0-4 inclusive number of jets) for the electron and muon channel, respectfully. The data are present as points with signal,

$\geq n$ jets	Data	$W \to \tau\nu$	$Z \to ee$	$Z \to \tau\tau$	$t\bar{t}$	Diboson	QCD	$W \to e\nu$
0	1849213	0.029	0.011	0.002	0.001	0.004	0.059	0.895
1	230222	0.019	0.021	0.001	0.004	0.012	0.178	0.765
2	39417	0.016	0.036	0.000	0.023	0.025	0.266	0.634
3	6662	0.011	0.041	0.000	0.103	0.029	0.292	0.524
4	1280	0.008	0.041	0.000	0.282	0.024	0.256	0.388

Table 6.6. Background estimation fraction for $W \to e\nu + \geq n$ jets. Data represents the number of candidates events in data passing our W selection criteria while $W \to e\nu$ is the measured W signal fraction via the total minus the background ($N(\text{data}) - \sum N(\text{backgrounds})$). Diboson represents WW, WZ, and $W\gamma^*$ production.

$\geq n$ jets	Data	$W \to \tau\nu$	$Z \to \mu\mu$	$Z \to \tau\tau$	$t\bar{t}$	Diboson	QCD	$W \to \mu\nu$
0	1309926	0.032	0.052	0.002	0.001	0.004	0.047	0.861
1	164843	0.028	0.054	0.001	0.005	0.014	0.083	0.816
2	26459	0.026	0.055	0.001	0.030	0.033	0.108	0.747
3	4383	0.020	0.049	0.000	0.143	0.038	0.117	0.633
4	857	0.013	0.032	0.000	0.380	0.030	0.102	0.442

Table 6.7. Background estimation fraction for $W \to \mu\nu + \geq n$ jets. Data represents the number of candidates events in data passing our W selection criteria while $W \to \mu\nu$ is the measured W signal fraction via the total minus the background ($N(\text{data}) - \sum N(\text{backgrounds})$). Diboson represents WW, WZ, and $W\gamma^*$ production.

QCD background estimation along with a combined EWK, diboson, and $t\bar{t}$ background prediction given as a stacked histogram. With respect to our fitting, each histogram bin represents a different set of fitting fractions as well as our pre-fit normalizations. As such, these figures serve a visual representation of our most basic W+jets result. We note that the total expectation is not guaranteed to be perfect with the data due to the different transverse mass range difference used in fitting and with our final result. However, the agreement is by the nature of the method quite good.

Next we present the flagship measurement of this analysis: the nth leading jet p_T distribution for $\geq n$ jets. The electron channel results (n=1-4) are shown in figures 6.18-6.21 while the muon channel results are likewise given in figures 6.33-6.36. For the purpose of comparison we normalize the background and signal prediction to the data in each plot. The take away point from these jet transverse momentum distributions is a basic consistency. Needless the say the fact that the W MC prediction appears slightly softer (more events at lower jet p_T) is ultimately the type of quantitative observation we desire in our final result when we compare to theoretical predictions.

The remaining plots of this section highlight a variety of basic quality control distributions concerning our W signal as well as relational kinematic plots between our selected jets with respect to our W selection. The main motivation for looking at these observables is to insure that our background estimation method does not introduce any unexpected bias. We desire our QCD estimation (more precisely our anti-selected lepton samples used to form the QCD template) along with our MC signal and background contributions to be in broad agreement across the phase space of various W+jets variables. It is possible to have an optimal fit with respect to the W transverse mass spectrum but for other distributions to have tell-tale signs of bias that can effect our final jet observables. For example, if one does not remove the anti-selected muon-jet (see section 5.3 on page 139) in the jet collection, the resulting sample not only has a noticeable muon low p_T bias but also poorly describes the transverse jet momentum distributions for the first and second leading jet.

Figures 6.8-6.12 show the W transverse mass distribution for $\geq$0-4 jets for the electron channel. Likewise, the muon channel version of M_T follows in figures 6.23-6.27. For

comparison we also highlight the missing energy ($\not{E}_T$) distributions for each jet multiplicity as well in figures 6.13-6.17 (electrons) and 6.28-6.32 (muons).

For completeness we also present a breakdown of the lepton and missing energy information. In the plots to be referenced in the remainder of this section, we actually break down the various background into their individual components rather than the "public relations" versions of figures 6.7-6.32. We start with the electron transverse energy (E_T) for each jet multiplicity which is shown in figures 6.37 (the total inclusive ≥ 0 jets sample) and 6.38 (inclusive jet multiplicities 1-4). Similarly we give the muon transverse momentum (p_T) in figures 6.49 and 6.50 for the total inclusive case and each jet inclusive multiplicity 1-4, respectively. We also measure the $\Delta\phi$ between the lepton and the missing energy ($\Delta\phi(\ell, \nu)$). The electron channel results are shown in figures 6.41 and 6.42 for ≥ 0 jets and the $\geq$1-4 jet multiplicities, respectively. The muon channel results are likewise presented in figures 6.53 and 6.54.

We reproduce the missing energy and transverse mass plots from before but this time with a full breakdown of individual background components and formatting as the previous referenced plots. The $\not{E}_T$ for the electron channel is shown in figures 6.39 and 6.40 while the muon results are given in figures 6.51 and 6.52. The M_T results are presented in figures 6.43 (6.55) for the total inclusive jet multiplicity for the electron (muon) channel. Likewise, figures 6.44 and 6.56 give the results for the higher inclusive jet multiplicities (1-4) for the electron and muon channels, respectively.

Figures 6.45 and 6.57 give the nth leading jet η distributions for $\geq n$ jets (1-4) with respect to the electron and muon results. Each plot also gives the $\pm 1\sigma_{\text{JES}}$ jet energy scale

correction (see section 5.6 on page 155) applied to the data and represented by a black line for each variation.

Next we present three distributions which look at the relative spacing between the selected lepton and a jet observable. First we look at the $\Delta R(\ell, j)$ (or simply $R(\ell, j)$) which is the η-ϕ separation between the lepton and the *closest* jet (as measured via $\Delta R(\ell, j)$). The electron channel results ($\Delta R(e, j)$) are presented in figure 6.46 while the muon results ($\Delta R(\mu, j)$) are shown in figure 6.58. We also look at just the separation in ϕ between the same variables ($\Delta \phi(\ell, j)$). Figure 6.47 are the $\Delta \phi(e, j)$ results for each jet multiplicity bin while figure 6.59 presents the $\Delta \phi(\mu, j)$ results, likewise. The comparison in these plots is still between the closest jet as measured in η-ϕ via ΔR. We observe the characteristic back-to-back bias in the data in the inclusive 1 jet case and the subsequent reduction to smaller values of $\Delta R/\Delta \phi$ of the available lepton-jet phase space as the just multiplicity increases.

Finally we consider a variation in the previous $\Delta \phi$ distributions where we look at the vector sum of jet energy and compare the resulting direction ($\wp$) with the lepton. We introduced this variable in the previous chapter (see section 5.5) and defined in via equation 5.2 on page 145. As noted, this $\Delta \phi(\ell, \wp)$ variable has the advantage of producing a spectrum that is approximately the same for all jet multiplicities and thus useful for checking for consistency between the signal and electro-weak based backgrounds and our QCD estimation. Figure 6.48 gives the $\Delta \phi(e, \wp)$ results while figure 6.60 shows the $\Delta \phi(\mu, \wp)$ distribution for each inclusive jet multiplicity (1-4). Both of the cited plots have a $\Delta \phi(\ell, \wp) < 2.95$ cut applied during selection.
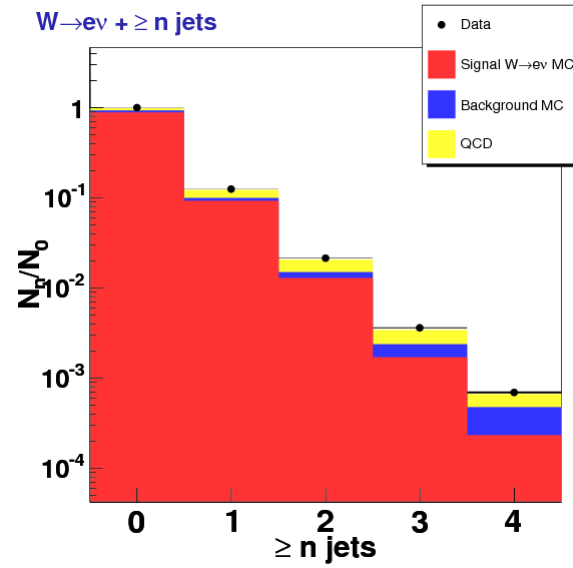
Figure 6.7. Inclusive jet multiplicity for $W \to e\nu + \geq n$ jets. The plot has been normalized to the total number of events in the data. The black points are the data, the red histogram is the signal MC, the blue histogram is all other MC based backgrounds summed together, and the yellow histogram is the QCD estimation.
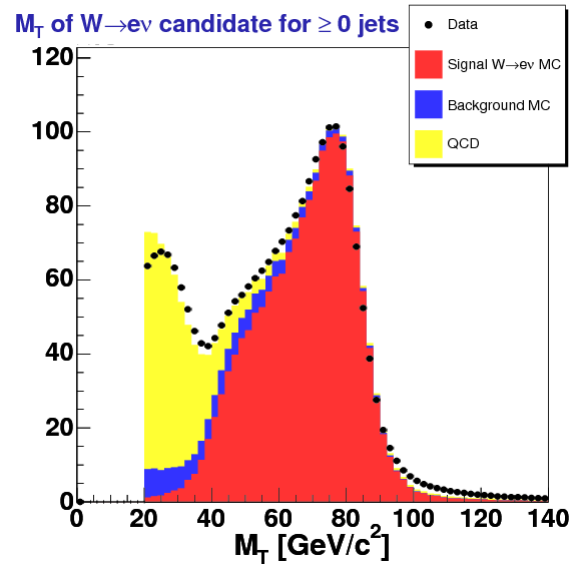
Figure 6.8. W transverse mass (M_T) for $W \to e\nu + \geq 0$ jets. This is before the final W selection cut of $M_T > 40$ GeV/c^2. The black points are the data, the red histogram is the signal MC, the blue histogram is all other MC based backgrounds summed together, and the yellow histogram is the QCD estimation.
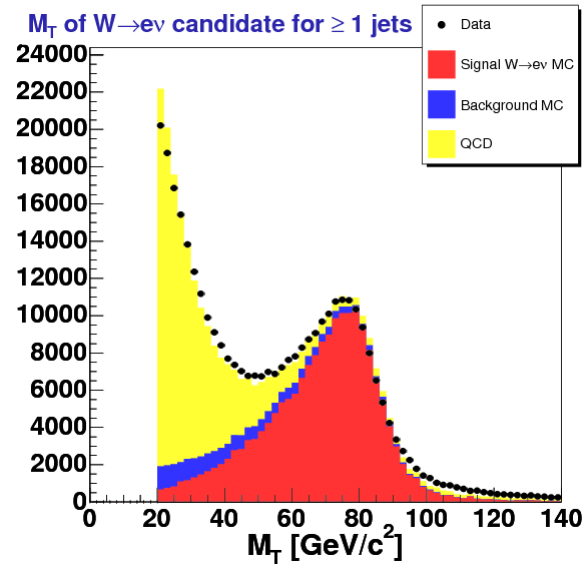
Figure 6.9. W transverse mass (M_T) for $W \to e\nu + \geq 1$ jets. This is before the final W selection cut of $M_T > 40$ GeV/c^2. The black points are the data, the red histogram is the signal MC, the blue histogram is all other MC based backgrounds summed together, and the yellow histogram is the QCD estimation.
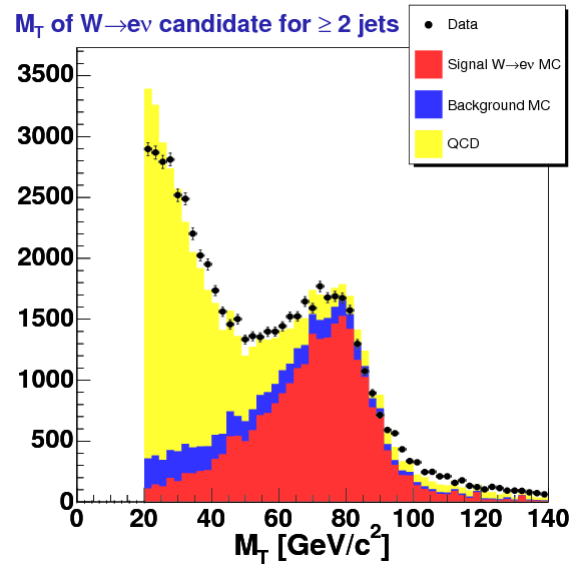
Figure 6.10. W transverse mass (M_T) for $W \to e\nu + \geq 2$ jets. This is before the final W selection cut of $M_T > 40$ GeV/c^2. The black points are the data, the red histogram is the signal MC, the blue histogram is all other MC based backgrounds summed together, and the yellow histogram is the QCD estimation.
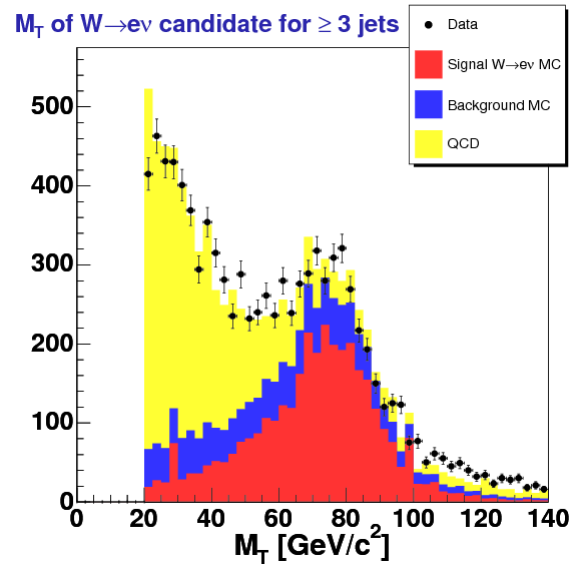
Figure 6.11. W transverse mass (M_T) for $W \rightarrow e\nu+ \geq 3$ jets. This is before the final W selection cut of $M_T > 40$ GeV/c^2. The black points are the data, the red histogram is the signal MC, the blue histogram is all other MC based backgrounds summed together, and the yellow histogram is the QCD estimation.
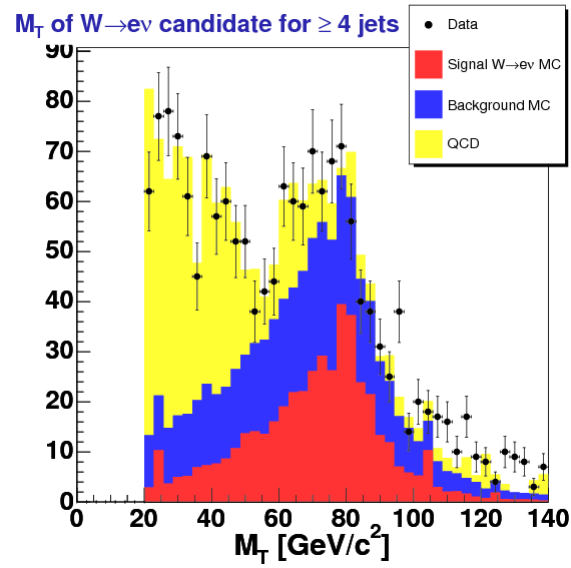
Figure 6.12. W transverse mass (M_T) for $W \rightarrow e\nu + \geq 4$ jets. This is before the final W selection cut of $M_T > 40$ GeV/c^2. The black points are the data, the red histogram is the signal MC, the blue histogram is all other MC based backgrounds summed together, and the yellow histogram is the QCD estimation.
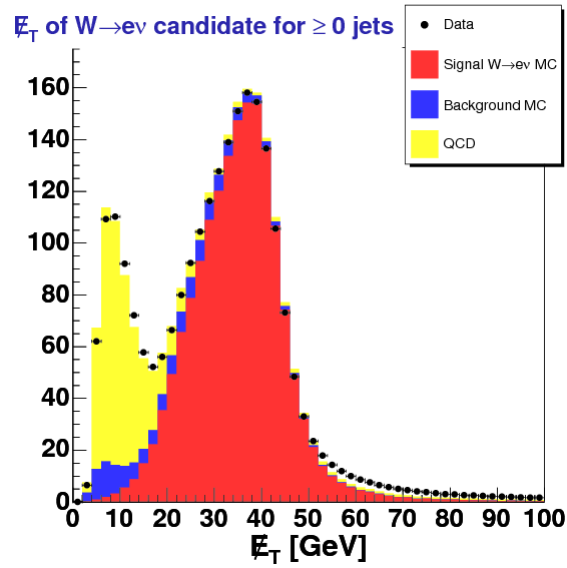
Figure 6.13. Missing transverse energy ($\not{E}_T$) for $W \to e\nu+ \geq 0$ jets. This is before the final W selection cut of $M_T > 40$ GeV/c^2. The black points are the data, the red histogram is the signal MC, the blue histogram is all other MC based backgrounds summed together, and the yellow histogram is the QCD estimation.
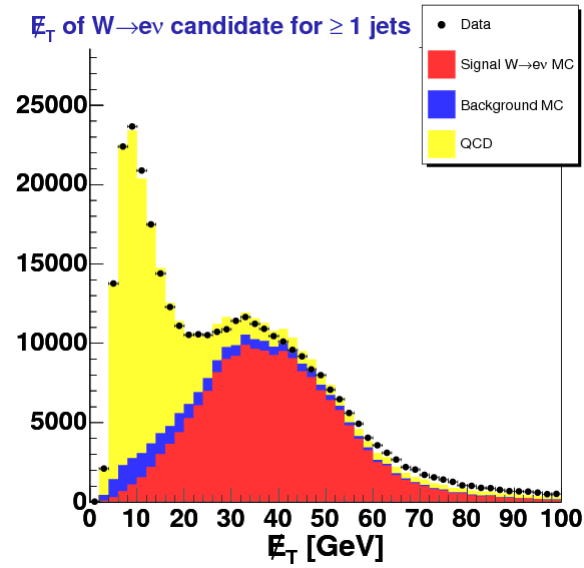
Figure 6.14. Missing transverse energy ($\not{E}_T$) for $W \to e\nu+ \geq 1$ jets. This is before the final W selection cut of $M_T > 40$ GeV/c^2. The black points are the data, the red histogram is the signal MC, the blue histogram is all other MC based backgrounds summed together, and the yellow histogram is the QCD estimation.
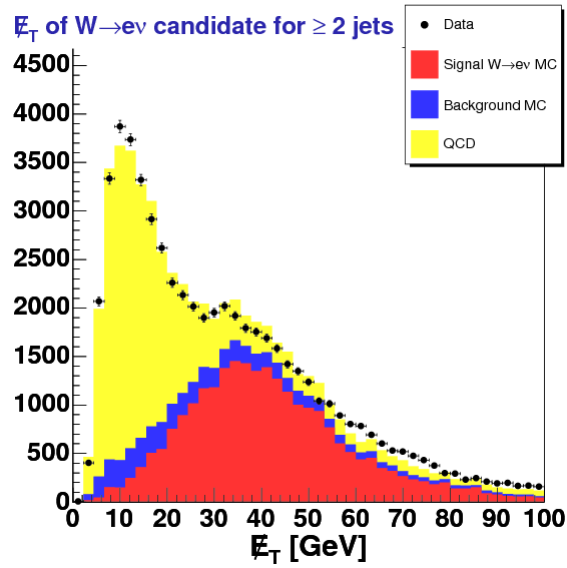
Figure 6.15. Missing transverse energy ($\not{E}_T$) for $W \to e\nu+ \geq 2$ jets. This is before the final W selection cut of $M_T > 40$ GeV/c^2. The black points are the data, the red histogram is the signal MC, the blue histogram is all other MC based backgrounds summed together, and the yellow histogram is the QCD estimation.
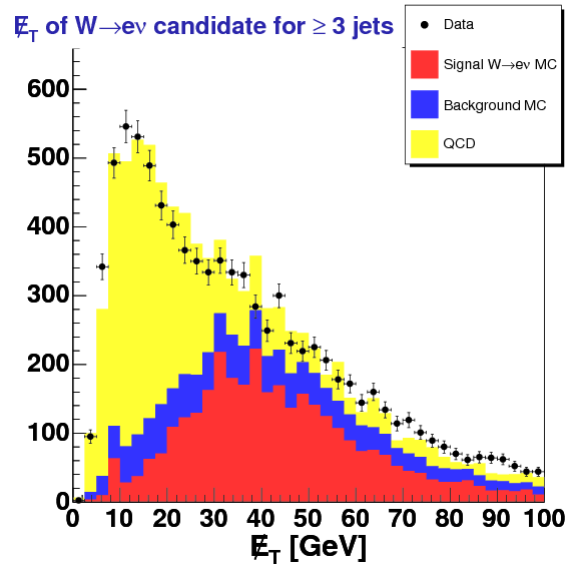
Figure 6.16. Missing transverse energy ($\not{E}_T$) for $W \to e\nu+ \geq 3$ jets. This is before the final W selection cut of $M_T > 40$ GeV/c^2. The black points are the data, the red histogram is the signal MC, the blue histogram is all other MC based backgrounds summed together, and the yellow histogram is the QCD estimation.
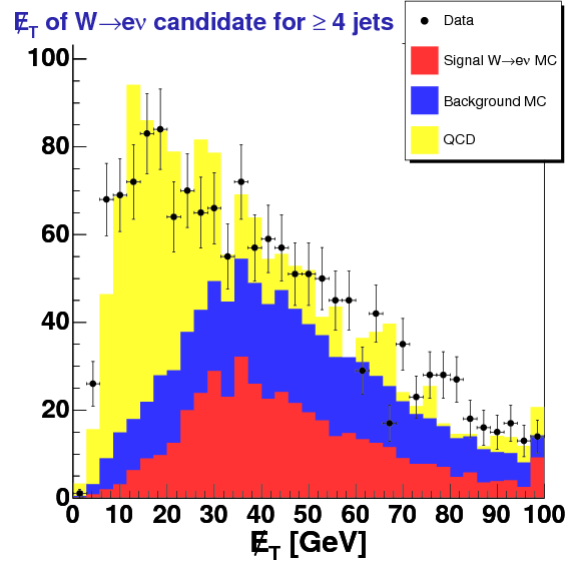
Figure 6.17. Missing transverse energy ($\not{E}_T$) for $W \rightarrow e\nu+ \geq 4$ jets. This is before the final W selection cut of $M_T > 40$ GeV/c^2. The black points are the data, the red histogram is the signal MC, the blue histogram is all other MC based backgrounds summed together, and the yellow histogram is the QCD estimation.
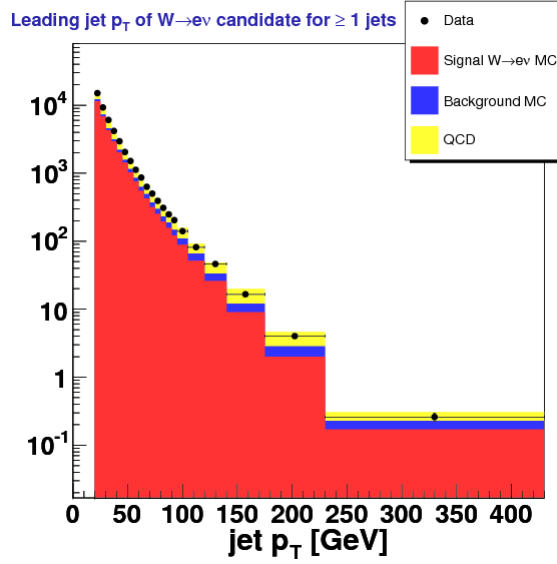
Figure 6.18. First leading jet transverse momentum (p_T) for $W \to e\nu+ \geq 1$ jets. The black points are the data, the red histogram is the signal MC, the blue histogram is all other MC based backgrounds summed together, and the yellow histogram is the QCD estimation.
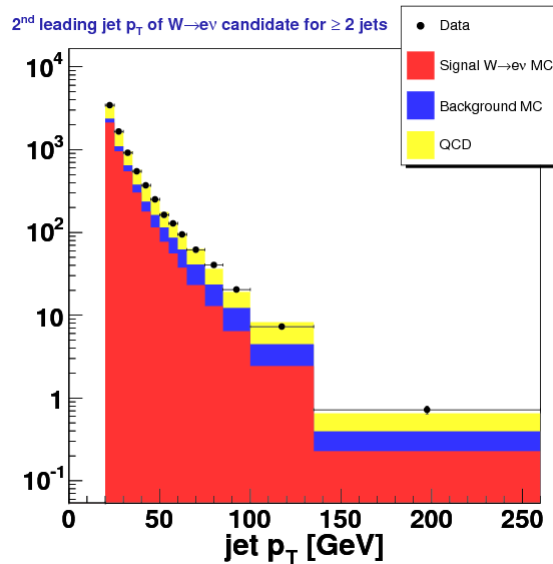
Figure 6.19. Second leading jet transverse momentum (p_T) for $W \to e\nu+ \geq 2$ jets. The black points are the data, the red histogram is the signal MC, the blue histogram is all other MC based backgrounds summed together, and the yellow histogram is the QCD estimation.
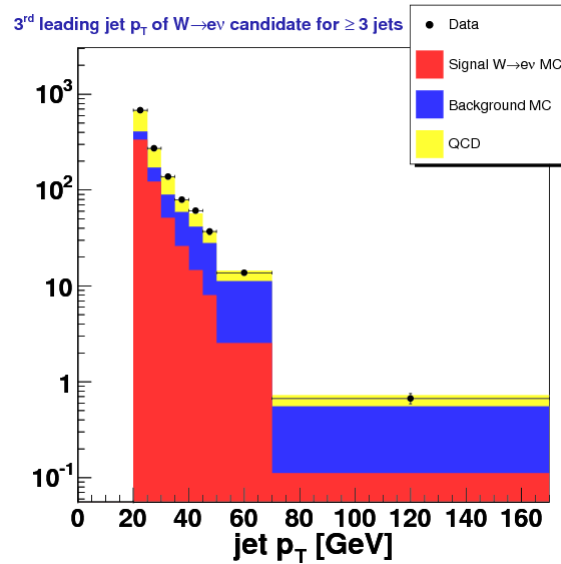
Figure 6.20. Third leading jet transverse momentum (p_T) for $W \to e\nu + \geq 1$ jets. The black points are the data, the red histogram is the signal MC, the blue histogram is all other MC based backgrounds summed together, and the yellow histogram is the QCD estimation.
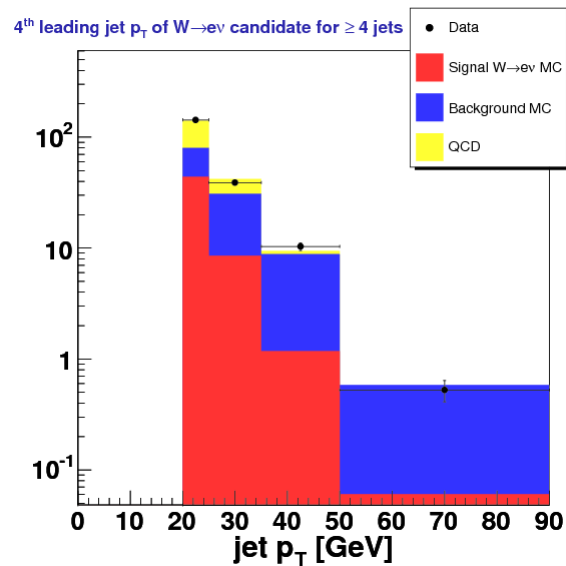
Figure 6.21. Forth leading jet transverse momentum (p_T) for $W \to e\nu + \geq 2$ jets. The black points are the data, the red histogram is the signal MC, the blue histogram is all other MC based backgrounds summed together, and the yellow histogram is the QCD estimation.
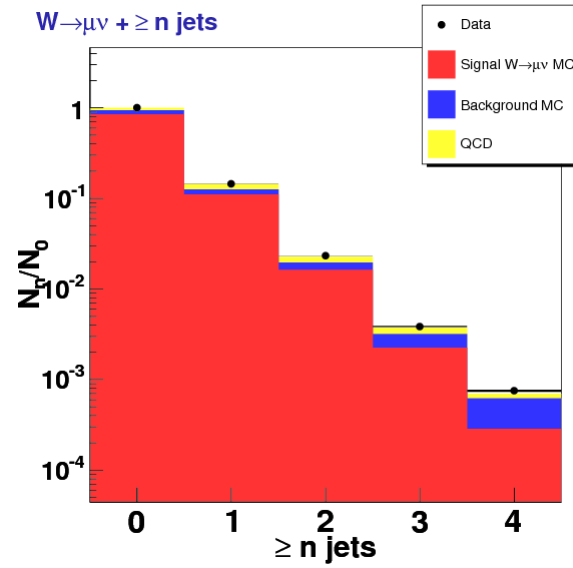
Figure 6.22. Inclusive jet multiplicity for $W \to \mu\nu + \geq n$ jets. The plot has been normalized to the total number of events in the data. The black points are the data, the red histogram is the signal MC, the blue histogram is all other MC based backgrounds summed together, and the yellow histogram is the QCD estimation.
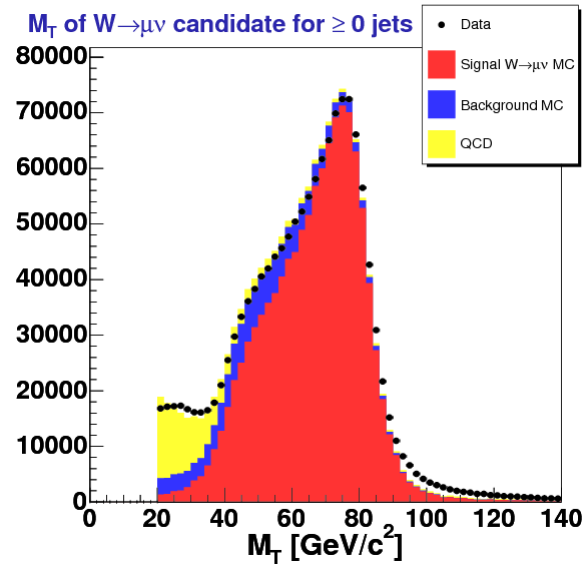
Figure 6.23. W transverse mass (M_T) for $W \to \mu\nu+ \geq 0$ jets. This is before the final W selection cut of $M_T > 30$ GeV/c^2. The black points are the data, the red histogram is the signal MC, the blue histogram is all other MC based backgrounds summed together, and the yellow histogram is the QCD estimation.
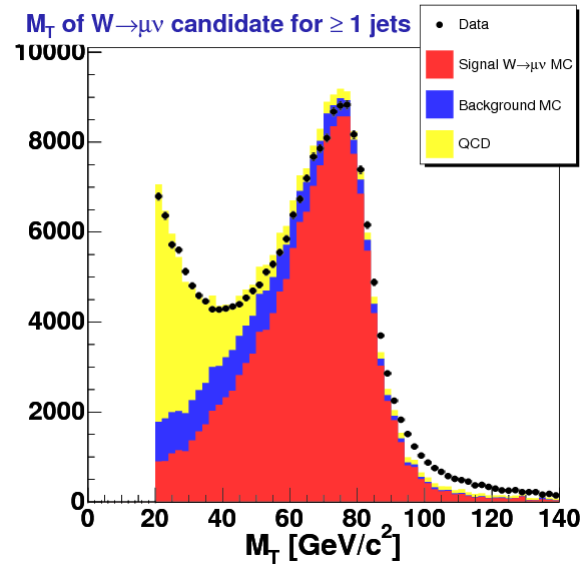
Figure 6.24. W transverse mass (M_T) for $W \rightarrow \mu\nu + \geq 1$ jets. This is before the final W selection cut of $M_T > 30$ GeV/c^2. The black points are the data, the red histogram is the signal MC, the blue histogram is all other MC based backgrounds summed together, and the yellow histogram is the QCD estimation.
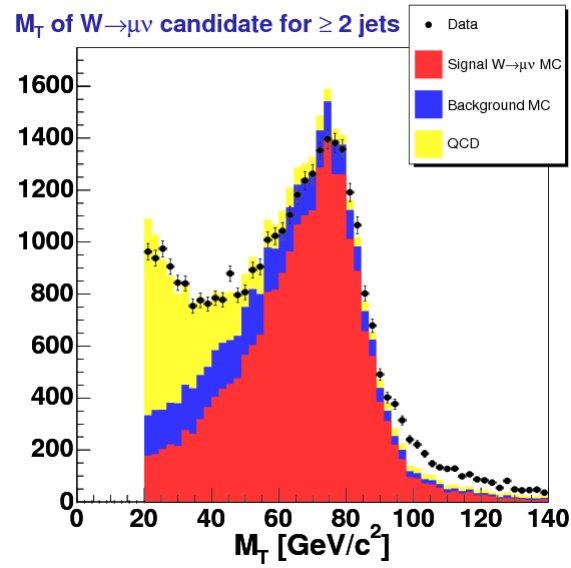
Figure 6.25. W transverse mass (M_T) for $W \to \mu\nu + {\geq}2$ jets. This is before the final W selection cut of $M_T > 30$ GeV/c^2. The black points are the data, the red histogram is the signal MC, the blue histogram is all other MC based backgrounds summed together, and the yellow histogram is the QCD estimation.
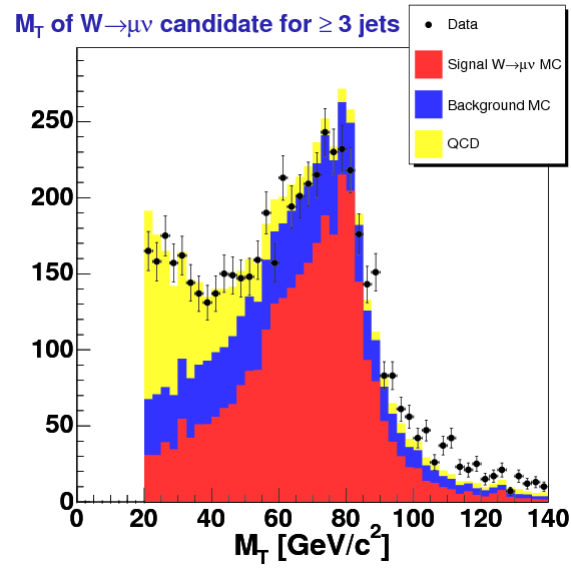
Figure 6.26. W transverse mass (M_T) for $W \to \mu\nu+ \geq 3$ jets. This is before the final W selection cut of $M_T > 30$ GeV/c^2. The black points are the data, the red histogram is the signal MC, the blue histogram is all other MC based backgrounds summed together, and the yellow histogram is the QCD estimation.
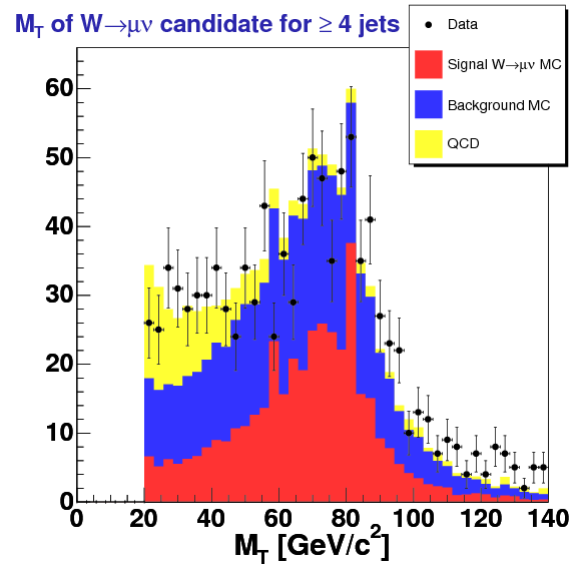
Figure 6.27. W transverse mass (M_T) for $W \to \mu\nu+ \geq 4$ jets. This is before the final W selection cut of $M_T > 30$ GeV/c^2. The black points are the data, the red histogram is the signal MC, the blue histogram is all other MC based backgrounds summed together, and the yellow histogram is the QCD estimation.
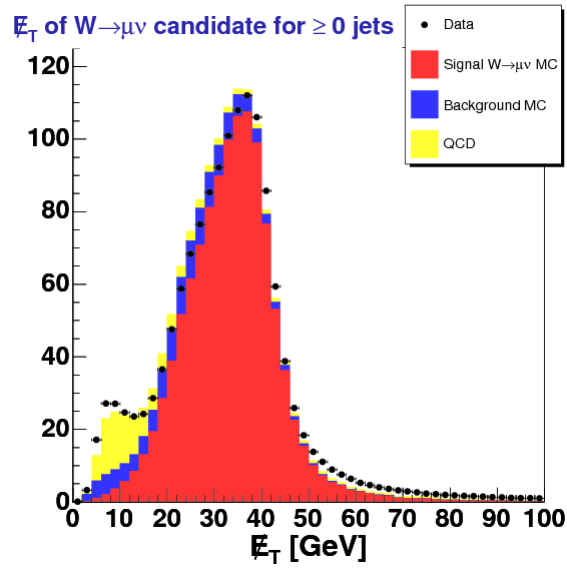
Figure 6.28. Missing transverse energy ($\not{E}_T$) for $W \to \mu\nu+ \geq 0$ jets. This is before the final W selection cut of $M_T > 30$ GeV/c^2. The black points are the data, the red histogram is the signal MC, the blue histogram is all other MC based backgrounds summed together, and the yellow histogram is the QCD estimation.
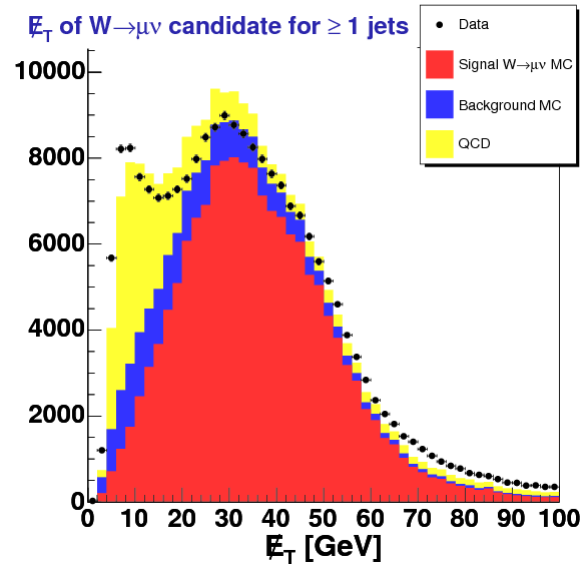
Figure 6.29. Missing transverse energy ($\not{E}_T$) for $W \to \mu\nu+ \geq 1$ jets. This is before the final W selection cut of $M_T > 30$ GeV/c^2. The black points are the data, the red histogram is the signal MC, the blue histogram is all other MC based backgrounds summed together, and the yellow histogram is the QCD estimation.

263
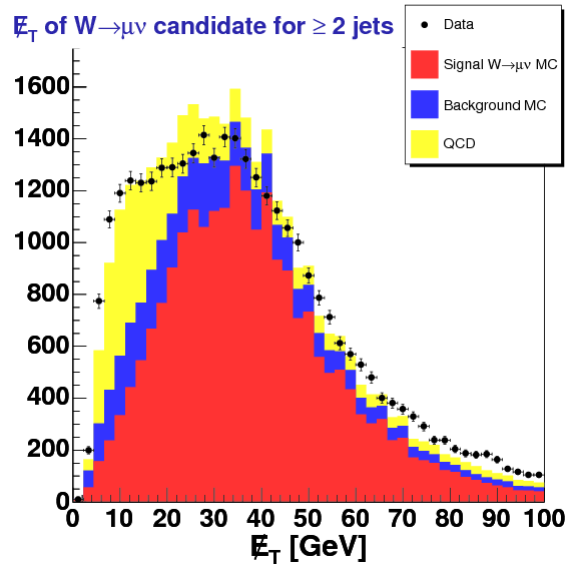
Figure 6.30. Missing transverse energy ($\not{E}_T$) for $W \to \mu\nu+ \geq 2$ jets. This is before the final W selection cut of $M_T > 30$ GeV/c^2. The black points are the data, the red histogram is the signal MC, the blue histogram is all other MC based backgrounds summed together, and the yellow histogram is the QCD estimation.
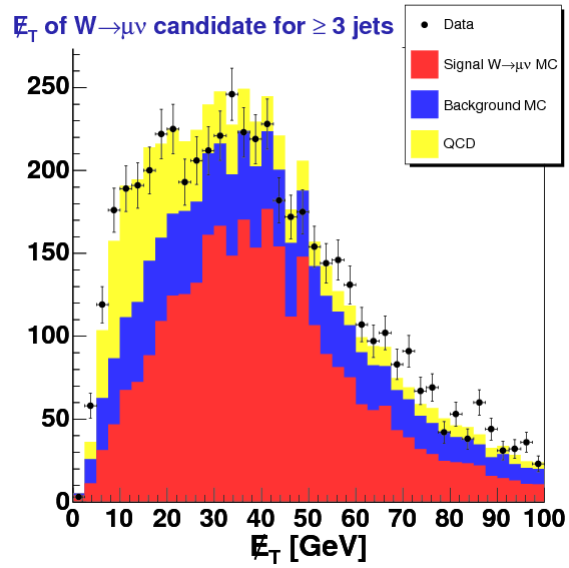
Figure 6.31. Missing transverse energy ($\not{E}_T$) for $W \to \mu\nu+ \geq 3$ jets. This is before the final W selection cut of $M_T > 30$ GeV/c^2. The black points are the data, the red histogram is the signal MC, the blue histogram is all other MC based backgrounds summed together, and the yellow histogram is the QCD estimation.
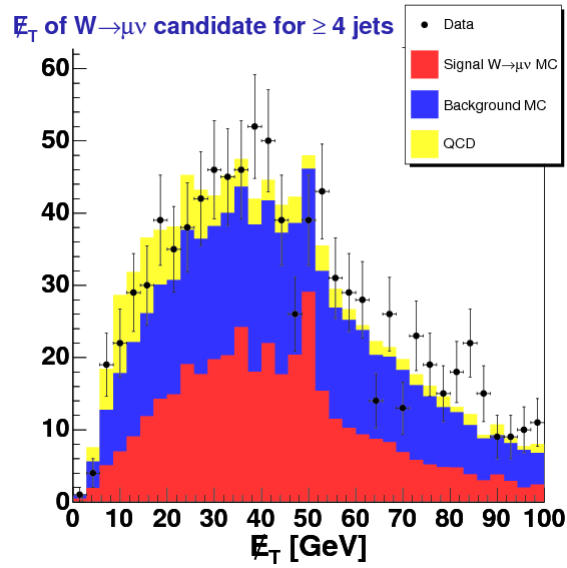
Figure 6.32. Missing transverse energy ($\not{E}_T$) for $W \to \mu\nu+ \geq 4$ jets. This is before the final W selection cut of $M_T > 30$ GeV/c^2. The black points are the data, the red histogram is the signal MC, the blue histogram is all other MC based backgrounds summed together, and the yellow histogram is the QCD estimation.
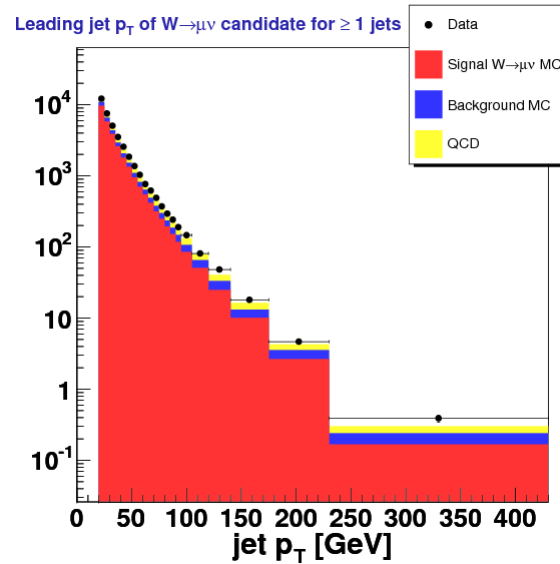
Figure 6.33. First leading jet transverse momentum (p_T) for $W \to \mu\nu + \geq 1$ jets. The black points are the data, the red histogram is the signal MC, the blue histogram is all other MC based backgrounds summed together, and the yellow histogram is the QCD estimation.
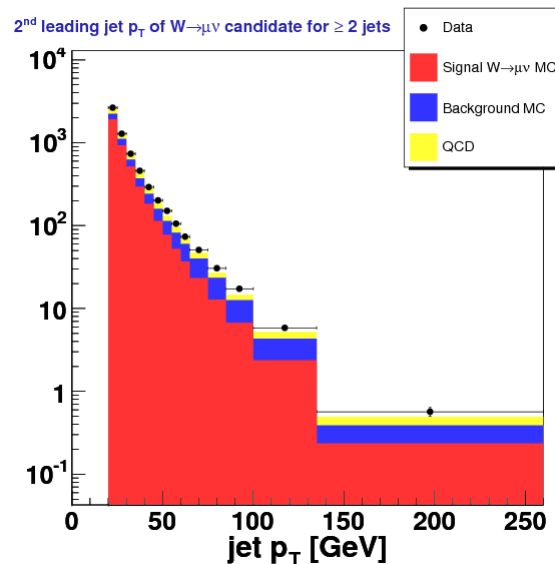
Figure 6.34. Second leading jet transverse momentum (p_T) for $W \to \mu\nu + \geq 2$ jets. The black points are the data, the red histogram is the signal MC, the blue histogram is all other MC based backgrounds summed together, and the yellow histogram is the QCD estimation.
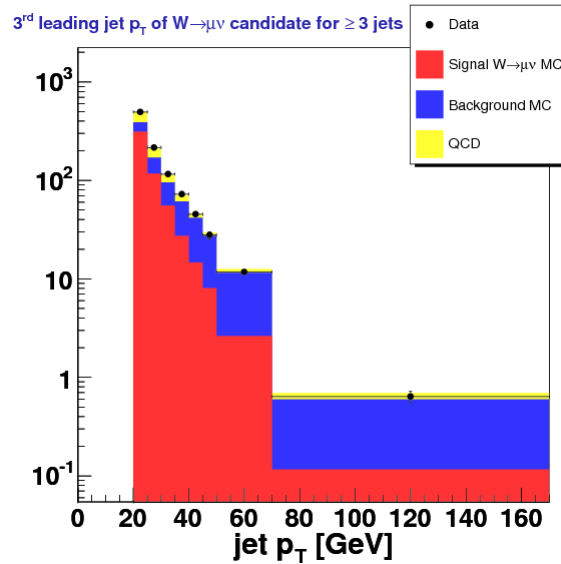
Figure 6.35. Third leading jet transverse momentum (p_T) for $W \to \mu\nu+ \geq 3$ jets. The black points are the data, the red histogram is the signal MC, the blue histogram is all other MC based backgrounds summed together, and the yellow histogram is the QCD estimation.
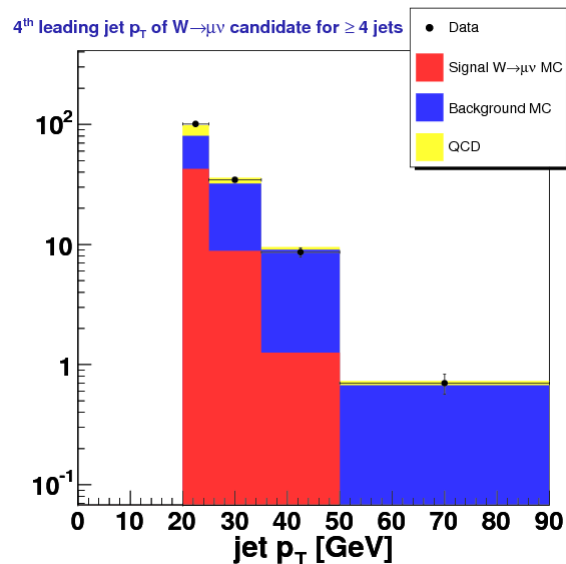
Figure 6.36. Forth leading jet transverse momentum (p_T) for $W \to \mu\nu+ \geq 4$ jets. The black points are the data, the red histogram is the signal MC, the blue histogram is all other MC based backgrounds summed together, and the yellow histogram is the QCD estimation.
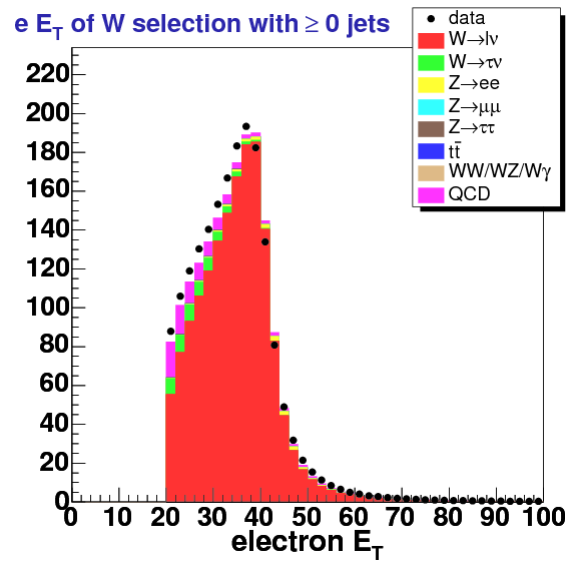
Figure 6.37. Electron transverse energy (E_T) for $W \to e\nu + \geq 0$ jets.
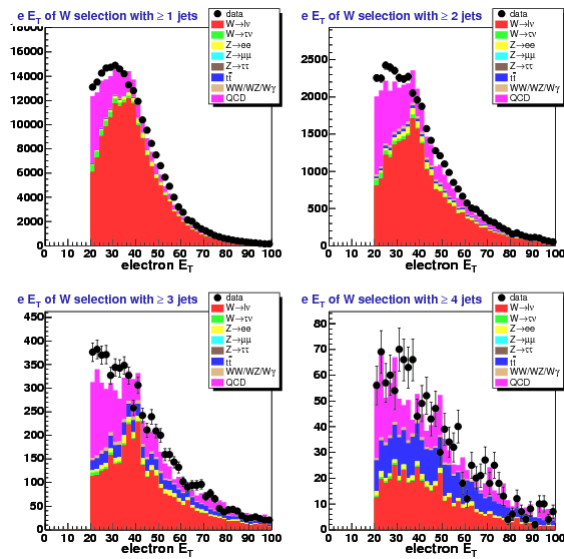
Figure 6.38. Electron transverse energy (E_T) for $W \to e\nu + \geq n$ jets. Upper-left plot is for ≥ 1 jets, upper-right for ≥ 2, lower-left for ≥ 3, and lower-right for ≥ 4.
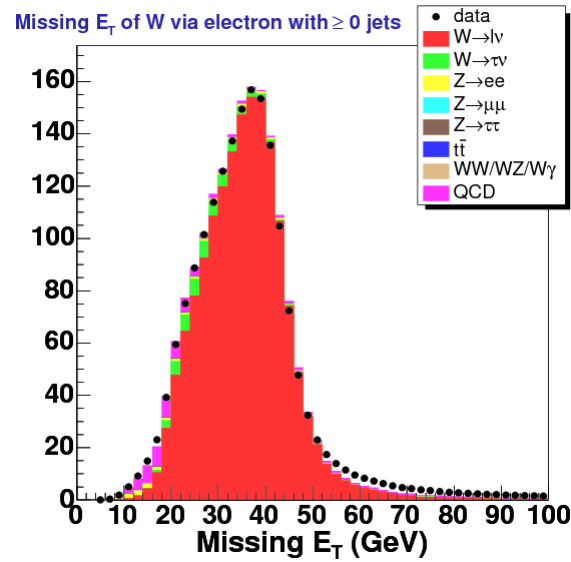
Figure 6.39. Missing transverse energy ($\not{E}_T$) for $W \to e\nu + \geq 0$ jets.
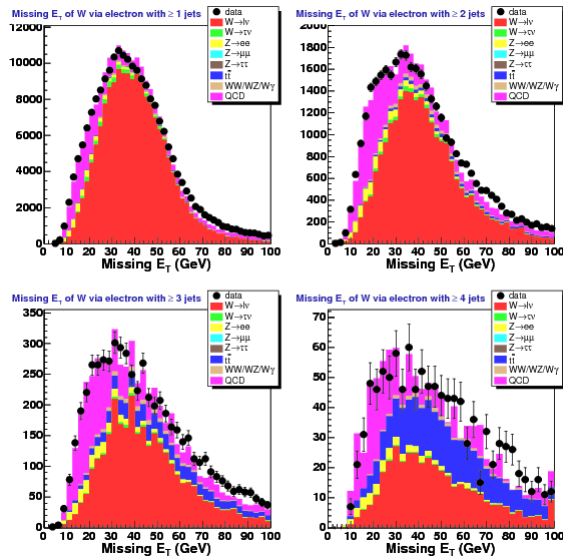
Figure 6.40. Missing transverse energy ($\not{E}_T$) for $W \to e\nu + \geq n$ jets. Upper-left plot is for ≥ 1 jets, upper-right for ≥ 2, lower-left for ≥ 3, and lower-right for ≥ 4.
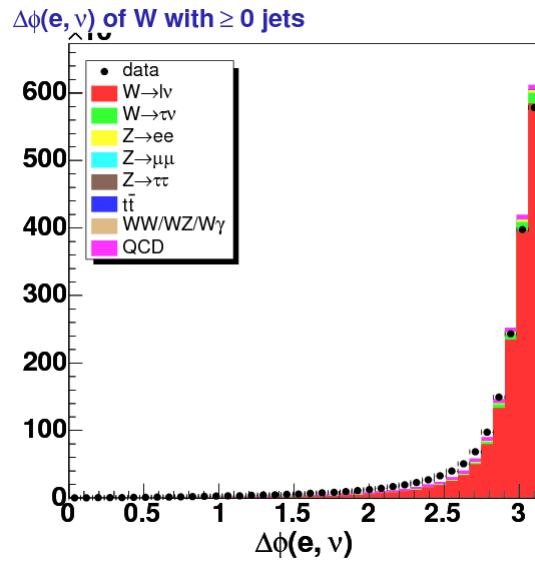
Figure 6.41. $\Delta\phi$ between missing transverse energy and the electron ($\Delta\phi$(e, ν)) for $W \rightarrow e\nu+ \geq 0$ jets.
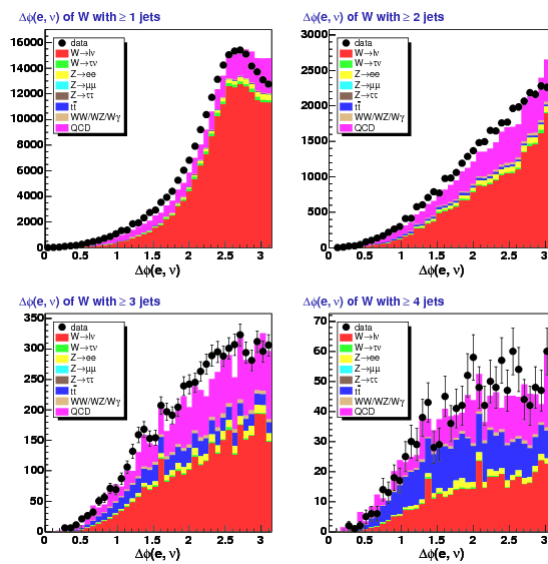
Figure 6.42. $\Delta\phi$ between missing transverse energy and the electron ($\Delta\phi$(e, ν)) for $W \rightarrow e\nu+ \geq n$ jets. Upper-left plot is for ≥ 1 jets, upper-right for ≥ 2, lower-left for ≥ 3, and lower-right for ≥ 4.
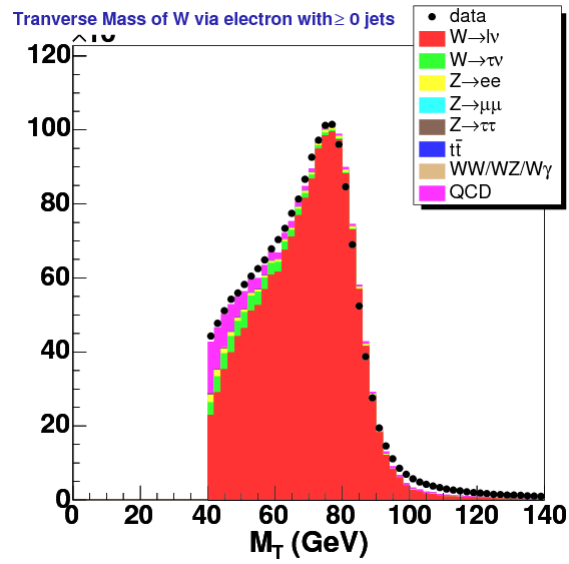
Figure 6.43. W transverse mass (M_T) for $W \to e\nu+\ \geq 0$ jets.
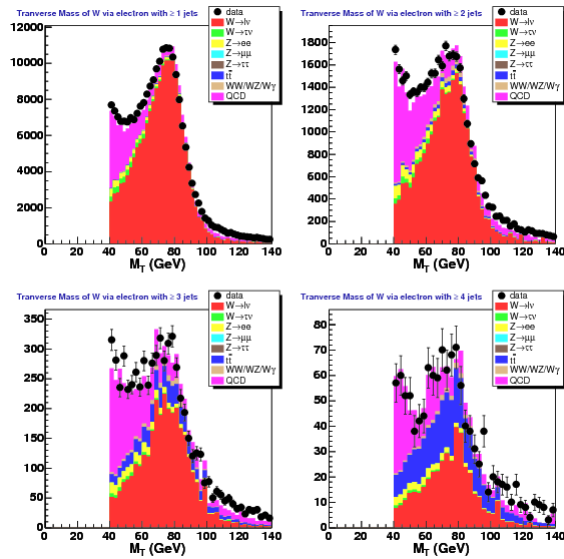
Figure 6.44. W transverse mass (M_T) for $W \to e\nu+\ \geq n$ jets. Upper-left plot is for ≥ 1 jets, upper-right for ≥ 2, lower-left for ≥ 3, and lower-right for ≥ 4.
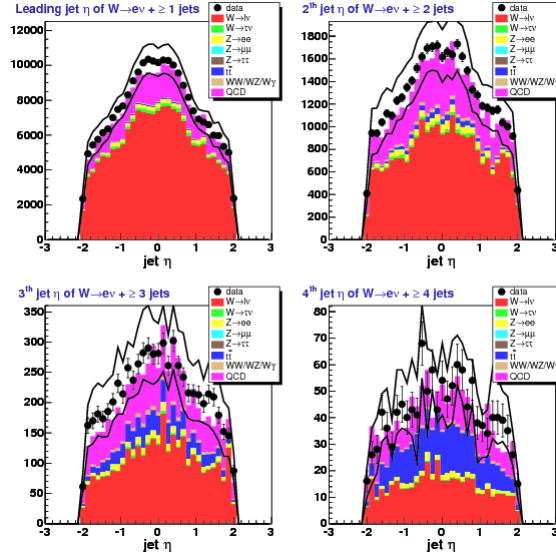
Figure 6.45. n^{th} leading jet η for $W \to e\nu + \geq n$ jets. The black lines represent the systematic on the jet energy scale. Upper-left plot is for ≥ 1 jets, upper-right for ≥ 2, lower-left for ≥ 3, and lower-right for ≥ 4.
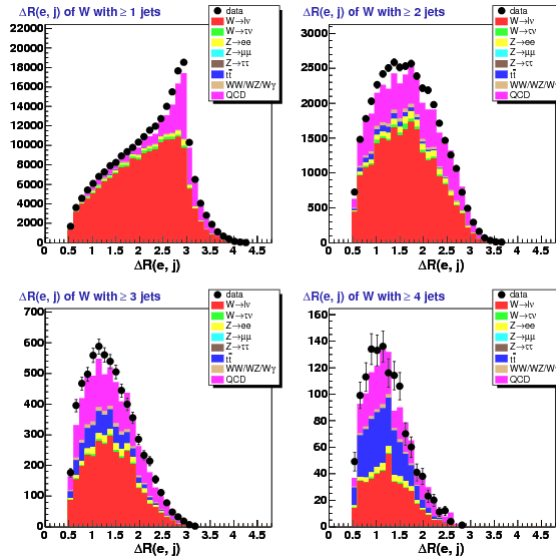
Figure 6.46. The $\eta - \phi$ separation ($\Delta R(e,j)$ with $\Delta R_{a,b} = \sqrt{(\eta_a - \eta_b)^2 + (\phi_a - \phi_b)^2}$) for $W \to e\nu + \geq n$ jets between the electron and the closest jet. Upper-left plot is for ≥ 1 jets, upper-right for ≥ 2, lower-left for ≥ 3, and lower-right for ≥ 4.
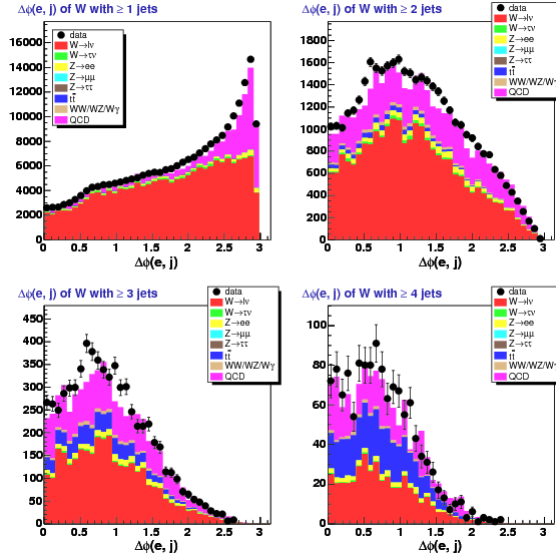
Figure 6.47. The $\Delta\phi$ between the electron and the closest jet for $W \rightarrow e\nu+ \geq n$ jets. Upper-left plot is for ≥ 1 jets, upper-right for ≥ 2, lower-left for ≥ 3, and lower-right for ≥ 4.
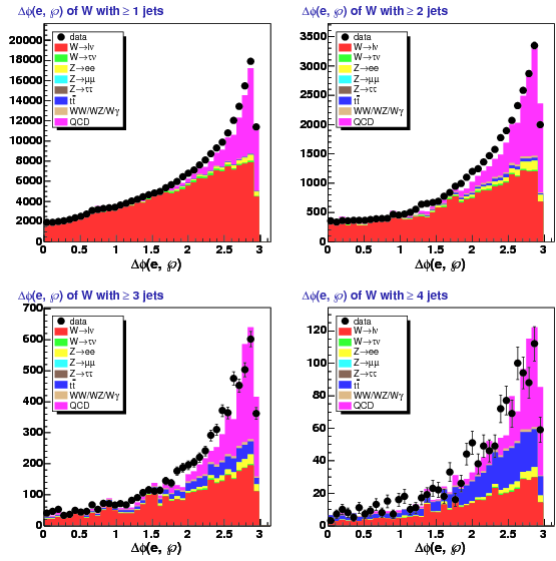
Figure 6.48. The $\Delta\phi$ between the electron and the jet vector sum, $\wp$ (as defined in equation 5.2 on page 145), for $W \rightarrow e\nu+ \geq n$ jets. Upper-left plot is for ≥ 1 jets, upper-right for ≥ 2, lower-left for ≥ 3, and lower-right for ≥ 4.
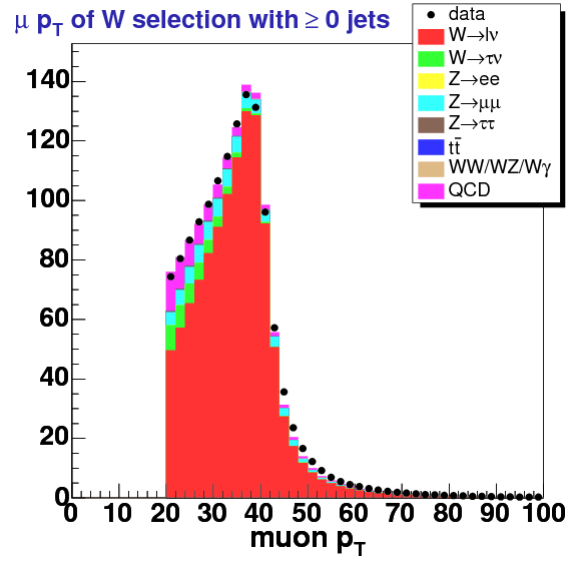
Figure 6.49. Muon transverse momentum (p_T) for $W \to \mu\nu+ \geq 0$ jets.
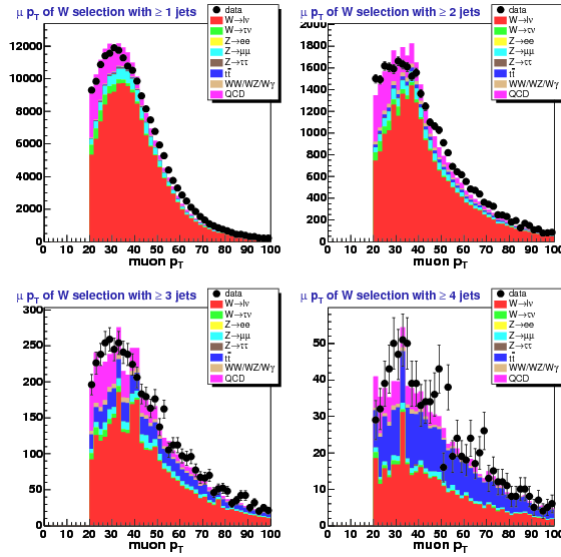
Figure 6.50. Muon transverse momentum (p_T) for $W \to \mu\nu+ \geq n$ jets. Upper-left plot is for ≥ 1 jets, upper-right for ≥ 2, lower-left for ≥ 3, and lower-right for ≥ 4.
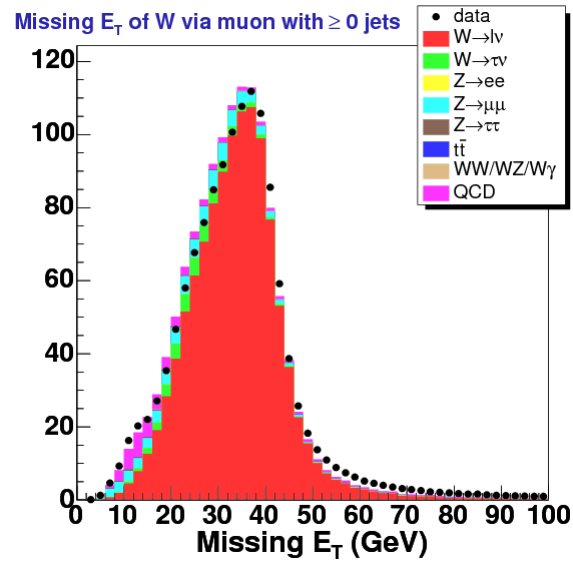
Figure 6.51. Missing transverse energy ($\not{E}_T$) for $W \to \mu\nu + \geq 0$ jets.
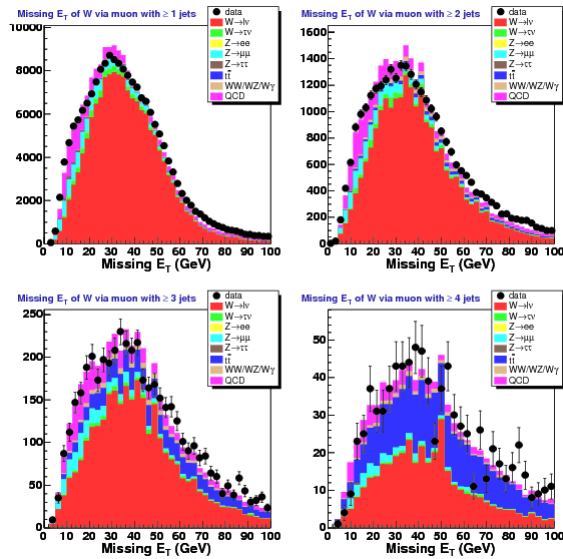
Figure 6.52. Missing transverse energy ($\not{E}_T$) for $W \to \mu\nu + \geq n$ jets. Upper-left plot is for ≥ 1 jets, upper-right for ≥ 2, lower-left for ≥ 3, and lower-right for ≥ 4.
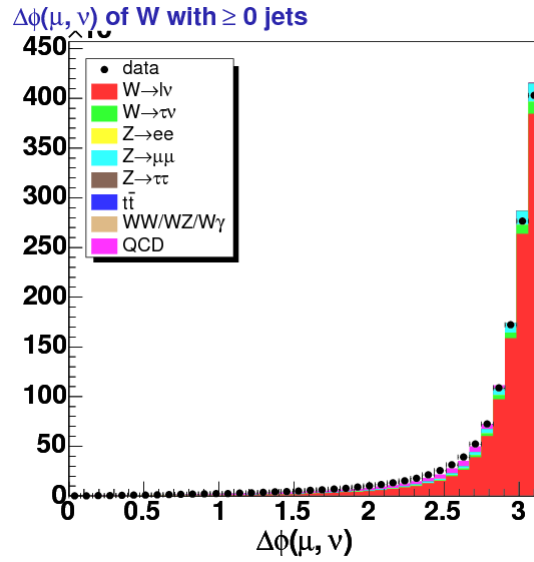
Figure 6.53. $\Delta\phi$ between missing transverse energy and the muon $(\Delta\phi(\mu,\nu))$ for $W \rightarrow \mu\nu+ \geq 0$ jets.
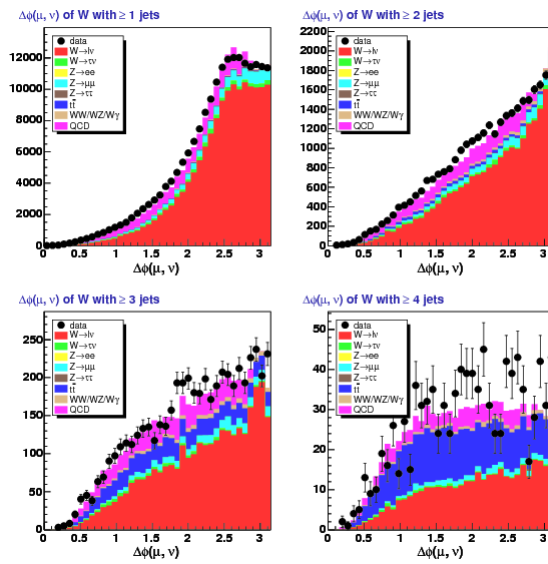
Figure 6.54. $\Delta\phi$ between missing transverse energy and the muon $(\Delta\phi(\mu,\nu))$ for $W \rightarrow \mu\nu+ \geq n$ jets. Upper-left plot is for ≥ 1 jets, upper-right for ≥ 2, lower-left for ≥ 3, and lower-right for ≥ 4.
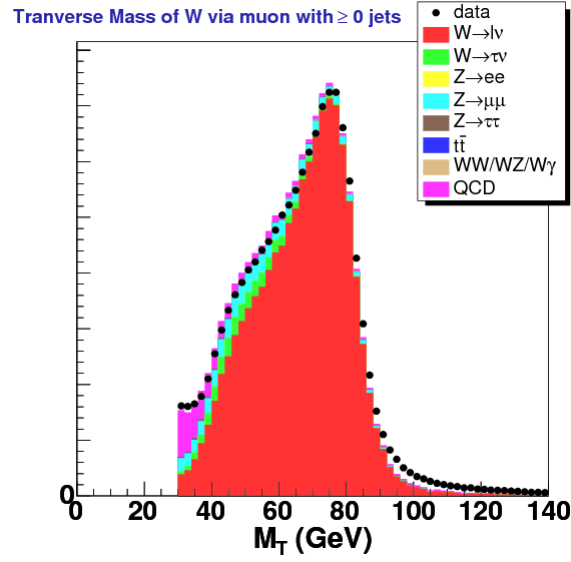
Figure 6.55. W transverse mass (M_T) for $W \to \mu\nu + \geq 0$ jets.
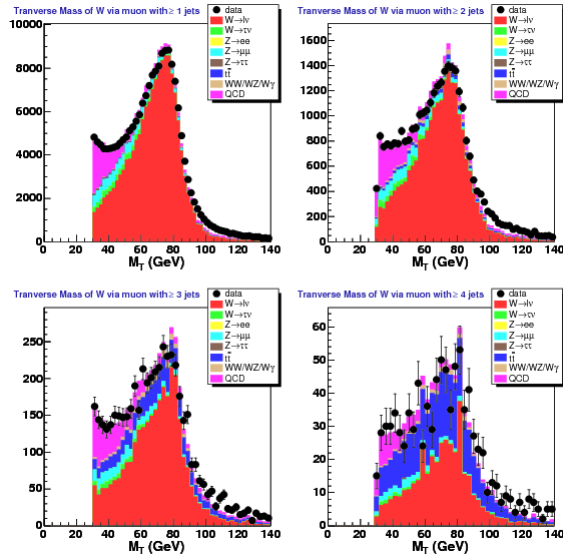
Figure 6.56. W transverse mass (M_T) for $W \to \mu\nu + \geq n$ jets. Upper-left plot is for ≥ 1 jets, upper-right for ≥ 2, lower-left for ≥ 3, and lower-right for ≥ 4.
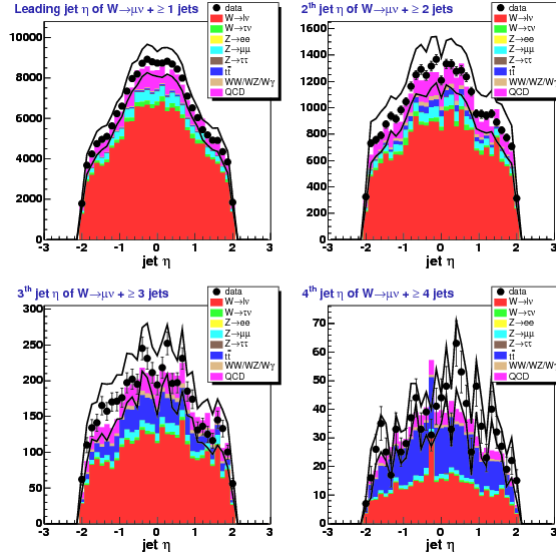
Figure 6.57. n^{th} leading jet η for $W \rightarrow \mu\nu+ \geq n$ jets. The black lines represent the systematic on the jet energy scale. Upper-left plot is for ≥ 1 jets, upper-right for ≥ 2, lower-left for ≥ 3, and lower-right for ≥ 4.
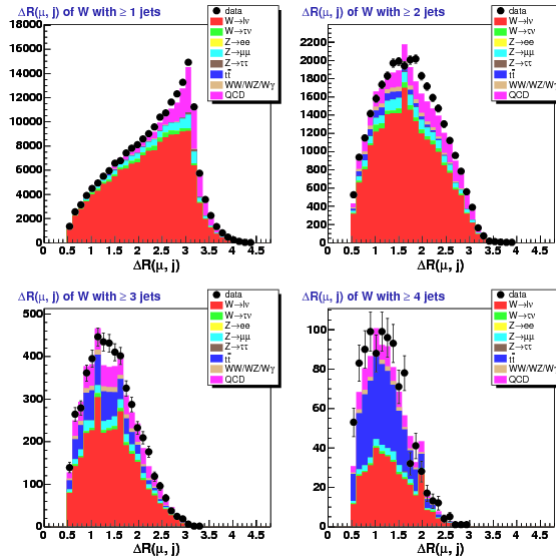
Figure 6.58. The $\eta - \phi$ separation ($\Delta R(\mu,j)$ with $\Delta R_{a,b} = \sqrt{(\eta_a - \eta_b)^2 + (\phi_a - \phi_b)^2}$) for $W \rightarrow \mu\nu+ \geq n$ jets between the muon and the closest jet. Upper-left plot is for ≥ 1 jets, upper-right for ≥ 2, lower-left for ≥ 3, and lower-right for ≥ 4.
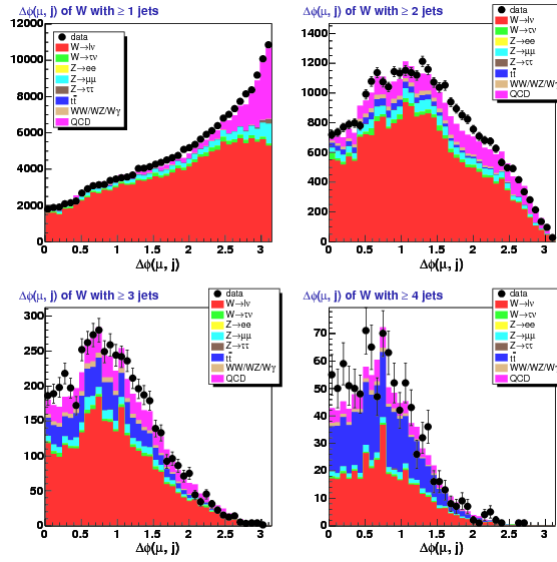
Figure 6.59. The $\Delta\phi$ between the muon and the closest jet for $W \to \mu\nu + \geq n$ jets. Upper-left plot is for ≥ 1 jets, upper-right for ≥ 2, lower-left for ≥ 3, and lower-right for ≥ 4.
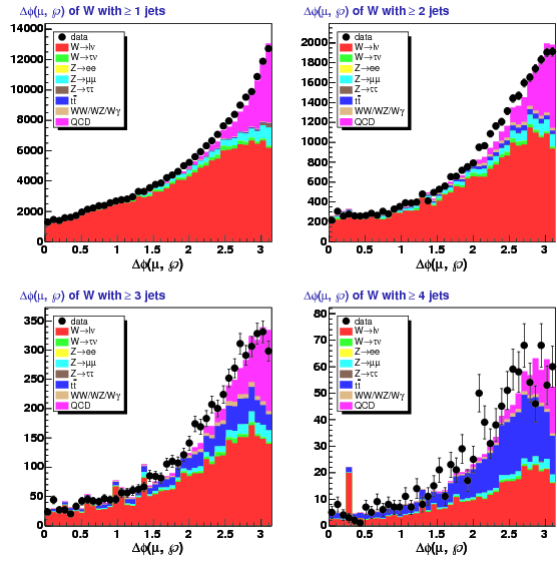
Figure 6.60. The $\Delta\phi$ between the muon and the jet vector sum, $\wp$ (as defined in equation 5.2 on page 145), for $W \to \mu\nu + \geq n$ jets. Upper-left plot is for ≥ 1 jets, upper-right for ≥ 2, lower-left for ≥ 3, and lower-right for ≥ 4.

6.6. MC Vertex Reweighing (Promotion)

As alluded to in sections 4.1 and 5.1 there is an additional background like effect that arises due to the potential for additional interactions to produce additional (that is non-primary vertex related) jets. For example, in the case of our signal sample we could have an event which has a candidate W (without loss of generalization, decaying to a muon and its neutrino) with 2 jets passing defining cuts. However, if one of these jets did not come from the primarily interactions it is not a $W+2$ jets event but rather a $W+1$ jet event with an additional jet via a separate interaction:

$$\langle p\bar{p} \rightarrow (W + 1\text{jet})\rangle \oplus \langle p\bar{p} \rightarrow (X + \text{jet})\rangle$$

This possibility for our signal to be "promoted" to higher jet multiplicities (e.g. n to $n+1$) is called promotion. We can think as this as an additional background like effect where we have to adjust our expectation modulo the relevant event information (luminosity, number of vertices, etc.).

The overall goal of this section is to survey and understand the problem piece by piece and then proceed to explain our treatment. First we will discuss the relevant details to the number of vertices (hereafter "# vertices") and jet multiplicity distributions in data as a mean to our end of understanding the number of interactions. Then we will examine the comparison between data and MC and formulate a better criteria for the number of additional interactions in an event. This together with a method for correcting (reweighting) the MC on the basis for this criteria serves as a means to our end in accounting for the promotion background. We deal with systematic associated with the variation between reweighting and our refitting of backgrounds later in section 8.4.

Consider figures 6.61 and 6.62 which show the luminosity dependence on the number of quality 12 vertices for inclusive $W \rightarrow e\nu$ and $W \rightarrow \mu\nu$, respectively. As these figures show, the luminosity has a clear effect on the number of additional quality 12 (or greater) vertices which in turn could manifest via promotion. The conclusion is that this is real effect that has to be quantified and dealt with. The previous version of this analysis [12] looked at the mini-bias sample and use this to construct a conversion matrix between the number of vertices (a good metric for additional interactions as explained later in this section) and jet multiplicity.

These plots demand a better understanding outside of our eventual goal of accounting for the jet promotion background/effect. A similar set of plots for the jet multiplicity is shown in Fig. 6.63 for electrons and Fig. 6.64. These are not particularly instructive by themselves so figures 6.65-6.66 were produced. In these plots the jet multiplicity for 4 different luminosity bins is normalized to the total (all luminosity) jet multiplicity so that they effectively have the same number of events. We note that in this approach, each jet bin is treated independently. These distributions are then divided by the nominal jet multiplicity. For example, if we measured the ≥ 2 jets multiplicity using only the $L > 150^{30}$ cm^{-2}/s sample it would be about 50% larger relative to our composite luminosity sample.

We now shift focus to the comparison between the MC and data. We first note that the previous MC sets for our $W + n$p came via `Alpgen`(v1.3)`+Herwig`. We observed a rather lackluster performance in the MC (with full CDF simulation) in generating events with additional vertices. The newer incarnation is much improved but still was not been tuned to give good agreement for moderate (1-4) number of vertices falls off very quickly
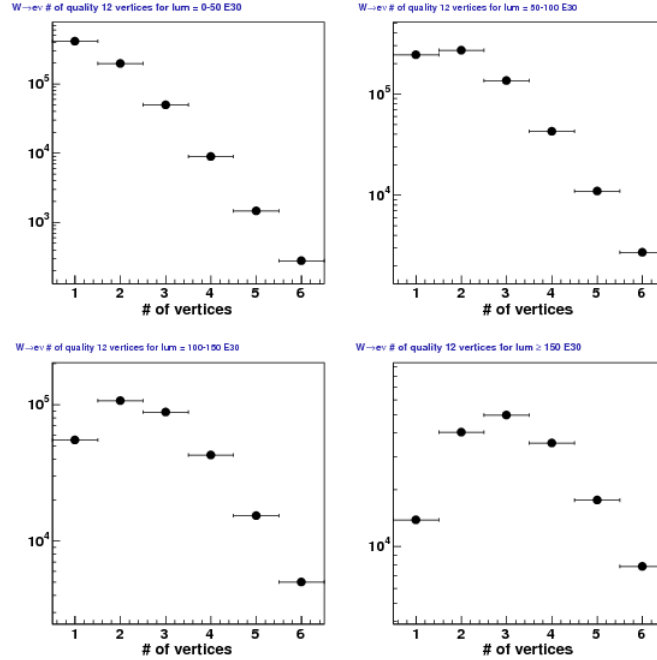
Figure 6.61. # of quality 12 vertices in $W \to e\nu$ Candidates for instantaneous luminosities (in units of $\times 10^{30}$ cm^{-2}/s) of 0-50 (upper-left), 50-100 (upper-right), 100-150 (lower-left), and $\geq$150 (lower-right).

for higher number of vertices. In figures 6.67 and 6.68 we show the # of quality 12 vertices for $W \to e\nu + \geq n$ jets. We present the same distributions for $W \to \mu\nu + \geq 0$ and n jets in figures 6.69 and 6.70. Again the prediction in the MC does not match up for the lower number of vertices and under performs for the higher number. On the positive side, in the case of the electrons, the data based QCD falls off roughly as the data does suggesting no # vertices dependence/bias.

In order to better understand the disagreement between MC and data we took the data based components (data candidates and QCD prediction) and compared them to the sum MC based predictions. We also simplified the # vertices to run to 1-6. Figures 6.71 and 6.72 are the (data-QCD) vs. MC version of figures 6.67 and 6.68, respectively, for the

electron channel. We produce the same (data-QCD) vs. MC plots for the muon channel
and these are shown in figures 6.73 and 6.74 for ≥ 0 jets and ≥ 1-4 jets, respectively. In
order to help make these comparisons with the # vertices, a Data/MC plot is shown in
figures 6.75 and 6.76 for the electron channel and the muon channel results are given
in figures 6.77 and 6.78 again for the ≥ 0 jets and ≥ 1-4 jets cases, respectively. These
Data/MC are literally the histogram division between are simplified data (minus QCD)
and MC estimation.
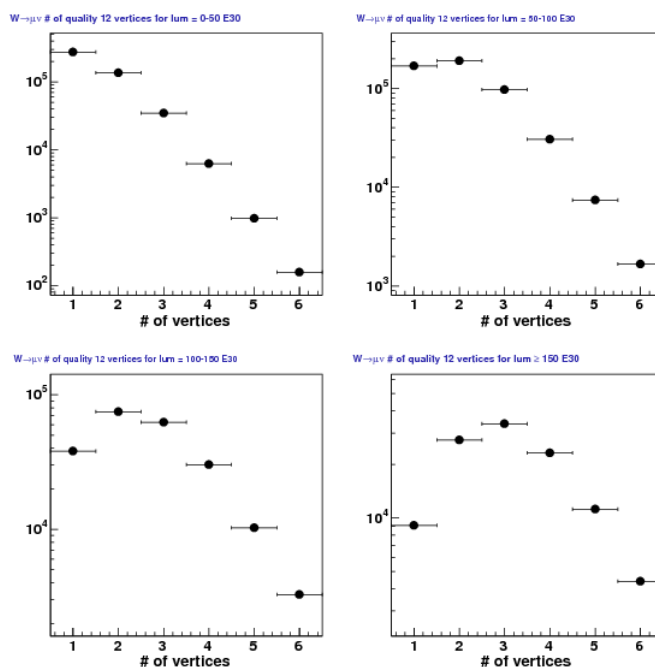
Figure 6.62. # of quality 12 vertices in $W \to \mu\nu$ Candidates for instantaneous luminosities (in units of $\times 10^{30}$ cm^{-2}/s) of 0-50 (upper-left), 50-100 (upper-right), 100-150 (lower-left), and ≥ 150 (lower-right).
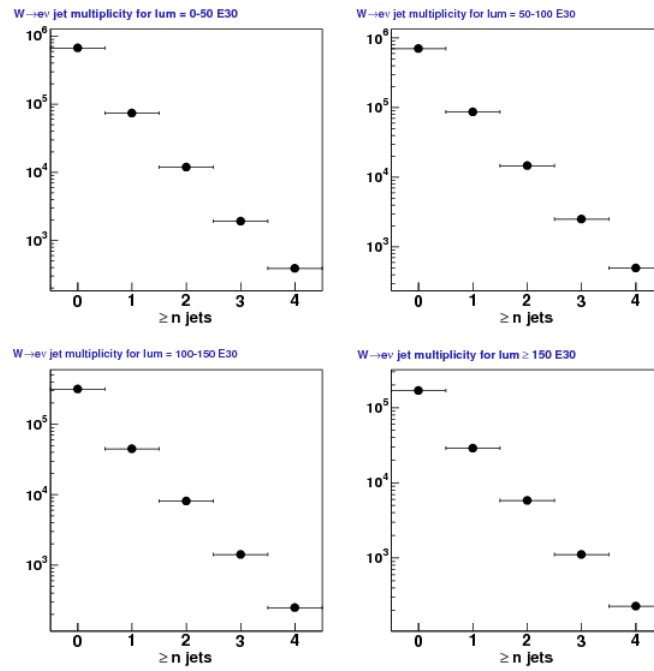
Figure 6.63. Jet Multiplicity for $W \rightarrow e\nu$ Candidates for instantaneous luminosities (in units of $\times 10^{30}$ cm^{-2}/s) of 0-50 (upper-left), 50-100 (upper-right), 100-150 (lower-left), and $\geq$150 (lower-right).

285
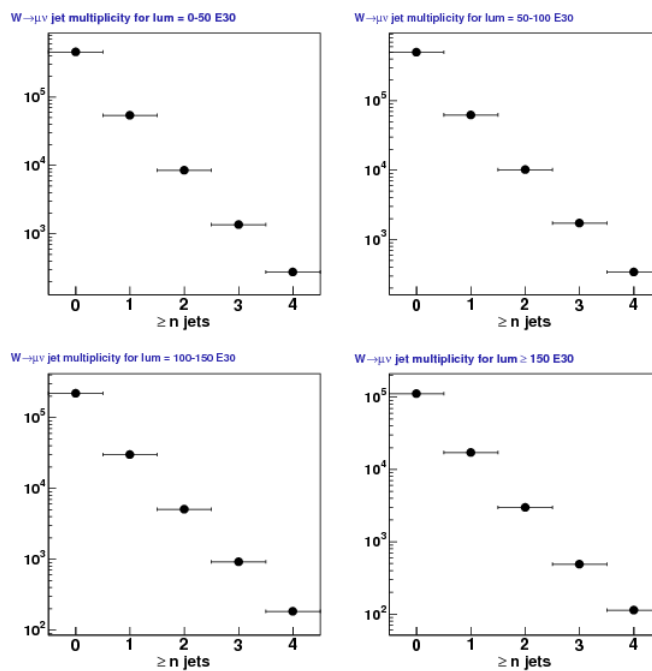
Figure 6.64. Jet Multiplicity for $W \rightarrow \mu\nu$ Candidates for instantaneous luminosities (in units of $\times 10^{30}$ cm^{-2}/s) of 0-50 (upper-left), 50-100 (upper-right), 100-150 (lower-left), and $\geq$150 (lower-right).
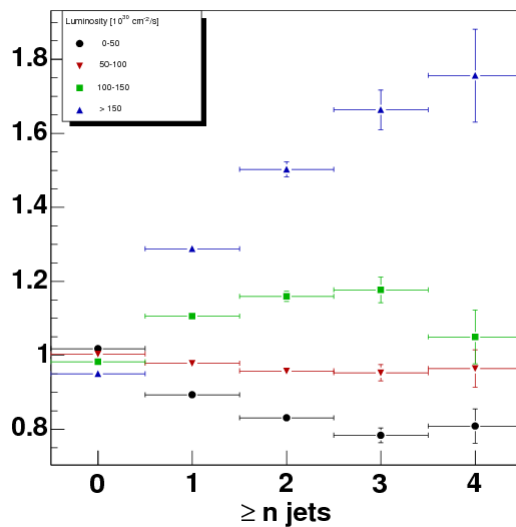
Figure 6.65. Jet Multiplicity for different instantaneous luminosity bins [0-50 (•), 50-100 (▼), 100-150 (■), and ≥150 (▲) in units of ×10³⁰ cm⁻²/s] normalized to and then divided by the total luminosity sample for $W \to e\nu$ Candidates
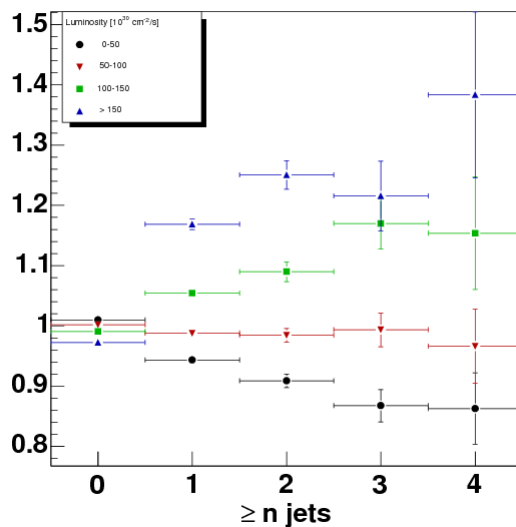
Figure 6.66. Jet Multiplicity for different instantaneous luminosity bins [0-50 (•), 50-100 (▼), 100-150 (■), and ≥150 (▲) in units of ×10³⁰ cm⁻²/s] normalized to and then divided by the total luminosity sample for $W \to \mu\nu$ Candidates

287
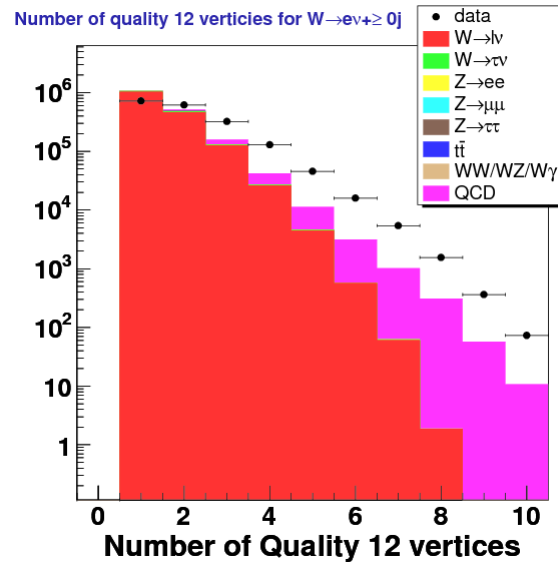
Figure 6.67. # quality 12 vertices for $W \to e\nu+ \geq 0$ jets
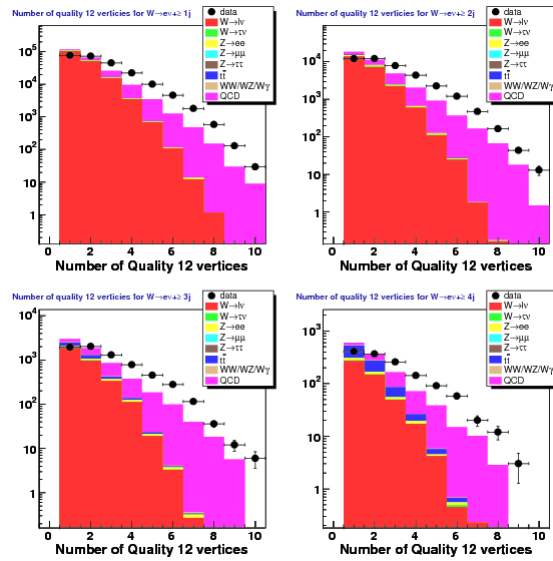
Figure 6.68. # quality 12 vertices for $W \to e\nu+ \geq$1-4 jets
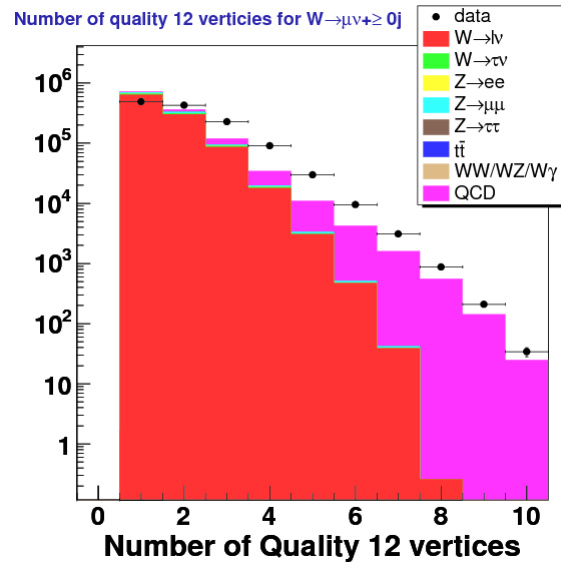
Figure 6.69. # quality 12 vertices for $W \to \mu\nu+ \geq 0$ jets
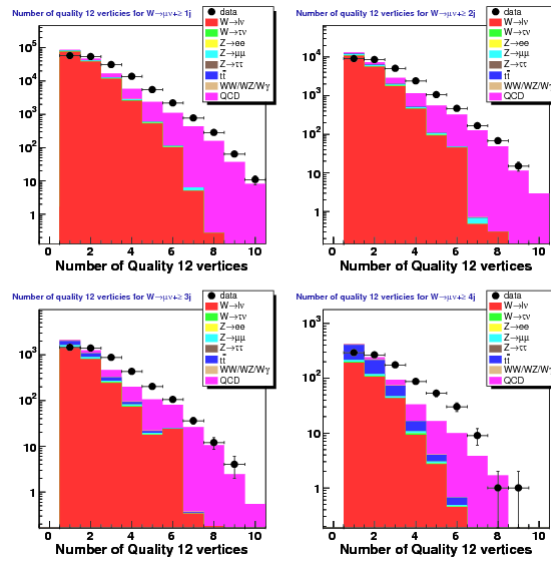
Figure 6.70. # quality 12 vertices for $W \to \mu\nu+ \geq$1-4 jets

289
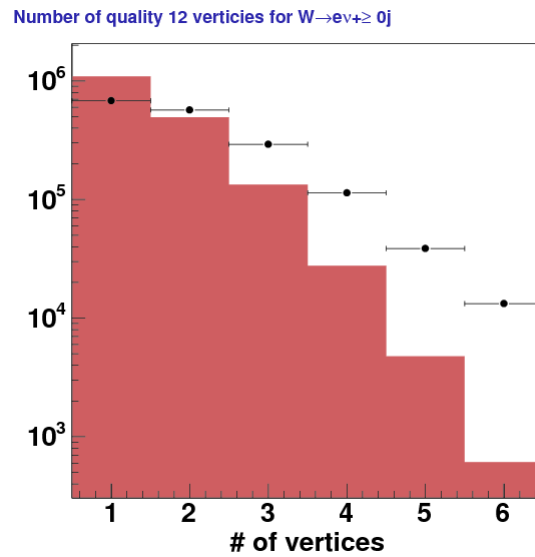
Figure 6.71. # quality 12 vertices for $W \to e\nu+ \geq 0$ jets. Here the red histogram represents the sum MC predictions of Fig. 6.67 while the data points represent Data-QCD
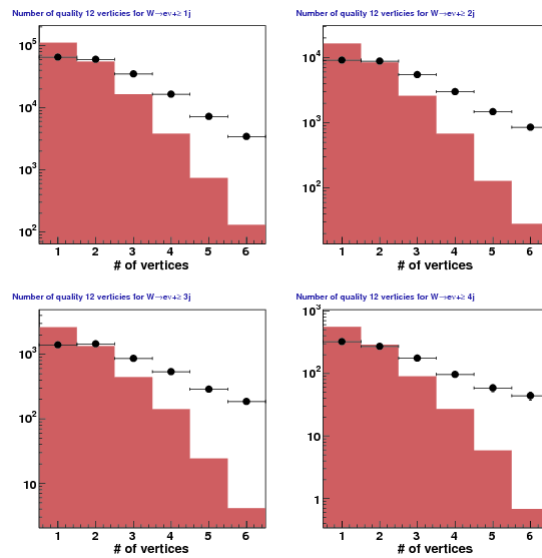
Figure 6.72. # quality 12 vertices for $W \to e\nu+ \geq$1-4 jets. Here the red histogram represents the sum MC predictions of Fig. 6.68 while the data points represent Data-QCD

290
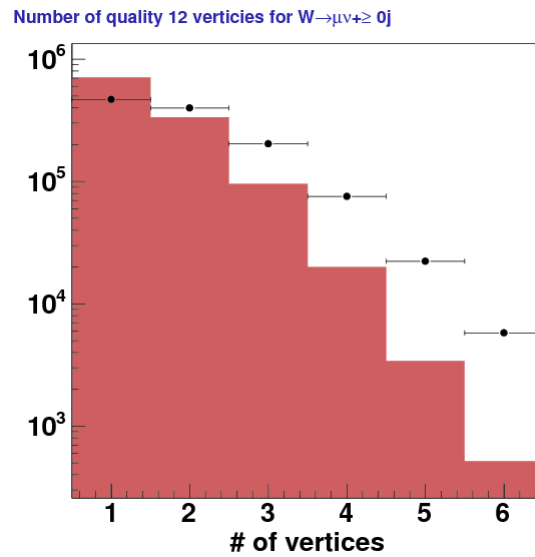
Figure 6.73. # quality 12 vertices for $W \rightarrow \mu\nu+ \geq 0$ jets. Here the red histogram represents the sum MC predictions of Fig. 6.69 while the data points represent Data-QCD
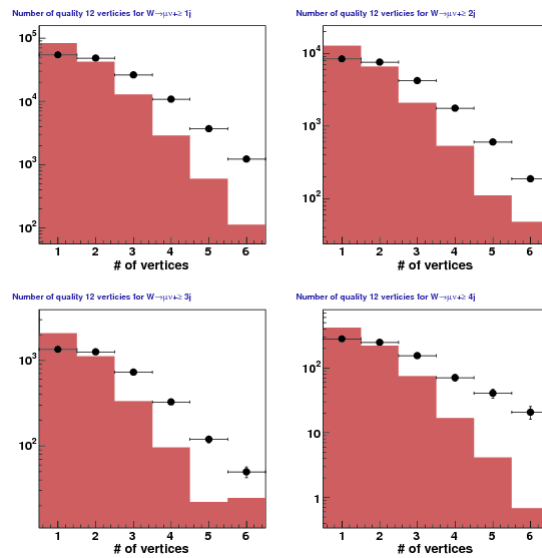
Figure 6.74. # quality 12 vertices for $W \rightarrow \mu\nu+ \geq$1-4 jets. Here the red histogram represents the sum MC predictions of Fig. 6.70 while the data points represent Data-QCD
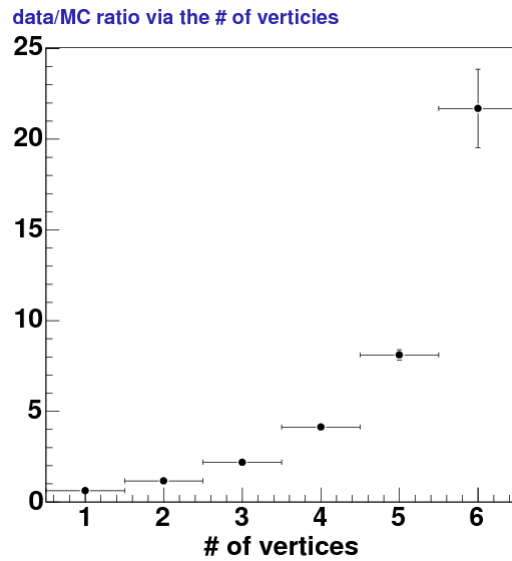
Figure 6.75. Data/MC comparison of # quality 12 vertices for $W \rightarrow e\nu+ \geq 0$ jets. This is a ratio of Data-QCD vs. MC from the Fig. 6.71.
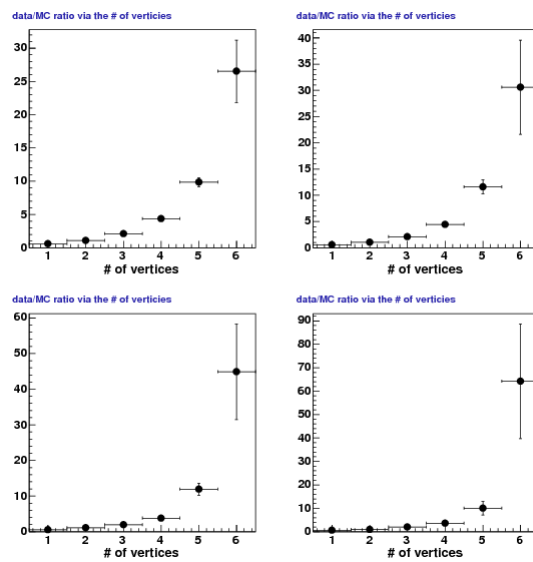
Figure 6.76. Data/MC comparison of # quality 12 vertices for $W \rightarrow e\nu+ \geq$1-4 jets. This is a ratio of Data-QCD vs. MC from the Fig. 6.72.
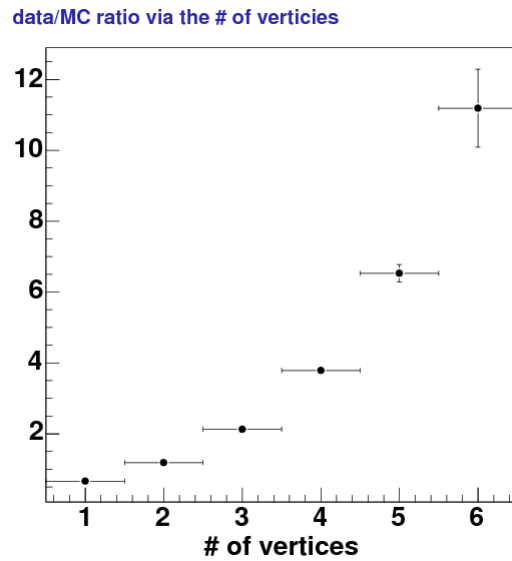
Figure 6.77. Data/MC comparison of # quality 12 vertices for $W \rightarrow \mu\nu+ \geq 0$ jets. This is a ratio of Data-QCD vs. MC from the Fig. 6.73.
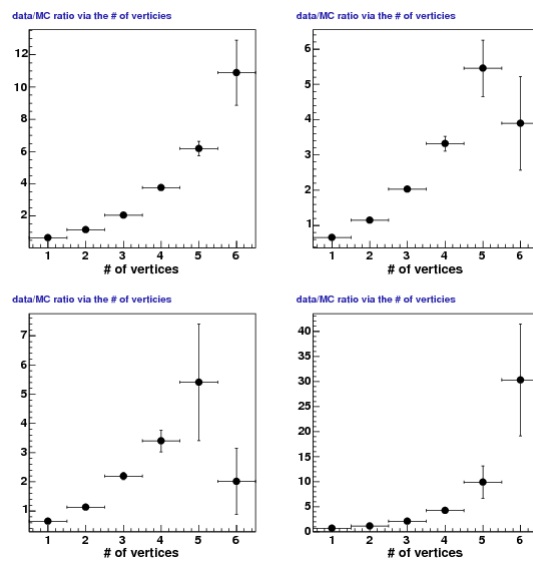
Figure 6.78. Data/MC comparison of # quality 12 vertices for $W \rightarrow \mu\nu+ \geq 1$-4 jets. This is a ratio of Data-QCD vs. MC from the Fig. 6.74.

293
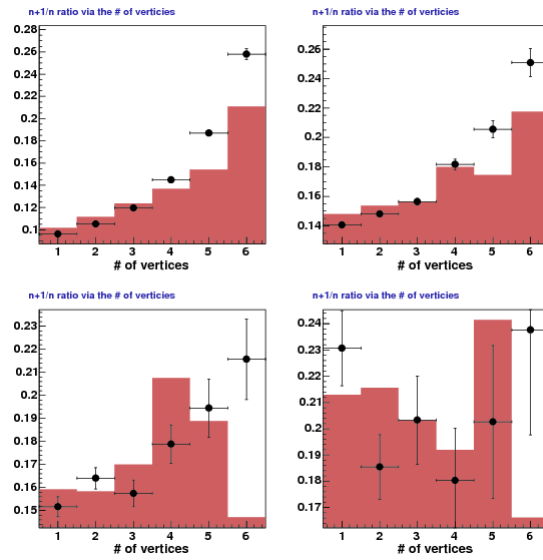
Figure 6.79. $(n + 1)/n$ jet multiplicity ratio comparison of # quality 12 vertices for $W \rightarrow e\nu + \geq n$ jets. Here the red histogram represents the MC prediction while the data points represent Data-QCD for each jet multiplicity ratio. Upper-left: 1/0, upper-right: 2/1, lower-left: 3/2, and lower-right: 4/3.
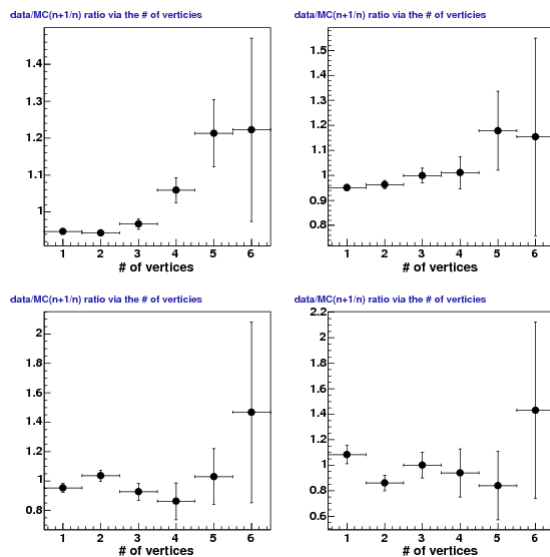
Figure 6.80. Data/MC ratio of the $(n+1)/n$ jet multiplicity ratio comparison of # quality 12 vertices for $W \rightarrow e\nu+ \geq n$ jets. This is a Data/MC ratio of Fig. 6.79. Upper-left: 1/0, upper-right: 2/1, lower-left: 3/2, and lower-right: 4/3.

295
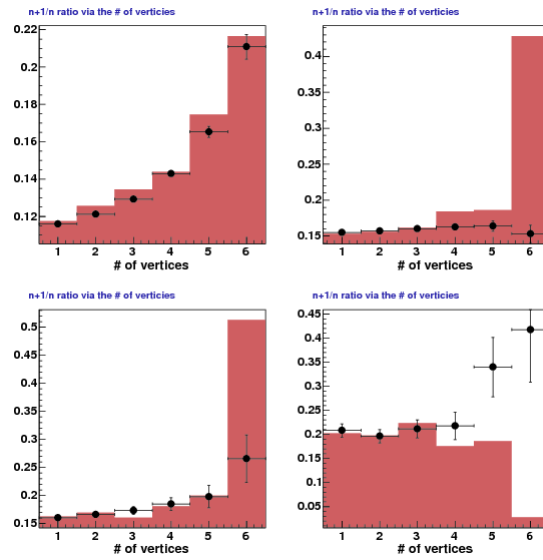
Figure 6.81. $(n + 1)/n$ jet multiplicity ratio comparison of # quality 12 vertices for $W \to \mu\nu + \geq n$ jets. Here the red histogram represents the MC prediction while the data points represent Data-QCD for each jet multiplicity ratio. Upper-left: 1/0, upper-right: 2/1, lower-left: 3/2, and lower-right: 4/3.

296
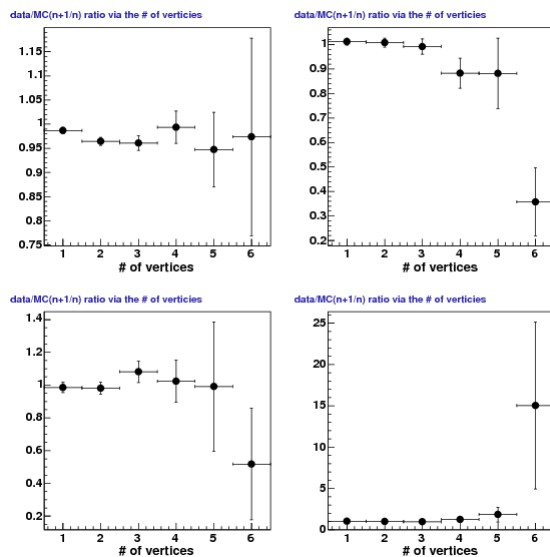
Figure 6.82. Data/MC ratio of the $(n+1)/n$ jet multiplicity ratio comparison of # quality 12 vertices for $W \to \mu\nu+ \geq n$ jets. This is a Data/MC ratio of figure 6.81. Upper-left: 1/0, upper-right: 2/1, lower-left: 3/2, and lower-right: 4/3.

These plots (figures 6.67-6.78) make it clear that the MC does a poor job of describing the # vertices distribution. However, our direct concern was whether or not there was a possible jet multiplicity dependence; i.e. was the discrepancy consistent verses the number of jets such that we could simply scale up the MC to resolve the issue. To this end, we also produced a set of jet multiplicity ratio plots between consecutive bins. Here we still plot the # vertices distribution but each plot represents a $(n+1)/n$ jet multiplicity ratio. For example, "2/1" represents the ratio between the # vertices shapes for ≥ 2 and ≥ 1 jets. Section 9.4 explains the motivation for this observable.

Figure 6.79 and its Data/MC comparison in figures 6.80 show the # vertices comparison where each plot represents a different $(n+1)/n$ jet multiplicity ratio for the electron channel. The results for the muon channel are similarly presented in figures 6.81 (data vs. MC) and 6.80 (data/MC). This observable speaks to the effect of promotion or more directly how well the MC could be use to describe the number of vertices for different jet multiplicities. The basic agreement is decent but less than stellar and past ≥ 3 or 4 vertices the MC would be limited in event size to describe the data. This result prompted us to study this further in order to get derive a method that would address these concerns as outline so far.

Before we describe our handling of the # vertices description and background promotion we consider two profile histogram plots and an additional set of plots dealing with our vertex description. The first (figure 6.83) is a histogram of the jet multiplicity plotted against the average # of quality 12 vertices for data and MC. The second (figure 6.84) is just the flipped version where the x-axis is the number of vertices and the jet multiplicity has been averaged for the profile histogram. Both plots are for the electron channel but

the effect would not be appreciably different in the muon channel. Next we looked at the sum p_T of each vertex ordered in descending values for vertexes #1-5. The first vertex will almost always be the triggered candidate high p_T lepton and this is shown in figures 6.85 and 6.87 for the total inclusive sample for the electrons and muons, respectively. Figures 6.86 (electron channel) and 6.88 (muon channel) shows the sum vertex p_T for vertices 2-5 and our predictions poorly describes the data. Finally we look at the difference between each *non-primary* vertex's z-position (z_{vtx}) with the primary vertex's z-position (z_0). This quantity, $z_0 - z_{vtx}$, is plotted over a wide range for the total inclusive case in figure 6.89 and then for inclusive jet multiplicities 1-4 in figure 6.90 for our electron results. The muons results are presented, likewise, in figures 6.91 and 6.92.

First we note that our jet transverse momentum requirement, $p_T^{jet} > 20\,\text{GeV/c}$, greatly reduces the possible effect of promotion. As noted at the beginning of the section, the promotion background will be heavily biased at low p_T [12]. Therefore, the simplest solution (at the cost of reducing the sample sizes at higher jet multiplicities) would be to just increase the p_T cut. However, with this knowledge we wondered if we could better quantify the number of additional interactions (e.g. via # vertices). We tested setting different p_T cuts to the *vertex* definition. Here the vertex momentum is defined by the sum track momentums with a common vertex. We denote the transverse momentum of the vertex via $\sum p_T^{vtx}$.
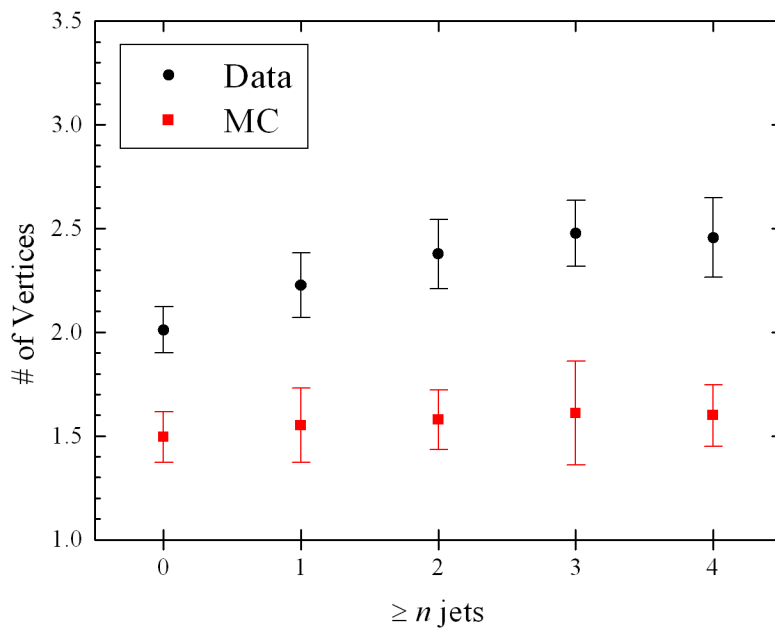
Figure 6.83. Profile histogram for the number of quality 12 vertices verses the jet multiplicity for $W \rightarrow e\nu + \geq n$ jets.
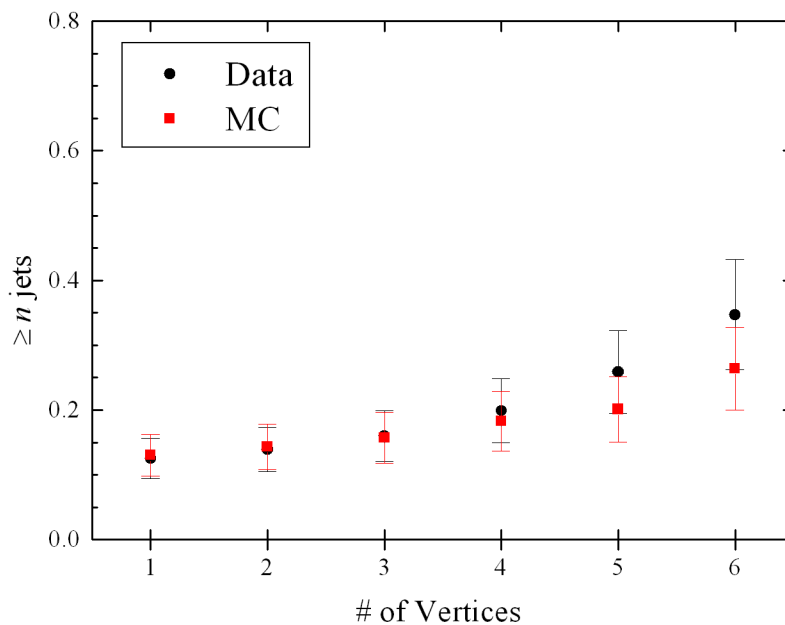
Figure 6.84. Profile histogram for the jet multiplicity verses the number of quality 12 vertices for $W \rightarrow e\nu + \geq n$ jets.
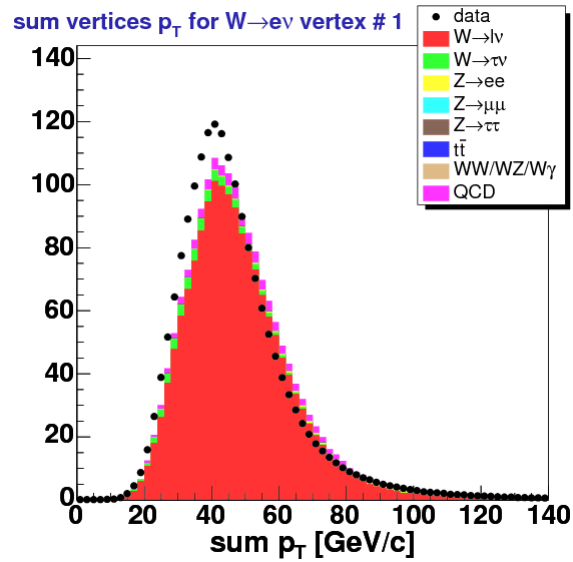
Figure 6.85. Vertex sum p_T $\left(\sum p_T^{vtx}\right)$ for the leading order vertex for $W \to e\nu+ \geq 0$ jets
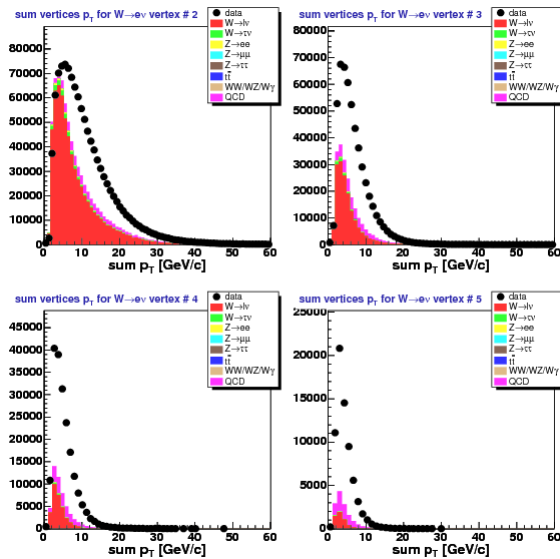
Figure 6.86. Vertex sum p_T $\left(\sum p_T^{vtx}\right)$ for ordered vertexes 2-5 for $W \to e\nu+ \geq 0$ jets
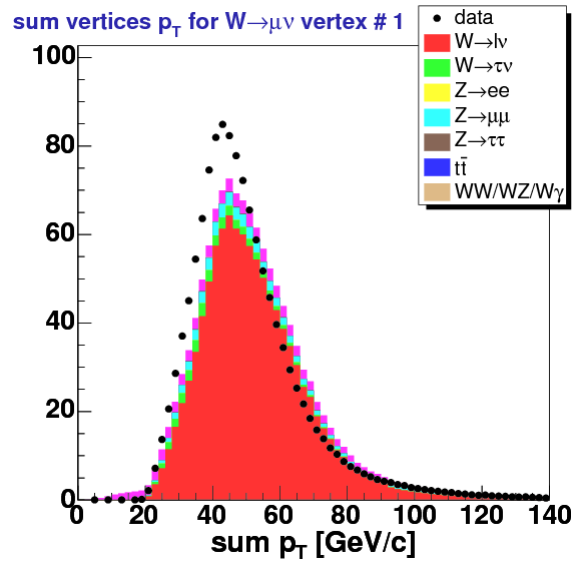
Figure 6.87. Vertex sum p_T ($\sum p_T^{vtx}$) for the leading order vertex for $W \to \mu\nu+ \geq 0$ jets
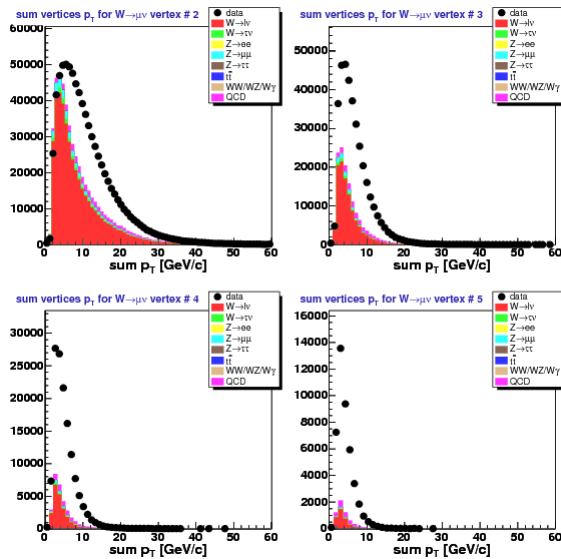
Figure 6.88. Vertex sum p_T ($\sum p_T^{vtx}$) for ordered vertexes 2-5 for $W \to \mu\nu+ \geq 0$ jets
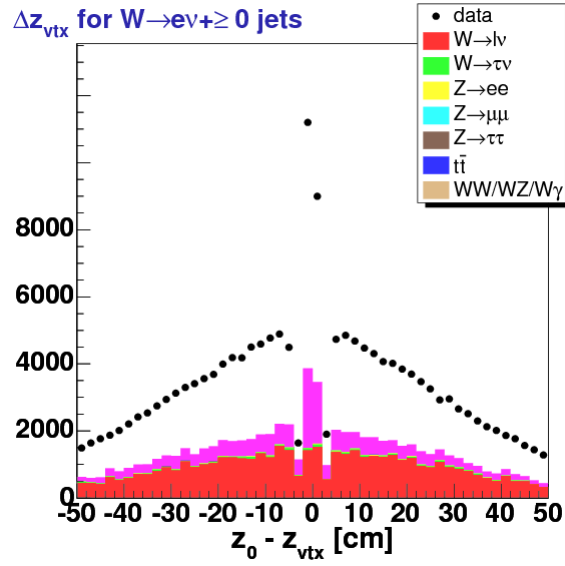
Figure 6.89. $z_0 - z_{vtx}$ for each vertex omitting the primary for $W \to e\nu + \geq 0$ jets
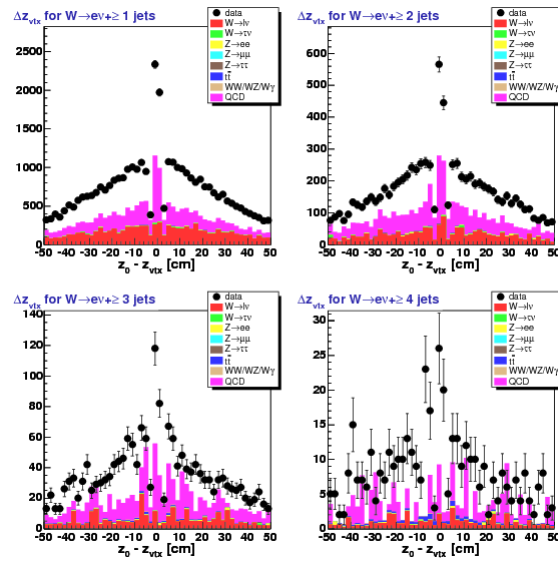
Figure 6.90. $z_0 - z_{vtx}$ for each vertex omitting the primary for $W \to e\nu + \geq 1$-4 jets

In figures 6.93 and 6.94, we present the same number of quality 12 vertices plots broken up into different instantaneous luminosities as done previously in figures 6.61 and 6.62
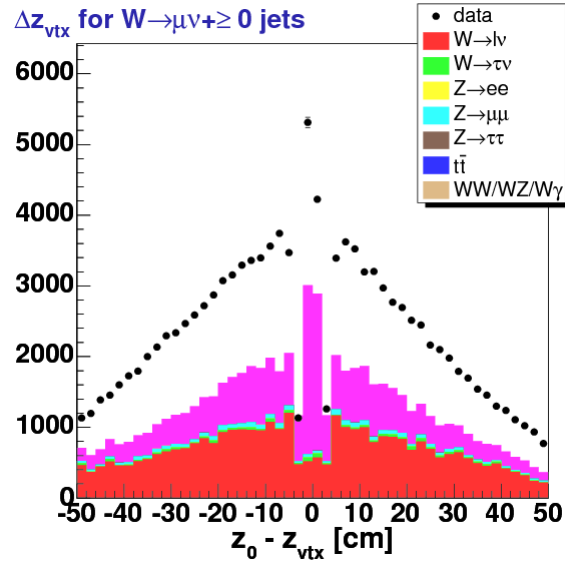
Figure 6.91. $z_0 - z_{vtx}$ for each vertex omitting the primary for $W \to \mu\nu + \geq 0$ jets
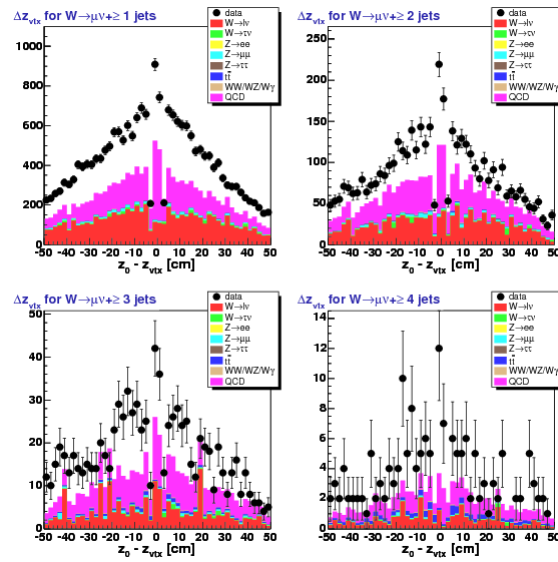
Figure 6.92. $z_0 - z_{vtx}$ for each vertex omitting the primary for $W \to \mu\nu + \geq 1$-4 jets

but with the additional requirement that $\sum p_T^{vtx} > 18$ GeV/c. The limit of 18 GeV/c

was chosen as an upper-limit for testing the sensitivity of this variable as this is the

trigger threshold. The plots with the redefined vertex criteria no longer have the extreme luminosity dependence. In particular this definition makes events with higher number of vertices more meaningful in terms of actually indicating additional activity outside of the triggered lepton. In the case of the electron channel, our lower luminosity cohort $(0\text{-}50\times10^{30}$ cm^{-2}/s$)$ shows a 3 order of magnitude drop between 1 and 3 vertices with the additional $\sum p_T^{vtx}$ cut (see figure 6.93). For the 100-150$\times10^{30}$ cm^{-2}/s cohort, it is a full 2 orders of magnitude between 1 and 3. Contrast this to figure 6.61 where the difference is a factor of 10 for the lower luminosity results and a factor of 2 *increase* for 1 to 3 vertices. The same analysis on the muon channel (contrast figure 6.94 to figure 6.62) yields the same result.

We tested various $\sum p_T^{vtx}$ cuts (8, 10, 15, and 18 GeV/c). We present results for $\sum p_T^{vtx} > 15$ GeV/c and limit the number of vertices in the event to 6 or less. We note that this upper number of vertices cut was chosen to basically make the MC based W acceptance unchanged. Figures 6.95 and 6.96 show the data verses prediction comparison for $W \rightarrow e\nu + \geq n$ jets. Based off of later comparisons with the muon channel, we expect consistent results but omit these plots for brevity. We make a data (i.e. data candidates minus QCD prediction) verses MC (i.e. MC signal+background predictions) in figures 6.97 and 6.98. We then show the $(n+1)/n$ jet multiplicity ratio (compare to the "no cut" versions in Fig. 6.79 and Fig. 6.80) between data components and MC in figure 6.99 and a ratio of said components in 6.100.

Ultimately we found the $\sum p_T^{vtx} > 10$ GeV/c to be optimal (modulo an additional constraint) for describing the data verses MC results and discussion that follow. Figures 6.101 and 6.102 are an updated version of the profile histograms (for $W \rightarrow e\nu + \geq n$

jets) noted before in 6.83 and 6.84 where we have included the $\sum p_T^{vtx} > 10$ GeV/c requirement. With respect to the MC the concern was whether we could adequately describe the effect of additional interactions for our promotion background. This meant having good relative agreement in # vertices for each different jet multiplicity. The limitation (as shown in figures 6.95-6.100) is that the MC starts to do poorly pass the third vertex. However this raised a different question with respect to the data, namely: what was the motivation for keeping events with many additional energetic vertices? Given our new $\sum p_T^{vtx}$ discriminate, we could veto events with high # vertices and thus take a small hit in our data candidate yield and W signal acceptance while removing events that are not descriptive of W+jets.
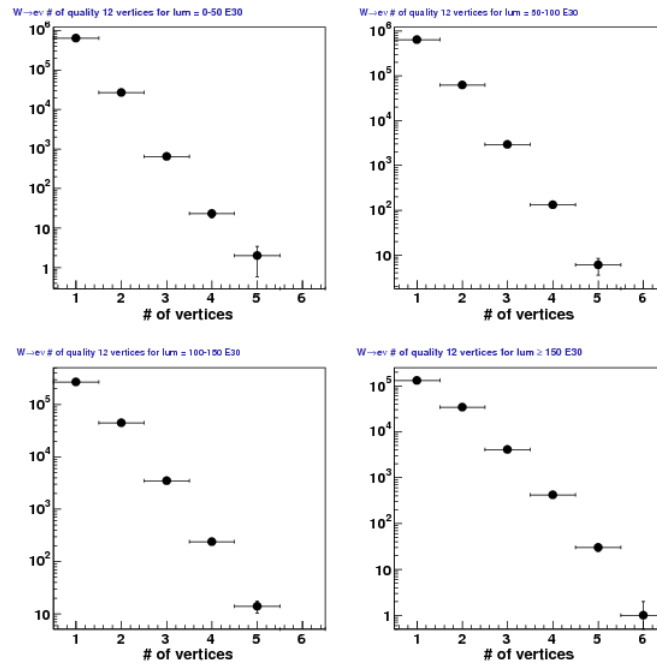
Figure 6.93. # of quality 12 vertices with $\sum p_T^{vtx} > 18$ GeV/c in $W \to e\nu$ Candidates for instantaneous luminosities (in units of $\times 10^{30}$ cm^{-2}/s) of 0-50 (upper-left), 50-100 (upper-right), 100-150 (lower-left), and $\geq$150 (lower-right). Compare to the no $\sum p_T^{vtx}$ cut version in Fig. 6.61
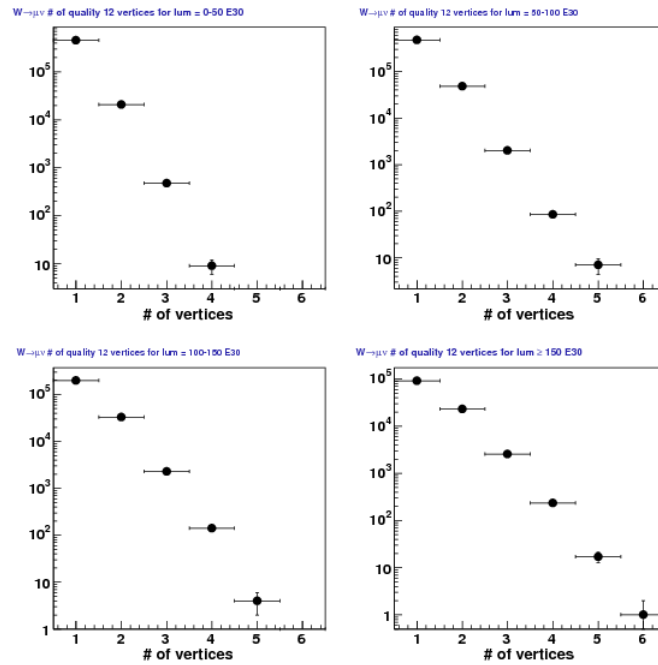
Figure 6.94. # of quality 12 vertices with $\sum p_T^{vtx} > 18$ GeV/c in $W \to \mu\nu$ Candidates for instantaneous luminosities (in units of $\times 10^{30}$ cm^{-2}/s) of 0-50 (upper-left), 50-100 (upper-right), 100-150 (lower-left), and ≥ 150 (lower-right). Compare to the no $\sum p_T^{vtx}$ cut version in Fig. 6.62

308
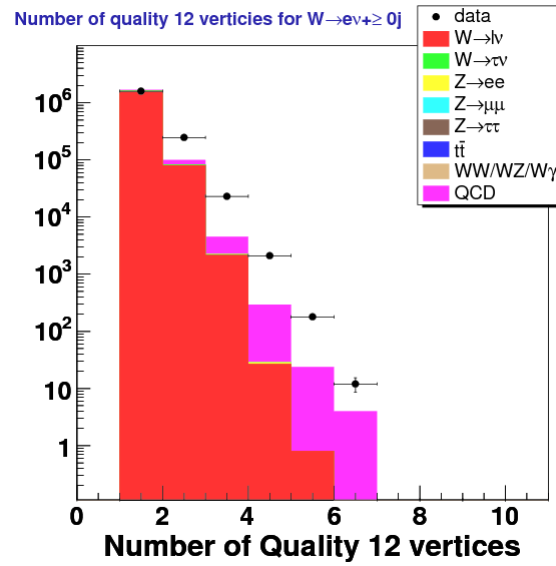
Figure 6.95. # quality 12 vertices (veto >6) with $\sum p_T^{vtx} > 15$ GeV/c for $W \to e\nu+ \geq 0$ jets
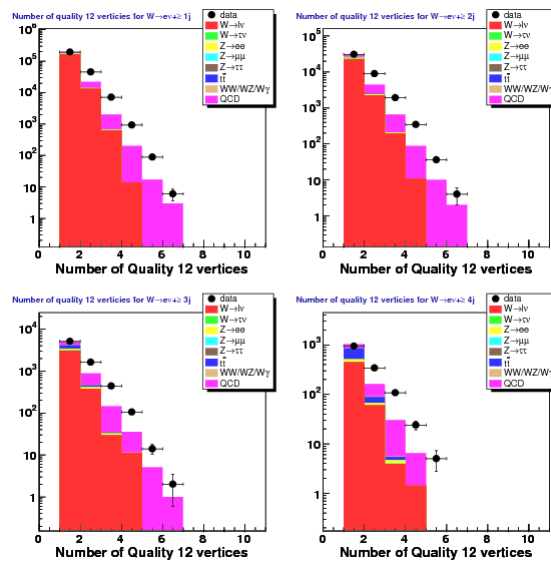
Figure 6.96. # quality 12 vertices (veto >6) with $\sum p_T^{vtx} > 15$ GeV/c for $W \to e\nu+ \geq 1$-4 jets

309
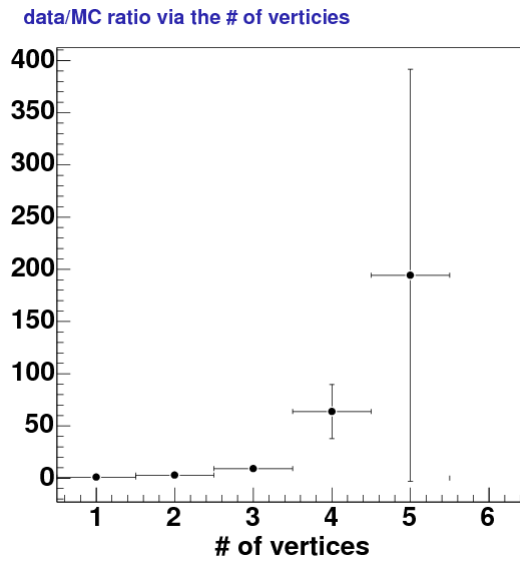
Figure 6.97. (Data-QCD)/MC comparison of # quality 12 vertices (veto >6) with $\sum p_T^{vtx} > 15$ GeV/c for $W \to e\nu+ \geq 0$ jets.
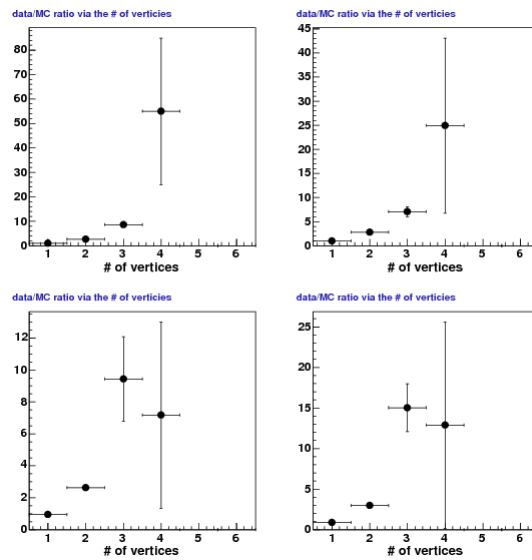
Figure 6.98. (Data-QCD)/MC comparison of # quality 12 vertices (veto >6) with $\sum p_T^{vtx} > 15$ GeV/c for $W \to e\nu+ \geq 1$-4 jets.
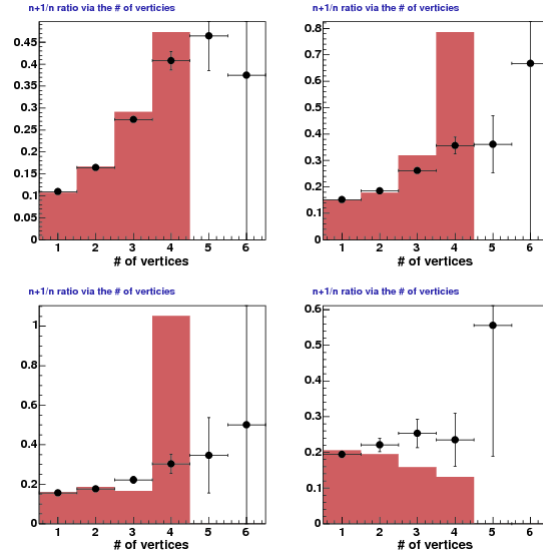
Figure 6.99. $(n+1)/n$ jet multiplicity ratio comparison of # quality 12 vertices (veto >6) with $\sum p_T^{vtx} > 15$ GeV/c for $W \rightarrow e\nu + \geq n$ jets. Here the red histogram represents the MC prediction while the data points represent Data-QCD for each jet multiplicity ratio. Upper-left: 1/0, upper-right: 2/1, lower-left: 3/2, and lower-right: 4/3.

311
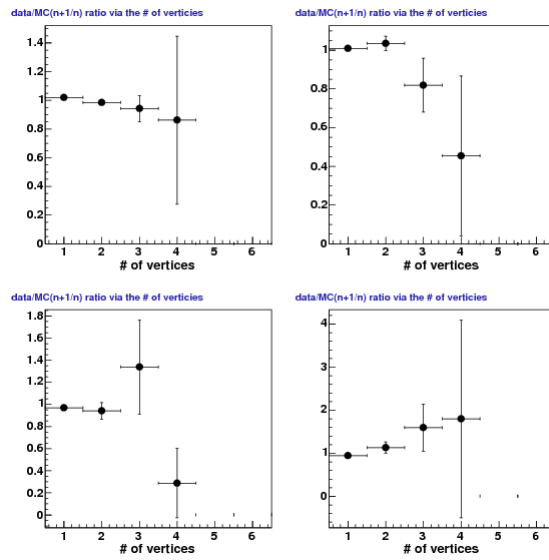
Figure 6.100. Data/MC ratio of the $(n+1)/n$ jet multiplicity ratio comparison of # quality 12 vertices (veto >6) with $\sum p_T^{vtx} > 15$ GeV/c for $W \to e\nu + \geq n$ jets. This is a Data/MC ratio of Fig. 6.99. Upper-left: 1/0, upper-right: 2/1, lower-left: 3/2, and lower-right: 4/3.
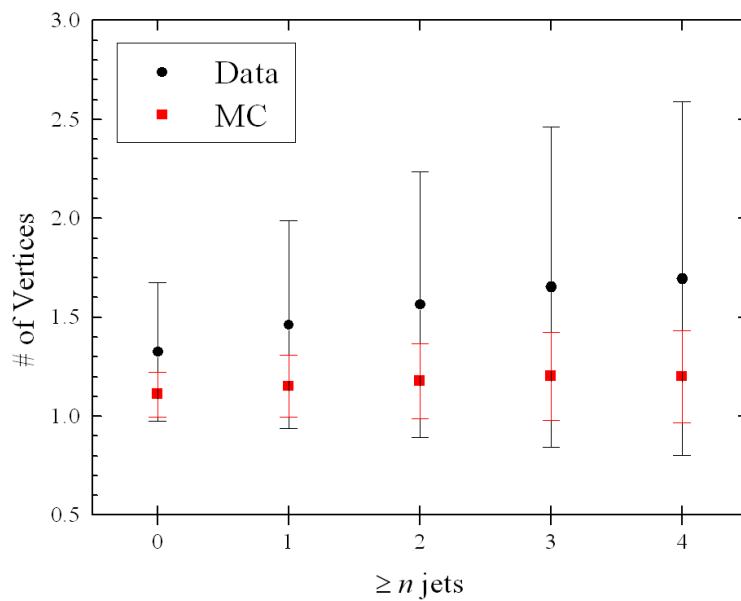
Figure 6.101. Profile histogram for the number of quality 12 vertices with $\sum p_T^{vtx} > 10$ GeV/c verses the jet multiplicity for $W \rightarrow e\nu + \geq n$ jets.
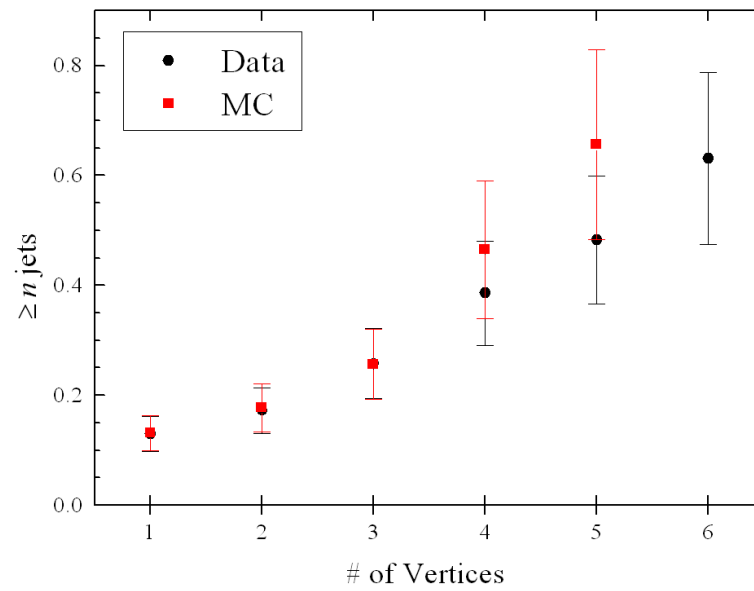
Figure 6.102. Profile histogram for the jet multiplicity verses the number of quality 12 vertices with $\sum p_T^{vtx} > 10$ GeV/c for $W \to e\nu + \geq n$ jets.

$\geq n$ jets	Electron Channel Reduction (%)	Muon Channel Reduction (%)
0	0.8	3.7
1	2.1	7.7
2	3.6	8.0
3	5.2	8.8
4	6.6	7.9

Table 6.8. Data Candidate Event Yield Reduction (%) using $\sum p_T^{vtx} > 10$ GeV/c and # vertices ≤ 3 for $W \rightarrow \ell\nu+ \geq n$ jets

In table 6.8 we show the reduction in the yield of data candidates for both electrons and muons using quality 12 vertices defined with $\sum p_T^{vtx} > 10$ GeV/c after vetoing events with # vertices ≤ 3. In absolute terms, we lose about 16k events in the ≥ 0 jet bin and 94 events for ≥ 4 jets in the electron channel. We also note the that our electron sample shows an obvious linear drop off (approximately 1.45% per inclusive jet). The vertex number veto described here barely effects our acceptance; the largest reduction is in the ≥ 1 jet bin which measures less than 0.7%. The efficiency drop off for muons is larger and constant ($\approx 8\%$) for one or more jet. This likely an artifact of the muon selection process where the # of vertices cut is biased toward cutting fakes (e.g. semi-leptonic decays). This was made explicit in an earlier version of our anti-selection muon procedure which included allowing the impact parameter (d_0) to fail. For example, this gave events with additional vertices that saturated the low $\sum p_T^{vtx}$ spectrum (the phenomena is still noticeable in figure 6.87 below 20 GeV/c).

Figures 6.103 and 6.105 show the $(n+1)/n$ jet multiplicity ratio taking using $\sum p_T^{vtx} >$ 10 GeV/c with a >3 vertices veto for the electron and muon channel, respectively. A data/MC version is also reproduced in figures 6.104 (electrons) and 6.106 (muons). These

jet multiplicity ratio plots show that there is no strong jet dependence or correlation and decent agreement at this stage between data and MC between 1 and 3 vertices.

At this point, we implement a fit of our # vertices distribution between data components and MC. The idea here is to reweight the MC (on subsequent passes in the analysis) so that it has the right profile. In effect, the MC will be corrected additional interactions and we simply fold in the promotion into our background and signal with this reweighting correction. Although we could reweight each vertex bin for each jet multiplicity, an ideal solution is to conduct the fit for the inclusive case and then apply it to the higher jet multiplicities which is feasible based on the results and discussion of figures 6.103-6.106. To do this we produce a plot like figure 6.75 or 6.97 were we have separated the data components from the MC and apply a reweight to the MC based on the ratio between Data and MC (i.e. Data/MC).
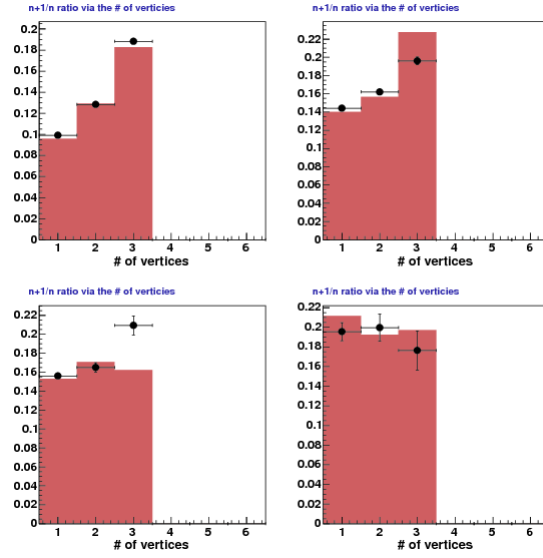
Figure 6.103. $(n+1)/n$ jet multiplicity ratio comparison of # quality 12 vertices (veto >3) with $\sum p_T^{vtx} > 10$ GeV/c for $W \rightarrow e\nu+ \geq n$ jets. Here the red histogram represents the MC prediction while the data points represent Data-QCD for each jet multiplicity ratio. Upper-left: 1/0, upper-right: 2/1, lower-left: 3/2, and lower-right: 4/3.
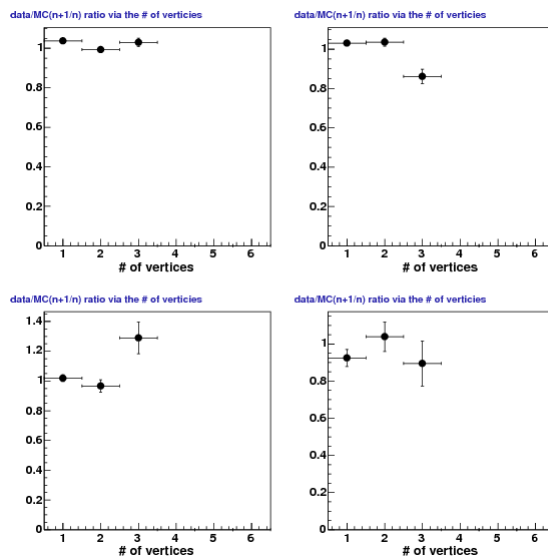
Figure 6.104. Data/MC ratio of the $(n + 1)/n$ jet multiplicity ratio comparison of # quality 12 vertices (veto >3) with $\sum p_T^{vtx} > 10$ GeV/c for $W \rightarrow e\nu+ \geq n$ jets. This is a Data/MC ratio of Fig. 6.103. Upper-left: 1/0, upper-right: 2/1, lower-left: 3/2, and lower-right: 4/3.
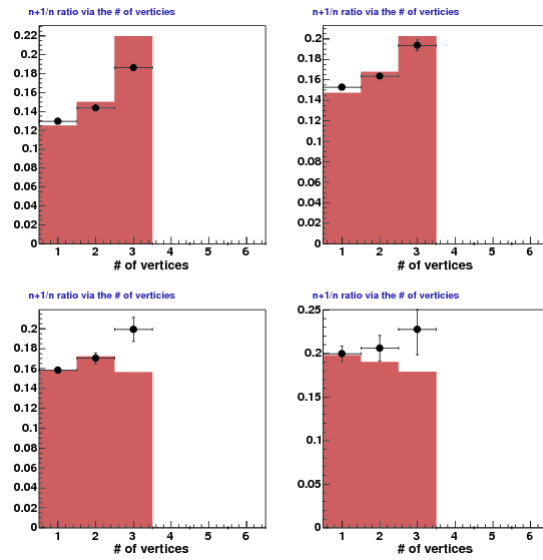
Figure 6.105. $(n+1)/n$ jet multiplicity ratio comparison of # quality vertices (veto >3) with $\sum p_T^{vtx} > 10$ GeV/c for $W \rightarrow \mu\nu + \geq n$ jets. Here the red histogram represents the MC prediction while the data points represent Data-QCD for each jet multiplicity ratio. Upper-left: 1/0, upper-right: 2/1, lower-left: 3/2, and lower-right: 4/3.
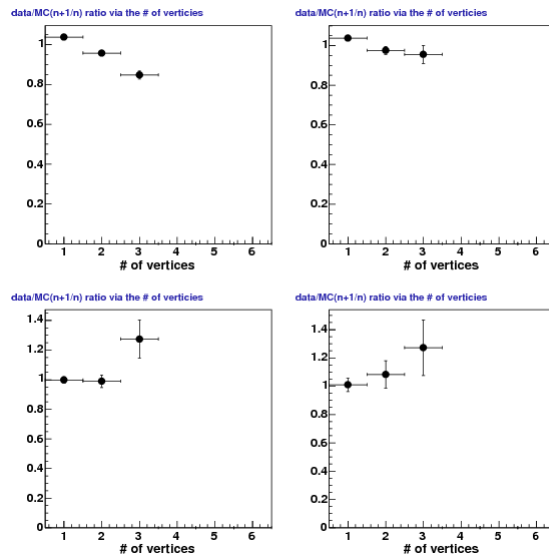
Figure 6.106. Data/MC ratio of the $(n+1)/n$ jet multiplicity ratio comparison of # quality 12 vertices (veto >3) with $\sum p_T^{vtx} > 10$ GeV/c for $W \to \mu\nu+ \geq n$ jets. This is a Data/MC ratio of Fig. 6.105. Upper-left: 1/0, upper-right: 2/1, lower-left: 3/2, and lower-right: 4/3.

There are a few important details to this vertex "fitting" and reweighting. The first is with respect to our vertex fitting procedure and reweighting is that the QCD background needs to be further split into components. Recall that the QCD estimation comes from a template made from the anti-lepton selection of the data *minus the MC contamination* from the same anti-lepton selection. If we ignore this the fitting iterations start to be divergent on the third vertex relative to the first two and we will always be systematically off in trying to describe the # vertices distribution. Thus the vertex reweighting correction (w(#vertex)) is the weight applied to all jet multiplicities for the # number of vertices using the number of events in the total inclusive (≥ 0) jet multiplicity. We define our base reweighting factor, w_0(# vertex), as

$$(6.3) \qquad\qquad w_0(\#\text{vertex}) = \frac{N_{\text{data}} - N_{\text{QCD−data}}}{N_{\text{MC}} + N_{\text{QCD−MC}}}$$

Here, N_{data} is the number of candidate W events in data, $N_{\text{QCD−data}}$ is the estimated QCD background without the MC contamination subtraction, N_{MC} is the sum of the signal W MC and all the MC based backgrounds, and $N_{\text{QCD−MC}}$ is the estimated contamination from non-QCD (i.e. MC) sources. For convenience we have suppressed the vertex dependence of these variables. Equation 6.3 needs a renormalization scale factor (see equation 6.4) which we now elaborate on.

The second vertex fitting detail is that the procedure invites re-running the analysis a few times to make sure it is stable. The reason for this is that our background fitting estimation (see section 6.4) has the potential to shift a bit after we reweight the MC. The result is that the agreement will never be perfect but a first pass should lock it in to a good agreement with marginal improvements with subsequent re-runnings of the analysis

with updated vertex weight values on the MC. In particular, equation 6.3 can acquire an additional degree of freedom where the number of events in the MC are not constrained in our vertex fit calculation and part of our desired weights are absorbed in our general background fitting. Our solution is to simply enforce the total number of events in the total inclusive case in the total MC sample. This effectively checks that the normalization of MC events is consistent iteration to iteration. We apply a correction factor using our initial weights $(w_0(k))$ of equation 6.3 to get our final normalized vertex weight

$$(6.4) \qquad w(\#\text{vertex}) = \left(\frac{\sum\limits_{k=1}^{3} N_{\text{MC}}}{\sum\limits_{k=1}^{3} w(k) N_{\text{MC}}} \right) w_0(\#\text{vertex})$$

where k is the # of vertices. This scale factor is by construction close to unity but it is important in order to achieve stability over multiple fitting iterations and between both lepton channels.

$\geq n$ jets	Vertex 1	Vertex 2	Vertex 3
0	0.8032	2.2180	6.3950
1	0.8336	2.2098	6.6951
2	0.8540	2.2907	6.2240
3	0.8669	2.1801	8.1484
4	0.8070	2.2794	6.9911
Average	0.8329	2.2356	6.8907
Std. Dev.	0.0281	0.0475	0.7616

Table 6.9. MC reweighting correction for the number of quality 12 vertices with $\sum p_T^{vtx} > 10$ GeV/c for $W \to e\nu + \geq n$ jets

In tables 6.9 and 6.10 we present our final results after 4 full iterations for our MC reweighting correction factors for # vertices (1-3) and for each inclusive jet multiplicity.

$\geq n$ jets	Vertex 1	Vertex 2	Vertex 3
0	0.8425	2.1120	4.9630
1	0.8723	2.0297	4.4379
2	0.9103	1.9742	3.7948
3	0.9275	1.9336	4.1604
4	0.9480	2.0535	6.0549
Average	0.9001	2.0206	4.6822
Std. Dev.	0.0426	0.0694	0.8778

Table 6.10. MC reweighting correction for the number of quality 12 vertices with $\sum p_T^{vtx} > 10$ GeV/c for $W \to \mu\nu + \geq n$ jets

The former is our electron results while the latter gives the muon channel results. We only use the total inclusive (≥ 0 jets) case to reweight the MC but present results for the higher jet multiplicities as well. In each table, as an added convenience for comparison and consistency checking, are the (unweighted) average and standard deviation (abbreviated "Std. Dev.") for each inclusive jet multiplicity for each vertex number.

It is important to make sure that our fitting procedure in converging well and to this end we show the MC reweighting correction results for each vertex. Table 6.11 gives the results over 4 fitting iterations for $W \to e\nu + \geq 0$ jets while table 6.12 likewise gives the results for $W \to \mu\nu + \geq 0$ jets. Both lepton channel results converge quickly; more so with the muon channel which has a smaller QCD background estimation and MC contamination and thus less interplay between our background estimation template fitting and our vertex reweighting procedure described here.

Fitting Iteration	Vertex 1	Vertex 2	Vertex 3
1st	0.8201	2.286	6.724
2nd	0.8077	2.231	6.457
3rd	0.8032	2.218	6.395
4th	0.8034	2.219	6.449
Average	0.8086	2.238	6.506
Std. Dev.	0.008	0.032	0.148

Table 6.11. MC reweighting correction for the number of quality 12 vertices with $\sum p_T^{vtx} > 10$ GeV/c for $W \to e\nu+ \geq 0$ jets over 4 fitting iterations

Fitting Iteration	Vertex 1	Vertex 2	Vertex 3
1st	0.8337	2.099	4.882
2nd	0.8445	2.113	4.778
3rd	0.8425	2.112	4.963
4th	0.8427	2.111	4.866
Average	0.8409	2.109	4.872
Std. Dev.	0.005	0.007	0.076

Table 6.12. MC reweighting correction for the number of quality 12 vertices with $\sum p_T^{vtx} > 10$ GeV/c for $W \to \mu\nu+ \geq 0$ jets over 4 fitting iterations

Finally, we want to resurvey our various # vertices related observables we began with at the start of this section and note the improvement and overall consistency in our results. First, we note that the Data verses MC mismatch (see figures 6.117 and 6.119 for the electron and muon channel, respectively), the variation across each jet multiplicity (table 6.9 for the electrons and 6.10 for the muons), and the variation between multiple iterations of fitting, reweighting, and re-running (tables 6.11 and 6.12) are all on the order of 2.5% for the first vertex. The conclusion is that method is stable with respect to our reweighting procedure over 3 iterations. We continue this discussion of the effect of our reweighting on our cross-section in section 8.4 (page 376) where we give our systematic with respect to this procedure and our results.

As a crosscheck we also looked directly at the relative change between no vertex reweighting (original/default) and with the latest set of vertex corrections in the first and second leading jet p_T cross-sections. For reference, the final cross-section plots are presented in figures 9.9-9.10 (electrons) and 9.13-9.14 (muons) with their description starting on page 424. We construct the relative difference observable $(\sigma_{vtx} - \sigma_{org})/\sigma_{vtx}$ where σ_{org} refers to the non-reweighted cross-section while σ_{vtx} is the fully reweighted. For our purpose here we present only the electron channel ($W \rightarrow e\nu$) although the trend is the same in the muon channel. The result for the first leading jet p_T is presented in figure 6.107 while the second leading jet p_T is shown in 6.108. The relative error ($\Delta\sigma/\sigma$) for σ_{vtx} is use as error bar for the observable. We see a relatively flat distribution that is consistent with our quoted 4.5% systematic of section 8.4.

In figures 6.109 and 6.110 we show our final results for the # vertices distribution for $W \rightarrow e\nu+ \geq n$ jets using our $\sum p_T^{vtx} > 10$ GeV/c requirement where we veto events with more than 3 vertices. Likewise, the $W \rightarrow \mu\nu+ \geq n$ jets results are shown in figures 6.111 and 6.112. A simplified version of these plots with the data and MC components put together are shown in figures 6.113 and 6.114 (electrons) and 6.115 and 6.116 (muons). The ratio of the data components to the MC are presented in figures 6.117 and 6.118 for the electron channel as well as 6.119 and 6.120 for the muon channel. The $(n+1)/n$ jet multiplicity ratio for the electron channel was already shown in figure 6.103 (data verses MC) and in figure 6.104 (data/MC ratio). In the same manner, the muon version of these plots are given in figures 6.105 (data verses MC) and in figure 6.106 (data/MC ratio).
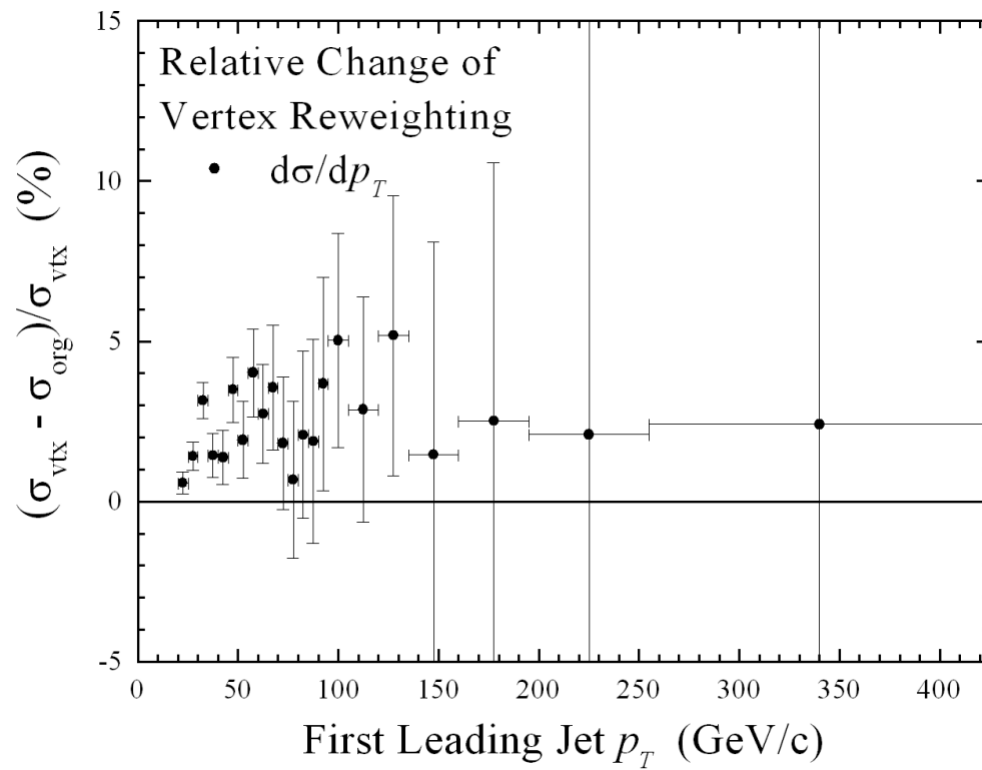
Figure 6.107. Relative change (%) in the first leading jet p_T for $W \rightarrow e\nu+ \geq 1$ jets. σ_{org} refers to the non-reweighted cross-section while σ_{vtx} is the fully reweighted. Note that the relative difference $((\sigma_{vtx} - \sigma_{org})/\sigma_{vtx})$ has been converted into a percentage and the error shown is the relative Poisson uncertainty on σ_{vtx}.
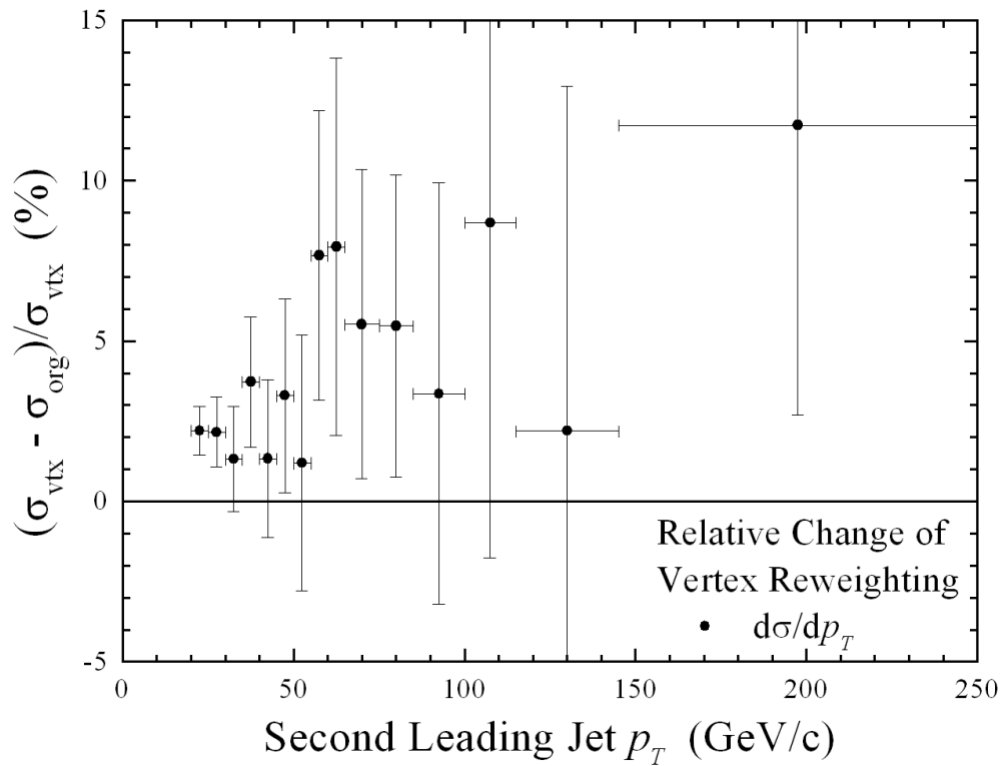
Figure 6.108. Relative change (%) in the second leading jet p_T for $W \rightarrow e\nu+ \geq 2$ jets. σ_{org} refers to the non-reweighted cross-section while σ_{vtx} is the fully reweighted. Note that the relative difference $((\sigma_{vtx} - \sigma_{org})/\sigma_{vtx})$ has been converted into a percentage and the error shown is the relative Poisson uncertainty on σ_{vtx}.
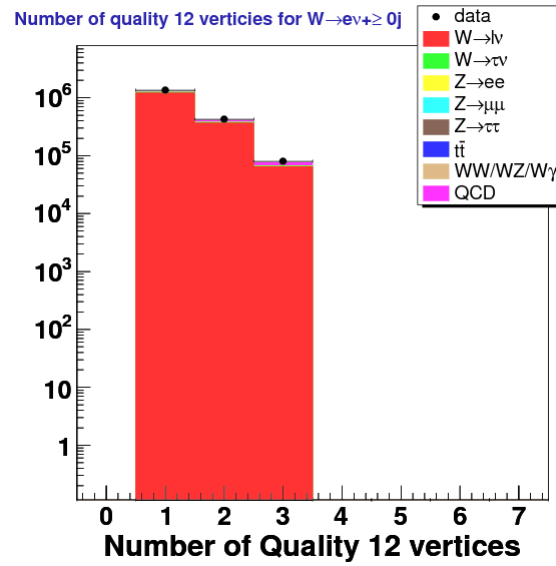
Figure 6.109. # quality 12 vertices with $\sum p_T^{vtx} > 10$ GeV/c for $W \rightarrow e\nu+ \geq 0$ jets
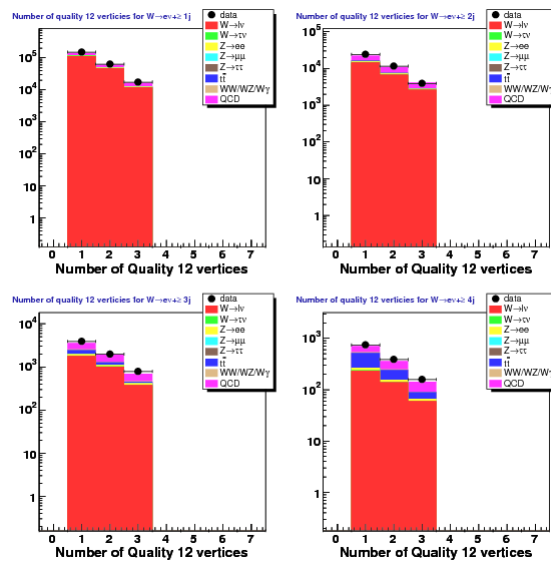
Figure 6.110. # quality 12 vertices with $\sum p_T^{vtx} > 10$ GeV/c for $W \rightarrow e\nu+ \geq 1\text{-}4$ jets
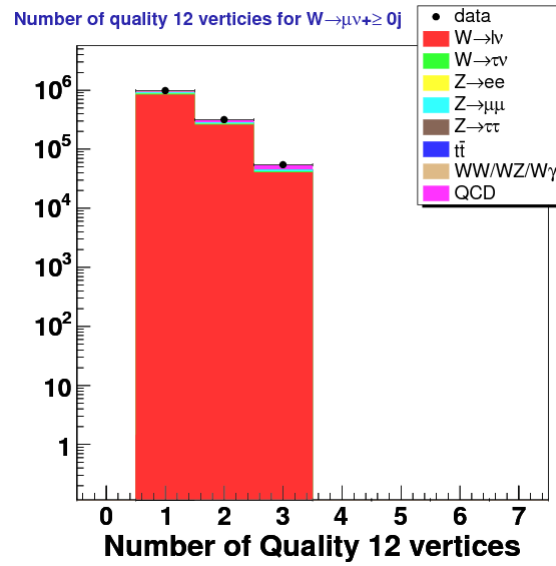
Figure 6.111. # quality 12 verticies with $\sum p_T^{vtx} > 10$ GeV/c for $W \to \mu\nu+ \geq 0$ jets
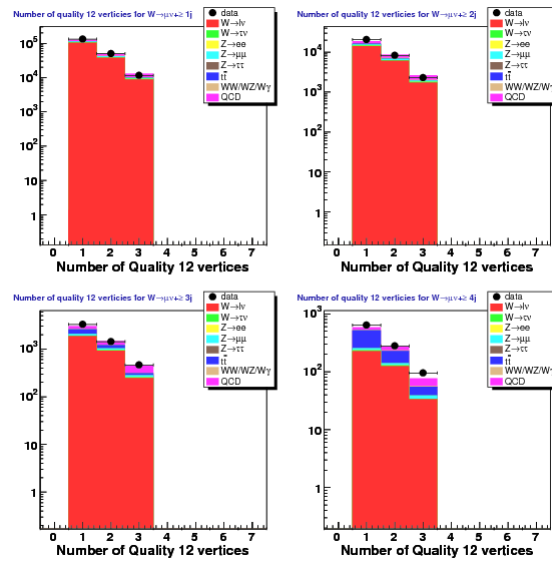
Figure 6.112. # quality 12 verticies with $\sum p_T^{vtx} > 10$ GeV/c for $W \to \mu\nu+ \geq$ 1-4 jets
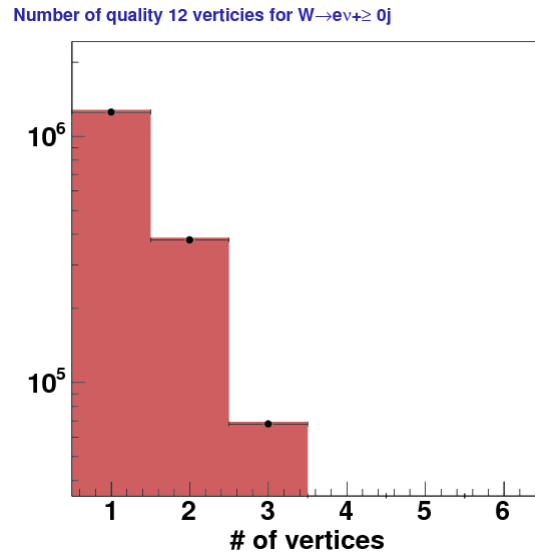
Figure 6.113. # quality 12 vertices with $\sum p_T^{vtx} > 10$ GeV/c for $W \rightarrow e\nu+ \geq 0$ jets. We veto events with more than 3 vertices. Here the red histogram represents the sum MC predictions of figure 6.109 while the data points represent Data-QCD
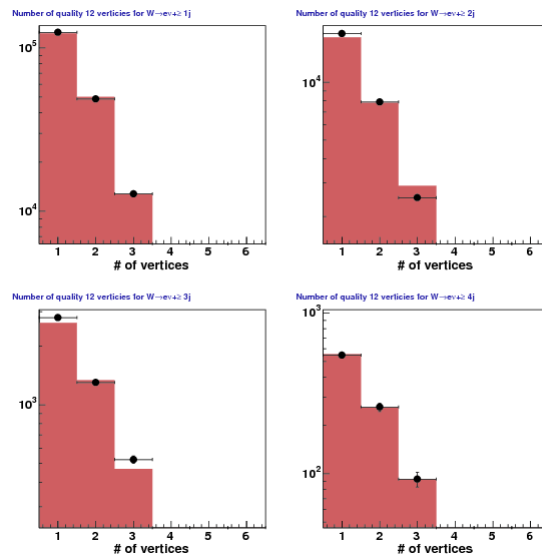
Figure 6.114. # quality 12 vertices with $\sum p_T^{vtx} > 10$ GeV/c for $W \rightarrow e\nu+ \geq 1$-4 jets. We veto events with more than 3 vertices. Here the red histogram represents the sum MC predictions of figure 6.110 while the data points represent Data-QCD
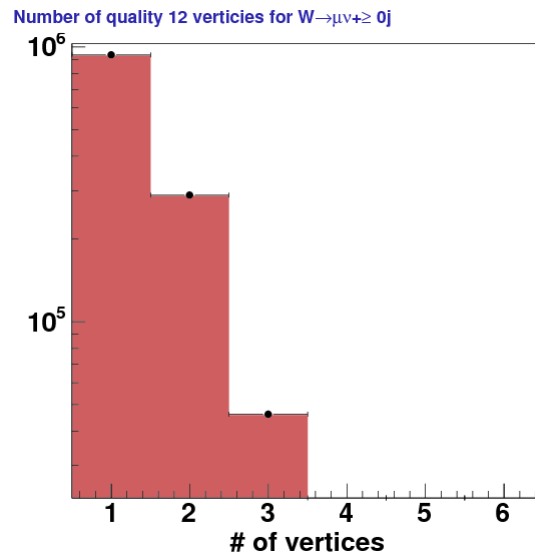
Figure 6.115. # quality 12 vertices with $\sum p_T^{vtx} > 10$ GeV/c for $W \to \mu\nu+ \geq 0$ jets. We veto events with more than 3 vertices. Here the red histogram represents the sum MC predictions of figure 6.111 while the data points represent Data-QCD
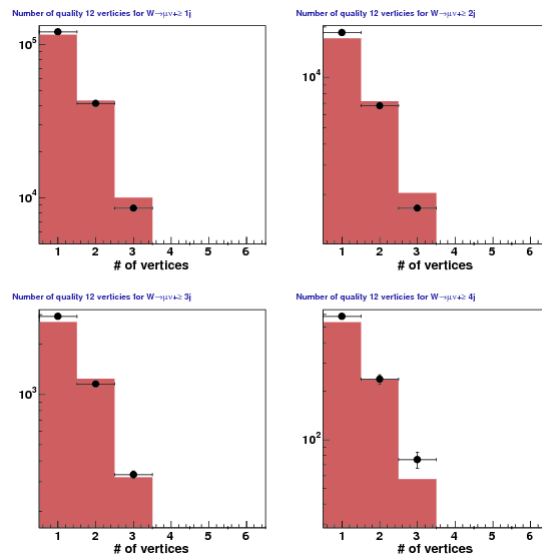
Figure 6.116. # quality 12 vertices with $\sum p_T^{vtx} > 10$ GeV/c for $W \to \mu\nu+ \geq 1$-4 jets. We veto events with more than 3 vertices. Here the red histogram represents the sum MC predictions of figure 6.112 while the data points represent Data-QCD

331
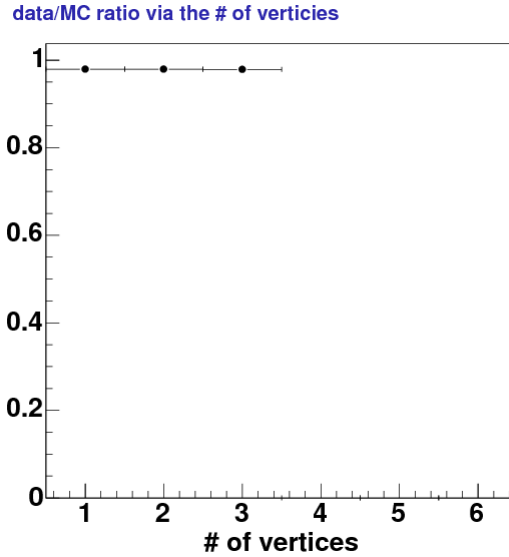
Figure 6.117. (Data-QCD)/MC comparison of # quality 12 vertices with $\sum p_T^{vtx} > 10$ GeV/c for $W \to e\nu + \geq 0$ jets. We veto events with more than 3 vertices. This is a ratio plot of Fig. 6.113.

As final cross check we also looked our two vertex related observables: the sum vertex transverse momentum $(\sum p_T^{vtx})$ for ordered vertexes 1-3 in the total inclusive case and the difference in the z-position between all non-primary vertices to the primary $(z_0 - z_{vtx})$ for all jet multiplicities. The non-reweighted no vertex cut/veto plots were given in figures 6.85-6.92. The post vertex reweighting $\sum p_T^{vtx}$ plots for $W \to e\nu + \geq 0$ jets are in figure 6.121 (leading vertex) and figure 6.122 (ordered vertexes 2-3). Likewise, the results for $W \to \mu\nu + \geq 0$ jets are given in figures 6.123 and 6.124. The updated $z_0 - z_{vtx}$ plots are shown in figures 6.125 and 6.126 for $W \to e\nu + \geq 0$ jets and ≥ 1-4 jets, respectively. The same version of these plots is show for the muon channel in figures 6.127 and 6.128, respectively. We note that the agreement is good and there are no signs of bias.
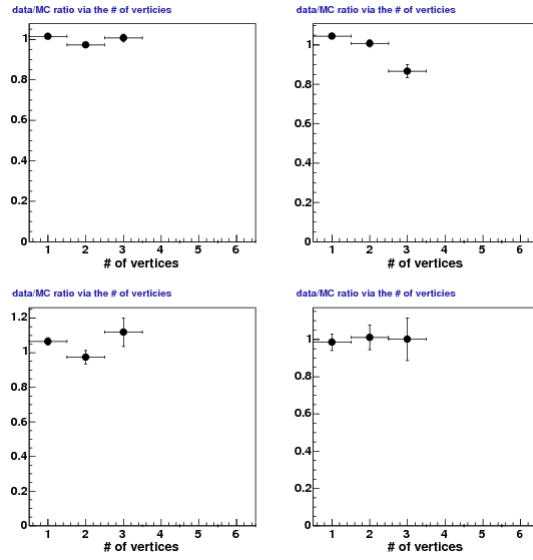
Figure 6.118. (Data-QCD)/MC comparison of # quality 12 vertices with $\sum p_T^{vtx} > 10$ GeV/c for $W \to e\nu+ \geq$1-4 jets. We veto events with more than 3 vertices. This is a ratio plot of Fig. 6.114.
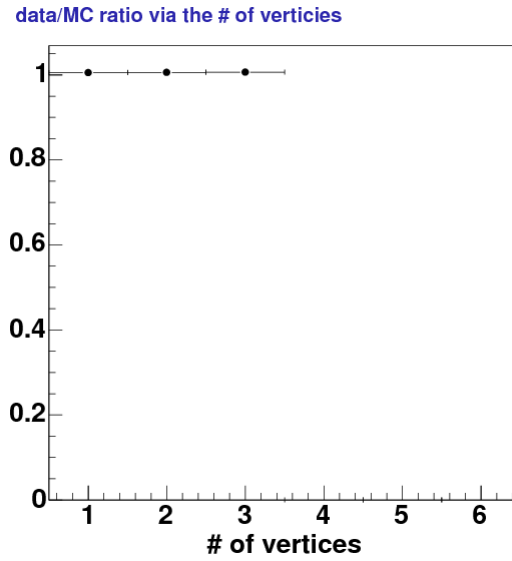
Figure 6.119. (Data-QCD)/MC comparison of # quality 12 vertices with $\sum p_T^{vtx} > 10$ GeV/c for $W \to \mu\nu+ \geq$0 jets. We veto events with more than 3 vertices. This is a ratio plot of figure 6.115.
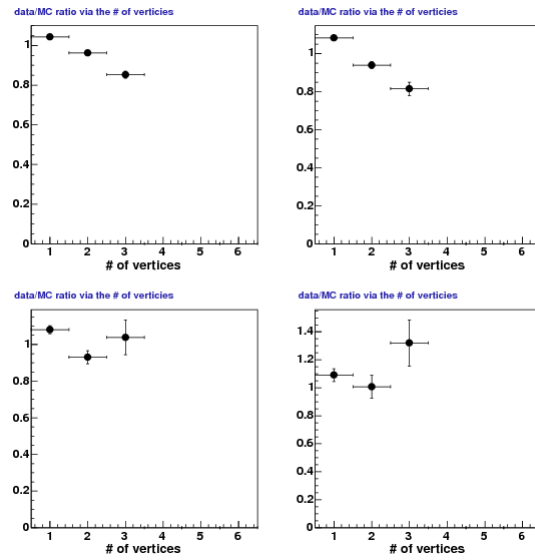
Figure 6.120. (Data-QCD)/MC comparison of # quality 12 vertices with $\sum p_T^{vtx} > 10$ GeV/c for $W \to \mu\nu+ \geq$1-4 jets. We veto events with more than 3 vertices. This is a ratio plot of figure 6.116.
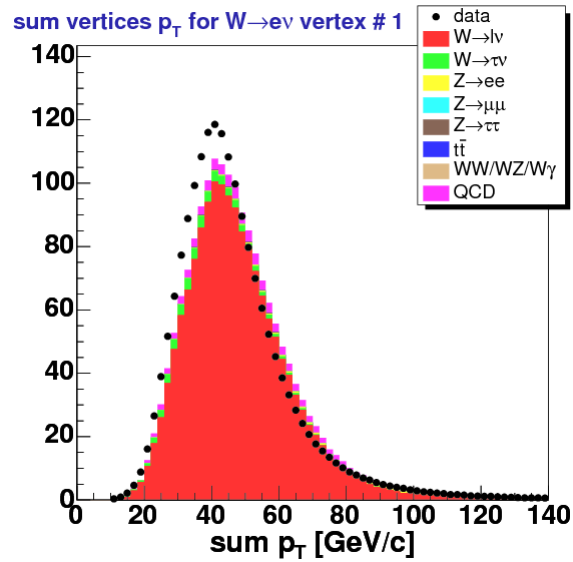
Figure 6.121. Vertex sum p_T ($\sum p_T^{vtx}$) for the leading order vertex for $W \to e\nu + \geq 0$ jets with $\sum p_T^{vtx} > 10$ GeV/c.
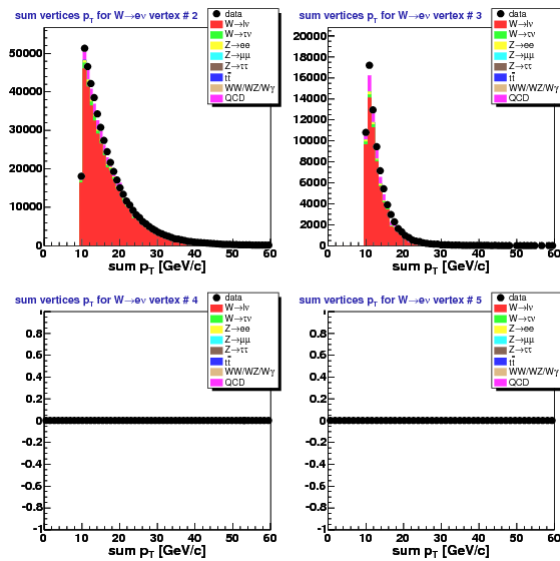
Figure 6.122. Vertex sum p_T ($\sum p_T^{vtx}$) for ordered vertexes 2-3 for $W \to e\nu + \geq 0$ jets with $\sum p_T^{vtx} > 10$ GeV/c and vertexes 4-5 vetoed
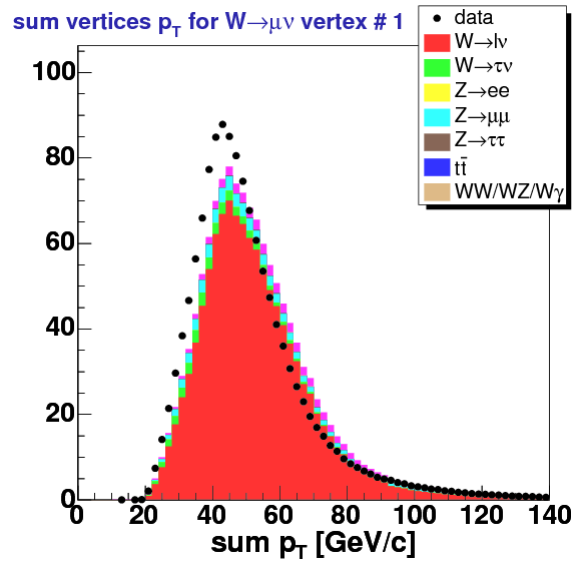
Figure 6.123. Vertex sum p_T ($\sum p_T^{vtx}$) for the leading order vertex for $W \to \mu\nu +\geq 0$ jets with $\sum p_T^{vtx} > 10$ GeV/c.
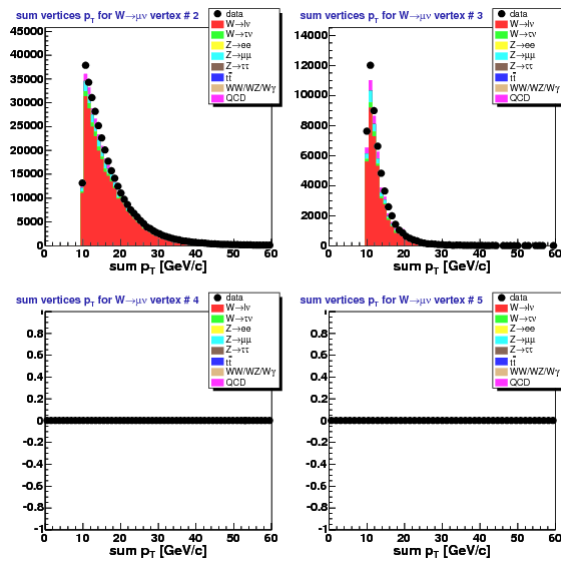
Figure 6.124. Vertex sum p_T ($\sum p_T^{vtx}$) for ordered vertexes 2-3 for $W \to \mu\nu +\geq 0$ jets with $\sum p_T^{vtx} > 10$ GeV/c and vertexes 4-5 vetoed
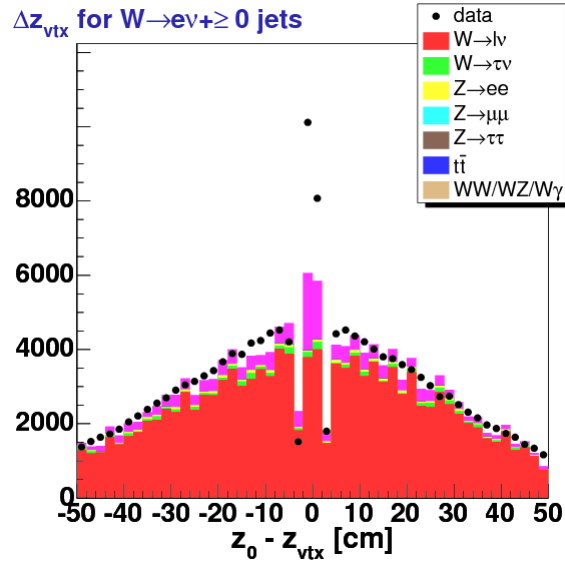
Figure 6.125. $z_0 - z_{vtx}$ for each vertex omitting the primary for $W \to e\nu+ \geq 0$ jets with $\sum p_T^{vtx} > 10$ GeV/c.
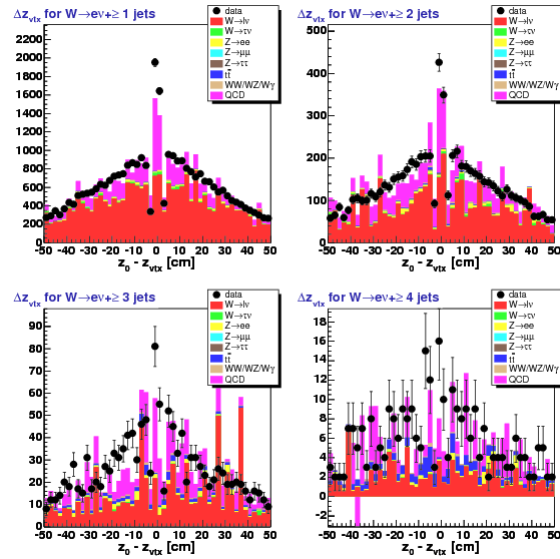
Figure 6.126. $z_0 - z_{vtx}$ for each vertex omitting the primary for $W \to e\nu+ \geq$1-4 jets with $\sum p_T^{vtx} > 10$ GeV/c.
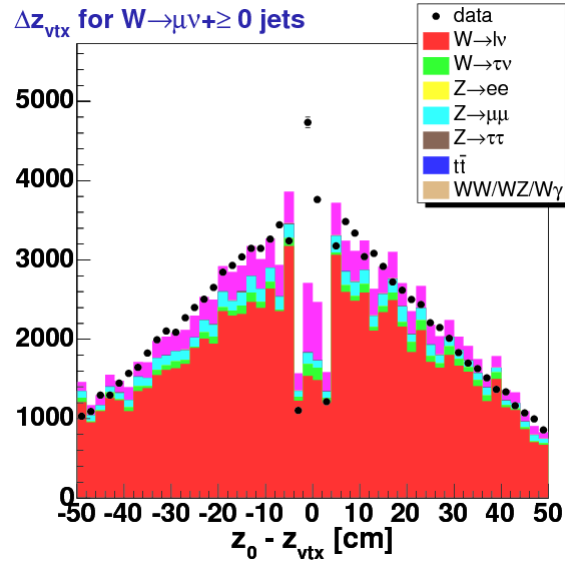
Figure 6.127. $z_0 - z_{vtx}$ for each vertex omitting the primary for $W \to \mu\nu+ \geq 0$ jets with $\sum p_T^{vtx} > 10$ GeV/c.
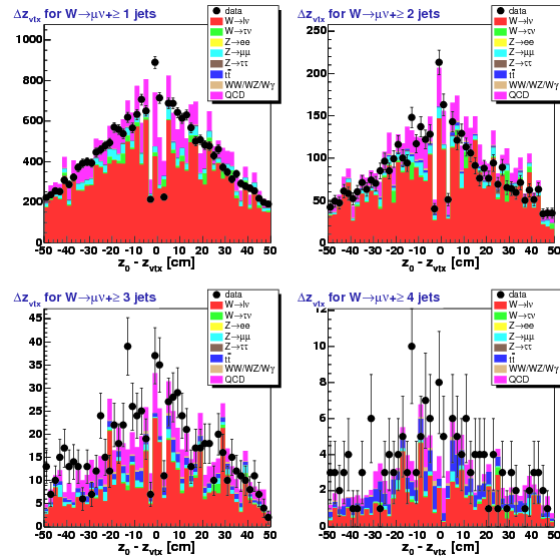
Figure 6.128. $z_0 - z_{vtx}$ for each vertex omitting the primary for $W \to \mu\nu+ \geq$1-4 jets with $\sum p_T^{vtx} > 10$ GeV/c.

CHAPTER 7

Acceptance and Efficiency

In this chapter we describe our W+jets acceptance and lepton efficiencies. These will be used in our final cross-section definition in section 9.1. Although the procedure is straightforward there are several details that are worth keeping in mind. The first is that our acceptance in addition to having a detector dependence based on the lepton sub-detector type (i.e. CEM, CMUP, CMX-Arch, and CMX-Mini) has the potential to have a jet multiplicity dependence as well.

Another acceptance issue is the potential bias due to the $W + n$p Alpgen MC and the fact that we do not know the *a priori* cross-section. The absolute cross-section is irrelevant but technically the relative weight between the n parton samples could bias the result and we wish to avoid this. We explain our solution to this in section 7.2 after giving an overview of the general procedure in 7.1.

A different acceptance concern deals with our desire to produce a more theory friendly cross-section (see section 9.1 for details). In additional to the typical "production level" acceptance, we define a reduced acceptance in section 7.4. Our nominal results are shown in section 7.3 while our modified reduced acceptance is presented in section 7.5.

Section 7.6 present our efficiency results for central (CEM) electrons and (CMUP and CMX) muons. Here the only concern is correctly apply the various lepton efficiencies for each run period with the corresponding luminosity. Finally in section 7.7 we describe how we combine the luminosity (L), the acceptance (A), and total efficiency (ϵ) in to a

final effective luminosity ($LA\epsilon$) by taking into account the lepton, jet multiplicity, and run period dependence.

7.1. Acceptance Procedure

Our acceptance procedure is straightforward. We use our signal MC, Alpgen $W+n$p, to systematically run through our W selection cuts and see what fraction of the generated number of events are accepted. As noted in chapter 4 our W selection cuts take on the basic kinematic and geometric cuts on the triggered lepton and missing energy in addition to some event level vetos (e.g. no cosmics). However, the effect of trigger as well as lepton reconstruction and identification are categorized as efficiencies and are measured with the data as noted later in section 7.6.

We can refer to the acceptance of a cut or a group of sequential cuts together by taking the quotient of the number of events accepted (passed) verses the number of events before cutting. For example, let (cut 1) and (cut 2) be two sequential cuts needed for the signal acceptance. Let $N(\text{cut 1})$ and $N(\text{cut 2})$ represent the number of events that pass the corresponding cut. Then the acceptance of (cut 2) relative to (cut 1) is

$$(7.1) \qquad\qquad A(\text{cut 2}) = \frac{N(\text{cut 2})}{N(\text{cut 1})}$$

and if (cut 1) really represents the first cut then trivially,

$$(7.2) \qquad\qquad A(\text{cut 1}) = \frac{N(\text{cut 1})}{N(\text{GEN})}$$

where $N(\text{GEN})$ is the number of events generated for the MC sample. Assuming the cuts are taken in a consistent order one can denote the total acceptance of two sets of cuts

by simply taking the product (i.e. the acceptance is homomorphic). Continuing with our examples from equations 7.1 and 7.2, let $A(\text{cut } 1)$ and $A(\text{cut } 2)$ be the relative acceptances for two sequential sets of cuts. Then

$$(7.3) \qquad A(\text{cut } 1 + 2) \;=\; A(\text{cut } 1)A(\text{cut } 2)$$

$$(7.4) \qquad A(\text{cut } 1 + 2) \;=\; \left(\frac{N(\text{cut } 1)}{N(\text{GEN})}\right)\left(\frac{N(\text{cut } 2)}{N(\text{cut } 1)}\right)$$

$$(7.5) \qquad A(\text{cut } 1 + 2) \;=\; \frac{N(\text{cut } 2)}{N(\text{GEN})}$$

where $A(\text{cut } 1 + 2)$ is the combined acceptance for both sets of cuts.

For reasons which will become clear in the next section, we define the p number of partons sample acceptance for j *exclusive* number of jets as $A_p(j)$. For our conveyance, we can omit the j jet dependence for A_p and our exclusive and inclusive jet multiplicity (parton depenedence removed) total acceptance. We do this for both electrons (i.e. candidate tight CEM electrons) and muons and have the ability to divide the muons into their respective sub-detector types (candidate tight CMUP, CMX-Arch, and CMX-Mini muons). These parton and jet dependent acceptances are shown later in tables 7.14-7.17.

| | $W \to e\nu$ | $W \to \mu\nu$ |
n jets	$N(\text{GEN})$	$N(\text{GEN})$
0	1524842	1412970
1	1424120	1301665
2	1146287	1187073
3	651802	779158
4	251888	331232

Table 7.1. Number of MC events generated ($N(\text{GEN})$) summed over all parton samples for each inclusive jet multiplicity in $W \to \ell\nu + \geq n$ jets

Finally in this section, we present the raw numbers for our acceptance calculation. Due to the need to be independent of any *ad hoc* scaling of the relative p parton sample we do not use these numbers directly but follow the definition and procedure outlined in the next section. Table 7.1 gives the number of events generated summed over all the parton MC samples for each inclusive jet multiplicity for both the electron and muon channel. In other words,

$$(7.6) \qquad\qquad N(\text{GEN}, n) = N(\text{GEN}) \equiv \sum_{\forall p} N_p^{\text{GEN}}$$

where $N_p^{\text{GEN}} = N_p^{\text{GEN}}(n)$ is the number of events generated via $W + p$ parton MC with $\geq n$ jets. We note that these are the proper number of events generated and that our MC selection does not have any good run list requirement as was noted in section 3.3. Table 7.2 defines the name of each cut which will be used in tables 7.3-7.7 which serve as a raw cut-by-cut breakdown of the acceptance for each lepton sub-detector type.

Cut Label (X)	Cut Definition for A(X)
CDL	Central Detector Lepton; in the lepton collection
η	Electron $|\eta| < 1.1$ cut
ρ	Muon COT exit radius cut (ρ)
fid	Fiducial detector lepton check
z_0	primary vertex cut; $|z_0| < 60$cm
vtx	# of vertices ≤ 3 with $\sum p_T^{vtx} > 10$GeV/c
p_T	Electron or muon high p_T requirement
E_T	Electron transverse energy cut
M_T	W transverse mass cut
e-jet	Electron-Jet separation requirement
μ-jet	Muon-Jet separation requirement
$\Delta\phi$	$\Delta\phi(\ell, \wp)$ cut
Total	This is the total acceptance across all cuts

Table 7.2. Acceptance cut label and definitions as used in tables 7.3-7.7 for A(X)

n jets	$A(\text{cdl})$	$A(\text{geo})$	$A(\text{kin})$	$A(e\text{-jet})$	$A(\Delta\phi)$	$A(\text{Total})$
0	0.961	0.487	0.641	1.000	1.000	0.300
1	0.957	0.599	0.524	0.997	0.957	0.287
2	0.967	0.672	0.475	0.992	0.958	0.293
3	0.970	0.719	0.454	0.985	0.957	0.298
4	0.970	0.760	0.466	0.979	0.954	0.322

Table 7.3. Raw CEM acceptance for each *exclusive* n jet multiplicity summed over all $W+m$p MC samples. For compactness, we use $A(\text{geo})$ and $A(\text{kin})$ as a product of individual cuts which are listed in greater detail via table 7.4. They are defined as follows: $A(\text{geo}) = A(\eta) \times A(\text{fid}) \times A(z_0) \times A(\text{vtx})$ and $A(\text{kin}) = A(p_T) \times A(E_T) \times A(M_T)$.

n jets	$A(\eta)$	$A(\text{fid})$	$A(z_0)$	$A(\text{vtx})$	$A(p_T)$	$A(E_T)$	$A(M_T)$
0	0.833	0.939	0.654	0.952	0.794	0.832	0.971
1	0.911	0.965	0.717	0.950	0.705	0.833	0.893
2	0.947	0.978	0.764	0.949	0.671	0.826	0.857
3	0.966	0.985	0.797	0.948	0.662	0.825	0.831
4	0.980	0.990	0.832	0.941	0.664	0.843	0.833

Table 7.4. Raw CEM acceptance for each *exclusive* n jet multiplicity summed over all $W+m$p MC samples for individual cuts. This table represents additional individual acceptance cuts that are combined as $A(\text{geo})$ and $A(\text{kin})$ in table 7.3.

7.2. Exclusive and Inclusive Acceptance Definitions

In this section we describe the process in which we take the acceptance for each (exclusive) jet multiplicity and parton sample combine this into a total (inclusive) jet multiplicity acceptance without parton dependence. As was our stated goal, we note that this procedure does not apply any special cross-section weight to the various Alpgen p number of partons samples. We begin by making an exclusive jet multiplicity acceptance calculation and then build on this to get our final inclusive jet multiplicity acceptance which then will be combined into our effective luminosity and in turn our cross-section measurements.

We define the acceptance for exclusive n jet multiplicity, $A^{ex} = A^{ex}(n)$, via the know distribution of the number of jets for each Alpgen+Pythia MC sample.

$$(7.7) \qquad A^{ex} = \sum_{\forall p} c_p^{ex} A_p$$

where A_p is the exclusive jet multiplicity dependent acceptance for the p parton MC sample and c_p^{ex} is proportional to the probability of getting n jets using a p parton MC sample and is normalized to give the composition of each parton sample for n jets. We define c_p^{ex} as

$$(7.8) \qquad c_p^{ex} \equiv \frac{\tilde{c}_p}{\displaystyle\sum_{\forall p} \tilde{c}_p}$$

with

(7.9)
$$\tilde{c}_p = \frac{N_p^{\text{GEN}}}{\sum\limits_{\forall j} N_p^{\text{GEN}}}$$

As noted in the previous section (see equation 7.6), N_p^{GEN} represents the number of generated events from the p parton MC samples for (exclusive) n jets. Equation 7.9 for $\tilde{c}_p = \tilde{c}_p(n)$ is just the number of events generated for a given p parton sample for exclusive jet multiplicity n normalized to the total number of events in the generated sample.

Some additional details for our methodology are as follows. The parton sum runs over all 5 $W+m$p samples with $m \in \{0, 1, 2, 3, 4\}$ and the exclusive jet number likewise with $n \in \{=0, =1, =2, =3, \geq 4\}$. Note that the 4 jet case is by default defined to be ≥ 4 jets. This is trivial to our inclusive jet multiplicity acceptance framework below but is a non-issue here as well. Recall that the Alpgen $W+4$p samples match to the inclusive ≥ 4 jet bin while $W+m$p is exclusively match for $m \neq 4$.

Tables 7.9 and 7.12 show the exclusive weight matrix (c_p^{ex}) for $W \rightarrow e\nu$ and $W \rightarrow \mu\nu$, respectively. These tables derive from the composition of generated events $(\tilde{c}_p)$ which are shown in tables 7.8 for electrons and table 7.11 for muons. We omit our tables for the total acceptance defined with exclusive jet multiplicity for brevity.

We define the acceptance for inclusive $\geq n$ jet multiplicity, $A = A(\geq n)$, to be consistent with what is given in Equation 7.7. The idea is to use the exclusive acceptance frame work to produce our desired inclusive acceptance by summing over the higher jet bins. Consider for example the inclusive 2 jet case which would symbolically look like:

$$(\geq 2) \Leftrightarrow (=2) \cup (=3) \cup (\geq 4)$$

This is our nominal acceptance that we will be using for all of our cross-section measurements modulo the discussion in section 7.4. We define A via

$$(7.10) \qquad A = \sum_{\forall j \geq n} \sum_{\forall p} c_p^{in}(j, n) A_p(j)$$

with implicit inclusive $\geq n$ jets dependence and where

$$(7.11) \qquad c_p^{in}(j, n) \equiv \frac{\tilde{c}_p(j)}{\displaystyle\sum_{\forall j \geq n} \sum_{\forall m} \tilde{c}_m}$$

The normalization to $\tilde{c}_p$ is a function of the inclusive jet bin. We note that $\tilde{c}_p$ and A_p depend on the *exclusive* number of jets (j) and parton sample and that the former was defined in equation 7.9.

Tables 7.10 and 7.13 are the equivalent weight matrix for inclusive jet multiplicity case. As noted before, the Alpgen+Pythia MC for W+4p is setup to match to $\geq$4 jets. Thus the results in the $\geq$4 jet bin will be equal by construction to the results given in the exclusive scenario. With equations 7.11 and 7.9 we just need to apply our exclusive jet multiplicity and parton number dependent acceptance to fully compose our final acceptance.

7.3. Electron and Muon Acceptance Results

We present our electron and muon channel acceptances in this section. First we present, for each lepton detector type, the $A_p(j)$ acceptances which are the p parton total acceptance for exclusive j jets. Using these along with the results from the previous section, we derive the total acceptance for $\geq n$ jets, $A = A(\geq n)$, via equation 7.10. Table

7.14 presents the CEM $A_p(j)$ while tables 7.15, 7.16, and 7.17 refer to the CMUP, CMX-Arch, and CMX-Mini $A_p(j)$ acceptances, respectively.

Finally we present our electron (CEM) and muon (CMUP, CMX-Arch, and CMX-Mini) total acceptance results in table 7.18. The average CEM acceptance works out to 0.308 ± 0.012 while the combined μ detector acceptance averages to 0.205 ± 0.013. We also note that the acceptance is roughly flat with jet multiplicity dependence. The relative error (standard deviation divided by average) in the spread of jet bins for the CEM is 4.0% while for the μ detectors it is 6.4%.

n jets	A(cdl)	$A(\rho)$	A(fid)	$A(z_0)$	A(vtx)	$A(p_T)$	$A(M_T)$	$A(\mu\text{-jet})$	A(Total)
0	0.311	1.000	0.511	0.961	0.988	0.823	0.986	1.000	0.122
1	0.393	1.000	0.527	0.960	0.982	0.815	0.915	0.959	0.140
2	0.427	1.000	0.543	0.959	0.975	0.795	0.890	0.914	0.140
3	0.447	0.999	0.556	0.957	0.970	0.775	0.871	0.863	0.134
4	0.463	0.999	0.570	0.954	0.963	0.751	0.857	0.785	0.122

Table 7.5. Raw CMUP acceptance for each *exclusive n* jet multiplicity summed over all $W+m$p MC samples

n jets	A(cdl)	$A(\rho)$	A(fid)	$A(z_0)$	A(vtx)	$A(p_T)$	$A(M_T)$	$A(\mu\text{-jet})$	A(Total)
0	0.099	0.768	0.966	0.976	0.988	0.846	0.988	1.000	0.059
1	0.122	0.775	0.966	0.976	0.985	0.831	0.922	0.960	0.065
2	0.131	0.781	0.963	0.974	0.980	0.811	0.895	0.919	0.063
3	0.136	0.787	0.962	0.974	0.974	0.792	0.878	0.873	0.059
4	0.141	0.792	0.961	0.972	0.970	0.775	0.864	0.797	0.054

Table 7.6. Raw CMX-Arch acceptance for each *exclusive n* jet multiplicity summed over all $W+m$p MC samples

n jets	A(cdl)	$A(\rho)$	A(fid)	$A(z_0)$	A(vtx)	$A(p_T)$	$A(M_T)$	$A(\mu\text{-jet})$	A(Total)
0	0.015	0.803	0.952	0.979	0.988	0.846	0.988	1.000	0.009
1	0.018	0.813	0.951	0.978	0.986	0.832	0.920	0.963	0.010
2	0.020	0.810	0.952	0.976	0.982	0.820	0.895	0.916	0.010
3	0.021	0.817	0.946	0.976	0.978	0.802	0.882	0.865	0.009
4	0.022	0.817	0.951	0.973	0.970	0.776	0.866	0.795	0.008

Table 7.7. Raw CMX-Mini acceptance for each *exclusive n* jet multiplicity summed over all $W+m$p MC samples

n jets	$0p$	$1p$	$2p$	$3p$	$4p$
0	0.9190	0.4154	0.1409	0.0416	0.0093
1	0.0777	0.5331	0.4631	0.2507	0.0937
2	0.0031	0.0491	0.3575	0.4392	0.2976
3	0.0002	0.0023	0.0367	0.2408	0.3748
4	0.0000	0.0002	0.0018	0.0276	0.2245

Table 7.8. Acceptance $\tilde{c}_m$ matrix (mp verses n jets) for $W \rightarrow e\nu + m$p MC

n jets	$0p$	$1p$	$2p$	$3p$	$4p$
0	0.6021	0.2722	0.0924	0.0273	0.0061
1	0.0548	0.3759	0.3265	0.1768	0.0661
2	0.0027	0.0428	0.3118	0.3831	0.2596
3	0.0003	0.0035	0.0561	0.3678	0.5723
4	0.0001	0.0007	0.0071	0.1087	0.8835

Table 7.9. Acceptance c_m^{ex} matrix (mp verses n jets) for $W \rightarrow e\nu + m$p MC. These results are derived from equation 7.8 and the $\tilde{c}_p$ results of table 7.8.

j	$\geq n$ jets	$0p$	$1p$	$2p$	$3p$	$4p$
0	0	0.5299	0.2395	0.0813	0.0240	0.0054
1	0	0.0058	0.0394	0.0343	0.0186	0.0069
2	0	0.0000	0.0006	0.0042	0.0052	0.0035
3	0	0.0000	0.0000	0.0001	0.0005	0.0008
4	0	0.0000	0.0000	0.0000	0.0000	0.0001
1	1	0.0480	0.3289	0.2857	0.1547	0.0578
2	1	0.0003	0.0048	0.0352	0.0432	0.0293
3	1	0.0000	0.0000	0.0006	0.0042	0.0065
4	1	0.0000	0.0000	0.0000	0.0001	0.0007
2	2	0.0024	0.0386	0.2814	0.3457	0.2343
3	2	0.0000	0.0003	0.0051	0.0335	0.0521
4	2	0.0000	0.0000	0.0000	0.0007	0.0059
3	3	0.0003	0.0032	0.0523	0.3428	0.5335
4	3	0.0000	0.0000	0.0005	0.0074	0.0599
4	4	0.0001	0.0007	0.0071	0.1087	0.8835

Table 7.10. Acceptance $c_p^{in}(j, n)$ matrix (mp/ verses $= j$ jets and $\geq n$ jets) as defined in equation 7.11 for $W \rightarrow e\nu + m$p MC

n jets	$0p$	$1p$	$2p$	$3p$	$4p$
0	0.9653	0.3305	0.0833	0.0184	0.0031
1	0.0323	0.6403	0.4100	0.1663	0.0460
2	0.0023	0.0275	0.4791	0.4509	0.2268
3	0.0001	0.0016	0.0261	0.3413	0.4131
4	0.0000	0.0001	0.0015	0.0230	0.3111

Table 7.11. Acceptance $\tilde{c}_m$ matrix (mp verses n jets) for $W \to \mu\nu + m$p MC

n jets	$0p$	$1p$	$2p$	$3p$	$4p$
0	0.6892	0.2360	0.0595	0.0131	0.0022
1	0.0249	0.4945	0.3166	0.1285	0.0355
2	0.0019	0.0232	0.4038	0.3800	0.1911
3	0.0002	0.0020	0.0334	0.4363	0.5281
4	0.0000	0.0003	0.0046	0.0686	0.9265

Table 7.12. Acceptance c_m^{ex} matrix (mp verses n jets) for $W \to \mu\nu + m$p MC. These results are derived from equation 7.8 and the $\tilde{c}_p$ results of table 7.11.

j	$\geq n$ jets	$0p$	$1p$	$2p$	$3p$	$4p$
0	0	0.6045	0.2070	0.0522	0.0115	0.0019
1	0	0.0026	0.0519	0.0332	0.0135	0.0037
2	0	0.0000	0.0004	0.0064	0.0060	0.0030
3	0	0.0000	0.0000	0.0001	0.0008	0.0010
4	0	0.0000	0.0000	0.0000	0.0000	0.0001
1	1	0.0213	0.4223	0.2704	0.1097	0.0303
2	1	0.0003	0.0030	0.0521	0.0491	0.0247
3	1	0.0000	0.0000	0.0005	0.0069	0.0083
4	1	0.0000	0.0000	0.0000	0.0001	0.0010
2	2	0.0017	0.0205	0.3570	0.3360	0.1690
3	2	0.0000	0.0002	0.0036	0.0473	0.0572
4	2	0.0000	0.0000	0.0000	0.0005	0.0069
3	3	0.0002	0.0019	0.0312	0.4081	0.4939
4	3	0.0000	0.0000	0.0003	0.0044	0.0599
4	4	0.0000	0.0003	0.0046	0.0686	0.9265

Table 7.13. Acceptance $c_p^{in}(j, n)$ matrix (mp/ verses $= j$ jets and $\geq n$ jets) as defined in equation 7.11 for $W \to \mu\nu + m$p MC

7.4. Reduced Acceptance Definition

The results of the previous section represent the typical acceptances for production level cross-sections. This means the cross-section for $p\bar{p}$ goes to some process X (we will omit the branching ratio and simply take X to represent a final state) takes the form

$$(7.12) \qquad \sigma(p\bar{p} \to \mathrm{X}) = \frac{N_{\mathrm{data}} - N_{\mathrm{bkgd}}}{LA\epsilon}$$

where the acceptance, A, is the acceptance via MC for process $p\bar{p}$ goes to final state X with full detector simulation. Clearly, N_{data} is the number of candidate W events in data while N_{bkgd} (or simply B, for brevity in later chapters) is the sum of all of our background estimation.

In this section we want to introduce the concept of a cross-section based on the reduced production phase space for our signal. The main motivation for our use of a reduce acceptance is to present a cross-section which is friendly to various theoretical predictions. In addition, the restriction of phase-space negates the potential problem of trusting the MC outside of the area of measurement in terms of a geometric and pure kinematic acceptance. Although we do not have to make any assumption about the MC treatment about the non-central, low M_T, etc. events, we do have to deal with an addition set of selection cuts made before CDF detector simulation.

In contrast to equation 7.12, we have

$$(7.13) \qquad \sigma(p\bar{p} \to \mathrm{X}|[a_{\mathrm{hepg}}]) = \frac{N_{\mathrm{data}} - N_{\mathrm{bkgd}}}{L\bar{A}\epsilon}$$

where $[a_{\mathrm{hepg}}]$ represents a set of cuts (as the variable implies, these cuts will be at the hepg level) that reduces of the available MC decay space for the process going to X and $\bar{A}$ represents the acceptance of X in simulation *given* the MC set already has $[a_{\mathrm{hepg}}]$ applied. Our luminosity and efficiency components (L and ϵ, respectively) are unchanged and our handling of the equivalent total effective luminosity, $L\bar{A}\epsilon$, is otherwise unchanged with respect to the procedure of the last section of this chapter (see section 7.7). Effectively equations 7.2 and 7.5 replace their usage of $N(\mathrm{GEN})$ with the number of events passing these generator (e.g. hepg variables) level cuts.

We construct this redefined cross-section by making the (potentially lepton dependent) cuts outlined in table 7.19. These cuts obviously mirror our detector level cuts in selecting the W. While it is possible to subdivide the muons into detector types, this is not called for when dealing with a global MC acceptance correction. We will explain the procedure in section 7.7.

Functionally, we select the leptons via there particle ID number in order to get the needed 4-momentum information in the hepg bank. We use the second pair of leptons that have as their parent the original leptons from the W decay. These daughters particles represent a post radiation correction state. The potential effect on the reduce acceptance relative to selecting the original (pre-radiation) leptons that are proper daughters of the original W in the collection is given as a systematic and described in section 8.3.

We define our reduced acceptance correction as a_{hepg} which is symbolically given by

$$(7.14) \qquad\qquad a_{\mathrm{hepg}} = \frac{N(M_T)}{N(\mathrm{GEN})}$$

where $N(M_T)$ represents the number of generated events that passed our final generator level cut. Of course, our actual procedure is to make a parton (MC sample) and exclusive jet multiplicity dependent acceptance to mirror that of our $A_p(j)$ term in equation 7.10. Following the same procedure and using the same definitions for c_p^{in} and $\tilde{c}_p$ in equations 7.11 and 7.9. This pseudo acceptance, a_{hepg}, is then a correction to our normally defined production acceptance, A, which becomes our reduced acceptance, $\bar{A}$. Then

$$(7.15) \qquad\qquad \bar{A} = \frac{A}{a_{\text{hepg}}}$$

which suggests with respect to equations 7.12 and 7.15 that

$$(7.16) \qquad\qquad \sigma(p\bar{p} \to \mathrm{X}|[a_{\text{hepg}}]) = (a_{\text{hepg}})\, \sigma(p\bar{p} \to \mathrm{X})$$

7.5. Reduced Acceptance Results

In table 7.20 we present the results for our acceptance correction factor, a_{hepg}, as defined in the previous section for both lepton channels. The variation in the acceptance values is 2.7% for the muons and 1.4% for the electrons. Regrettably the acceptance values for our reduced cross-section are different enough to make it unlikely that the electron and muons results could combined together. This is somewhat expected given that the cuts are not entirely equivalent (see table 7.19) and thus making them different cross-sections. The reduced acceptance, $\bar{A}$, results follow from the nominal acceptance results in table 7.18 which are simply scaled via equation 7.15. They are presented for completeness in table 7.21.

7.6. Lepton Efficiencies

In this section we present the various lepton efficiencies based on the work done by the Lepton and Joint Physics working groups [71][33]. Unlike our acceptance results which we take from MC, we define efficiencies as a data measured component (for high p_T leptons this is typically done with Zs) that would result in missing events. The procedure for electron efficiencies is described fully in [72]. These results (up to and including period 17) are taken from [73]. Likewise [74] describes the procedure for the central muon efficiencies which are derived via [75].

Efficiencies for a given detector break down into several categories. First is the trigger efficiency (ϵ_{trig}) which is the efficiency for triggering a high p_T lepton. The second is the ID (identification) efficiency (ϵ_{ID}) which represents the efficiency of a lepton passing its set of quality cuts (e.g. CES Δz, HAD/EM, and isolation, etc.). Next we consider two muon only related efficiencies. The first is the reconstruction efficiency (ϵ_{reco}) which is a measurement of the stub-track/muon reconstruction efficiency. In order to match the results given by the joint physics we will always present the combined efficiency between the ID and reconstruction and call this the "ID Efficiency". There is an additional efficiency that we have trivially added for muons based on our χ^2_{COT} cut. As noted in section 4.3, this cut was found to be extremely efficient for our data as well as in the signal MC. Luckily, the Joint Physics group has measured this χ^2_{COT} efficacy (ϵ_{χ^2}) and find it consistent with unity (100%) with (purely negative) uncertainties on the order of 0.04-0.08%. We trivially combine this with our ID efficiency for the purpose of book-keeping.

We also account for our additional Δz_{vtx} cut which is applied both lepton channels. We reproduce the Joint Physics/Lepton group procedure of selecting tight leptons via

Z selection and noting the efficiency of our final $|\Delta z_{vtx}| < 2.0$ cm cut. The efficiency is denoted as $\epsilon_{\Delta z}$ and averages 98.7% (99.2%) for electrons (muons) over all run periods [**76**]. We did not estimate or include any systematic uncertainty for this track based efficiency. Finally, there is an lepton independent efficiency that we apply with respect to the vertex position cut ($|z_0| < 60$ cm) which we will reference with ϵ_{z_0}. The details on this final measurement are documented in [**77**].

The total efficiency (ϵ_{total} or simply ϵ) is just the product of all the various efficiencies for each lepton detector type.

$$(7.17) \qquad\qquad \epsilon = \epsilon_{\text{total}} \equiv (\epsilon_{\text{trig}})(\epsilon_{\text{ID}})(\epsilon_{\text{reco}})(\epsilon_{\Delta z})(\epsilon_{z_0})$$

We have for each of the 13 different run periods (see section 3.2) the corresponding set of efficiencies as well as scale factors as was already noted in section 3.4 and follow from the general procedure of [**32**]. The total run period dependent efficiency for each lepton detector type will then be combined with the luminosity in each period along with the total acceptance into a combined effective luminosity which we discuss in the next section.

In table 7.22 we present the ID and trigger efficiency results for CEM electrons. The results for CMUP are shown in table 7.23. The CMX muon efficiencies are broken down for arches (CMX-Arch) and miniskirt (CMX-Mini) in tables 7.24 and 7.25, respectively. Recall that we will present the ID and reconstruction efficiencies together and for convenience and consistency refer to it as the ID efficiency. We do not present the efficiencies for our muon based χ^2_{COT} cut separately and as also noted before combine this with our formal ID efficiency. In each of the four tables (7.22-7.25) the total efficiency *includes* the lepton vertex position (z_0) efficiency. These results are individually given in table 7.26.

7.7. Effective Luminosity ($LA\epsilon$)

We currently have a detector dependent acceptance based off of our two sets of W MC for each lepton channel, and a detector and run dependent set of efficiencies and luminosities over our 13 different run periods. Here we are going to combine these pieces together into our effective luminosity term. This will then basically become our dominator term for our cross-section measurements (see section 9.1). The second goal for this section is to explain the resulting error propagation which will become important in the next chapter (in particular, sections 8.2-8.3).

First we recall tables 3.1 and 3.2 which define our run periods and the luminosity in each period. Let L_i be the luminosity and ϵ_i the total CEM efficiency for enumerated period i and let $A_{CEM} = A(CEM)$ be total acceptance for electrons. Then the effective luminosity ($LA\epsilon$) goes as

$$(7.18) \qquad (LA\epsilon)_e \equiv \sum_{\forall\ i} (L_i \epsilon_i)\, A_{CEM}$$

When we have multiple sub-detectors as is the case for the muons things are slightly more involved:

$$(7.19) \qquad (LA\epsilon)_\mu = \sum_{\forall\ k} (LA\epsilon)_k$$

$$(7.20) \qquad\qquad = \sum_{\forall\ k} \sum_{\forall\ i} (L_{i,k} \epsilon_{i,k})\, A_k$$

where k represents the three muon sub-detectors such that

$$k \in \{\text{CMUP,CMX–Arch,CMX–Mini}\}$$

For the purpose of understanding how the errors propagate we note that the error on the run period luminosity and efficiency are independent of other periods. Thus the error goes linearly for the efficiency. We take the acceptances to be independent as well. We note that the trivial luminosity error is easy to deal with (see section 8.1 for details) as it will be taken as a universal relative error. As such we will only derive the dependence of the less trivial acceptance and efficiency calculations.

Let ΔA_k be the absolute acceptance error (with possible sub-detector dependence k) and $\Delta \epsilon_{i,k}$ is the absolute error on the total lepton efficiency for run period i and sub-detector lepton k. We denote the effective luminsoity error (due to ΔA and $\Delta \epsilon_i$) error via $\Delta (LA\epsilon)_\ell$. For electrons,

$$(7.21) \qquad \Delta(LA\epsilon)_e = (LA\epsilon)_e \sqrt{\left(\frac{\Delta A}{A}\right)^2 + \left(\frac{\sum\limits_{\forall\, i} L_i \Delta \epsilon_i}{\sum\limits_{\forall\, i} L_i \epsilon_i}\right)^2}$$

while for the muons,

$$(7.22) \qquad \Delta(LA\epsilon)_\mu = \sum_{\forall\, k}(LA\epsilon)_k \left(\frac{(LA\epsilon)_k}{(LA\epsilon)_\mu}\right) \sqrt{\left(\frac{\Delta A_k}{A_k}\right)^2 + \left(\frac{\sum\limits_{\forall\, i} L_{i,k} \Delta \epsilon_{i,k}}{\sum\limits_{\forall\, i} L_{i,k} \epsilon_{i,k}}\right)^2}$$

Table 7.27 notes the numerical values for our effective luminosities for electrons and combined muons. The error included is the Poisson based error which we have been sighting from table 7.22-7.26. This random error is very small and will be shown to be negligible to the 6.0% luminosity, the parton distribution functions (PDF), and final state radiation (FSR) systematics (see sections 8.1, 8.2, and 8.3, respectively).

n jets	$0p$	$1p$	$2p$	$3p$	$4p$
0	0.2817	0.3210	0.3441	0.3471	0.3344
1	0.2256	0.2565	0.3042	0.3237	0.3267
2	0.2578	0.2836	0.2627	0.3012	0.3185
3	0.3373	0.2839	0.3330	0.2767	0.3084
4	0.2942	0.3385	0.3565	0.3702	0.3151

Table 7.14. CEM $A_p(j)$

n jets	$0p$	$1p$	$2p$	$3p$	$4p$
0	0.1171	0.1311	0.1400	0.1484	0.1426
1	0.0806	0.1373	0.1447	0.1480	0.1469
2	0.1035	0.0894	0.1390	0.1424	0.1436
3	0.0780	0.1045	0.0941	0.1332	0.1377
4	0.1248	0.0882	0.0961	0.0959	0.1245

Table 7.15. CMUP $A_p(j)$

n jets	$0p$	$1p$	$2p$	$3p$	$4p$
0	0.0568	0.0623	0.0688	0.0652	0.0692
1	0.0373	0.0638	0.0664	0.0676	0.0653
2	0.0582	0.0390	0.0626	0.0638	0.0627
3	0.0303	0.0449	0.0397	0.0596	0.0607
4	0.0000	0.0189	0.0434	0.0404	0.0551

Table 7.16. CMX Arches (CMX-Arch) $A_p(j)$

n jets	$0p$	$1p$	$2p$	$3p$	$4p$
0	0.0089	0.0095	0.0102	0.0104	0.0090
1	0.0061	0.0099	0.0103	0.0104	0.0116
2	0.0079	0.0066	0.0098	0.0100	0.0101
3	0.0141	0.0103	0.0070	0.0093	0.0094
4	0.0000	0.0000	0.0072	0.0060	0.0086

Table 7.17. CMX Miniskirt (CMX-Mini) $A_p(j)$

n jets	A(CEM)	A(CMUP)	A(Arch)	A(Mini)
0	0.308	0.128	0.061	0.009
1	0.298	0.145	0.066	0.010
2	0.300	0.142	0.063	0.010
3	0.306	0.136	0.060	0.009
4	0.329	0.125	0.055	0.009

Table 7.18. Total Acceptance for each lepton detector type for $W \to \ell\nu+ \geq n$ jets

Generator Level Cut	$W \to e\nu$	$W \to \mu\nu$
$|\eta_e| < 1.1$	✓	
$|\eta_\mu| < 1.0$		✓
$p_T^\ell > 20$ GeV/c	✓	✓
$M_T^W > 40$ GeV/c^2	✓	
$M_T^W > 30$ GeV/c^2		✓

Table 7.19. Generator level cuts for the reduced acceptance $\bar{A}$ for $W \to \ell\nu + m$ partons MC

n jets	$W \to e\nu$ a_{hepg}	$W \to \mu\nu$ a_{hepg}
0	0.578	0.600
1	0.578	0.582
2	0.568	0.575
3	0.562	0.568
4	0.562	0.558

Table 7.20. Reduced acceptance correction (a_{hepg}) for $W \to \ell\nu + n$ jets

n jets	$\bar{A}$(CEM)	$\bar{A}$(CMUP)	$\bar{A}$(Arch)	$\bar{A}$(Mini)
0	0.533	0.213	0.102	0.015
1	0.516	0.249	0.113	0.017
2	0.528	0.247	0.110	0.017
3	0.544	0.239	0.106	0.016
4	0.585	0.224	0.099	0.016

Table 7.21. Total Reduced Acceptance for each lepton detector type for $W \to \ell\nu+ \geq n$ jets

Run Period	ϵ_{ID} ID Efficiency	ϵ_{trig} Trigger Efficiency	ϵ Total Efficiency
0d	0.802 ± 0.003	0.962 ± 0.007	0.739 ± 0.006
0h	0.796 ± 0.003	0.976 ± 0.006	0.744 ± 0.006
5-7	0.786 ± 0.004	0.979 ± 0.004	0.737 ± 0.005
8	0.788 ± 0.005	0.959 ± 0.007	0.732 ± 0.007
9	0.789 ± 0.005	0.960 ± 0.002	0.733 ± 0.005
10	0.787 ± 0.004	0.959 ± 0.002	0.731 ± 0.004
11	0.777 ± 0.004	0.961 ± 0.004	0.723 ± 0.005
12	0.772 ± 0.005	0.960 ± 0.003	0.720 ± 0.005
13	0.784 ± 0.004	0.957 ± 0.003	0.729 ± 0.004
14	0.805 ± 0.010	0.960 ± 0.030	0.751 ± 0.025
15	0.792 ± 0.005	0.963 ± 0.005	0.741 ± 0.006
16	0.790 ± 0.006	0.961 ± 0.005	0.738 ± 0.007
17	0.781 ± 0.005	0.962 ± 0.003	0.730 ± 0.005

Table 7.22. CEM Efficiencies

Run Period	ϵ_{ID} ID Efficiency	ϵ_{reco} Reconstruction Efficiency	ϵ_{trig} Trigger Efficiency	ϵ Total Efficiency
0d	0.846 ± 0.005	0.927 ± 0.004	0.902 ± 0.004	0.678 ± 0.006
0h	0.850 ± 0.005	0.916 ± 0.003	0.919 ± 0.004	0.686 ± 0.005
5-7	0.825 ± 0.006	0.918 ± 0.004	0.918 ± 0.005	0.666 ± 0.007
8	0.814 ± 0.008	0.931 ± 0.005	0.913 ± 0.006	0.670 ± 0.009
9	0.836 ± 0.008	0.927 ± 0.005	0.927 ± 0.007	0.696 ± 0.009
10	0.845 ± 0.006	0.913 ± 0.005	0.866 ± 0.007	0.647 ± 0.008
11	0.797 ± 0.007	0.905 ± 0.005	0.862 ± 0.010	0.602 ± 0.009
12	0.816 ± 0.008	0.916 ± 0.006	0.842 ± 0.012	0.612 ± 0.011
13	0.834 ± 0.006	0.913 ± 0.005	0.828 ± 0.009	0.613 ± 0.009
14	0.843 ± 0.016	0.904 ± 0.012	0.894 ± 0.022	0.662 ± 0.022
15	0.830 ± 0.009	0.892 ± 0.007	0.879 ± 0.010	0.633 ± 0.011
16	0.821 ± 0.010	0.893 ± 0.009	0.894 ± 0.013	0.637 ± 0.014
17	0.839 ± 0.008	0.890 ± 0.006	0.889 ± 0.010	0.645 ± 0.010

Table 7.23. CMUP Efficiency

Run Period	ϵ_{ID} ID Efficiency	ϵ_{reco} Reconstruction Efficiency	ϵ_{trig} Trigger Efficiency	ϵ Total Efficiency
0d	0.877 ± 0.007	0.994 ± 0.002	0.967 ± 0.004	0.807 ± 0.007
0h	0.853 ± 0.007	0.991 ± 0.002	0.955 ± 0.004	0.773 ± 0.007
5-7	0.859 ± 0.008	0.987 ± 0.003	0.954 ± 0.005	0.775 ± 0.009
8	0.846 ± 0.011	0.989 ± 0.004	0.946 ± 0.007	0.766 ± 0.012
9	0.861 ± 0.011	0.980 ± 0.005	0.930 ± 0.008	0.760 ± 0.012
10	0.859 ± 0.008	0.986 ± 0.003	0.929 ± 0.009	0.762 ± 0.010
11	0.820 ± 0.010	0.982 ± 0.004	0.927 ± 0.010	0.723 ± 0.012
12	0.843 ± 0.012	0.981 ± 0.005	0.900 ± 0.014	0.723 ± 0.016
13	0.838 ± 0.009	0.977 ± 0.004	0.893 ± 0.009	0.710 ± 0.011
14	0.872 ± 0.025	0.989 ± 0.011	0.890 ± 0.027	0.747 ± 0.032
15	0.854 ± 0.012	0.968 ± 0.006	0.923 ± 0.013	0.741 ± 0.015
16	0.816 ± 0.015	0.966 ± 0.009	0.894 ± 0.024	0.686 ± 0.023
17	0.789 ± 0.011	0.963 ± 0.006	0.898 ± 0.014	0.662 ± 0.015

Table 7.24. CMX-Arch Efficiency

Run Period	ϵ_{ID} ID Efficiency	ϵ_{reco} Reconstruction Efficiency	ϵ_{trig} Trigger Efficiency	ϵ Total Efficiency
0d	0.000 ± 0.000	0.000 ± 0.000	0.000 ± 0.000	0.000 ± 0.000
0h	0.817 ± 0.014	0.926 ± 0.009	0.772 ± 0.014	0.560 ± 0.015
5-7	0.836 ± 0.017	0.926 ± 0.012	0.744 ± 0.019	0.552 ± 0.019
8	0.849 ± 0.025	0.880 ± 0.022	0.884 ± 0.009	0.639 ± 0.026
9	0.850 ± 0.027	0.821 ± 0.025	0.866 ± 0.008	0.585 ± 0.027
10	0.846 ± 0.021	0.858 ± 0.018	0.929 ± 0.009	0.653 ± 0.022
11	0.830 ± 0.023	0.820 ± 0.020	0.927 ± 0.010	0.611 ± 0.023
12	0.858 ± 0.028	0.832 ± 0.024	0.900 ± 0.014	0.624 ± 0.029
13	0.824 ± 0.022	0.849 ± 0.020	0.893 ± 0.009	0.607 ± 0.022
14	0.935 ± 0.059	0.894 ± 0.052	0.890 ± 0.027	0.724 ± 0.066
15	0.806 ± 0.030	0.882 ± 0.023	0.923 ± 0.013	0.638 ± 0.031
16	0.812 ± 0.041	0.873 ± 0.035	0.894 ± 0.024	0.616 ± 0.043
17	0.839 ± 0.026	0.912 ± 0.020	0.898 ± 0.014	0.668 ± 0.027

Table 7.25. CMX-Mini Efficiency

Run Period	ϵ_{z_0} z_0 Cut Efficiency
0d	0.958 ± 0.002
0h	0.958 ± 0.002
5-7	0.958 ± 0.002
8	0.968 ± 0.002
9	0.968 ± 0.002
10	0.968 ± 0.002
11	0.968 ± 0.002
12	0.972 ± 0.001
13	0.972 ± 0.001
14	0.972 ± 0.001
15	0.972 ± 0.001
16	0.972 ± 0.001
17	0.972 ± 0.001

Table 7.26. Vertex position cut efficiency (ϵ_{z_0})

$\geq n$	$(LA\epsilon)_e$ (pb^{-1})	$(LA\epsilon)_\mu$ (pb^{-1})
0	593 ± 11.7	364 ± 7.0
1	580 ± 14.6	369 ± 8.5
2	595 ± 9.4	360 ± 6.4
3	625 ± 9.9	347 ± 6.5
4	709 ± 9.9	330 ± 5.8

Table 7.27. Effective Luminosity ($(LA\epsilon)_\ell$) for $W \rightarrow \ell\nu+ \geq n$ jets. The given uncertainties are due to the associated (run dependent) total efficiency uncertainty ($\Delta\epsilon$) and do not include the universal 6% uncertainty nor the PDF or FSR acceptance related systematics of sections 8.1-8.3.

CHAPTER 8

Systematics

In this chapter we detail the various systematics we consider that will go into our final cross-section measurements. Some of these considerations are straightforward (e.g. the luminosity systematic uncertainty) while others are unique to this analysis (e.g. vertex reweighing/promotion systematic). It is useful to generalize about the nature of systematics and how they effect our final cross-section measurements. Consider the following "blue-print" for our treatment of systematics in forming a final cross-section (compare to equation 9.2),

$$(8.1) \qquad \Delta\sigma = \Delta(\text{Unfolding}) \left[\Delta(\text{JES}) \left[\frac{\Delta(\text{Promotion}) \left[\Delta(\text{Background})\right]}{\Delta(\text{Luminosity} + \text{Acceptance})} \right] \right]$$

Here $\Delta(\text{Unfolding})$ and $\Delta(\text{JES})$ represents a bin-by-bin systematic in our unfolding correction and jet energy scale corrections to our total cross-section which are presented in sections 8.8 and 8.7, respectively. The former represents a systematic for the whole cross-section via the response in the signal MC while the latter individually effects our candidates in data, the background estimation, and our acceptance.

The $\Delta(\text{Background})$ term in equation 8.1 represents the two systematics for the background estimation which are also bin-by-bin effects on our final cross-section histograms. First we present our general background fitting estimation systematic in section 8.5. Secondly, we consider the top ($t\bar{t}$ theoretical cross-section based) background estimation in

section 8.6. The Δ(Promotion) term signifies an additional treatment/correction for promotion which can be thought of as a background. This is actually our vertex reweighting systematic and is described in section 8.4. Finally Δ(Luminosity+Acceptance) represents two sets of contributions to our effective luminosity. First the straightforward contribution of the systematic on the effective luminosity which is dominated by the actual luminosity detector uncertainty as noted in section 8.1. The second set of contributions effect our acceptance and efficiency calculation and deal with our methodological handling and assumptions concerning our use of PDFs (parton distribution functions) and FSR (final state radiation of the leptonic W decay). We describe these systematics in sections 8.2 and 8.3, respectively.

Special considerations, such as addressing cancellation of systematics in our normalized cross-sections will be addressed. In particular, we highlight in section 8.9 our treatment of how we combined systematics to obtain a total systematic. In the last section 8.10, we show the relative uncertainty for each systematic for each nontrivial cross-section which is in parallel to our presentation of our cross-section results in the next chapter.

8.1. Luminosity Measurement

Our final cross-section measurements involve our effective luminosity term was the effective product of the CLC luminosity, W acceptance, and various lepton efficiencies as defined in section 7.7. In that section we gave an uncertainty term, $\Delta(LA\epsilon)$, (equations 7.21 and 7.22) which was defined in terms of uncertainties in our acceptance (ΔA) and efficiency ($\Delta \epsilon$). This section deals with the direct uncertainty in our measurement of the

luminosity and not the other components of the effective luminosity. More precisely this is the CLC detector uncertainty on the measured integrated luminosity[78].

The systematic due to the uncertainty in the luminosity measurement is straightforward to account for due to its placement in the dominator of our cross-section calculation and not having any lepton, jet multiplicity, or analysis observable dependence. We apply a 6.0% global uncertainty to all non-normalized cross-sections. To be pedagogical, the cross-section error $(\Delta\sigma)$ for an abstract cross-section observable (σ) would simply be

$$(8.2) \qquad\qquad \Delta_{\mathrm{Lum}} \equiv \Delta\sigma = (0.06)\sigma$$

In the case of cross-section ratios (such as normalized cross-section), this luminosity uncertainty completely cancels due to its independence. Note that the luminosity systematic is not presented in any of the relative uncertainty plots in section 8.10 as it is completely trivial. We will later denote the pure luminosity (as oppose to the total effective luminosity) systematic via Δ_{Lum}.

The two dominate acceptance and efficiency related systematics follow in the next two sections. The first (section 8.2) deals with the systematic due to our choice of parton distribution function and its associated error. We also naturally incorporate the uncertainties in our efficiency via our effective luminosity calculation mentioned above. The second section of note (section 8.3) deals with the variation with our given choice of pre- or post-radiation lepton selection in our reduced cross-section (as defined in section 9.1) as well as its indirect effect on the PDF acceptance systematic.

8.2. Parton Density Function (PDF) Acceptance

The acceptance systematic described in this section comes from our knowledge of the parton distribution functions (PDF) we use. The general procedure we followed is given here [**79**]. The basic concept is to vary different PDF sets and apply a weight based off of the relative value of the default `CTEQ5L` set to *each* event. We then calculate the acceptance for each PDF variation and compute a systematic based off of the spread in that distribution. There is an additional PDF and acceptance related systematic based on our knowledge of the strong coupling constant, α_S. We also fold in the uncertainty in our efficiency measurements the results of which was presented in section 7.6.

The general procedure begins by running over each MC sample (taking care to run in the same event number order) and produce a PDF root file that has a weight value for each event and for each PDF set used. We look at a total of 46 sets: `CTEQ5L` (weight values are 1.0000 by definition), `MRST72`, `MRST75`, `CTEQ6L`, `CTEQ6L1`, `CTEQ6M` (central value), and the 20 pairs of orthogonal `CTEQ6M` eigen vectors that represent $\pm 90\%$ CL [**80**][**81**].

In order to produce a relative weight one needs to reproduce the event's squared momentum transfer, Q^2, and the parton momentum fractions for the initial patrons, x_1 and x_2. Although this information is not saved during generation it is possible to reconstruct the values by looking at the `hepg` bank. In the case of the `Alpgen` MC the choice of generator Q^2 is chosen via the `iqopt` option which is set to 1 in this case. This (default) option sets Q^2 to

$$(8.3) \qquad Q^2 = M_W^2 + \sum_{\forall \text{ jets}} p_T^2$$

Here, M_W^2 is the squared mass of the W in the `hepg` bank. Pedagogically, we always take the "second" W in the bank which has as its parent the generated W (we use the PDG Monte Carlo particle numbering scheme[83]). However, the W mass by construction does not change (only its 4-momentum components as needed relative to the changes in the final state radiation leptons) and thus there is no final state radiation (FSR) correction due to our choice in Q^2. Note that we consider the additional effect of our choice in the post-final radiation state verses pre-final state radiation with respect to our reduced acceptance (see section 7.4) as a separate systematic to be described in the next section.

The sum in equation 8.3 is over all the generated *partons* that are quarks or gluons. While these are not jets *per se*, the notation is hopefully clear that these are hadronic partons and that the p_T of the W nor its leptons is used. We calculate the squared transverse momentum in the normal way via the `hepg` momentum components: $p_T^2 = p_x^2 + p_y^2$. Although we do not have a say in the matter, we note that this is a logical choice in Q^2 with M_W^2 and $M_W^2 + p_{T(W)}^2$ as the typical sighted values in the Run I CDF W+jets paper [84].

For the momentum fractions, unfolding the initial values proves to be more involved. The method by some is not particularly rigorous [85], e.g.

$$x_1 = \frac{E_1 + |p_{1,z}|}{\sqrt{s_0}}$$

We derive x_1 and x_2 by using a similar method outlined in [86]. The notation and discussion in [87] is also instructive.

$$(8.4) \qquad\qquad x_F = x_1 - x_2$$

$$(8.5) \qquad\qquad \tau = x_1 x_2$$

x_F is the Feynman x which is chosen, without loss of generality, to be the difference between the proton based parton (p_1) momentum fraction and the anti-proton based parton (p_2) momentum fraction. The product of the momentum fractions is defined to be τ.

We can then write x_1 and x_2 in terms of these quantities:

$$(8.6) \qquad\qquad x_1 = +\frac{1}{2}\left(x_F + \sqrt{x_F^2 + 4\tau} \right)$$

$$(8.7) \qquad\qquad x_2 = -\frac{1}{2}\left(x_F - \sqrt{x_F^2 + 4\tau} \right)$$

In order to calculate Equations 8.6 and 8.7 we need use the 4-momentum of the patrons p_1 and p_2 via the `hepg` bank in combination with τ and x_F. For the former, recall that the momentum fraction is defined via the relationship $p_i = x_i P_i$ where P_i is the proton or anti-proton 4-momentum and is taken to be $P_{1,2} = (980, 0, 0, \pm 980)$, without loss of generality. Substituting $x_i P_i$ in for p_i for

$$(8.8) \qquad\qquad \hat{s} = (p_1 + p_2)^2$$

$$(8.9) \qquad\qquad \hat{s} = s_0(x_1 x_2) + (m_1^2 + m_2^2)$$

Ignoring the minor mass correction which is small relative to the beam energy, τ can thus be written as the quotient of the square of the center of mass energy of the event ($\hat{s}$) and the square of the total beam-on-beam energy ($s_0 = (2{\times}980 \text{ GeV})^2$) or

$$(8.10) \qquad \tau = \frac{\hat{s}}{s_0}$$

Therefore, we use Equation 8.10 via Equation 8.8 to calculate τ.

For x_F, again recall $p_i = x_i P_i$. It is not kosher to define a scaler quantity in terms of a ratio of 4-momentums so we begin with

$$(8.11) \qquad x_1 - x_2 = \frac{P_1 P_2}{P_1 P_2}(x_1 - x_2)$$

$$(8.12) \qquad = \frac{p_1 P_2 - P_1 p_2}{P_1 P_2}$$

$$(8.13) \qquad = \frac{980(E_1 + p_{1z}) - 980(E_2 - p_{2z})}{2(980)^2}$$

$$(8.14) \qquad x_F = \frac{(E_1 - E_2) + (p_{1z} + p_{2z})}{2(980)}$$

The x_F quantity has the behavior one would expect for various simple test cases. It is also similar to the result in equation 12 in [86]. Using the above, it is simply a matter of calling the needed PDF libraries via `Pythia` and `CTEQ6` methods to obtain the desired structure function weight for each event.

Initially we investigated the two `MRST` sets PDF sets: `MRST72` and `MRST75` [82]. This proved to be a useful exercise in understanding the effect of the PDF on the acceptance but does not use the more rigorous `CTEQ6M` method which we outline below. However, under this frame work we could measure the PDF uncertainty via the difference between the

nominal `CTEQ5L` and `MRST72` acceptances. An additional acceptance related systematic, this time for α_S, came via the difference of `MRST72` and `MRST75` acceptances [**79**].

In figure 8.1 we plot the acceptance for six PDF sets normalized to the default `CTEQ5L` acceptance for $W \to e\nu + 0$ jets. The behavior for muons was the same though there was an expected error dependence due to the η coverage of the different muon detectors. There was no effect in the relative acceptance pattern between jet multiplicities though the acceptance differences were largest for ≥ 1 jet.

The method for determining the PDF uncertainty and which will be the dominate acceptance systematic came via using `CTEQ6M` and its 20 eigen vector/parameter pairs. The motivation came from the fact that the old paradigm on focusing on the older PDF sets was out of date and most groups defaulted to this method. The procedure allows for an asymmetric error and is dependent on the relative difference to the central value (`CTEQ6M`). We denote the central value via A_0 and the 40 additional acceptances via $A_i^{\pm}$ with i=1-20. The PDF uncertainty, $\Delta A^{\pm}$ is given by [**79**]

$$(8.15) \qquad \Delta A^+ = \sqrt{\sum_{i=1}^{20} \left(\mathrm{Max}[(A_i^+ - A_0), (A_i^- - A_0), 0] \right)^2}$$

$$(8.16) \qquad \Delta A^- = \sqrt{\sum_{i=1}^{20} \left(\mathrm{Max}[(A_0 - A_i^+), (A_0 - A_i^-), 0] \right)^2}$$

We calculate $\Delta A^{\pm}$ for each jet multiplicity and for each lepton/detector type. For comparison purposes only, we look at the raw combined muon results which are taken by throwing caution to the wind and treating the muons as a single detector sample. The electron (CEM) and combined muon (μ) results are presented in table 8.1 while the proper

muon results (CMUP, CMX-Arch, and CMX-Mini) are shown in table 8.2. The errors presented and more generally all the acceptance uncertainties (in the form of ΔA) are given as a percent and are relative to the cross-section measurement or the nominal acceptance, equivalently. The corresponding plot for tables 8.1-8.2 is shown in Fig. 8.2 where the positive (negative) error maps to the positive (negative) acceptance uncertainty axis. The notation and convention here is straightforward; the acceptance uncertainty due to our `CTEQ6M` PDF method is given by $\pm \Delta A^{\pm}$.

$\geq n$ jets	ΔA^+_{CEM}	ΔA^-_{CEM}	ΔA^+_{μ}	ΔA^-_{μ}
0	0.91	1.54	0.49	0.74
1	1.19	1.99	0.75	1.11
2	0.69	1.25	0.40	0.75
3	0.70	1.26	0.43	0.92
4	0.64	0.95	0.37	0.61

Table 8.1. Asymmetric PDF Acceptance Uncertainty (%) for Electrons and Combined Muons Using `CTEQ6M`

$\geq n$ jets	ΔA^+_{CMUP}	ΔA^-_{CMUP}	ΔA^+_{Arch}	ΔA^-_{Arch}	ΔA^+_{Mini}	ΔA^-_{Mini}
0	0.64	0.95	0.49	0.75	0.38	0.67
1	0.91	1.32	0.74	1.12	0.65	1.21
2	0.49	0.80	0.40	0.77	0.36	0.81
3	0.50	0.93	0.41	0.94	0.41	1.04
4	0.49	0.75	0.38	0.67	0.33	0.46

Table 8.2. Asymmetric PDF Acceptance Uncertainty (%) for Muons Using `CTEQ6M`

In general the negative systematic uncertainty for the PDF (ΔA^-) is larger than the positive (ΔA^+). For convenience we take a conservative total acceptance based symmetric uncertainly by adding the errors in quadrature which we denote via ΔA.

$$\Delta A = \sqrt{(\Delta A^+)^2 + (\Delta A^-)^2}$$
(8.17)
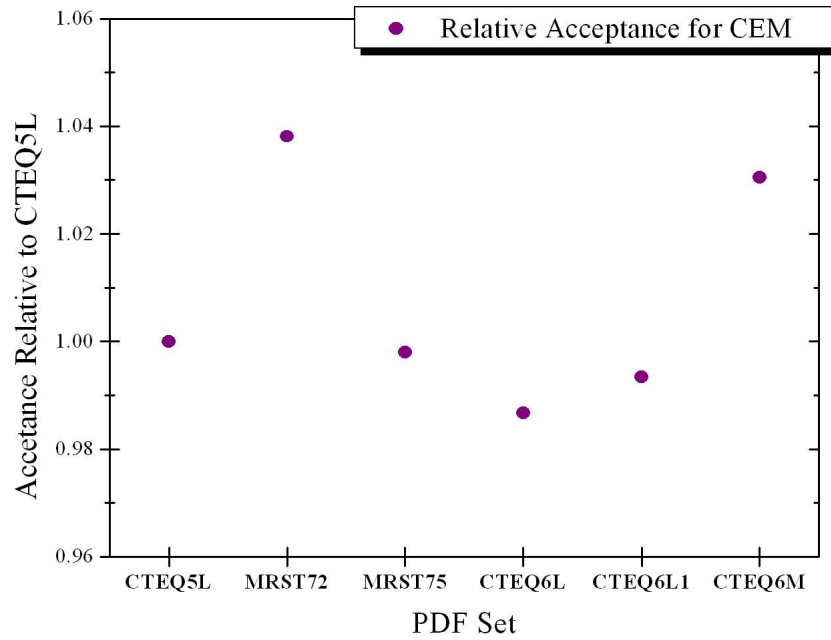
Figure 8.1. Total Inclusive CEM Acceptance for PDF Sets Relative to CTEQ5L Acceptance for $W \to e\nu + \geq 0$ jets
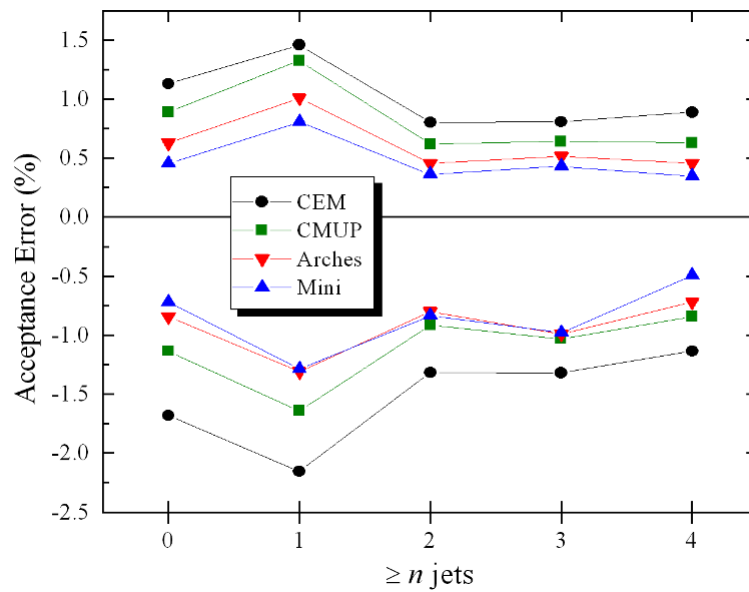
Figure 8.2. Asymmetric PDF Systematic Uncertainty (%) for each lepton detector vs. $\geq n$ jets

$\geq n$ jets	$\Delta A_{CEM}^{\alpha_S}$	$\Delta A_{CMUP}^{\alpha_S}$	$\Delta A_{Arch}^{\alpha_S}$	$\Delta A_{Mini}^{\alpha_S}$
0	0.67	0.61	0.39	0.25
1	0.85	0.98	0.70	0.49
2	0.41	0.38	0.22	0.11
3	0.41	0.40	0.30	0.17
4	0.61	0.39	0.25	0.05

Table 8.3. α_S Acceptance Uncertainty (%) for $W \to \ell\nu+ \geq n$ Jets Using `CTEQ6L/L1`

We note that ΔA is still taken to be detector and jet multiplicity dependent. These combined results is shown in figure 8.3 and again in table 8.4. Consistent with our previous presentation of this section, these acceptance based systematics uncertainties are relative to the acceptance.
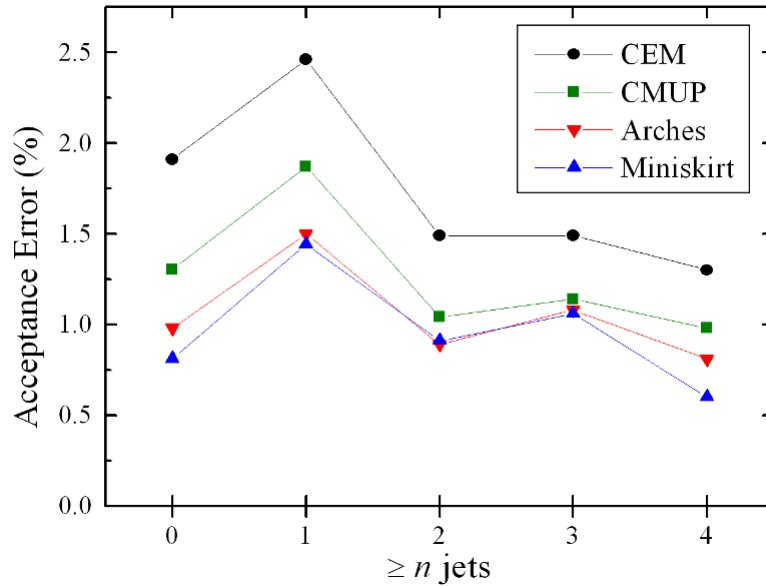
Figure 8.3. Final Acceptance Systematic Uncertainty for each lepton detector vs. $\geq n$ jets

The total PDF error, ΔA, on our cross-section will follow from our treatment of the effective luminosity (see section 7.7) via equation 7.21 (page 356) for electrons (CEM) and equation 7.22 for muons (CMUP, CMX-Arch, and CMX-Mini). As noted above, the

$\geq n$ jets	ΔA_{CEM}	ΔA_{CMUP}	ΔA_{Arch}	ΔA_{Mini}
0	1.8	1.2	0.9	0.8
1	2.3	1.6	1.3	1.3
2	1.4	1.0	0.9	0.9
3	1.4	1.1	1.0	1.0
4	1.2	0.9	0.8	0.6

Table 8.4. Total PDF Acceptance Uncertainty (%) for $W \rightarrow \ell\nu + \geq n$ Jets Using `CTEQ6M`

acceptance uncertainty given in this section have been relative to the appropriate lepton and jet multiplicity acceptance and measured as a percentage whereas equations 7.21 and 7.22 denote ΔA as an absolute error in the acceptance. We directly apply ΔA_{CEM}, etc. to the relative acceptance error term $(\Delta A/A)$ in those equations. We combine this with the systematic associated with our total efficiency information $(\Delta\epsilon)$ as described in section 7.6. The systematic error $(\Delta\sigma)$ for a given cross-section (σ) is given by

$$(8.18) \qquad \Delta_{\mathrm{PDF}} \equiv \Delta\sigma = \left(\frac{\Delta(LA\epsilon)_\ell}{(LA\epsilon)_\ell} \right) \sigma$$

We will later use Δ_{PDF} to signify our general acceptance (PDF and α_S) systematic as well as our jet multiplicity independent efficiency uncertainty.

8.3. Final State Radiation (FSR)

This section deals with another aspect of our acceptance systematic which recursively effects our PDF calculation and directly effects our reduced acceptance of section 7.4. At tree level for a 2 to 2 particle process (for reference see the W decay diagram in figure 8.4) there is no accounting for the higher order effects such as *bremsstrahlung*[88] of the charged lepton via photon emission given in QED or the equivalent radiation of the initial

state partons which includes emission of additional partons as described in QCD. We described these higher order contributions as ISR and FSR for initial state and final state radiation, respectively.
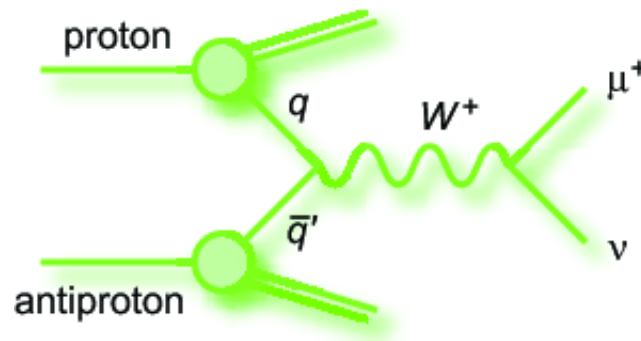
Figure 8.4. Tree level (leading order) Feynman digram for $p\bar{p} \to W \to \mu\nu$ [89]

The potential effect of the initial state radiation (ISR) of our observables is affirmatively and explicitly ignored in this analysis as our measurement (the jet kinematics of W events) *is this effect.* In other words, since we tag the event via the leptonic decay of W to electrons and muons (with their associated neutrinos) the jets we measure necessarily come from radiation of the initial (color charged) partons from the $p\bar{p}$ interaction. Potentially, our results can inform perturbative quantum chromodynamics (pQCD) and this very effect.

Final state radiation (FSR) in the case of a W decay to a charged lepton and its neutrino would be represented by photon emission on the charged member. FSR is an observable detector effect [90] but for our purpose here it also impacts our methodological use of PDFs of the previous section. For our PDF systematic analysis we selected the post-FSR generated W and we observed how different PDF choices varied our acceptance via our signal MC. Here we want to apply an additional systematic due to our choice of

post-FSR verses pre-FSR leptons on our reduced acceptance definition of section 7.4. As noted in the previous section, there is no FSR dependence on our momentum transfer and thus no effect on our signal MC via full detector simulation. However, for our reduced acceptance, the cuts we make on the charged lepton and on the transverse W mass (explicit cuts given in table 7.19 on page 358) are affected by our selection at the `hepg` bank.

We define two reduced acceptances by our systematic choice in which 4-momentums we use for the lepton decay pair. We do this by selecting leptons via their particle ID as well as their parent (particle) ID. The pre-FSR reduced acceptance ($\bar{A}_{\mathrm{pre}}$) uses the "original" leptons that have the W as its parent. By default, we use the post-FSR variables for our reduced acceptance ($\bar{A} = \bar{A}_{\mathrm{post}}$). These are the daughter particles of the pre-FSR lepton pair.

We assign a FSR systematic uncertainty ($\Delta\sigma$) to our reduced cross-section (σ) based off of the relative difference in the calculated reduced acceptance cross-section:

$$(8.19) \qquad \Delta_{\mathrm{FSR}} \equiv \Delta\sigma = |\sigma_{\mathrm{post-FSR}} - \sigma_{\mathrm{pre-FSR}}|$$

where the cross-section terms ($\sigma = \sigma_{\mathrm{post-FSR}}$ and $\sigma_{\mathrm{pre-FSR}}$) use the respective reduced acceptances ($\bar{A}_{\mathrm{post}}$ and $\bar{A}_{\mathrm{pre}}$) as described in section 9.1. This is effectively just the relative difference of a pre/post a_{hepg} (see equations 7.14 and 7.15 on page 351). We will denote this FSR error as Δ_{FSR}.

Table 8.5 give our FSR (reduced acceptance) systematic for each jet multiplicity and both lepton channels. There is a modest jet multiplicity dependence (1-2% difference between the 0 and 4 inclusive jet bins). The uncertainty is also systematically larger in

$\geq n$ jets	$W \rightarrow e\nu$ $\Delta\sigma/\sigma$ (%)	$W \rightarrow \mu\nu$ $\Delta\sigma/\sigma$ (%)
0	4.5	2.6
1	4.7	3.4
2	4.8	3.3
3	5.3	3.6
4	5.6	4.7

Table 8.5. The relative final state radiation (FSR) systematic uncertainty on the reduced acceptance cross-section (as defined in section 7.4) for $W \rightarrow \ell\nu + \geq n$jets as defined by equation 8.19. For non-reduced acceptance cross-sections where we use the normal CDF detector acceptance without limiting generator with cuts at the `hepg` level, there is no associated FSR systematic.

the electron channel and this may be just an artifact of the difference in our `hepg` cuts we apply. This hypothesis is consistent with the PDF systematic of the previous section.

8.4. Vertex Reweighting

In this section we detail our systematic concerning our reweighing of the MC number of vertices distribution. As noted already in section 6.6, we reweight the MC based on the number of vertices ("# vertices") behavior seen in the data. To recount, the motivation is to remove the instantaneous luminosity dependence on the jet multiplicity and to account for the effect jet promotion. In the latter case, additional interactions in the event may produce additional jets which are not associated with the primary W interaction. The effect would show up as an event being "promoted" into a higher jet multiplicity. Our solution to reweight the MC was shown to mitigate this. Here, however, we wish to estimate a systematic based on the variation in our jet multiplicity cross-section due to the effect of different # vertices fittings and reweightings. Based off of the expected and observed (see figures 6.107 and 6.108 starting on page 325 for example) n^{th} leading jet p_T

behavior, our vertex reweighting systematic does not warrant a bin-by-bin correction to our observables outside of the application of a jet multiplicity dependent systematic.

In section 6.6 we highlighted the results of 4 iterations where we would "fit" the # vertices distributions (for quality 12 vertices 1-3 with $\sum p_T^{vtx} > 10$ GeV/c) by effectively taking the ratio of our data (more precisely, candidate data minus QCD prediction) with our MC based signal and background estimations (see equation 6.3 on page 320). Once we verified basic consistency in the results for high jet multiplicity, we use the total inclusive (≥ 0 jets) multiplicity results to then reweight the MC. This process was repeated 3 more times (iterations 2-4) such that we have the default reweighting cross-section results along with 3 potential variations in our cross-section results. The reweighting results were presented in tables 6.11 and 6.12 for the electron and muon channels, respectively. We will now present the jet multiplicity cross-section values normalized to the average cross-section for each jet multiplicity over the four iterations as well as the standard deviation of these values. The normalization to the average allows greater ease in comparison between different iterations and jet multiplicities. The electron channel results are present in table 8.6 while the muon channel results are given in 8.7.

To obtain our final systematic for our vertex reweighting procedure to address the effect of multiple interactions and the potential for promotion, we looked at the relative difference between our final analysis result (i.e. 3$^\text{rd}$ iteration) and our default (no vertex redefinition and default MC weighting). Symbolically, our jet multiplicity dependent uncertainty would be

(8.20)
$$\frac{\left|\sigma_\text{default} - \sigma_\text{final}\right|}{2}$$

$\geq n$ jets	0th iteration	1st iteration	2nd iteration	3rd iteration	Standard Deviation
0	1.003	1.004	0.996	0.997	0.004
1	1.006	1.015	0.989	0.990	0.013
2	1.012	1.019	0.984	0.986	0.018
3	1.031	1.016	0.975	0.978	0.028
4	1.044	1.037	0.958	0.961	0.047

Table 8.6. $W \rightarrow e\nu + \geq n$ jet multiplicity cross-sections normalized to the average over all iterations. The three iterations (1st-3rd) are for the vertex fitting and subsequent MC reweighting while the 0th iteration represents the default reweighing. The standard deviation is taken over each of the four measurements for each jet multiplicity.

$\geq n$ jets	0th iteration	1st iteration	2nd iteration	3rd iteration	Standard Deviation
0	0.976	0.991	1.017	1.017	0.020
1	0.982	0.992	1.013	1.013	0.015
2	0.985	0.996	1.010	1.010	0.012
3	1.006	0.985	1.005	1.005	0.010
4	1.047	1.039	0.957	0.957	0.050

Table 8.7. $W \rightarrow \mu\nu + \geq n$ jet multiplicity cross-sections normalized to the average over all iterations. The three iterations (1st-3rd) are for the vertex fitting and subsequent MC reweighting while the 0th iteration represents the default reweighing. The standard deviation is taken over each of the four measurements for each jet multiplicity.

Of course, the standard deviation given in tables 8.6 and 8.7 is in good agreement with the prior approach but better captures the spread in the fitting procedure itself. We also note that the standard deviation calculation of the 4 different iterations is larger for all jet multiplicities. Therefore, we take the conservative of these two methods and use the standard deviation in the cited tables as our relative vertex reweighting systematic uncertainty. We will reference the systematic for a given cross-section using Δ_{Vtx}. To be pedagogical, for each cross-section iteration ($\sigma(i)$) for a given lepton and jet multiplicity

the cross-section uncertainty ($\Delta\sigma$) is defined as

$$(8.21) \qquad\qquad \Delta_{\text{Vtx}} = \Delta\sigma = \sum_{i=0}^{3} \frac{(\sigma(i) - \bar{\sigma})^2}{4 - 1}$$

We performed an additional cross-check of our vertex reweighting procedure by looking at the relative difference in our results with respect to our jet energy corrections (as described in section 5.6). It is possible that after applying $\pm\sigma_{\text{JES}}$ variation we could have an additional systematic effect via the jet energy scale on our reweighting results outline here. As it turn out, the effect is hardly detectable: less than 0.05% change between the $+\sigma_{\text{JES}}$ and $-\sigma_{\text{JES}}$ results.

8.5. Background Estimation Fitting

Our background estimation procedure has the potential to systematically shift our result. Unlike previous systematics discussed so far, this would necessarily be dependent on the actual shape of our jet kinematic observables rather than effectively changing our acceptance which is simply jet multiplicity dependent. This systematic that we turn to now would be a bin-by-bin effect to our background estimation via our various histograms of analysis observables beyond the normal Poisson uncertainty associated with the number of events in each bin.

We consider two different concerns. First there is the systematic uncertainty associated with our actual background estimation fitting procedure as described in section 6.4. This method of using our EWK and QCD templates (sections 6.2 and 6.3, respectively) to arrive at a jet multiplicity independent background estimation is dealt with in this section. Second, we have to consider the theoretical cross-section uncertainty in the case of our

diboson and $t\bar{t}$ backgrounds where we directly reweight events via an effective luminosity (see section 6.1). These "fixed" (i.e. not fitted) estimations which are dominated by the theoretical uncertainty in the $t\bar{t}$ cross-section are dealt with in the next section.

In section 6.5 we presented our background fitting fractions via tables 6.4 ($W \rightarrow e\nu + \geq n$ jets) and 6.5 ($W \rightarrow \mu\nu + \geq n$ jets) which included the fitting uncertainty (Δk_{EWK} and Δk_{QCD}) for each jet multiplicity. We recalculate our cross-sections by varying the number of background events by

$$(8.22) \qquad \Delta B_{\text{Fit}} = |\Delta k_{EWK}(N_{EWK}) - \Delta k_{QCD}(N_{QCD})|$$

where ΔB_{Fit} is the background estimation from our non-diboson and non-$t\bar{t}$ processes (i.e. $W \rightarrow \tau\nu$, $Z \rightarrow \ell\ell$, $Z \rightarrow \tau\tau$, and QCD). We note that N_{EWK} and N_{QCD} are the number of events in our EWK and QCD templates *after* we normalized via n_{EWK} and n_{QCD} (see tables 6.2 and 6.3), respectively. Equation 8.22 takes its form due to the fitting fraction being 100% anti-correlated. As a result, the uncertainty tends to be dominated by one of the templates which varies based on the number of events in each bin of our histogram observables.

Like our previous systematics outlined in this chapter, we abstractly define our background fitting cross-section uncertainty ($\Delta\sigma$) based off of our nominal cross-section definition (section 9.1) as

$$(8.23) \qquad \Delta_{\text{Fit}} \equiv \Delta\sigma = u\frac{\Delta B_{\text{Fit}}}{LA\epsilon}$$

where our effective luminosity (section 7.7) is noted with $LA\epsilon$ and u is our unfolding fraction (section 5.8). We will reference the systematic uncertainty due to our non-$t\bar{t}$ background estimation and fitting via Δ_{Fit}.

The uncertainty is not technically flat due to the background being composed of events not from our EWK or QCD templates (e.g. $t\bar{t}$ estimation) and hence the relative error is allowed to shift. As section 8.10 will show however, this systematic is smooth bin-by-bin and flat relative to a simple Poisson error of the expected signal. For the third and fourth inclusive jet bins, this is not the case in our second background estimation related systematic (as discussed in the next section) for the theoretical $t\bar{t}$ cross-section uncertainty.

We investigated the potential for a correlation systematic effects in our vertex reweighting procedure as well as our jet energy scale systematic. Once we accounted for the expected change in the templates (i.e. N_{EWK} and N_{QCD} of equation 8.23) we found virtually identical results in both cases. This is an artifact of the procedure itself as our fitting is dependent on the W M_T shape for the EWK and QCD templates and not issues more sensitive to our jet related observables.

8.6. $t\bar{t}$ Background Estimation

The second background related uncertainty to our cross-section measurement comes from the a theoretical cross-sections we use to directly estimate the backgrounds for diboson and $t\bar{t}$ production. These contributions which were "fixed" relative to our background fitting procedure were explained in section 6.1. We investigated the effect of varying the

WW, WZ, and $W\gamma^*$ cross-sections but found these to have almost no effect on our measurement. They are known to $\approx$6-8% (see table 6.1 on page 6.1) and only account for $\approx$3% of the total candidate number of events in data (see tables 6.6 and 6.7 starting on page 238). In addition, the jet related kinematics for an accepted event tends to overlap with the other electro-weak based backgrounds.

Conversely, we found that the $t\bar{t}$ background estimation requires a formal procedure (this section) to account for the potential variation in our measurement given the $\approx$12% theoretical cross-section error and account for $\approx$10-37% of our events in the inclusive third and fourth jet bins. This fact alone would require us to understand the possible variation in our total background estimation for jet multiplicity cross-section. Equally distressing, top pair kinematics are fairly distinct due to producing energetic and heavy jets via a lepton+jets decay. Our goal in this section is to account for the potential discrepancy in our results due to our $t\bar{t}$ cross-section being systematically off. Like the previous section, this systematic will be calculated bin-by-bin for each of our analysis histogram observables.

Our approach is to effectively rerun the entire analysis and vary the theoretical cross-section via its uncertainty as given in table 6.1. This then propagates as an effective MC weight change as described in section 3.6. The key here is that we are not free to just shift the cross-section universally as this change will can effect our fitting fractions for our EWK and QCD templates. As a result, we follow the same background estimation procedure where we derive new fitting fractions based off of the M_T spectrum in data minus the estimated contributions of dibosons and our weight modified $t\bar{t}$ sample. We then calculate our W cross-section as normal (see section 9.1) for both the positive and

negative deviations in the theory cross-section. We shall denote these recalculated cross-sections as σ_+ and σ_-, respectively. This necessarily means that our $t\bar{t}$ background estimation systematic is constructed to allow for asymmetric errors.

For a given cross-section (σ) we define the spread in our $t\bar{t}$ variation cross-section $\sigma_\pm$ $(\Delta\sigma)$ as

$$(8.24) \qquad \Delta\sigma = \frac{|\sigma_+ - \sigma_-|}{2}$$

The actual asymmetric cross-section error which we distinguish as Δ_{Top} is given by

$$(8.25) \qquad \Delta_{\text{Top}} \equiv \Delta\sigma \pm (\bar{\sigma}_\pm - \sigma)$$

where $\bar{\sigma}_\pm$ is simply the average of both variations:

$$(8.26) \qquad \bar{\sigma}_\pm = \frac{\sigma_+ + \sigma_-}{2}$$

Methodologically, we check to make sure that our error band always contains the central value. Theoretically, it is possible to construct such a scenario but this never happens and our systematic uncertainty is effectively symmetric for our analysis observables. Indeed, the systematic of this section is also a general test of our theory independent background estimation procedure which was formally addressed in the previous section.

8.7. Jet Energy Scale Corrections

The dominate systematic in many analyses looking at jet kinematics is the jet energy scale (JES) and this is certainly true in ours. Jet energy corrections were discussed in section 5.6, in particular, along with our definition and treatment of jets in chapter 5,

generally. This section overviews and describes the general procedure for the jet energy corrections systematic. We deal with the related issue of applying a systematic to our unfolding correction in the next section.

We are fortunate that the CDF jet energy correction group has a very streamlined procedure for applying jet energy correction and for getting appropriate $\pm\sigma_{\mathrm{JES}}$ uncertainties for our JES systematic [55][57]. (We note that the $\pm\sigma_{\mathrm{JES}}$ represents the plus-or-minus one standard deviation in the jet energy scale uncertainty and not the generic cross-section, σ, used elsewhere in this chapter.) We apply the level 5 (i.e. relative, multiple interactions, and absolute) jet corrections the via the procedure on the *Jet Energy Corrections Systematic Uncertainties* page via the `ROOT` interface.

From the technical point of view this simply requires us running the full analysis three times: once for the nominal (corrected) result and then once each changing the corrections by $\pm\sigma_{\mathrm{JES}}$. This amounts to inputing a simple systematic flag (±1 for $\pm\sigma_{\mathrm{JES}}$ or 0 for the default correction) when we set up our jet corrections for each event. From this we construct three sets of cross-sections in parallel (see section 9.1 for our cross-section definition discussion). The cross-sections can deviate bin-by-bin with respect to the nominal based on the variation in the number of candidates in data as well as our background estimation and even a change in our acceptance. We account for all of these considerations.

In order to calculate the JES systematic we construct a bin-by-bin error based on the deviation between the nominal "central" result and our two systematic variations. We define the latter cross-sections to be $\sigma_{\pm}$. Let σ be the cross-section measurement for one of our observables (e.g. n^{th} leading jet p_T) and let $\Delta\sigma$ be the prescribed JES systematic

uncertainty for σ. We construct $\Delta\sigma$ via σ_+ and σ_- as follows,

$$(8.27) \qquad \Delta\sigma = \frac{|\sigma_+ - \sigma_-|}{2}$$

However, for some distributions bin-by-bin variations may produce $\Delta\sigma$ values where the central value is outside of the range of σ_+ and σ_-. In order to correct for this, our final uncertainly is scaled by twice the distance to the nearest variation. The two cases are as follows:

$$(8.28) \qquad \text{if} (\sigma_+ < \sigma) \Rightarrow \Delta\sigma = (\sigma - \sigma_+) + \frac{|\sigma_+ - \sigma_-|}{2}$$

$$(8.29) \qquad \text{if} (\sigma_- > \sigma) \Rightarrow \Delta\sigma = (\sigma_- - \sigma) + \frac{|\sigma_+ - \sigma_-|}{2}$$

The notation in equation 8.27 (likewise equations 8.28 and 8.29) suggests a symmetric systematic error and indeed it is just the variation between the mean value between σ_+ and σ_-. Like our $t\bar{t}$ systematic we account for the difference in the average via $\bar{\sigma}_\pm$ (equation 8.26 in the previous section) and define our asymmetric error of σ using

$$(8.30) \qquad \Delta_{\text{JES}} \equiv \Delta\sigma \pm (\bar{\sigma}_\pm - \sigma)$$

which takes the same form as equation 8.25. In order to account for all the systematics together, we will later refer to our jet energy systematic uncertainty as Δ_{JES}.

8.8. Hadron Level Unfolding Correction

Our final systematic deals with our unfolding of our calorimeter based measurements into a hadronic cross-section. This hadron level unfolding was explained in section 5.8.

Using equation 5.6 (page 181) we are using the W MC to get a bin-by-bin or universal but jet multiplicity dependent correction via the quotient of the pre-simulation hadron level based jets with the normal detector reconstructed (via full simulation) jets. As a result, our systematic is primarily limited to the Poisson random fluctuation of the components of the ratio to form our unfolding fraction u.

In addition, we use an averaged unfolding fraction (as described in section 5.9) when we have a relative flat distribution. As a result, our unfolding systematic on our cross-sections, $\Delta\sigma$, is calculated using one of the two Δu calculation. In the case of a bin-by-bin unfolding (e.g. jet p_T) we use equation 5.7 for Δu and derive our cross-section systematic uncertainty for the unfolding as

$$(8.31) \qquad \Delta\sigma = \sigma\Delta u = \sigma\sqrt{\left(\frac{\Delta\sigma_{HAD}}{\sigma_{HAD}}\right)^2 + \left(\frac{\Delta\sigma_{CAL}}{\sigma_{CAL}}\right)^2}$$

with σ being our final cross-section measurement (bin-by-bin for our analysis observables as appropriate) using the calorimeter based cross-section via the data with the unfolding fraction, u, applied. Similarly, we apply equation **??** using $\bar{\Delta}u$ to obtain our systematic when the unfolding is consistent with 0-slope line of order unity:

$$(8.32) \qquad \Delta\sigma = \sigma\bar{\Delta}u$$

In either case, we will signify our unfolding systematic from the others in this chapter via $\Delta_{\mathrm{u}} \equiv \Delta\sigma$ using equation 8.31 or 8.32 as appropriate.

We observe in passing that since σ_{HAD} and σ_{CAL} are psudeo-cross-sections (their acceptances are not calculated as they are by definition equal and will cancel) they really

amount to a number of events in each bin for each jet definition. Thus the relative error for the terms effectively goes as the square root of one over the number of events $(1/\sqrt{N})$. On a different note, there are no observables that we deem (based on their behavior) needing an additional shape systematic. Thus, we are ignoring potential correlations and dependence at this stage and hence the uncertainty in Δ_u is being taken simply in quadrature. Since the unfolding fraction, u or $\bar{u}$ is a ratio we regard this as a conservative estimation. However, we do consider and factor in possible correlations with the jet energy scale correction systematic in the next section.

8.9. Systematics Combination and Correlated Systematics Treatment

The focus of this section is to describe the treatment of combining our systematics. The procedure here will give us our final total systematic error. There are actually two different concerns here. The first is that for a given differential cross-section we want to account for non-diagonal terms in our error matrix. The second issue is when we normalize our cross-sections or otherwise take ratios between two of them (e.g. σ_{n+1}/σ_n of section 9.4). The resulting quotients can have rather substantial and intentional correlations that need to be accounted for.

For convenience we will denote these two concerns via the following short hand. Let f be a differential cross-section given by

(8.33) $$f = \frac{\mathrm{d}\sigma}{\mathrm{d}X}$$

With respect to our normalized cross-sections we refer to these as f/σ where this is understood as

$$\text{(8.34)} \qquad \frac{f}{\sigma} = \frac{f}{\sigma_n} = \frac{\mathrm{d}\sigma/\mathrm{d}X}{\mathrm{d}\sigma/\mathrm{d}n}$$

where $\mathrm{d}\sigma/\mathrm{d}n$ is the jet multiplicity cross-section via the notation of section 9.3. As noted previously there are also two observables (the afore mentioned σ_{n+1}/σ_n and $r_{\Delta\eta}$ of section 9.9) that are effectively ratios of full differential cross-sections. We will note these special considerations later in this section.

For the most part systematics are done in such a way as to minimize any directly "induced" correlation. In addition, we have directly investigated the potential interplay of our systematics in the proceeding sections save the one mentioned at the end of the previous section. For example, when varying the $t\bar{t}$ cross-section (see section 8.6) we effectively repeat the analysis and allow for a different background fitting and this is independent of our background fitting systematic (section 8.5). The jet energy scale (JES) systematic also has this feature of being independent of the background systematic and we even recalculate the acceptance when coming up with our $\sigma_\pm$ (see section 8.7, equation 8.27). Likewise, our vertex reweighting scheme of section 8.4 accounted for the potential interplay when we would refit our background estimations after applying the last iterations of weights. We also observed that varying the jet energy scale even in the highest jet multiplicities had a $<0.2\%$ effect on our MC vertex weight calculation.

The one combination of systematics that we would expect full correlation (more precisely full *anti-correlation*) and have not addressed is in the unfolding factor being applied with the jet energy scale. This follows as the jet energy scale effects our calorimeter based

cross-section and in our unfolding via the MC (see equation 5.6 on page 181). A similar correlation was internally address for our background fitting estimation systematic which had our fitting fractions completely correlated due to their sum being unity. Taking all the other systematics as uncorrelated we have the total (bin-by-bin) systematic uncertainty, Δf, as

$$(8.35) \qquad \Delta f = \sqrt{\Delta_{\mathrm{Lum}}^2 + \Delta_{\mathrm{Vtx}}^2 + \Delta_{\mathrm{PDF}}^2 + \Delta_{\mathrm{FSR}}^2 + \Delta_{\mathrm{Fit}}^2 + \Delta_{\mathrm{Top}}^2 + (\Delta_{\mathrm{JES}} - \Delta_{\mathrm{u}})^2}$$

Here we have denoted the various error components of Δf as Δ_{sys} for each systematic, sys $\in$ {Lum, Vtx, PDF, FSR, Fit, Top, JES, u} via each of the proceeding section of this chapter. The mapping of the systematics is straightforward. The key here is that we have accounted for the effect of the anti-correlation between the jet energy scale (JES) and the unfolding (u) in equation 8.35 while the remaining systematic errors are taken in quadrature.

We now consider $\Delta(f/\sigma)$ the error for our differential cross-sections normalized to the relevant inclusive jet multiplicity cross-section. Technically we are still applying the resulting ratio (f/σ) to the basic formulation of equation 8.35 but now we have to consider the total correlation of the *same* systematics. For example, the jet energy scale systematics for the jet multiplicity for ≥ 1 cross-section (σ_1) will obviously correlate (positively) with the first leading jet p_T cross-section $(\mathrm{d}\sigma_1/\mathrm{d}p_T^{1st})$.

We calculate the uncertainty for a given systematic by varying both numerator and dominator together and noting the difference. Let Δf be the systematic uncertainty on the differential cross-section for a given systematic and like wise for $\Delta\sigma$ for the jet

multiplicity cross-section. The the uncertainty on the quotient, $\Delta(f/\sigma)$, goes as

$$(8.36) \qquad \Delta\left(\frac{f}{\sigma}\right) = \frac{1}{2}\left|\frac{f+\Delta f}{\sigma+\Delta\sigma} - \frac{f-\Delta f}{\sigma-\Delta\sigma}\right|$$

which can also be written in terms of an absolute difference between the relative errors:

$$(8.37) \qquad \Delta\left(\frac{f}{\sigma}\right) = \left(\frac{f/\sigma}{1-(\Delta\sigma/\sigma)^2}\right)\left|\frac{\Delta f}{f} - \frac{\Delta\sigma}{\sigma}\right|$$

The latter equation without the $(\Delta\sigma/\sigma)^2$ term would be identical to the case where we have 100% negative correlation. Once $\Delta(f/\sigma)$ has been calculated for all systematics via equation 8.36 we then treat the measurement as we did in equation 8.35. We note, as advertised in section 8.1 that the pure luminosity systematic will completely cancel since there is no dependence jet multiplicity or otherwise. As a result, Δ_{Lum} will uniformly negated in our (bin-by-bin) relative error. The acceptance related systematics will also cancel out if the differential cross-section (f) and (σ) are of the same jet multiplicity. This is true for our PDF, FSR (if applicable), and vertex reweighting (Vtx). An example where acceptance does not go to zero is $(\mathrm{d}\sigma/\mathrm{d}n)/\sigma_0$ for the $n \neq 0$ bins.

The are two additional ratio measurements that we make that we will note in passing. First the σ_{n+1}/σ_n and secondly $r_{\Delta\eta}$. It turns out that the basic solution is to follow the procedure outline above (using equation 8.36) by noting that now the dominator caries a bin-by-bin error rather than a flat error to be compared to the nominator bin-by-bin. Let us define f and g to be differential cross-sections with the same basic observable and histogram binning. Furthermore, let Δf and Δg be their respected error for a given

systematic. We account for the systematic uncertainty in f/g via $\Delta(f/g)$ defined by

$$(8.38) \qquad \Delta\left(\frac{f}{g}\right) = \frac{1}{2}\left|\frac{f+\Delta f}{g+\Delta g} - \frac{f-\Delta f}{g-\Delta g}\right|$$

We then combine the systematics as normal via equation 8.35.

On a final note when dealing with potentially asymmetric systematic errors (such as the jet energy) we always check to guarantee that the positive and negative errors bracket the central value. In the rare cases where this is not the case we revert to the procedure use for the jet energy scale using equations 8.28 and 8.29 where $\sigma_\pm$ are the respective upper and bottom limit for the error bar.

8.10. Relative Systematic Uncertainties

In this section we present our systematic uncertainties for each cross-section distribution (see the next chapter). In these plots the systematic uncertainties are presented as the relative error to the cross-section measurement (i.e. $\Delta\sigma/\sigma$). We do this across the range of the observable in question (e.g. m_{jj} for $\mathrm{d}\sigma/\mathrm{d}m_{jj}$) to show the potential bin-by-bin dependence. The total systematic (which is potentially asymmetric) is added together via the prescription in the previous section and this systematic (absent the luminosity which is held separate) is then present in our final cross-section plots which are detailed in the next section. Appendix will feature this total systematic uncertainty in table form.

As noted in section 8.1, the luminosity error is not shown due to it having no dependence variable. For a similar reason, we also omit the global systematic we apply

via our vertex reweighting in section 8.4 and likewise for FSR (assuming it is applicable). We do include the acceptance error (denoted as **Acceptance**) via our PDF, α_S, and efficiency uncertainties as described section 8.2 which only has a jet multiplicity dependence but is otherwise flat in our jet kinematic related differential cross-sections. We reiterate that these last four systematics completely cancel out in many of our ratio cross-section/observables or reduced cross-sections (see section 9.1).

For comparison, we include the natural random uncertainty in the bin-by-bin sample size and denote this as the **Poisson** error. The background fitting systematic of section 8.5 will be noted as **Background**. The other background systematic comes from the $t\bar{t}$ cross-section of section 8.6 which we label as **$t\bar{t}$ σ(Theory)**. The jet energy scale systematic discussed in section 8.7 we refer to as **Jet Energy**. Finally the unfolding systematic from section 8.8 is unimaginatively called **Unfolding**.

Our relative systematic uncertainties or, more simply, our relative errors start at figure 8.5 and end at figure 9.52. Rather than write out a description of each figure in detail we provide a mapping via table 8.8 for our relative errors with respect to their corresponding cross-sections. The Cross-section and Section columns of the table describe the differential cross-section (or ratio of) and its corresponding section in the next chapter. Table 8.8 then provides the relative error plot's figure number (#) and then its associated cross-section. The third and fourth columns are for the electrons results while the latter two are for the muons. There are no direct systematic error plots corresponding with the results of figures 9.25 through 9.32 as these are identical to our normalized results for $d\sigma/dp_T^{n^{\text{th}}}$. In other words, figures 8.19-8.26 map to 9.25-9.32, correspondingly.

Cross-section	Section #	$W \to e\nu$ $\Delta\sigma/\sigma$ Figure #	$W \to e\nu$ σ Figure #	$W \to \mu\nu$ $\Delta\sigma/\sigma$ Figure #	$W \to \mu\nu$ σ Figure #
$\frac{\mathrm{d}\sigma}{\mathrm{d}n}$	9.3	8.5	9.3	8.6	9.4
$\frac{\sigma_n}{\sigma_0}$	9.3	8.7	9.5	8.8	9.6
$\frac{\sigma_{n+1}}{\sigma_n}$	9.4	8.9	9.7	8.10	9.8
$\frac{\mathrm{d}\sigma}{\mathrm{d}p_T^{1st}}$	9.5	8.11	9.9	8.15	9.13
$\frac{\mathrm{d}\sigma}{\mathrm{d}p_T^{2nd}}$	9.5	8.12	9.10	8.16	9.14
$\frac{\mathrm{d}\sigma}{\mathrm{d}p_T^{3rd}}$	9.5	8.13	9.11	8.17	9.15
$\frac{\mathrm{d}\sigma}{\mathrm{d}p_T^{4th}}$	9.5	8.14	9.12	8.18	9.16
$\frac{\mathrm{d}\sigma/\mathrm{d}p_T^{1st}}{\sigma_1}$	9.5	8.19	9.17	8.23	9.21
$\frac{\mathrm{d}\sigma/\mathrm{d}p_T^{2nd}}{\sigma_2}$	9.5	8.20	9.18	8.24	9.22
$\frac{\mathrm{d}\sigma/\mathrm{d}p_T^{3rd}}{\sigma_3}$	9.5	8.21	9.19	8.25	9.23
$\frac{\mathrm{d}\sigma/\mathrm{d}p_T^{4th}}{\sigma_4}$	9.5	8.22	9.20	8.26	9.24
$\frac{\mathrm{d}\sigma}{\mathrm{d}m_{jj}}$	9.7	8.27	9.33	8.28	9.34
$\frac{\mathrm{d}\sigma/\mathrm{d}m_{jj}}{\sigma_2}$	9.7	8.29	9.35	8.30	9.36
$\frac{\mathrm{d}\sigma}{\mathrm{d}R_{jj}}$	9.8	8.31	9.37	8.32	9.38
$\frac{\mathrm{d}\sigma/\mathrm{d}R_{jj}}{\sigma_2}$	9.8	8.33	9.39	8.34	9.40
$\frac{\mathrm{d}\sigma_2}{\mathrm{d}\Delta\eta}$	9.9	8.35	9.43	8.36	9.44
$\frac{\mathrm{d}\sigma_2/\mathrm{d}\Delta\eta}{\sigma_2}$	9.9	8.37	9.45	8.38	9.46
$\frac{\mathrm{d}\sigma_3}{\mathrm{d}\Delta\eta}$	9.9	8.39	9.47	8.40	9.48
$\frac{\mathrm{d}\sigma_3/\mathrm{d}\Delta\eta}{\sigma_3}$	9.9	8.41	9.49	8.42	9.50
$r_{\Delta\eta}$ (Eq. 9.6)	9.9	8.43	9.51	8.44	9.52

Table 8.8. The mapping of each relative error ($\Delta\sigma/\sigma$) figure with its corresponding cross-section (σ) figure for each cross-section observable
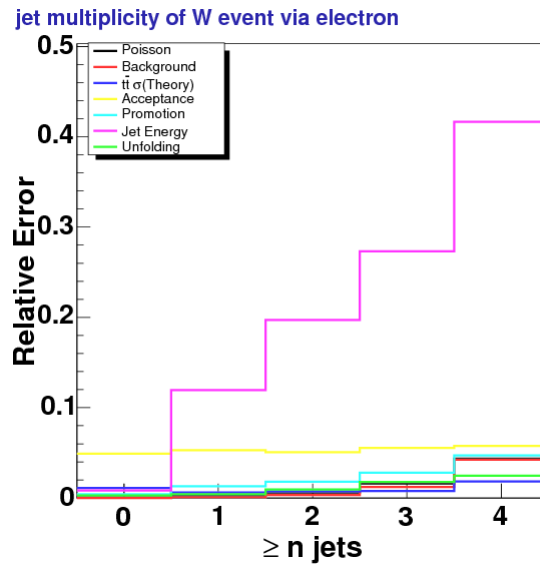
Figure 8.5. Relative Errors for $W \to e\nu$ jet multiplicity (companion of Fig. 9.3)
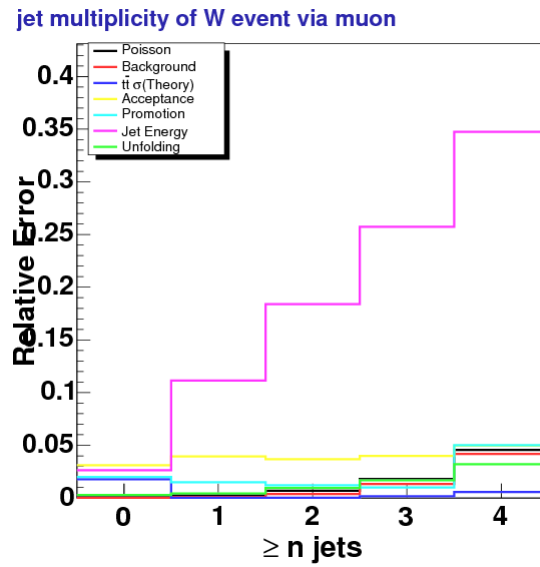
Figure 8.6. Relative Errors for $W \to \mu\nu$ jet multiplicity (companion of Fig. 9.4)
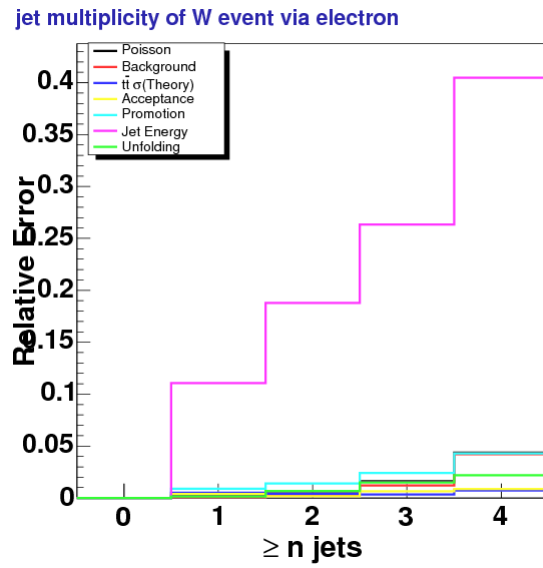
Figure 8.7. Relative Errors for $W \to e\nu$ jet multiplicity (companion of Fig. 9.5)
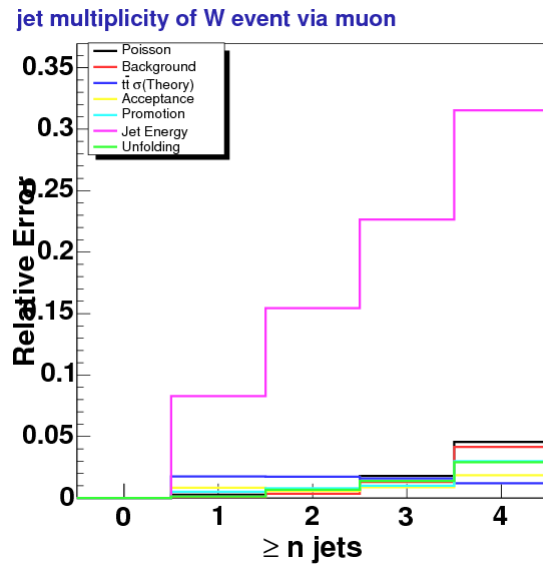
Figure 8.8. Relative Errors for $W \to \mu\nu$ jet multiplicity (companion of Fig. 9.6)
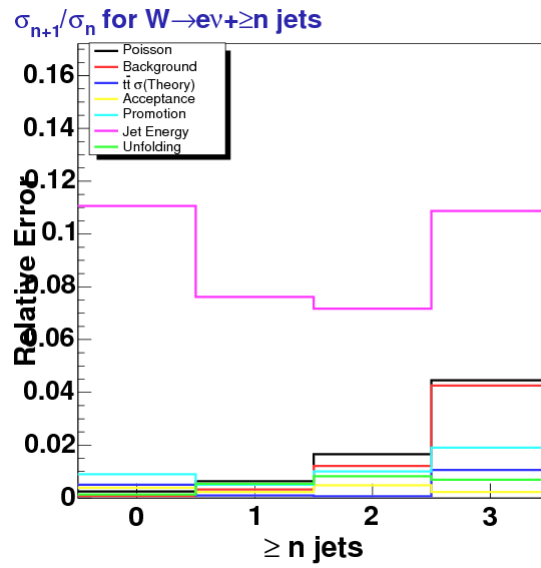
Figure 8.9. Relative Errors for $W \to e\nu$ σ_{n+1}/σ_n (companion of Fig. 9.7)
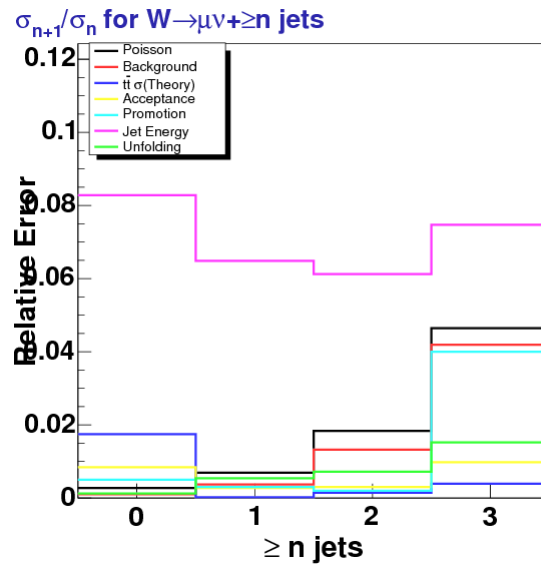
Figure 8.10. Relative Errors for $W \to \mu\nu$ σ_{n+1}/σ_n (companion of Fig. 9.8)
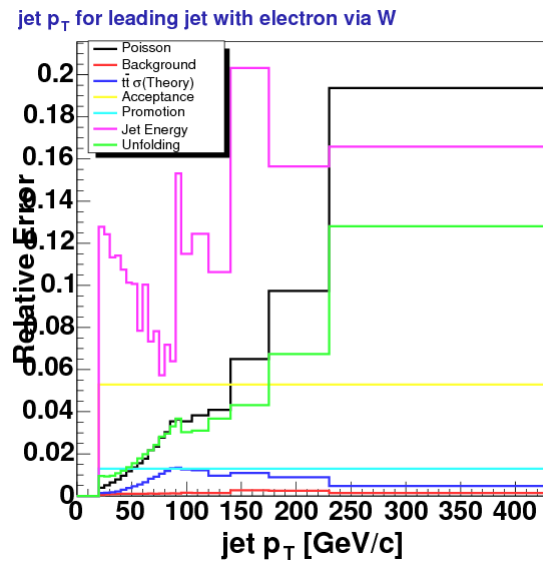
Figure 8.11. Relative Errors for Leading jet p_T for $W \to e\nu + \geq 1$ jet (companion of Fig. 9.9)
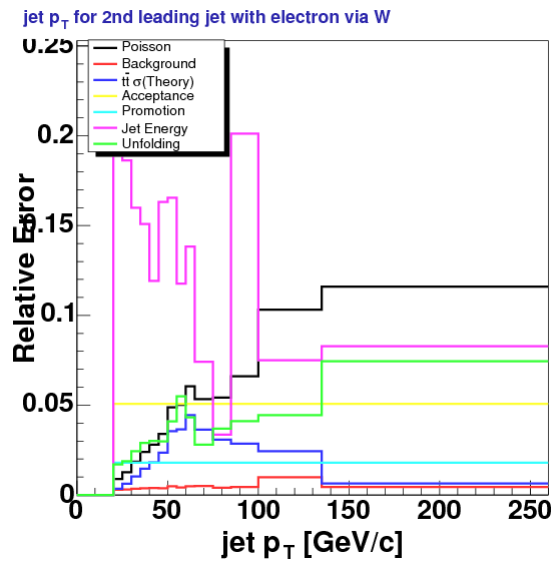
Figure 8.12. Relative Errors for 2nd leading jet p_T for $W \to e\nu + \geq 2$ jets (companion of Fig. 9.10)
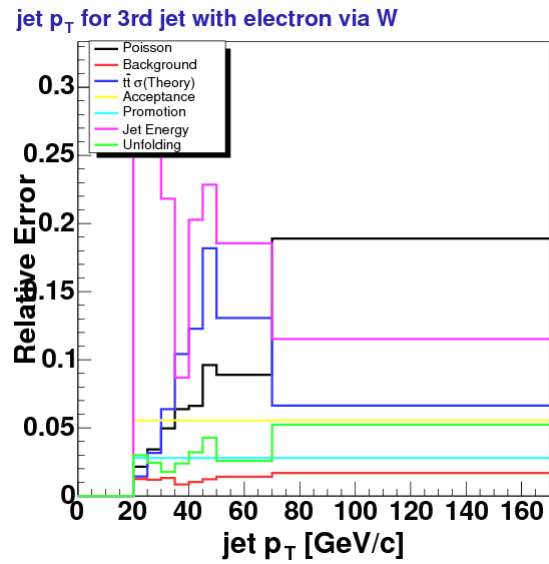
Figure 8.13. Relative Errors for 3rd leading jet p_T for $W \to e\nu+ \geq 3$ jets (companion of Fig. 9.11)
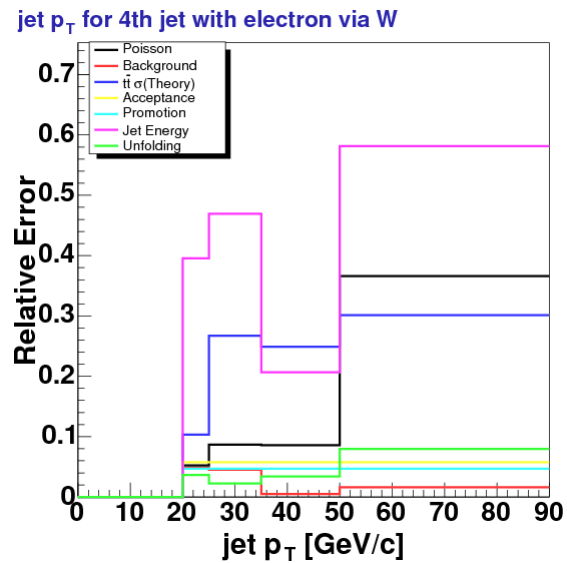
Figure 8.14. Relative Errors for 4th leading jet p_T for $W \to e\nu+ \geq 4$ jets (companion of Fig. 9.12)
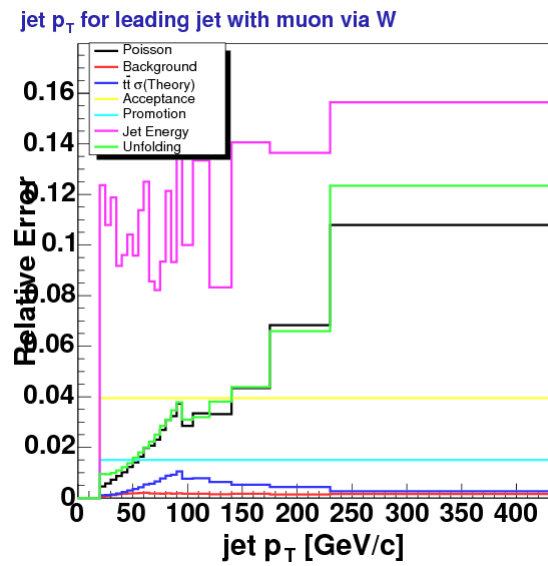
Figure 8.15. Relative Errors for Leading jet p_T for $W \to \mu\nu + \geq 1$ jet (companion of Fig. 9.13)
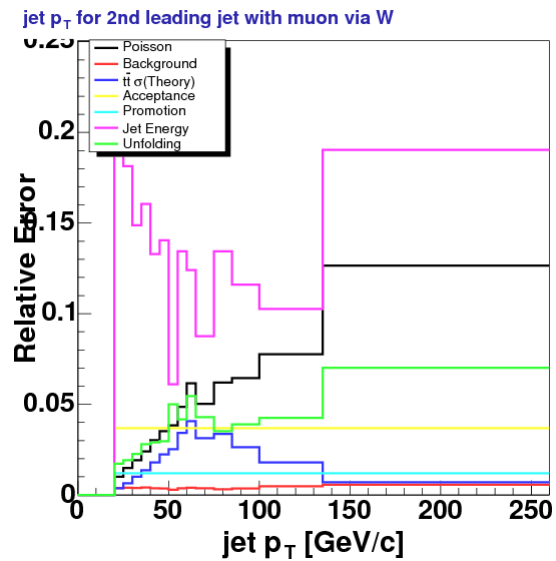
Figure 8.16. Relative Errors for 2nd leading jet p_T for $W \to \mu\nu + \geq 2$ jets (companion of Fig. 9.14)
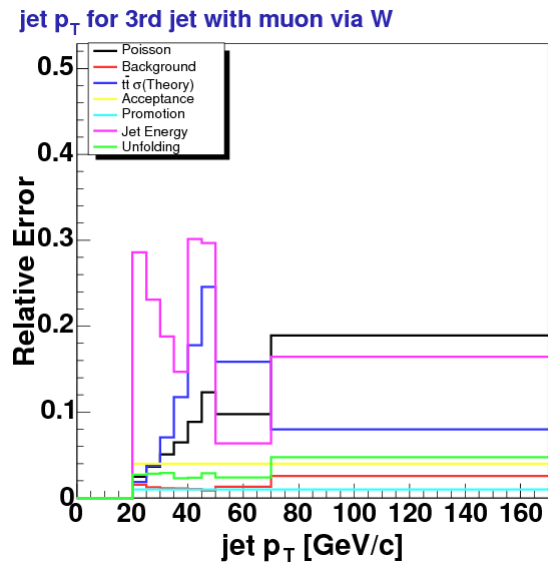
Figure 8.17. Relative Errors for 3rd leading jet p_T for $W \to \mu\nu + \geq 3$ jets (companion of Fig. 9.15)
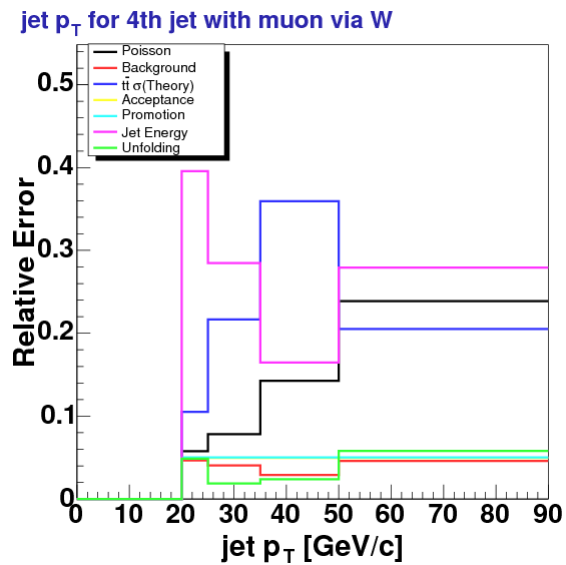
Figure 8.18. Relative Errors for 4th leading jet p_T for $W \to \mu\nu + \geq 4$ jets (companion of Fig. 9.16)
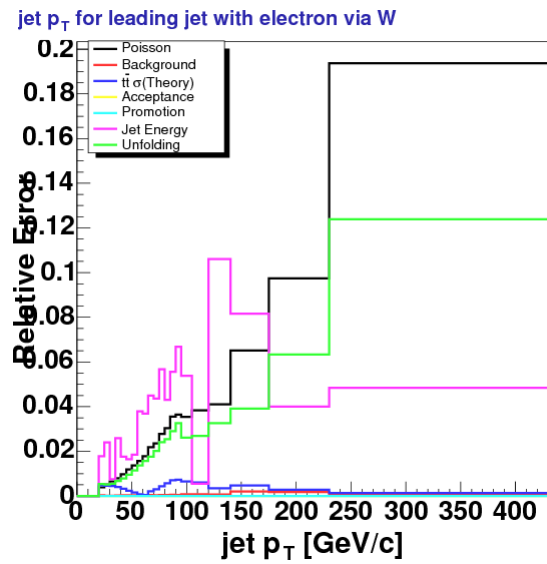
Figure 8.19. Relative Errors for Leading jet p_T for $W \rightarrow e\nu+ \geq 1$ jet (companion of Fig. 9.17)
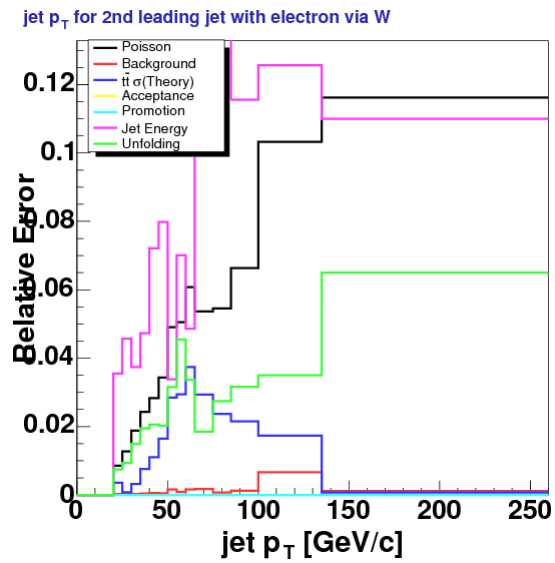
Figure 8.20. Relative Errors for 2nd leading jet p_T for $W \rightarrow e\nu+ \geq 2$ jets (companion of Fig. 9.18)
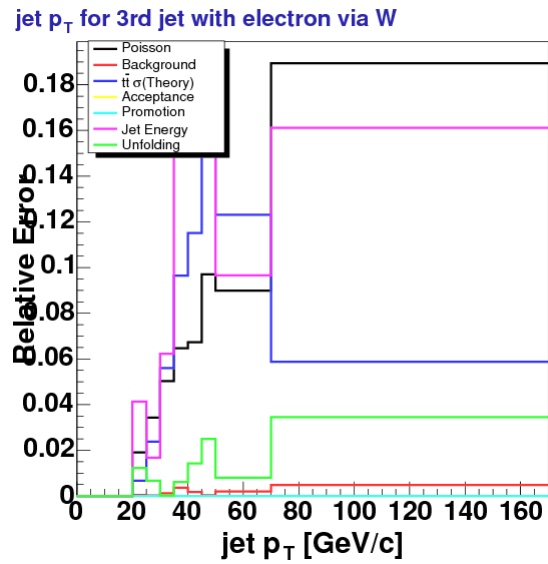
Figure 8.21. Relative Errors for 3rd leading jet p_T for $W \to e\nu + \geq 3$ jets (companion of Fig. 9.19)
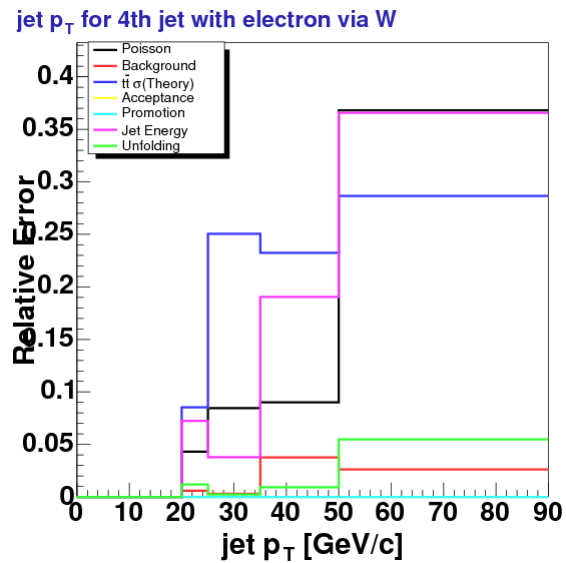
Figure 8.22. Relative Errors for 4th leading jet p_T for $W \to e\nu + \geq 4$ jets (companion of Fig. 9.20)
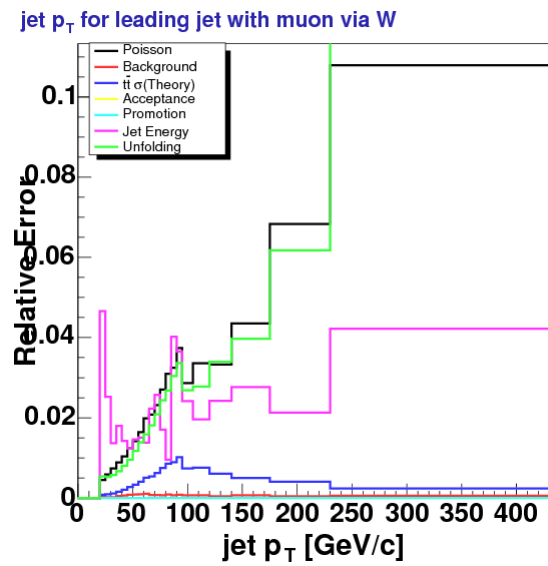
Figure 8.23. Relative Errors for Leading jet p_T for $W \to \mu\nu+ \ge 1$ jet (companion of Fig. 9.21)
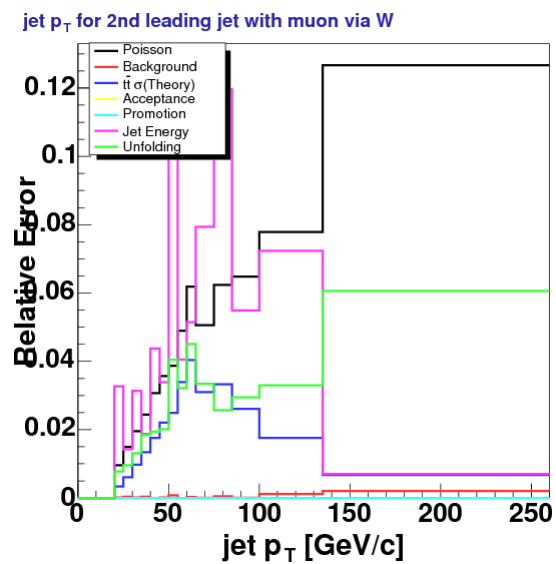
Figure 8.24. Relative Errors for 2nd leading jet p_T for $W \to \mu\nu+ \ge 2$ jets (companion of Fig. 9.22)

404
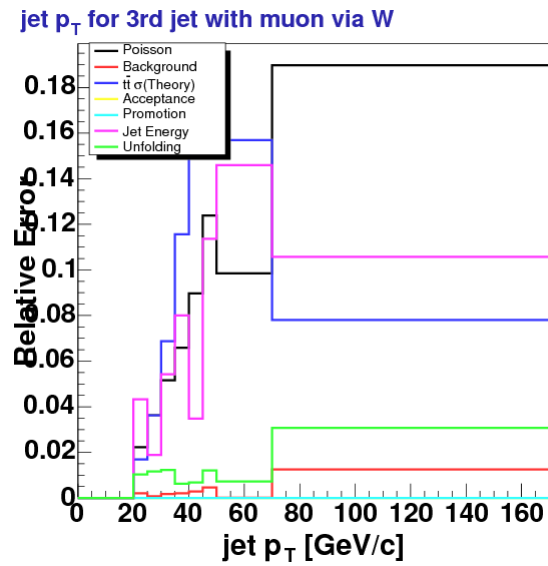
Figure 8.25. Relative Errors for 3rd leading jet p_T for $W \rightarrow \mu\nu + \geq 3$ jets (companion of Fig. 9.23)
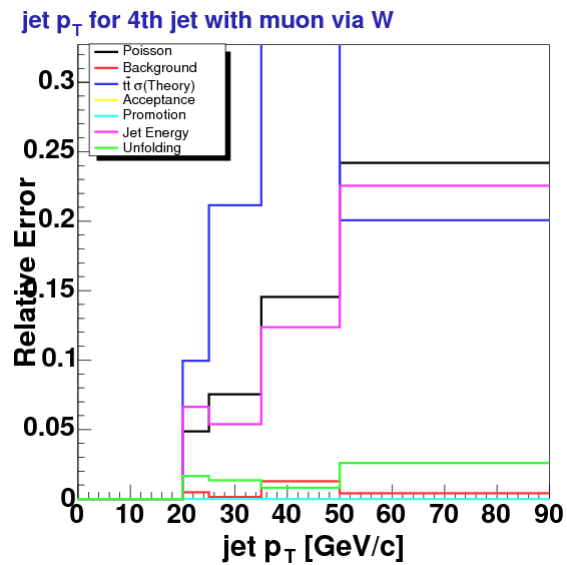
Figure 8.26. Relative Errors for 4th leading jet p_T for $W \rightarrow \mu\nu + \geq 4$ jets (companion of Fig. 9.24)

405
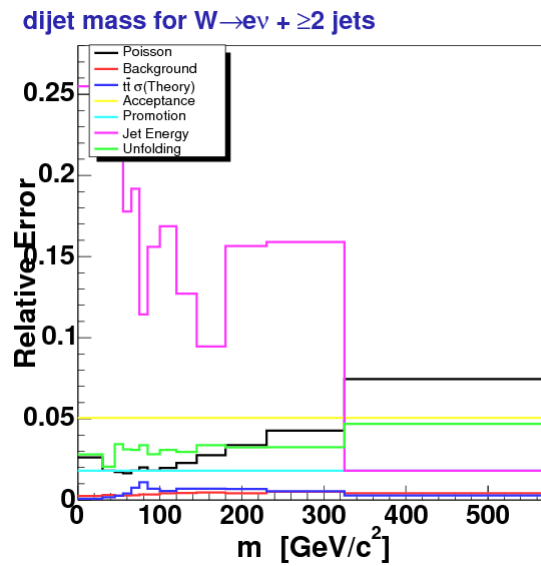
Figure 8.27. Relative Errors for Dijet Mass Cross-section for $W \to e\nu+ \geq$ 2 jets (companion of Fig. 9.33)
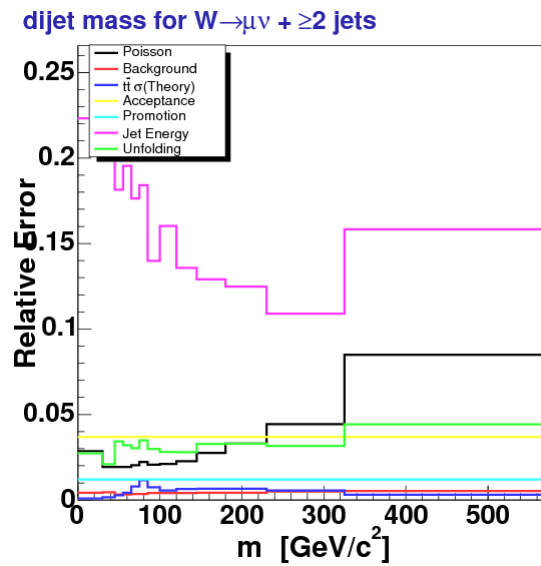
Figure 8.28. Relative Errors for Dijet Mass Cross-section for $W \to \mu\nu+ \geq$ 2 jets (companion of Fig. 9.34)
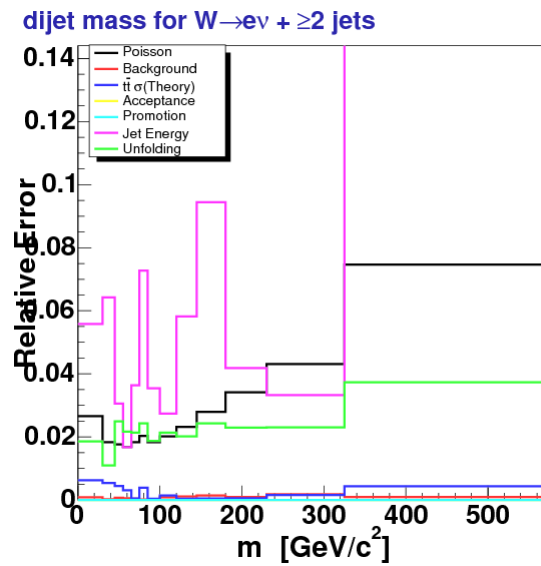
Figure 8.29. Relative Errors for Dijet Mass Cross-section for $W \to e\nu+ \geq$ 2 jets (companion of Fig. 9.35)
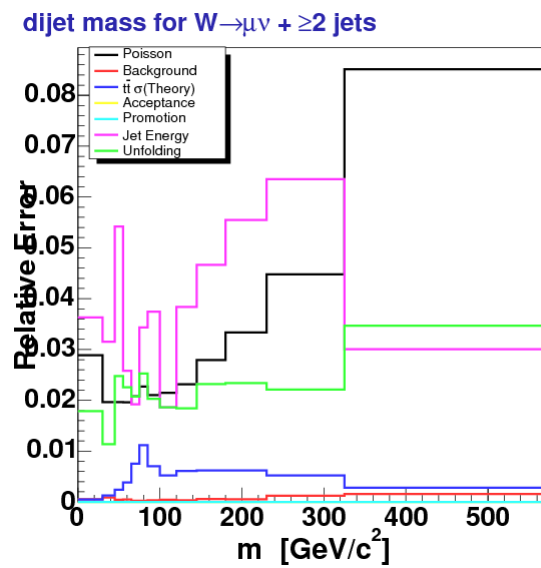
Figure 8.30. Relative Errors for Dijet Mass Cross-section for $W \to \mu\nu+ \geq$ 2 jets (companion of Fig. 9.36)
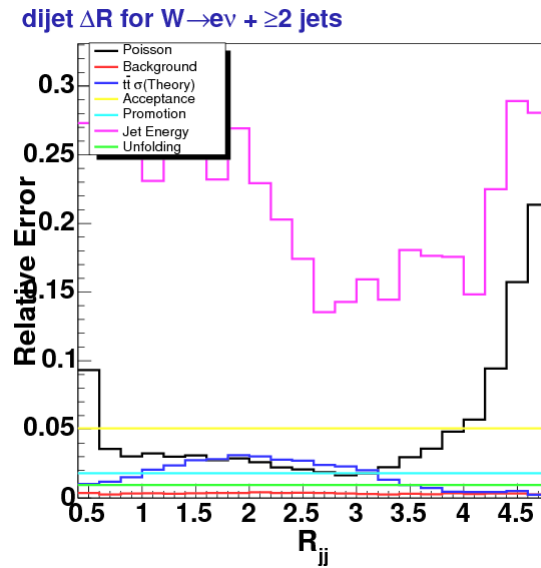
Figure 8.31. Relative Errors for Dijet Separation Cross-section for $W \to e\nu+ \geq 2$ jets (companion of Fig. 9.37)
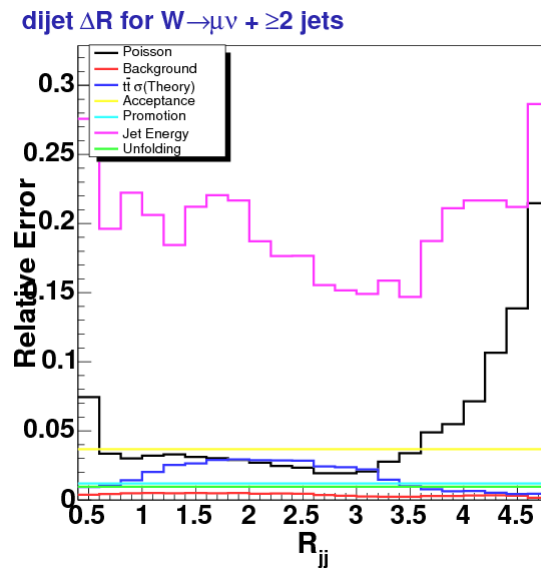
Figure 8.32. Relative Errors for Dijet Separation Cross-section for $W \to \mu\nu+ \geq 2$ jets (companion of Fig. 9.38)

408
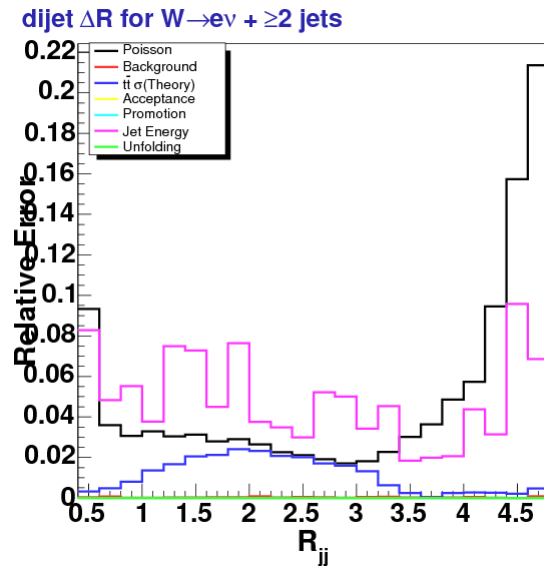
Figure 8.33. Relative Errors for Dijet Separation Cross-section for $W \to e\nu+ \geq 2$ jets (companion of Fig. 9.39)
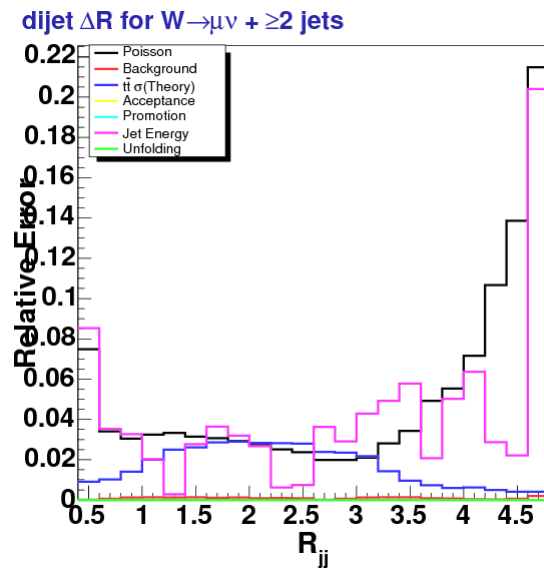
Figure 8.34. Relative Errors for Dijet Separation Cross-section for $W \to \mu\nu+ \geq 2$ jets (companion of Fig. 9.40)
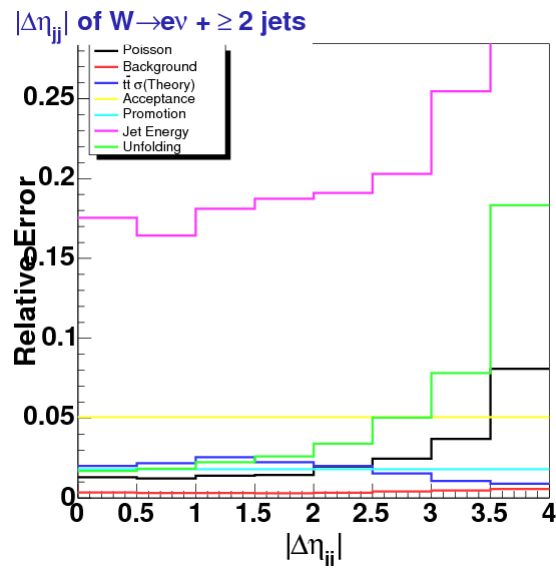
Figure 8.35. Relative Errors for $\Delta\eta$ Cross-section for $W \rightarrow e\nu+ \geq 2$ jets (companion of Fig. 9.43)
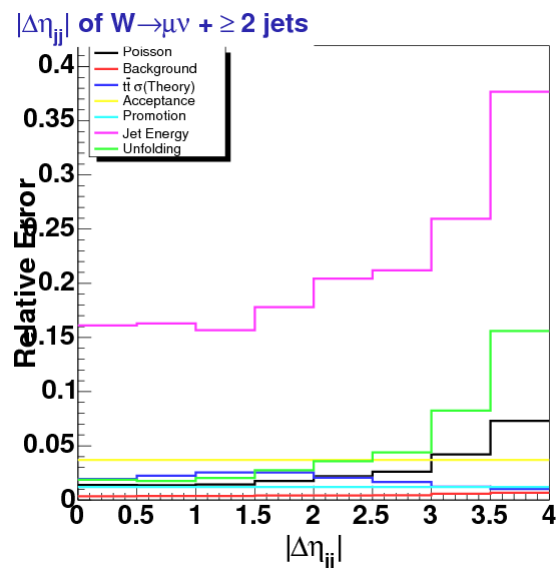
Figure 8.36. Relative Errors for $\Delta\eta$ Cross-section for $W \rightarrow \mu\nu+ \geq 2$ jets (companion of Fig. 9.44)
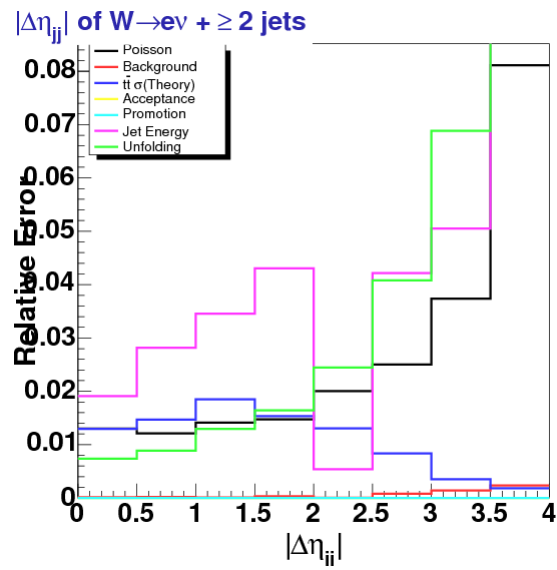
Figure 8.37. Relative Errors for $\Delta\eta$ Cross-section for $W \rightarrow e\nu + \geq 2$ jets (companion of Fig. 9.45)
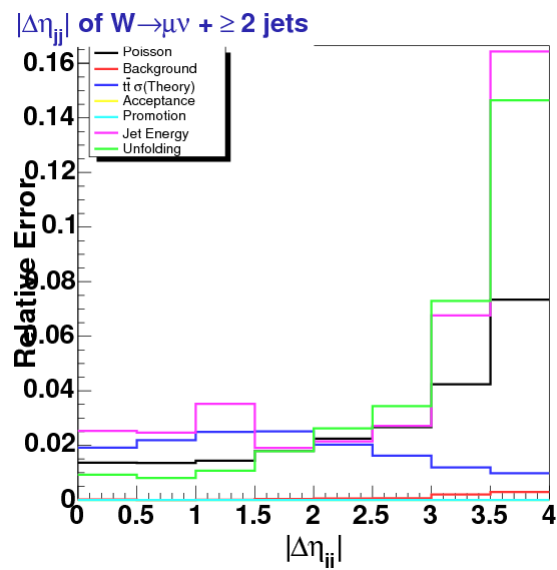
Figure 8.38. Relative Errors for $\Delta\eta$ Cross-section for $W \rightarrow \mu\nu + \geq 2$ jets (companion of Fig. 9.46)
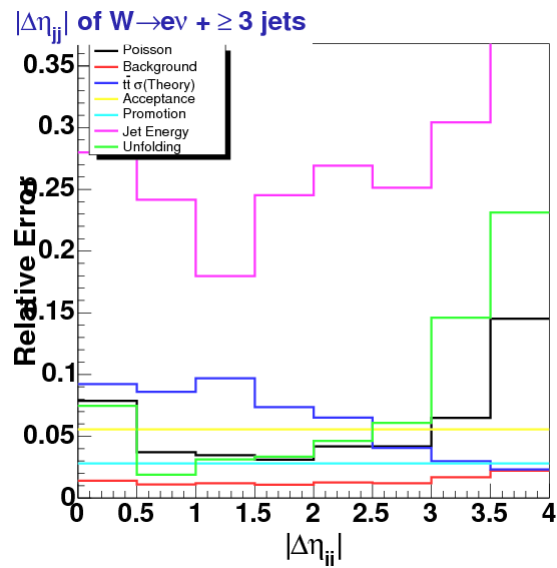
Figure 8.39. Relative Errors for $\Delta\eta$ Cross-section for $W \to e\nu+ \geq 3$ jets (companion of Fig. 9.47)
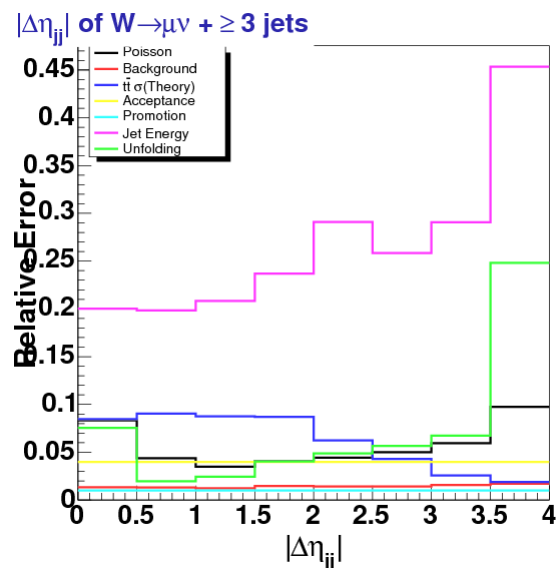
Figure 8.40. Relative Errors for $\Delta\eta$ Cross-section for $W \to \mu\nu+ \geq 3$ jets (companion of Fig. 9.48)
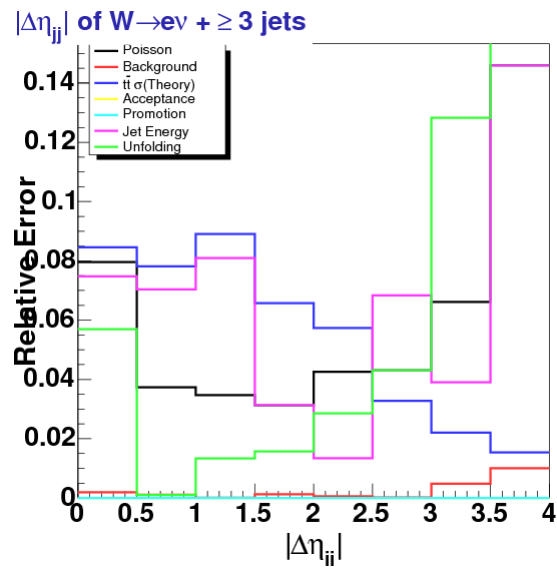
Figure 8.41. Relative Errors for $\Delta\eta$ Cross-section for $W \rightarrow e\nu+ \geq 3$ jets (companion of Fig. 9.49)
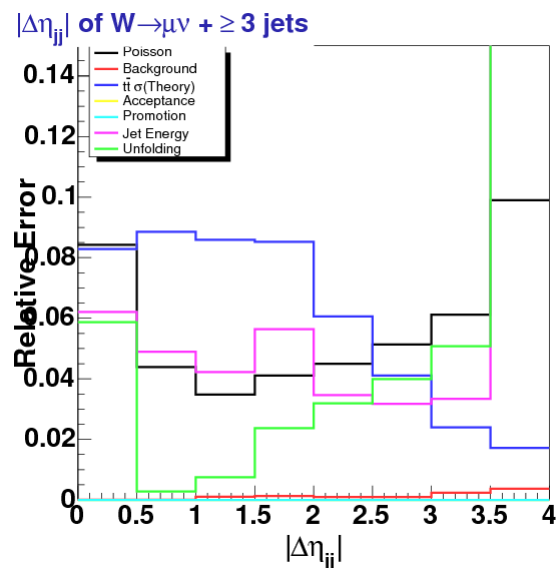
Figure 8.42. Relative Errors for $\Delta\eta$ Cross-section for $W \rightarrow \mu\nu+ \geq 3$ jets (companion of Fig. 9.50)
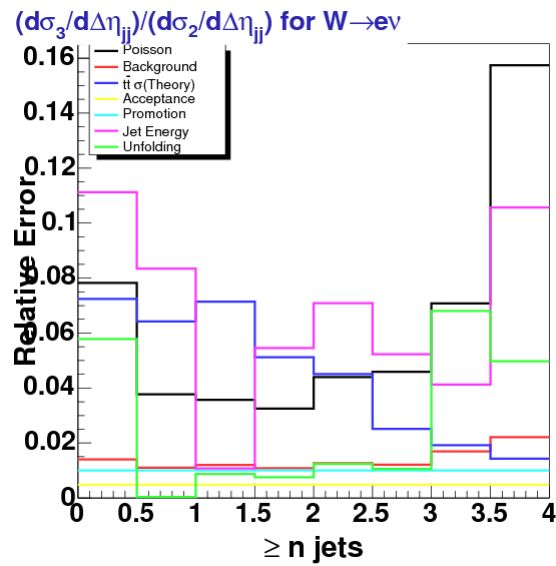
Figure 8.43. Relative Errors for $\Delta\eta$ Cross-section for $W \to e\nu+ \geq 3$ jets (companion of Fig. 9.51)
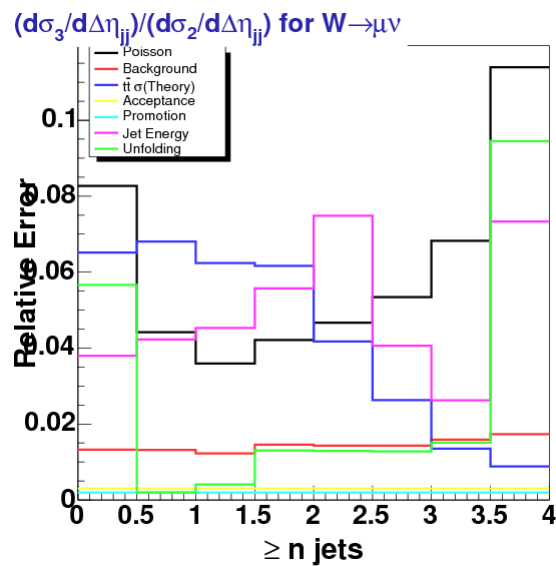
Figure 8.44. Relative Errors for $\Delta\eta$ Cross-section for $W \to \mu\nu+ \geq 3$ jets (companion of Fig. 9.52)

CHAPTER 9

Results

In this chapter we present our final results. These include various differential cross-sections for jet kinematic variables. Cross-section measurements can be defined as production level (e.g. $\sigma(p\bar{p} \to W+ \geq n \text{ jets})$) or as an acceptance limited cross-section where the reduced acceptance as defined in Section 7.4. The motivation for the former is to have the actual extrapolated production cross-section at the Tevatron. This will be used on our jet multiplicity cross-section in section 9.3. While slightly unorthodox, the latter reduced cross-section definition is motivated as a way to remove any MC acceptance dependence for non-acceptable Ws at the `hepg` level and to generally provide a more theory friendly result for comparison. In particular, this cross-section definition can be used to compare to NLO theoretical results assuming the same W acceptance space definition. However, we do not present cross-sections that have been corrected to the particle level but rather corrected to the hadron level in order to remove detector and simulation dependence (as explained in section 5.8).

In addition, we present normalized cross-sections that are normalized to the respective inclusive n^{th} jet multiplicity cross-section such that their integral is unity. Ergo these shape observables provided a means of comparison between predictions outside any universal scale factor. The other big motivation, is that normalizing to the inclusive jet multiplicity cross-section also cancels out or diminishes the systematic uncertainties.

Luminosity, acceptance, efficiency, and vertex reweighing (promotion) systematics completely cancel as they are common in both measurements. We also account for the correlated effect between systematics as explained at the end of section 8.9. This effectively reduces our systematics for the dominate uncertainties like the jet energy scale and thus strengthening the power for comparison.

We present our general cross-section definition in the next section. In section 9.2, we briefly touch on our use of Alpgen as a basic theoretical comparison to our data and highlight on future NLO predictions. Each of the later sections gives the appropriate definitions for our observables and then, typically, incorporates our observables into a differential cross-section and present and explained our results therein.

We begin presenting our results starting with the inclusive jet multiplicity cross-section of section 9.3. Also presented are some cross-section ratios between different quantiles. This includes the jet multiplicity ratios of section 9.4. Next we present the nth leading jet p_T differential cross-sections for n=1-4 in section 9.5. The subsequent section provides the results of comparing the bin-by-bin ratio of our n^{th} leading order jet p_T differential cross-section with a simple theoretical prediction from our W Alpgen MC in order to facilitate a better comparison.

Sections 9.7 and 9.8 deal with two of our dijet cross-sections. The former is the dijet mass (m_{jj}) spectrum while the latter is for the dijet separation (R_{jj}). We discuss our pseudo-rapidity separation of the farthest two jets ($\Delta \eta$) results in section 9.9 which includes results for both ≥ 2 and ≥ 3 results as well as a bin-by-bin ratio for said results.

In addition to the discussion of these results in each respective section, we also present these same results in table form with the relevant observables (cross-sections, shapes,

and ratios etc.) in appendix . It includes the measured value from data and the total systematic error (generally asymmetric with respect to the central value) for each variable bin. We provide a summary of the analysis as a whole in the final chapter.

9.1. Cross-section definition

In this analysis we are looking for cross-sections which we denote as a production cross-section with branching ratio for the final state (which we write explicitly)

$$\sigma_{\text{production}} = \sigma(p\bar{p} \to W + \text{jets}) \times Br(W \to \ell\nu)$$

or via equation 7.16 (page 352)

$$\sigma_{\text{reduced}} = \sigma(p\bar{p} \to W + \text{jets}|[a_{\text{hepg}}]) \times Br(W \to \ell\nu)$$

or

$$\sigma_{\text{reduced}} = a_{\text{hepg}} \times \sigma_{\text{production}} \tag{9.1}$$

for our reduce cross-section. We define our cross-section (denoted here as simply σ)

$$\sigma = u \left(\frac{N_{data} - B}{LA\epsilon} \right) \tag{9.2}$$

where u is the unfolding scale factor of section 5.9, N_{data} is the number of candidate W events from data, B is the sum of all the estimated backgrounds, and $LA\epsilon$ is the effective luminosity. The last quantity is the total summed product of the measured integrated luminosity, the W and jet acceptance via MC, and the detector and trigger efficiencies for

each run period and subdetector types (the latter applicable to muons only) as defined in chapter 7.

The only difference between the nominal production cross-section and the reduced version is in the acceptance as noted in section 7.4. Thus we substitute $\bar{A} = A/a_{hepg}$ in the equation above for A and calculating the reduced cross-section (alternatively this follows from equation 9.1). In point of fact we only consider the production level cross-section for our first observable: the inclusive jet multiplicity (see section 9.3). Otherwise, all cross-sections (including derivative observables) use the reduce cross-section definition.

Derived observables using cross-section ratios (normalized cross-sections and quantities like σ_{n+1}/σ_n defined below) are calculated by simply performing the desire quotient. No simplification is used in eliminating terms that ought to cancel. This is done to have these results in lock step with the procedure for calculating systematics and the potential for systematics to cancel due to correlations. It also serves as good cross-check for the general procedure.

9.2. Theory Predictions

For the purpose of this analysis we have utilized our Alpgen MC ($W + \#$p samples explained in section 3.5) as the theoretical prediction. Originally, we were going to compare to NLO theory predictions from two different groups looking at up to ≥ 3 jets for V+jets. The first was MCFM NLO [91] and the other was "BlackHat" [92]. Unfortunately, we were not able to implement these comparisons for this work. However, given the detail in which we present our results (i.e. the full cross-section results in appendix) this work remains open to further inquiry.

$W \to e\nu$	$W \to \mu\nu$
$|\eta_e| \leq 1.1$	$|\eta_\mu| \leq 1.0$
$p_T^e \geq 20$ GeV/c	$p_T^\mu \geq 20$ GeV/c
$M_T^W \geq 40$ GeV/c^2	$M_T^W \geq 30$ GeV/c^2

Table 9.1. $W \to \ell\nu$ generator level selection cuts used in our redefined cross-section with reduced acceptance. We use the *post* final state radiation lepton for our cuts in order to be consistent with our treatment in section 7.4 (page 350). While similar, the electron and muon channels have different cuts and thus theory predictions would necessarily represent different cross-section observables as noted in section 7.5.

For the purpose of completeness, we present the necessary generator/theory cuts to be consistent with our redefined cross-section in table 9.1 which is a restatement of the cuts for our reduced acceptance noted in table 7.19 (page 358). From the stand point of MC simulation, these cuts exclude kinematic areas that may not be well modeled or understood and that do not contribute to the bulk of our expected W signal. From a theoretical prediction stand point (e.g. NLO predictions via MCFM), excluding these regions makes the calculation safer from the stand point of infrared and collinear divergences.

9.3. Jet Multiplicity Cross-section

In this section we show the results of the number of W events with an greater than or equal to n jets where $n \in \{0, 1, 2, 3, 4\}$. We formally note the jet multiplicity cross-section as a differential cross-section with $\geq n$ jets as $d\sigma/dn$. However, for simplicity and ease of use with other results, we shall hereafter refer to the jet multiplicity cross-section as σ_n.

The jet multiplicity measurement is the base observable in this W+jets analysis and is used to normalize the cross-sections to get the shape of various jet kinematic variables that follow in later sections. Note that our measurement of the total inclusive ($W+ \geq 0$ jets) cross-section is not competitive to the already systematics limited analysis by CDF
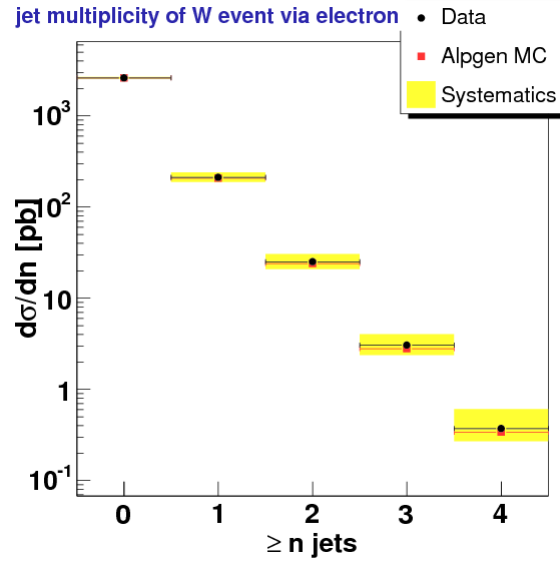
Figure 9.1. $W \rightarrow e\nu + \geq n$ jet multiplicity production level cross-section.

with 72 pb^{-1} [**93**], however it provides a good benchmark for comparison with the pure EWK measurement. In that W and Z analysis, the $W \rightarrow e\nu$ and $W \rightarrow \mu\nu$ had respective total inclusive cross-sections measurements of $2780 \pm 14 \pm 60$ pb and $2768 \pm 16 \pm 64$ pb (the given uncertainty includes the Poisson and total systematic uncertainty excluding the luminosity systematic of ± 166 pb). Our inclusive W cross-section measurement (σ_0) is $2710 \pm 2 \,^{+71}_{-62}$ pb and $2720 \pm 3 \,^{+119}_{-104}$ pb for the electron and muon channel, respectively. Our jet multiplicity cross-sections are presented numerically in tables .2 and .3. Thus as a crosscheck, these total inclusive results are consistent with each other and are also consistent with lepton universality.

The production level cross-section for the inclusive jet multiplicity is given in figures 9.1 ($W \rightarrow e\nu$) and 9.2 ($W \rightarrow \mu\nu$).

Figures 9.3 and 9.4 are the jet multiplicity cross-sections for the electron and muon channel, respectively. These and subsequent results have been corrected by our reduced
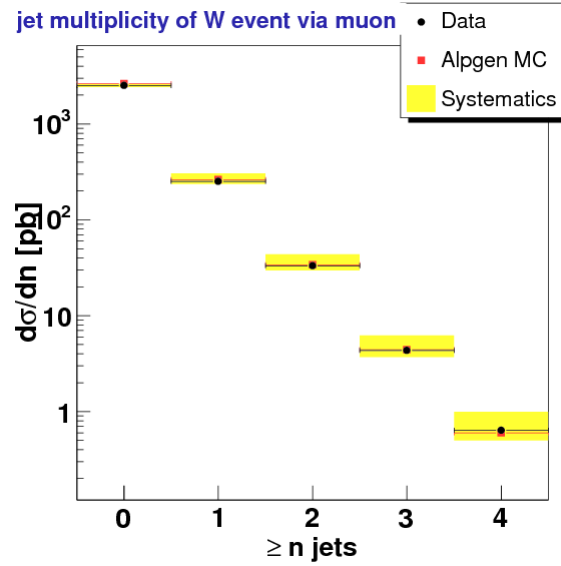
Figure 9.2. $W \to \mu\nu + \geq n$ jet multiplicity production level cross-section.

acceptance and no longer represent pure production level cross-sections. Figures 9.5 and 9.6 are normalized to the total inclusive cross-section (σ_0) and can be represented as $\sigma_n/\sigma 0$. All of these results are set to a common log scale showing, to a first approximation, an exponential decay structure. A better method of comparing the rate of cross-section change verses jet multiplicity is done in the next section.

Our understanding of the jet multiplicity cross-section is constrained in the higher jet multiplicities by the jet energy scale systematic as well as our $t\bar{t}$ background systematic. We investigated higher jet multiplicities (≥ 5 jets) but low event yields (for both data and background estimation) coupled by high systematics and technical limitations prevent us from presenting these results.
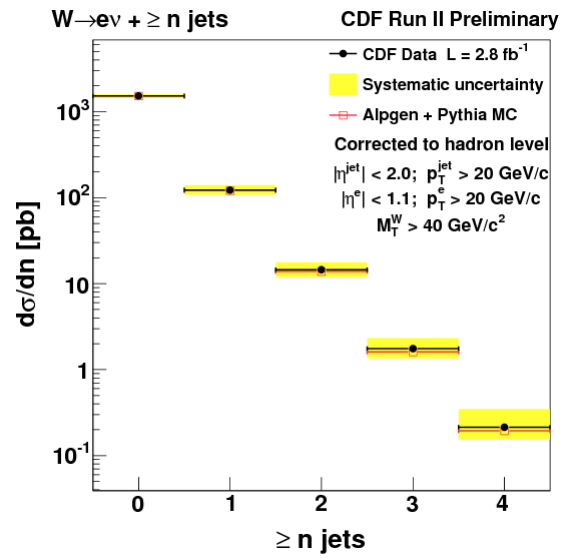
Figure 9.3. $W \to e\nu + \geq n$ jet multiplicity cross-section ($\sigma_n = \mathrm{d}\sigma/\mathrm{d}n$).
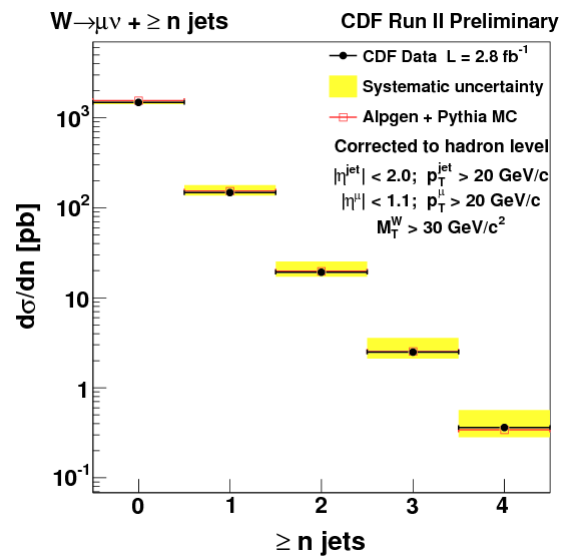
Figure 9.4. $W \to \mu\nu + \geq n$ jet multiplicity cross-section ($\sigma_n = \mathrm{d}\sigma/\mathrm{d}n$).
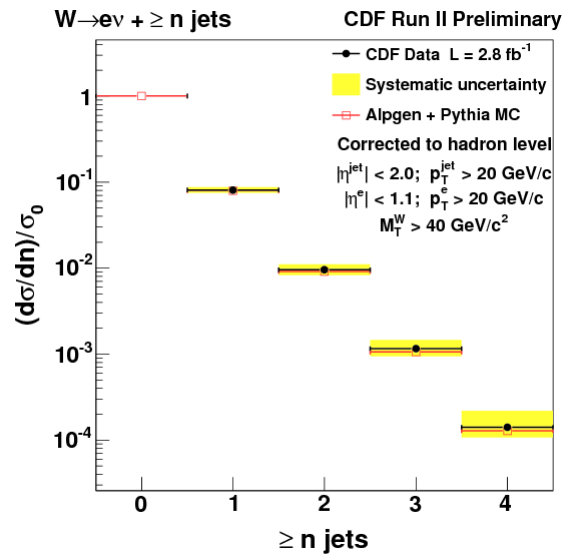
Figure 9.5. $W \to e\nu + \geq n$ jet multiplicity cross-section normalized to the total inclusive W cross-section (σ_n/σ_0). The first data point is unity without uncertainty by definition.
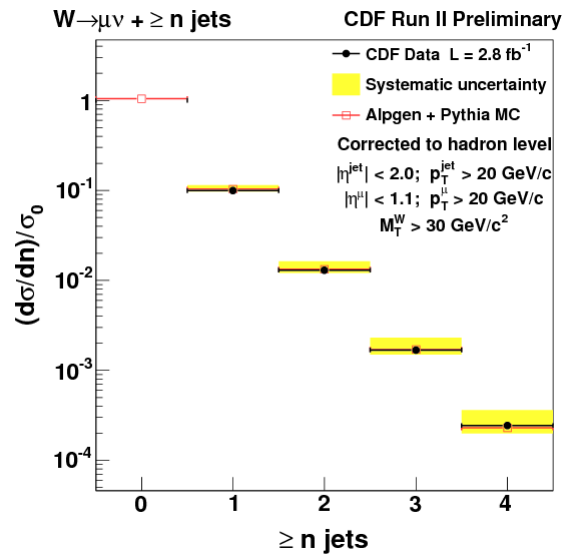
Figure 9.6. $W \to \mu\nu + \geq n$ jet multiplicity cross-section normalized to the total inclusive W cross-section (σ_n/σ_0). The first data point is unity without uncertainty by definition.
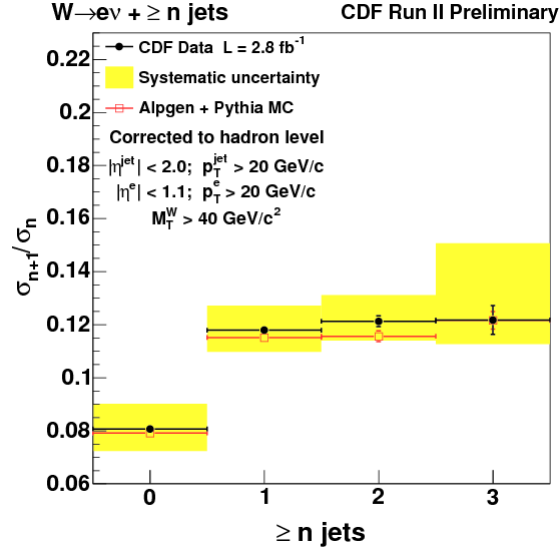
Figure 9.7. $W \to e\nu$ jet multiplicity cross-section ratio between $\geq (n+1)$ and $\geq n$ (σ_{n+1}/σ_n).

9.4. Jet Multiplicity Ratio, σ_{n+1}/σ_n

Via the results of the previous section, we construct a quotient based on the number of (inclusive) jets in a higher bin relative to the lower. For example, the $n{=}0$ ratio observable would be the $W+ \geq 1$ jet cross-section divided by the total inclusive W (i.e. ≥ 0 jets) cross-section. In general, via our notation of the previous section, we express this jet multiplicity ratio as

$$\frac{\sigma_{n+1}}{\sigma_n}$$

Note that although systematics are reduced by this ratio as they were in the σ_n/σ_0 observable, the acceptance×efficiency and other jet multiplicity dependent systematics do not completely cancel. The results are shown in figure 9.7 and figure 9.8 for the electrons and muons, respectively.
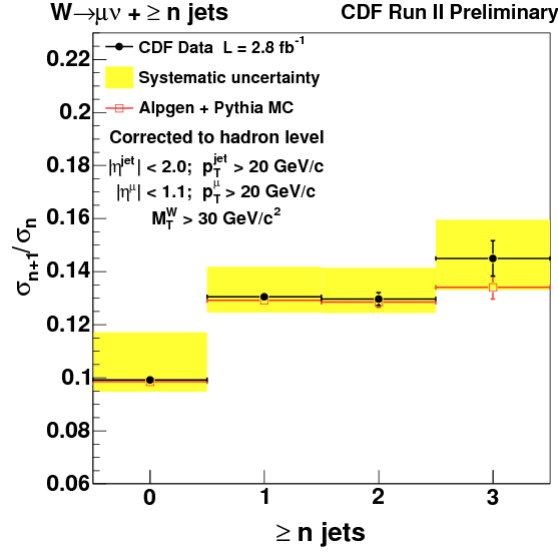
Figure 9.8. $W \to \mu\nu$ jet multiplicity cross-section ratio between $\geq (n+1)$ and $\geq n$ (σ_{n+1}/σ_n).

Both results show an uptick in the ratio between $n = 0$ and $n = 1$ but appears to plateau for the higher jet multiplicity ratios. We interrupt this result as the difference between the exclusive jet multiplicity ratio between 0 and 1 jets verses 1 and 2 (or more) jets. We observe that the Alpgen MC prediction correctly describes this feature.

9.5. n^{th} Leading Jet p_T Differential Cross-section

The jet p_T spectrum for the nth leading jet is the flagship measurement for this analysis. Jets are ranked via their transverse momentum and based on its rank is assigned to the appropriate $\geq n$ jets bin. This then forms the $\mathrm{d}\sigma/\mathrm{d}p_T$ (or more pedagogically $\mathrm{d}\sigma_n/\mathrm{d}p_T^{n^{\text{th}}}$) n^{th} leading order differential cross-section for $\geq n$ jets. The results are presented in figures 9.9 through 9.16. The first four (figures 9.9-9.12) are the jet p_T results for the electron channel (one figure for each inclusive jet multiplicity, 1-4) followed by the four plots (figures 9.13-9.16) for the muon channel, likewise.

The jet energy scale, unfolding factor, and, for ≥ 3 or ≥ 4 jets, $t\bar{t}$ background estimation are the dominate uncertainties. The systematics are largest at the highest momentum bins for each jet multiplicity and are generally larger for high multiplicities which is consistent with the previous sections (this follows for later results as well). The variable binning for these distributions and the binning of our final observables in general was set by making the Poisson (statistical) uncertainty approximately flat and total systematic uncertainty likewise or otherwise smooth and controlled increasing scaling. Of course, the jet energy scale, unfolding correction, and $t\bar{t}$ systematics (all of which are bin-by-bin effects) along with poor event yield always conspires to make the highest jet bin's systematics large and the high energy bins and jet multiplicities will necessarily have the largest total systematic error.

Systematics can be reduced due to inherent correlations normalizing the to the total inclusive cross-section (via our previous notation, σ_n). For the purpose of comparing to theory (or direct full-simulation MC corrected to the hadron level, etc.) this is fine as the relative shape difference is sufficient to test the relative hardness or softness of a given theoretical prediction. We will comment on this in the next section when we compare the data to theory by forming a simple quotient and comparing to unity. We denote these normalized distributions via $(\mathrm{d}\sigma_n/\mathrm{d}p_T^{n^{\mathrm{th}}})/\sigma_n$ or more simply as $(\mathrm{d}\sigma/\mathrm{d}p_T)/\sigma_n$ where the jet multiplicity order signifies the nth leading jet p_T differential cross-section. These jet p_T shapes are shown in figures 9.17 through 9.24. The lepton channel and jet multiplicity is presented in the same order as given before for figures 9.9 through 9.16.
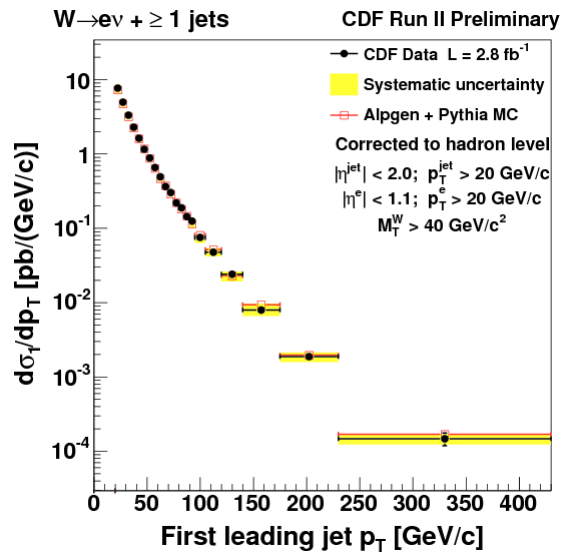
Figure 9.9. Leading jet p_T differential cross-section $(\mathrm{d}\sigma_1/\mathrm{d}p_T)$ for $W \to e\nu+ \geq 1$ jet.
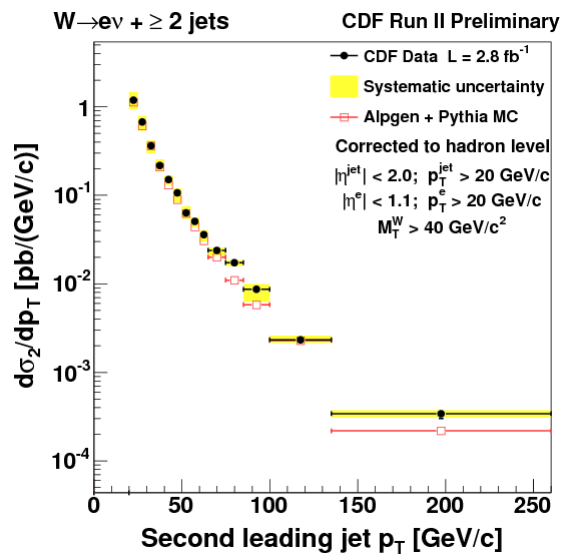
Figure 9.10. 2nd leading jet p_T differential cross-section $(\mathrm{d}\sigma_2/\mathrm{d}p_T)$ for $W \to e\nu+ \geq 2$ jets.
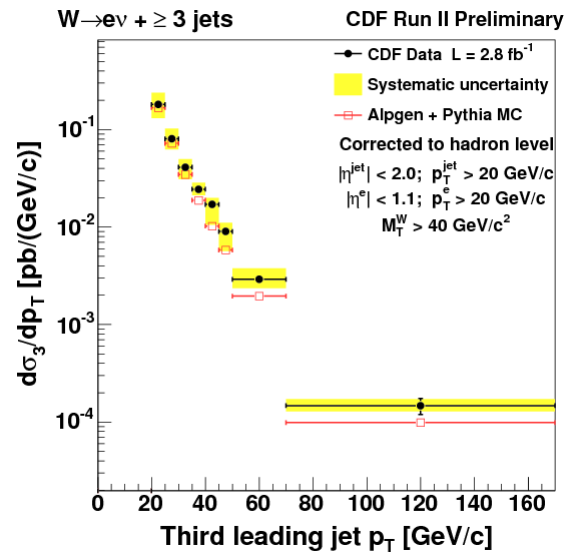
Figure 9.11. 3rd leading jet p_T differential cross-section ($\mathrm{d}\sigma_3/\mathrm{d}p_T$) for $W \to e\nu+ \geq 3$ jets.
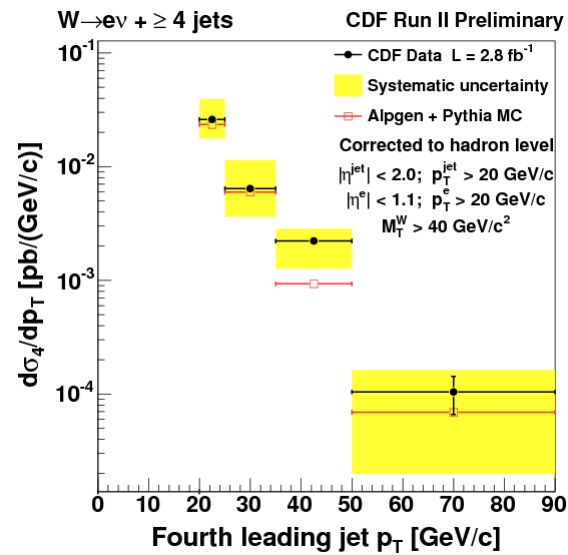
Figure 9.12. 4th leading jet p_T differential cross-section ($\mathrm{d}\sigma_4/\mathrm{d}p_T$) for $W \to e\nu+ \geq 4$ jets.
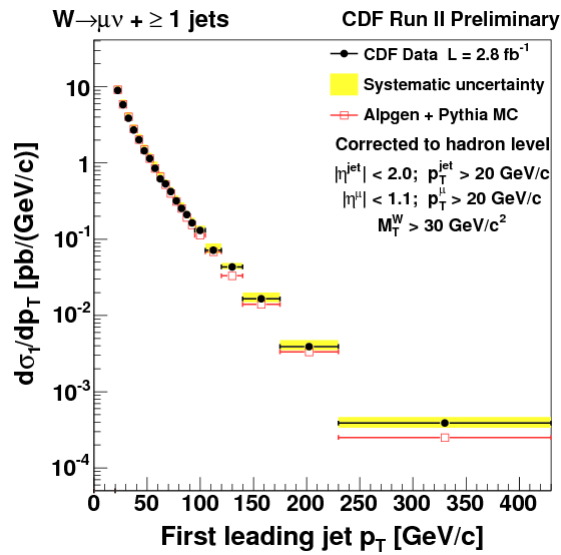
Figure 9.13. Leading jet p_T differential cross-section $(\mathrm{d}\sigma_1/\mathrm{d}p_T)$ for $W \to \mu\nu+ \geq 1$ jet.
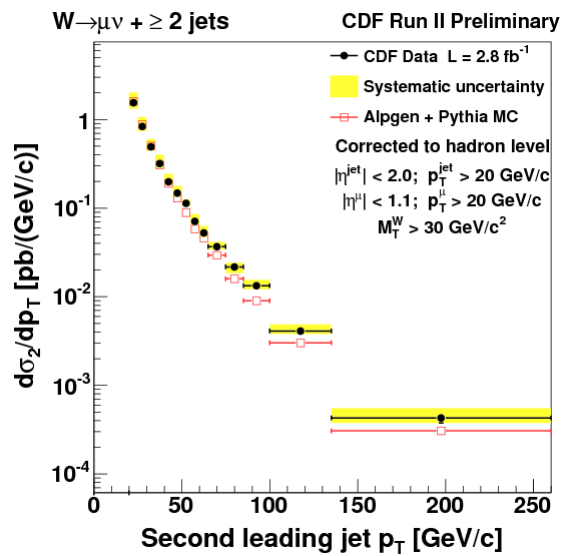
Figure 9.14. 2nd leading jet p_T differential cross-section $(\mathrm{d}\sigma_2/\mathrm{d}p_T)$ for $W \to \mu\nu+ \geq 2$ jet.
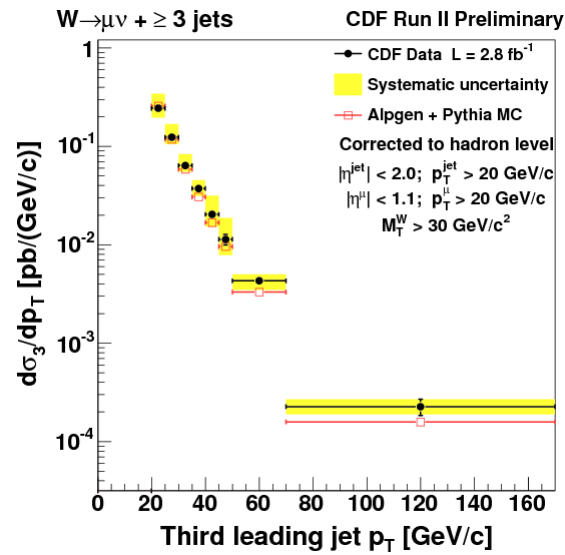
Figure 9.15. 3rd leading jet p_T differential cross-section $(\mathrm{d}\sigma_3/\mathrm{d}p_T)$ for $W \to \mu\nu+ \geq 3$ jet.
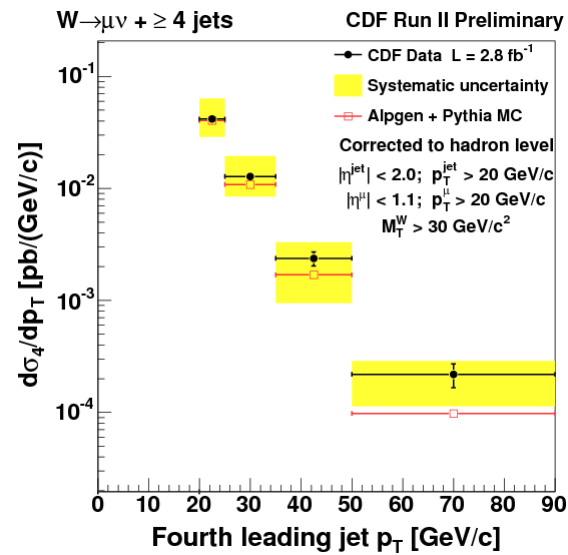
Figure 9.16. 4th leading jet p_T differential cross-section $(\mathrm{d}\sigma_4/\mathrm{d}p_T)$ for $W \to \mu\nu+ \geq 4$ jet.
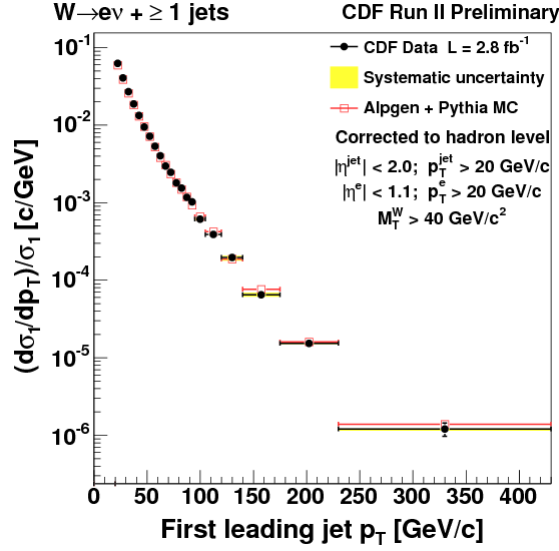
Figure 9.17. Leading jet p_T differential cross-section normalized to the inclusive ≥ 1 jet multiplicity cross-section $((\mathrm{d}\sigma_1/\mathrm{d}p_T)/\sigma_1)$ for $W \to e\nu+ \geq 1$ jet.

9.6. Ratio of data to theory for n^{th} leading jet p_T differential cross-section

Due to the nature of the $\mathrm{d}\sigma_n/\mathrm{d}p_T$ distribution falling several orders of magnitude on a common log scale plot, it is advantageous to present the results by dividing the measurement in data to the theoretical prediction. As noted in section 9.2, we investigated possible NLO QCD predictions but do not include them here. For the purpose of comparison we will continue to use the Alpgen W MC results as our "Theory" prediction. Clearly, this data divided by theory observable can be repeated once a full set of theoretical predictions are available. Note that this ratio of data to theory does not effect the systematics in anyway; the relative uncertainties remain unchanged while the result can be plotted linearly with results expected to fall roughly around unity.
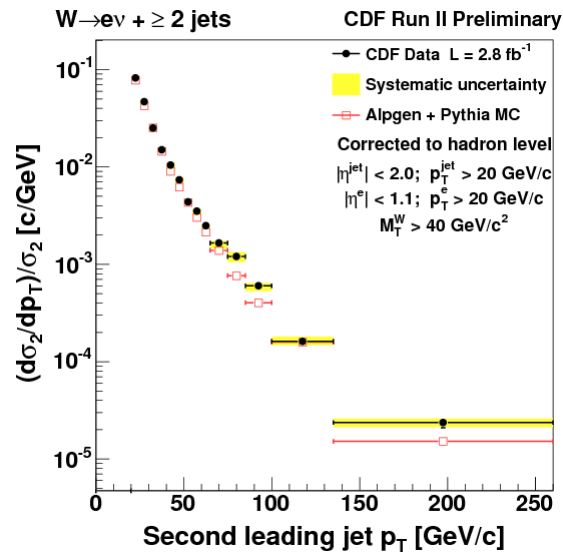
Figure 9.18. 2nd leading jet p_T differential cross-section normalized to the inclusive ≥ 2 jet multiplicity cross-section $((\mathrm{d}\sigma_2/\mathrm{d}p_T)/\sigma_2)$ for $W \to e\nu + \geq 2$ jet.
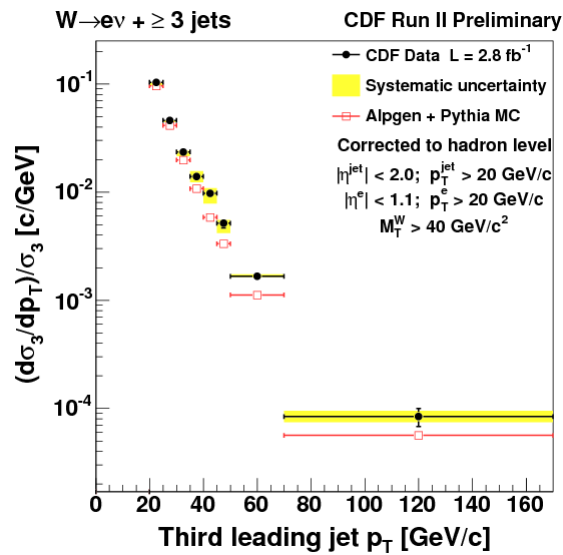
Figure 9.19. 3rd leading jet p_T differential cross-section normalized to the inclusive ≥ 3 jet multiplicity cross-section $((\mathrm{d}\sigma_3/\mathrm{d}p_T)/\sigma_3)$ for $W \to e\nu + \geq 3$ jet.
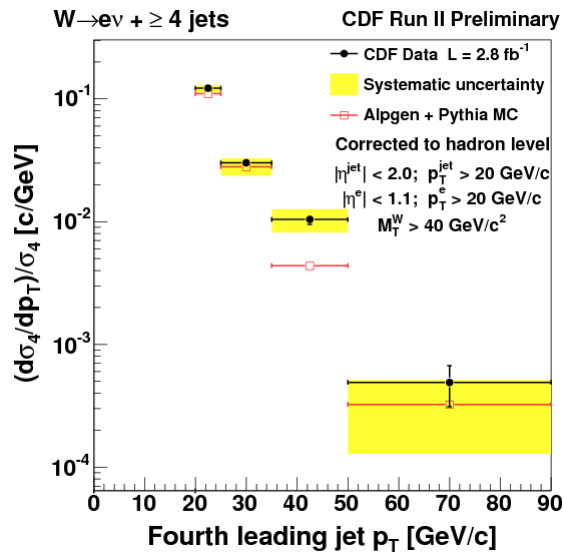
Figure 9.20. 4th leading jet p_T differential cross-section normalized to the inclusive ≥ 4 jet multiplicity cross-section $((\mathrm{d}\sigma_4/\mathrm{d}p_T)/\sigma_4)$ for $W \to e\nu+ \geq 4$ jet.
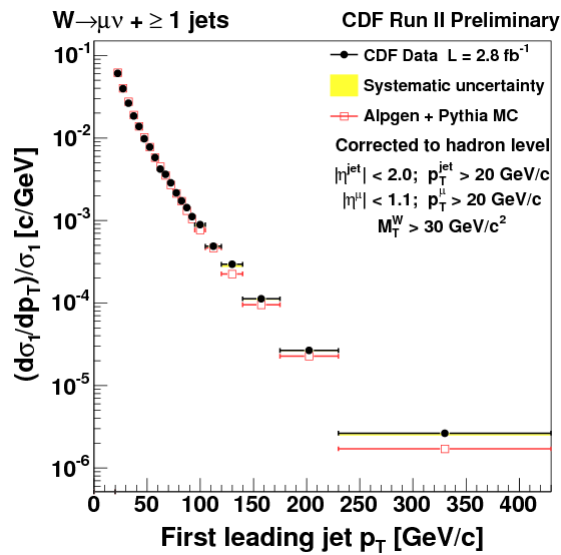
Figure 9.21. Leading jet p_T differential cross-section normalized to the inclusive ≥ 1 jet multiplicity cross-section $((\mathrm{d}\sigma_1/\mathrm{d}p_T)/\sigma_1)$ for $W \to \mu\nu+ \geq 1$ jet.

Figure 9.22. 2nd leading jet p_T differential cross-section normalized to the inclusive ≥ 2 jet multiplicity cross-section $((\mathrm{d}\sigma_2/\mathrm{d}p_T)/\sigma_2)$ for $W \to \mu\nu+ \geq 2$ jet.

Figure 9.23. 3rd leading jet p_T differential cross-section normalized to the inclusive ≥ 3 jet multiplicity cross-section $((\mathrm{d}\sigma_3/\mathrm{d}p_T)/\sigma_3)$ for $W \to \mu\nu+ \geq 3$ jet.
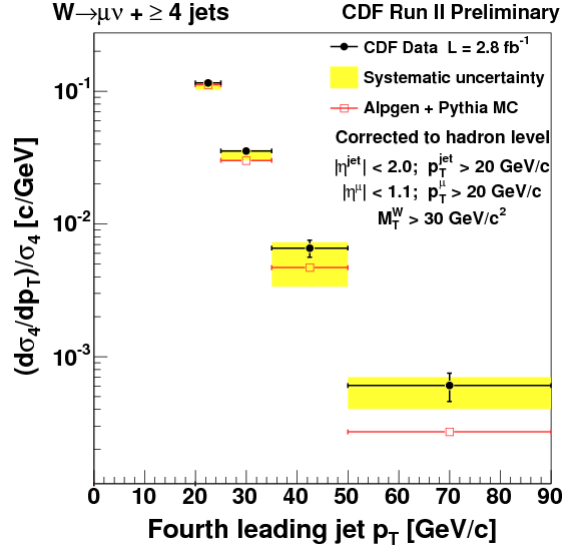
Figure 9.24. 4th leading jet p_T differential cross-section normalized to the inclusive ≥ 4 jet multiplicity cross-section $((\mathrm{d}\sigma_4/\mathrm{d}p_T)/\sigma_4)$ for $W \to \mu\nu + \geq 4$ jet.

These Data/Theory plots for jet p_T are shown in figures 9.25-9.28 (electron channel for multiplicities 1-4, respectively) and figures 9.29-9.32 (muons, likewise).

If a jet p_T spectrum increases (trending above unity) we classify the theory prediction as soft or under represents the data at high transverse momentum. Conversely, a decreasing trend suggest the p_T spectrum is hard or over represents the data at high transverse momentum. The general trend is for our data cross-section to be larger than our prescribed theory prediction suggesting that our Alpgen MC distribution by comparison is soft. In the next section, we look at the dijet mass and likewise fine the MC prediction to be soft at higher mass bins which is consistent with the findings of this section.

The agreement in shape between the electron and muon jet p_T cross-sections is good for the higher jet multiplicities ($\geq$2-4 jets) but there a slight difference for the first leading jet p_T for one or more jets (see figures 9.25 and 9.29). Indeed, the electron channel

shows a slight trend toward the data being underrepresented at high p_T. The behavior between jet p_T shapes between jet multiplicities is difficult to comment on due to our systematics being large relative to our data/theory measurement. Keeping in mind the obvious difference in our p_T range between the first and fourth jet, the data points suggest the MC increasingly under perform going from ≥ 1 to ≥ 4 jets. However, given our total statistical and systematic error, each jet multiplicity is consistent with the same basic trend.
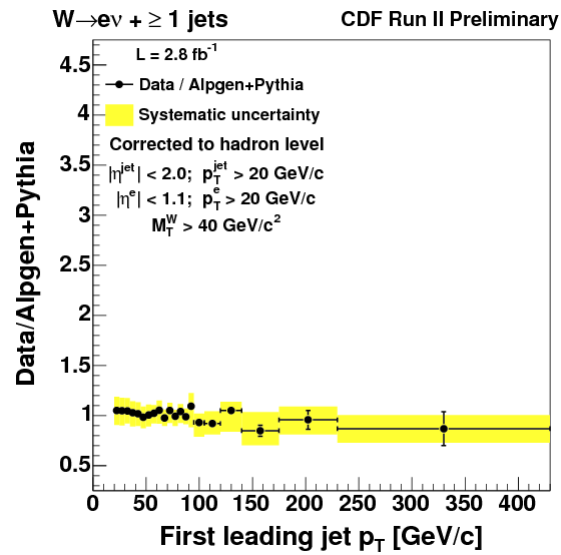
Figure 9.25. Data/Theory leading jet p_T for $W \to e\nu + \geq 1$ jet.
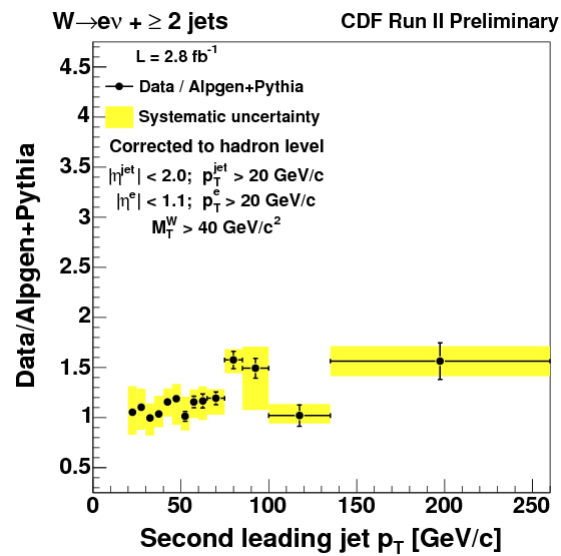
Figure 9.26. Data/Theory 2nd leading jet p_T for $W \to e\nu + \geq 2$ jets.
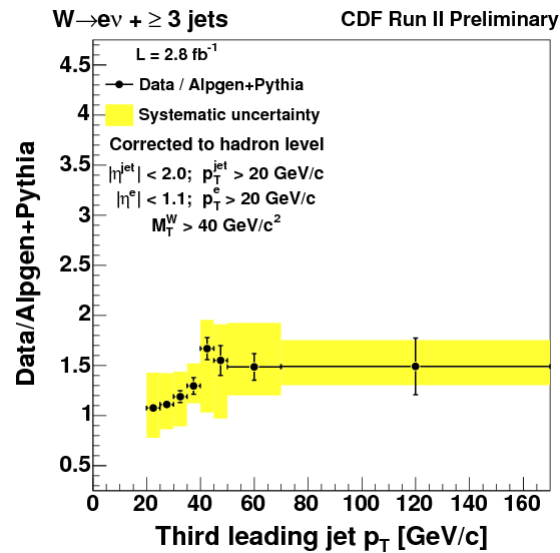
Figure 9.27. Data/Theory 3rd leading jet p_T for $W \to e\nu + \geq 3$ jets.
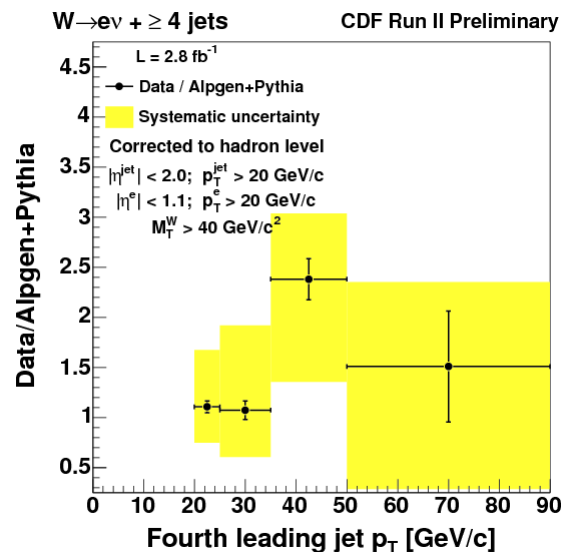
Figure 9.28. Data/Theory 4th leading jet p_T for $W \to e\nu + \geq 4$ jets.

9.7. Dijet Mass Cross-section

In this section and the next we consider two dijet variables. A dijet event is one that has at least two jets. Here we look at the dijet mass for event with ≥ 2 jets. We do this
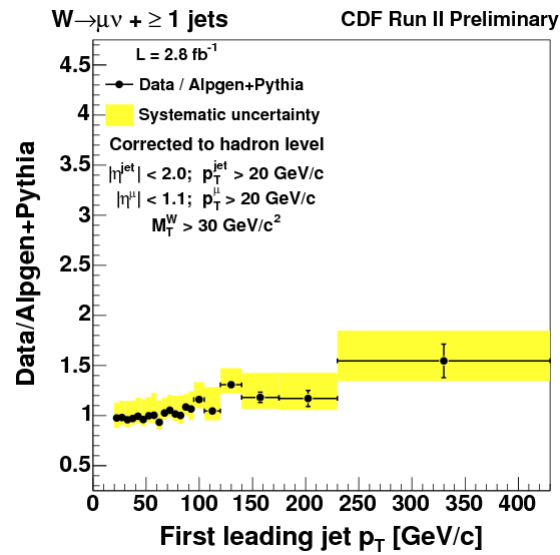
Figure 9.29. Data/Theory leading jet p_T for $W \to \mu\nu + \geq 1$ jet.
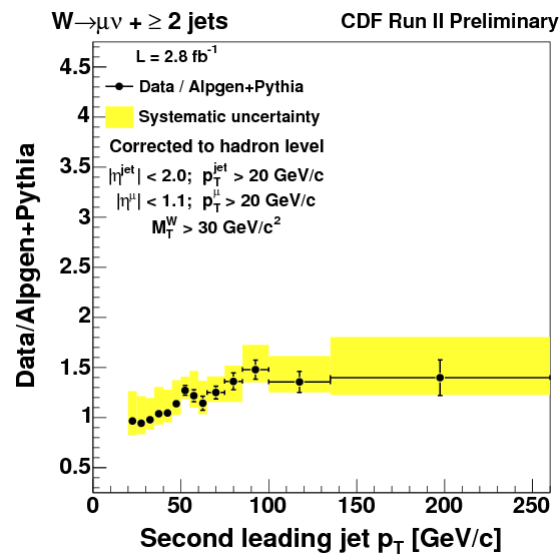
Figure 9.30. Data/Theory 2nd leading jet p_T for $W \to \mu\nu + \geq 2$ jets.

by selecting the two leading (largest) jets in p_T. We then construct a mass observable
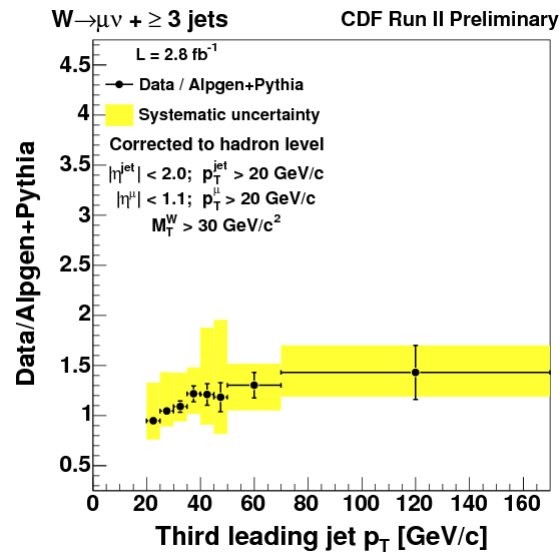
Figure 9.31. Data/Theory 3rd leading jet p_T for $W \to \mu\nu + \geq 3$ jets.
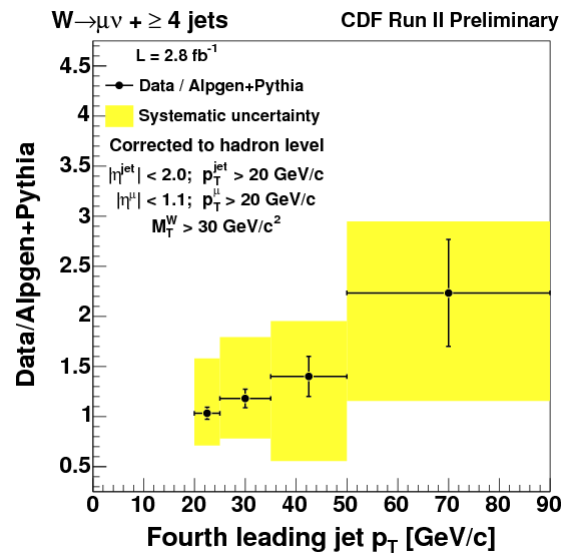
Figure 9.32. Data/Theory 4th leading jet p_T for $W \to \mu\nu + \geq 4$ jets.

(m_{jj}) for the jet pair via

$$(9.3) \qquad\qquad m_{jj}^2 = (p_1 + p_2)^2$$

where p_j is the equivalent of the four-momentum from the detector, $p_j = (E_j, \vec{p}_j)$.

The results of the dijet mass differential cross-section are presented in figure 9.33 and figure 9.34 for the electron and muon results, respectively. We use the notation $\mathrm{d}\sigma/\mathrm{d}m_{jj}$ to signify this cross-section. Similar to the jet p_T results, the we use variable bins (roughly optimized based on the systematic and statistical errors) and present the results normally on a common log scale.
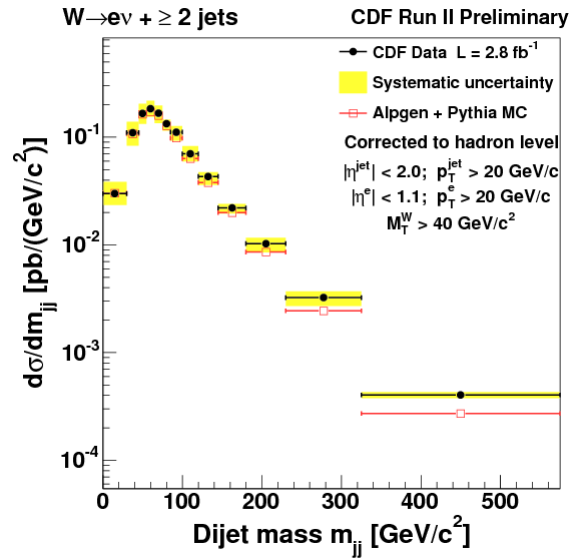
Figure 9.33. Dijet mass cross-section ($\mathrm{d}\sigma/\mathrm{d}m_{jj}$) for $W \to e\nu + \geq 2$ jets.

As with the jet p_T cross-section, it is useful to remove the overall normalization in the plot by dividing by the inclusive 2 jet cross-section (σ_2). We represent this normalized cross-section via $(\mathrm{d}\sigma/\mathrm{d}m_{jj})/\sigma_2$. As was the case for our previous results, this reduces total systematic uncertainty but the jet energy scale as well as our hadron level unfolding systematics are still relatively large at the the larger mass bins. The normalized version of these dijet mass results are shown in figure 9.35 for electrons and figure 9.36 for muons.
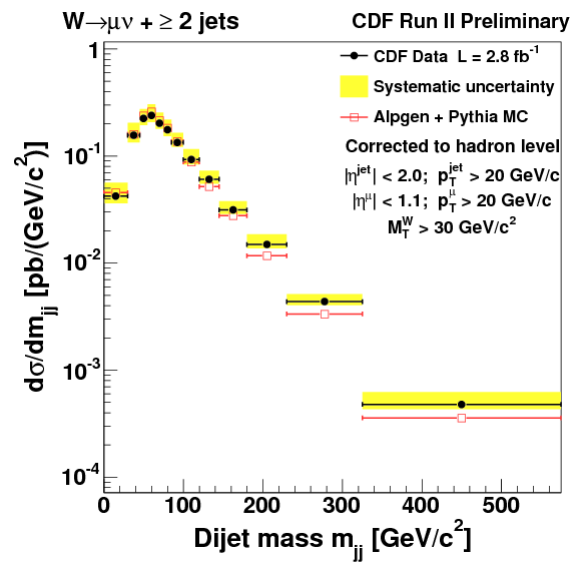
Figure 9.34. Dijet mass cross-section $(\mathrm{d}\sigma/\mathrm{d}m_{jj})$ for $W \to \mu\nu + \geq 2$ jets.
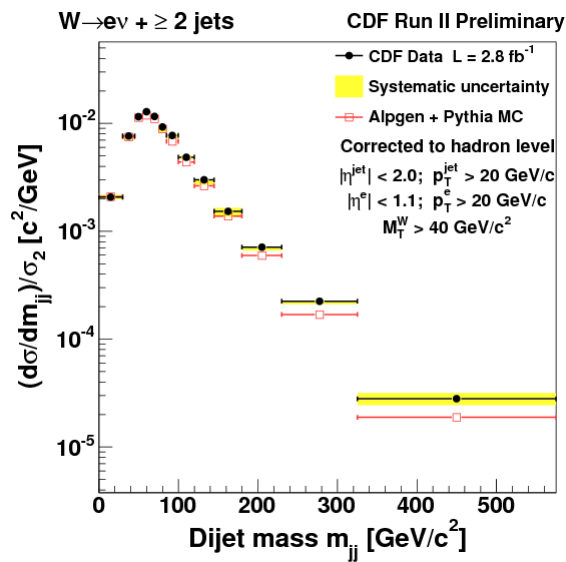
Figure 9.35. Dijet mass cross-section normalized to the inclusive two jet multiplicity cross-section $((\mathrm{d}\sigma/\mathrm{d}m_{jj})/\sigma_2)$ for $W \to e\nu + \geq 2$ jets.

As noted in the previous section, the comparison between data and theory suggests our Alpgen MC prediction underestimates the data in the higher mass bins.
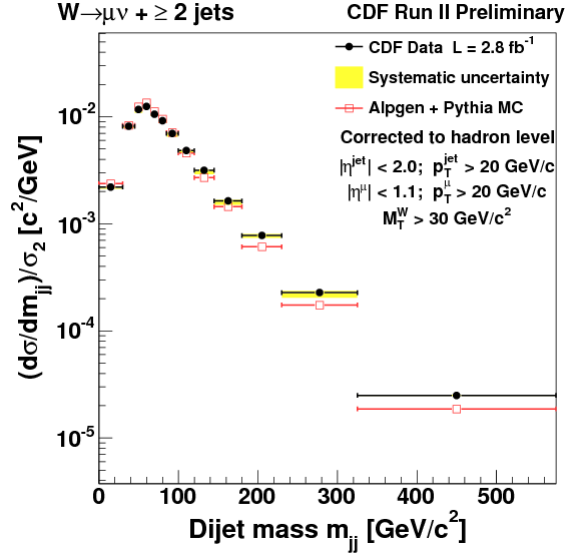
Figure 9.36. Dijet mass cross-section normalized to the inclusive two jet multiplicity cross-section $((\mathrm{d}\sigma/\mathrm{d}m_{jj})/\sigma_2)$ for $W \to \mu\nu + \geq 2$ jets.

9.8. Dijet Separation Cross-section

The second dijet cross-section we consider is the dijet separation cross-section. Taking the same highest jet p_T pair as before in events with ≥ 2, jets we construct an angular separation measurement ($R_{jj} = \Delta R(1^{\mathrm{st}}\mathrm{jet}, 2^{\mathrm{nd}}\mathrm{jet})$) based on the jet η and ϕ. Via equation 5.1 and taking 1 and 2 to represent the first and second jet, we define the separation in the normal way via

$$(9.4) \qquad R_{jj} = \sqrt{(\eta_1 - \eta_2)^2 + (\phi_1 - \phi_2)^2}$$

Note that the difference in the azimuthal angles ($\Delta\phi$) is done by taking the absolute value of the difference and then, if this value is larger than π, taking $\Delta\phi = 2\pi - |\phi_1 - \phi_2|$ ($\Delta\phi$ is constrained between 0 and π).

We denote this cross-section with $\mathrm{d}\sigma/\mathrm{d}R_{jj}$ and its normalized (unitless) version with $(\mathrm{d}\sigma/\mathrm{d}R_{jj})/\sigma_2$. The nominal cross-section results are presented in figure 9.37 and figure 9.38 for electrons and muons, respectively. Similarly, the normalized cross-section results are showcased in figure 9.39 and figure 9.40. We note the reduction in the total systematic uncertainty in the latter pair of plots due to our method's power in canceling correlated systematics as explained in Section 8.9. The decrease is more dramatic for these results as the largest systematics are relatively flat (bin-by-bin) and correlated with the total inclusive $W+ \geq 2$ jets cross-section.

This follows as our unfolding and jet every scale correction are less sensitive to geometric changes especially the difference of two energetic jets. The next section deals with the related $|\eta_{jj}|$ observable and these results as well will have them systematics greatly reduces when normalized to the appropriate cross-section.
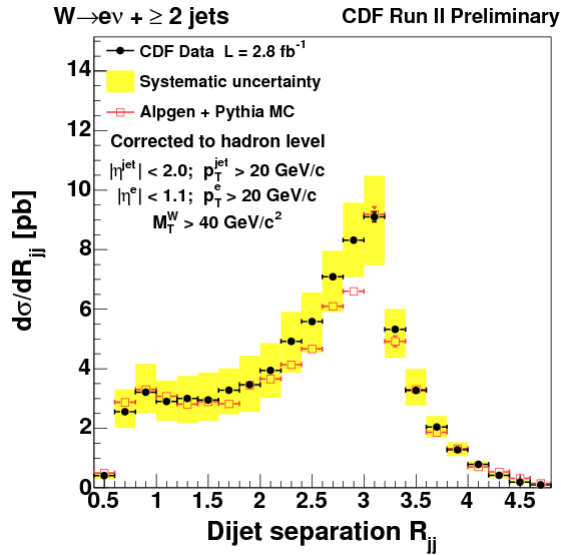
Figure 9.37. Dijet separation cross-section $(\mathrm{d}\sigma/\mathrm{d}R_{jj})$ for $W \to e\nu+ \geq 2$ jets.
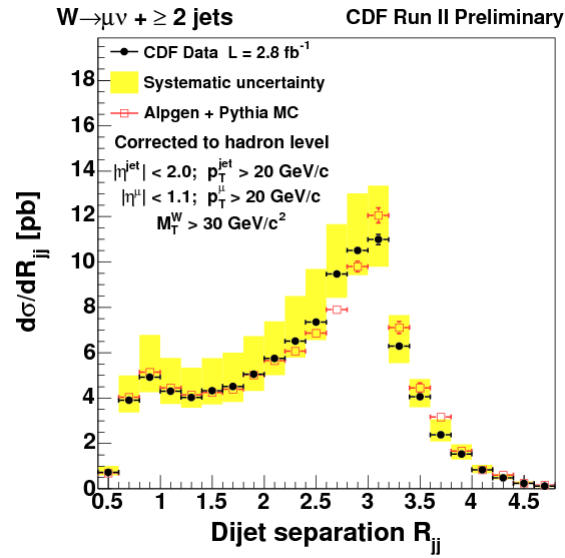
Figure 9.38. Dijet separation cross-section $(\mathrm{d}\sigma/\mathrm{d}R_{jj})$ for $W \to \mu\nu+ \geq 2$ jets.
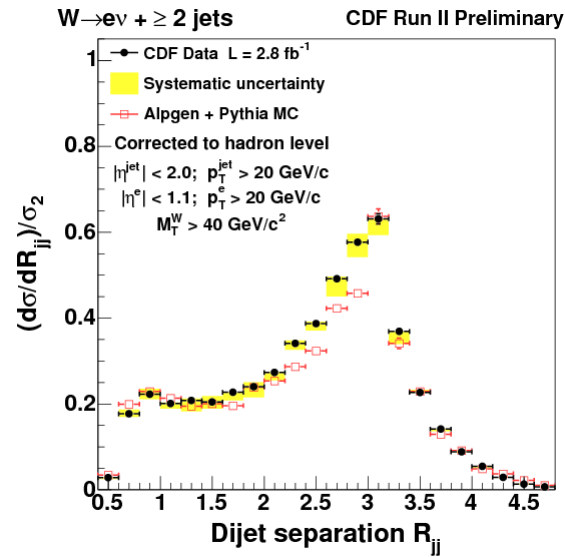
Figure 9.39. Dijet separation cross-section normalized to the inclusive two jet multiplicity cross-section $((\mathrm{d}\sigma/\mathrm{d}R_{jj})/\sigma_2$ for $W \to e\nu+ \geq 2$ jets.

There is an interesting feature of our theory result which is not seen in the data. For values of R_{jj} around π the MC prediction appears to be sharper suggesting more back-to-back (in ϕ) events. Meanwhile our theory comparison via Alpgen under accounts for
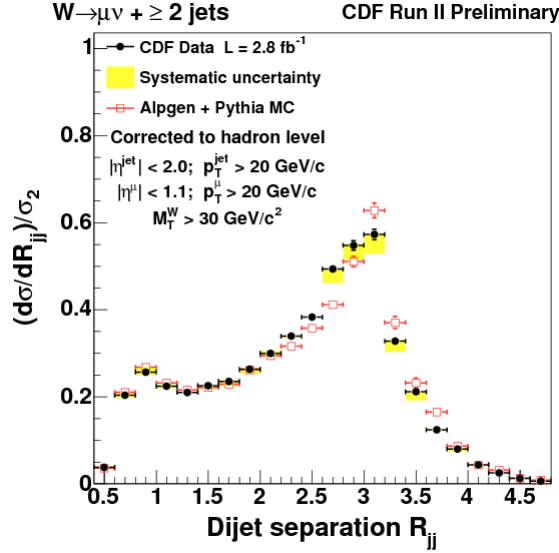
Figure 9.40. Dijet separation cross-section normalized to the inclusive two jet multiplicity cross-section $((\mathrm{d}\sigma/\mathrm{d}R_{jj})/\sigma_2$ for $W\to\mu\nu+\geq 2$ jets.

events between R_{jj} of 2.3 and π. The effect is a bit more pronounced in the muon channel where there is even an over representation on the R_{jj} falling edge. During our investigation of our MC and when developing our hadron level unfolding procedure (section 5.8) we discovered a likely explanation to this issue. The MC seems to not smear the $W+0$p sample as can be seen in figures 9.41 and 9.42. These plots (for the electron and muon channels, respectively) show hadron level jets from the MC with each histogram stack representing each of the 5 parton W samples (as explained in section 5.8). The $W\to\ell\nu+0$p Alpgen+Pythia sample has most of its events in the peak and falling edge (starting at $R_{jj}=\pi$) while the other samples (1-4 partons) gives a more expected leading jet pair spectrum. One hypothesis is that Pythia (which hadronizes the Alpgen particle level MC generation) generates these jets nearly back-to-back. This feature has been observed in the results of others.
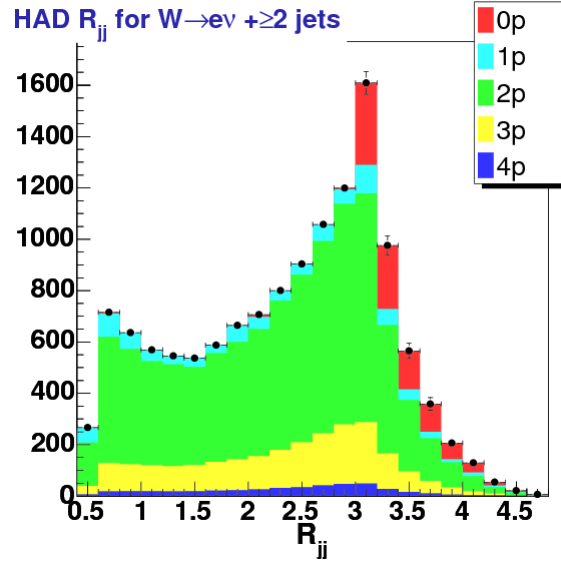
Figure 9.41. Dijet separation (R_{jj}) of the $W \to e\nu + \geq 2$ jets using hadron level jets via the post-shower/pre-cdf-detector-sim Alpgen+Pythia MC. The stacked histogram shows the contributions from each of the 5 partons samples ($W \to e\nu$+0-4p).

9.9. $\Delta\eta$ Cross-sections

In this and the next section we consider jet variables dealing with the forwardness of jets using the separation of two or more jets in pseudo-rapidity. This is interesting as it is complementary to looking at the jet p_T spectrum. In both cases, different theoretical predictions and methods may offer different results [95].

We define $\Delta\eta_{jj}$ or for brevity $\Delta\eta$ as the absolute difference in pseudo-rapidity in the two *farthest* jets. We then consider two cross-sections based on this observable: $\mathrm{d}\sigma_2/\mathrm{d}\Delta\eta$ and $\mathrm{d}\sigma_3/\mathrm{d}\Delta\eta$. The binning of $\Delta\eta$ is the same in both of our ≥ 2 and ≥ 3 jets results so that we can form a easily form a quotient observable between both results as explained later in this section. Like our other results, we consider the shape observable of these distributions by normalizing to the appropriate inclusive jet multiplicity cross-section or
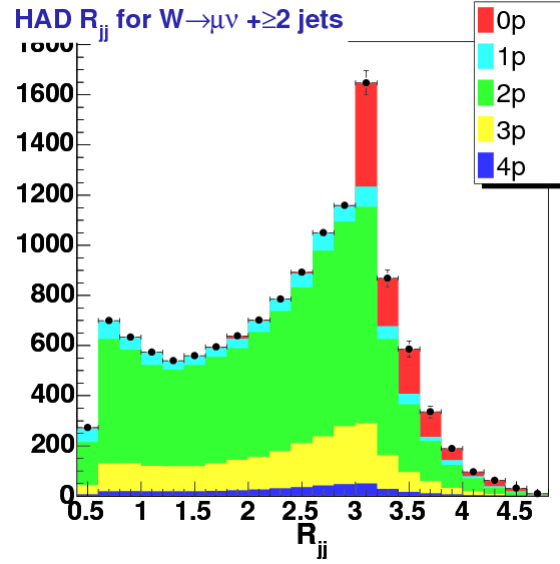
Figure 9.42. Dijet separation (R_{jj}) of the $W \to \mu\nu+ \geq 2$ jets using hadron level jets via the post-shower/pre-cdf-detector-sim Alpgen+Pythia MC. The stacked histogram shows the contributions from each of the 5 partons samples ($W \to \mu\nu+$0-4p).

symbolically: $(\mathrm{d}\sigma_2/\mathrm{d}\Delta\eta)/\sigma_2$ and $(\mathrm{d}\sigma_3/\mathrm{d}\Delta\eta)/\sigma_3$. Note that because of our definition of $\Delta\eta$ (as appose to the procedure for the dijet separation) the inclusive 2 jet differential cross-section necessarily includes the inclusive 3 jet $\Delta\eta$ events. We can see this by writing out the components as done in equation 9.5.

$$(9.5) \qquad \frac{\mathrm{d}\sigma_{\geq 2}}{\mathrm{d}\Delta\eta} = \frac{\mathrm{d}\sigma_{=2}}{\mathrm{d}\Delta\eta} + \frac{\mathrm{d}\sigma_{\geq 3}}{\mathrm{d}\Delta\eta}$$

The electron and muon $\Delta\eta$ cross-section results for the inclusive 2 jet case are shown in figure 9.43 and figure 9.44, respectively. The normalized plots are shown in figure 9.45 and figure 9.46. The inclusive 3 jet case follows in figure 9.47 and figure 9.48 for the differential cross-section for electrons and muons while figure 9.49 and figure 9.50 show
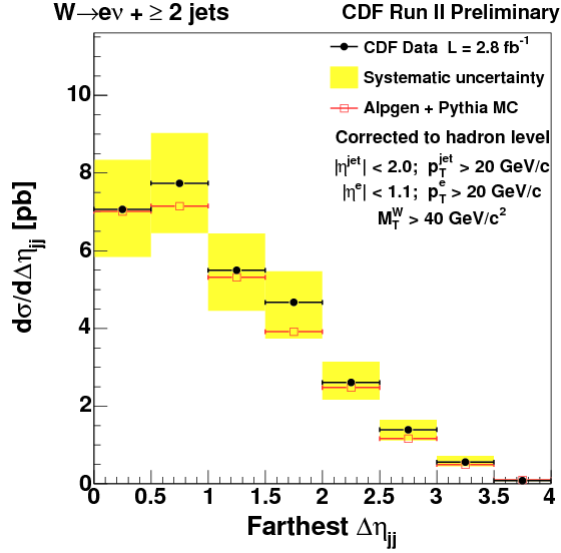
Figure 9.43. Absolute pseudo-rapidity difference of the farthest two jets ($\Delta\eta_{jj}$) differential cross-section ($\mathrm{d}\sigma_2/\mathrm{d}\Delta\eta_{jj}$) for $W \to e\nu+ \geq 2$ jets.

the normalized shape plots. In each case, we label $\Delta\eta$ as the "Farthest $\Delta\eta_{jj}$" in order to distinguish between the separation of the highest transverse momentum jets.

The $\mathrm{d}\sigma_2/\mathrm{d}\Delta\eta$ and $\mathrm{d}\sigma_3/\mathrm{d}\Delta\eta$ cross-sections are relatively well described by the MC and there is no distinguishing feature as seen in our R_{jj} cross-section of the previous section. In particular, the inclusive ≥ 2 and ≥ 3 jets mimic the basic behavior of the expected result (base on our jet phase-space with our jet η cut) of $\Delta\eta$ with exclusive 2 and 3 jets.

Finally we consider a ratio measurement that examines the behavior in $\Delta\eta$ between our two different jet multiplicities: ≥ 2 or ≥ 3 jets. We define $r_{\Delta\eta}$ as the quotient of the previous measurements:

$$(9.6) \qquad r_{\Delta\eta} = \frac{\mathrm{d}\sigma_3/\mathrm{d}\Delta\eta}{\mathrm{d}\sigma_2/\mathrm{d}\Delta\eta}$$
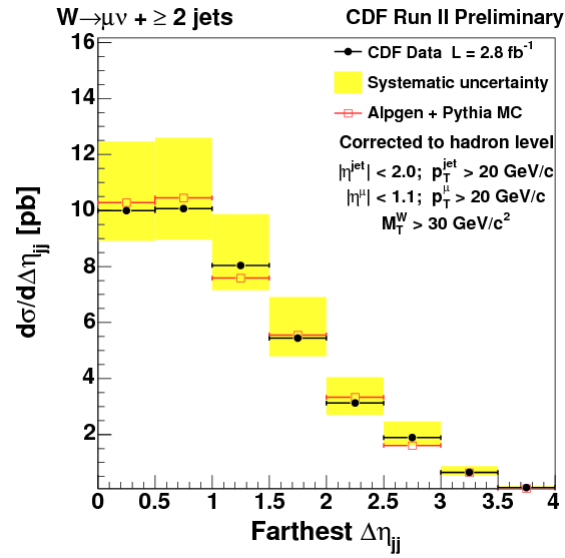
Figure 9.44. Absolute pseudo-rapidity difference of the farthest two jets ($\Delta\eta_{jj}$) differential cross-section ($\mathrm{d}\sigma_2/\mathrm{d}\Delta\eta_{jj}$) for $W \to \mu\nu+ \geq 2$ jets.
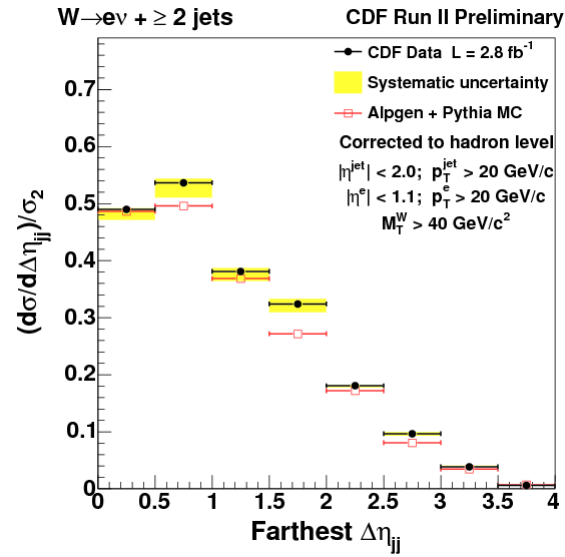
Figure 9.45. Absolute pseudo-rapidity difference of the farthest two jets ($\Delta\eta_{jj}$) differential cross-section normalized to the inclusive two jet multiplicity cross-section (($\mathrm{d}\sigma_2/\mathrm{d}\Delta\eta_{jj})/\sigma_2$) for $W \to e\nu+ \geq 2$ jets.
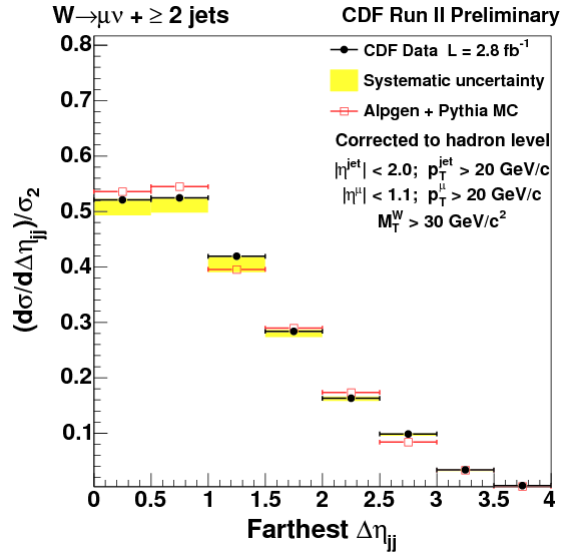
Figure 9.46. Absolute pseudo-rapidity difference of the farthest two jets ($\Delta\eta_{jj}$) differential cross-section normalized to the inclusive two jet multiplicity cross-section (($\mathrm{d}\sigma_2/\mathrm{d}\Delta\eta_{jj})/\sigma_2$) for $W \to \mu\nu + \geq 2$ jets.
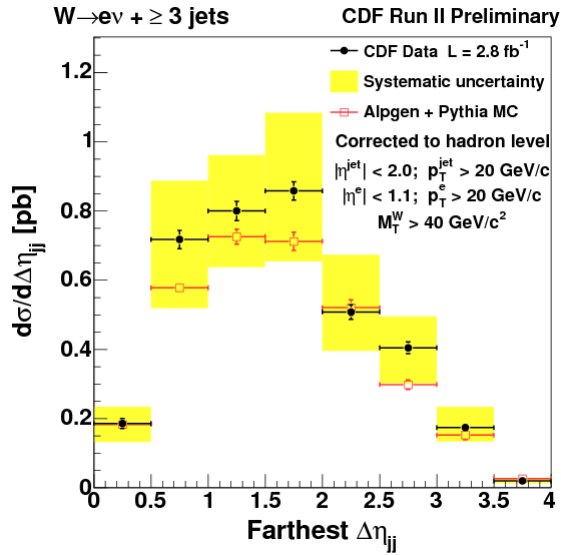
Figure 9.47. Absolute pseudo-rapidity difference of the farthest two jets ($\Delta\eta_{jj}$) differential cross-section ($\mathrm{d}\sigma_3/\mathrm{d}\Delta\eta_{jj}$) for $W \to e\nu + \geq 3$ jets.
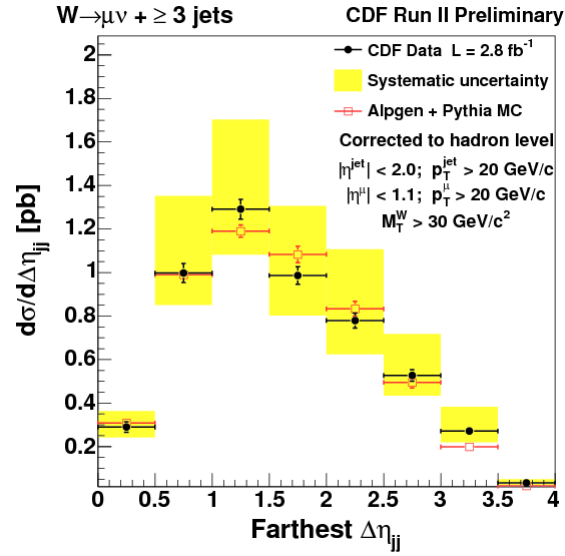
Figure 9.48. Absolute pseudo-rapidity difference of the farthest two jets ($\Delta\eta_{jj}$) differential cross-section ($\mathrm{d}\sigma_3/\mathrm{d}\Delta\eta_{jj}$) for $W \to \mu\nu+ \geq 3$ jets.
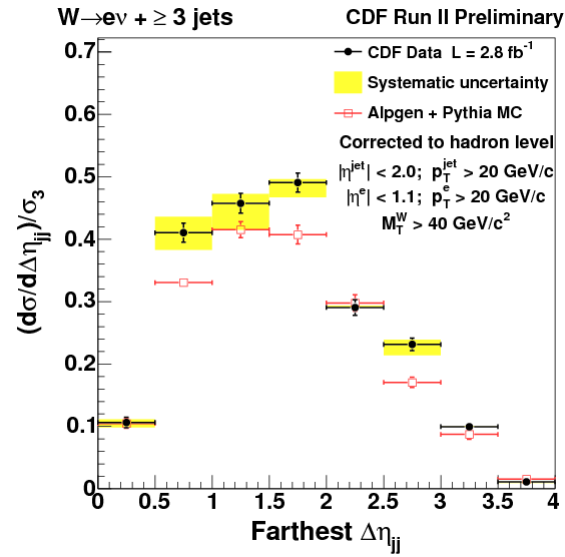
Figure 9.49. Absolute pseudo-rapidity difference of the farthest two jets ($\Delta\eta_{jj}$) differential cross-section normalized to the inclusive three jet multiplicity cross-section (($\mathrm{d}\sigma_3/\mathrm{d}\Delta\eta_{jj})/\sigma_3$) for $W \to e\nu+ \geq 3$ jets.
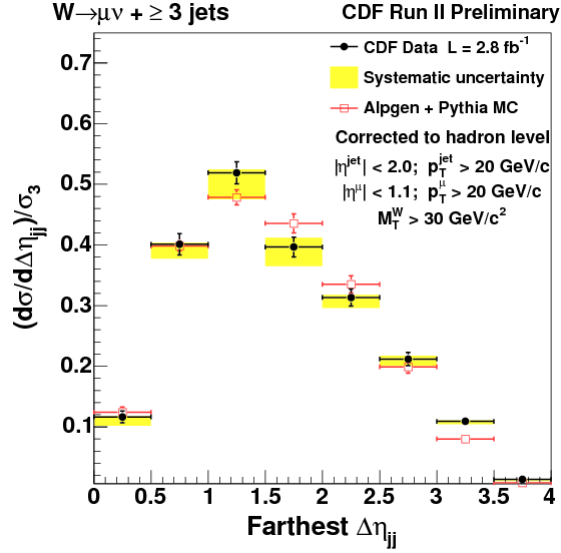
Figure 9.50. Absolute pseudo-rapidity difference of the farthest two jets ($\Delta\eta_{jj}$) differential cross-section normalized to the inclusive three jet multiplicity cross-section (($\mathrm{d}\sigma_3/\mathrm{d}\Delta\eta_{jj})/\sigma_3$) for $W \to \mu\nu + \geq 3$ jets.

As noted before, that the bin size is the same in the 2 and 3 inclusive jet case for $\Delta\eta$ in order to make $r_{\Delta\eta}$ relatively easy to produce. The results as shown in figure 9.51 (electron channel) and figure 9.52 (muon channel).

The observable $r_{\Delta\eta}$ gives us a composite picture of the same variable ($\Delta\eta$) over two different jet multiplicities. The end product is a ruffly linear spectrum. The utility of this plot for the highest $\Delta\eta$ bins is questionable due to both jet multiplicities cross-sections approaching zero at the jet acceptance boundary of $\Delta\eta = 4$. The uncertainties for our differential cross-section for $\Delta\eta$ and our ratio $r_{\Delta\eta}$ are dominated by our unfolding and jet energy scale although these systematics do reduce when normalized to the respective integrated cross-sections (σ_2 and σ_3)
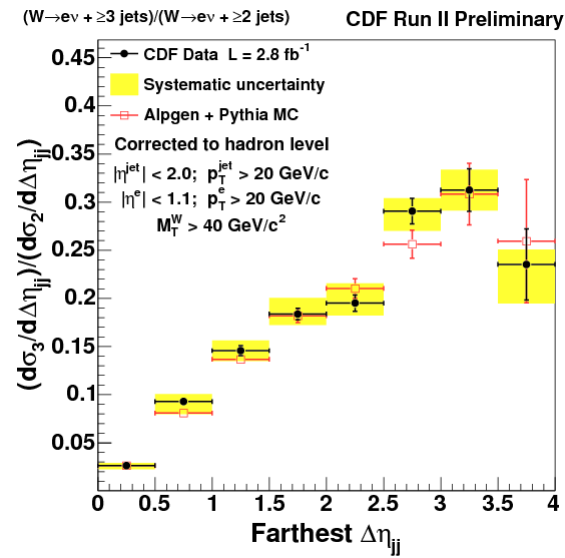
Figure 9.51. Absolute pseudo-rapidity difference of the farthest two jets $(\Delta\eta_{jj})$ differential cross-section ratio between ≥ 2 and ≥ 3 jets $((\mathrm{d}\sigma_2/\mathrm{d}\Delta\eta)/(\mathrm{d}\sigma_3/\mathrm{d}\Delta\eta))$ for $W \to e\nu$.
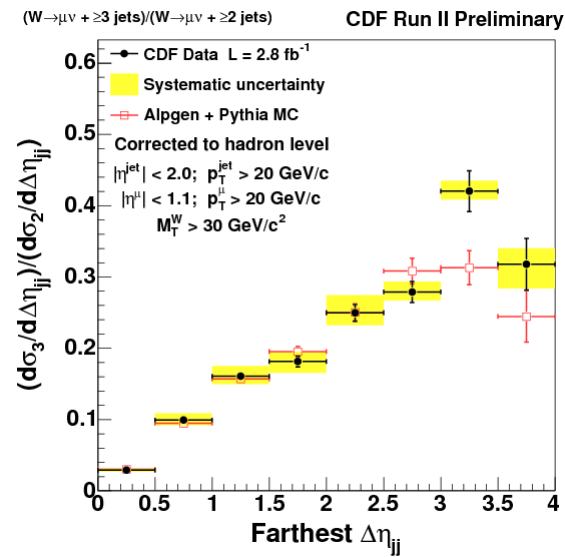
Figure 9.52. Absolute pseudo-rapidity difference of the farthest two jets $(\Delta\eta_{jj})$ differential cross-section ratio between ≥ 2 and ≥ 3 jets $((\mathrm{d}\sigma_2/\mathrm{d}\Delta\eta)/(\mathrm{d}\sigma_3/\mathrm{d}\Delta\eta))$ for $W \to \mu\nu$.

CHAPTER 10

Summary

This thesis represents the cumulative work over several years as part of the CDF collaboration in an effort to measure basic cross-sections with jet kinematic variables of events associated with a leptonic decay of the W. The goal was to focus on a set of well defined experimental measurements which could later be compared to better theoretical comparisons.

We started in chapter 1 by giving a basic introduction for W+jets and providing a basic description of our intermediate and final analysis goals. In chapter 2 we gave a description of the Tevatron at the Fermilab and an overview of the CDF Run II detector and the relevant systems and detector components needed in the analysis. After discussing various details on our data and MC samples, we preceded to discuss our lepton selection criteria in chapter 4 in order to build our W candidate sample in data as well as to prepare our background estimations. We next define our jet selection and discuss both jet energy (detector) corrections as well as hadron level corrections in chapter 5.

The next stage in our analysis was calculate our expected backgrounds in chapter 6. This work required bringing together our understanding of our W+jets candidates in data, MC predictions from samples with a given theoretical/experimental cross-section weight, MC predictions where we could not explicitly assume any such weight to a void begging the question, and finally a sample of QCD/fakes background events derived from the data events that mimic our basic kinematic selection but fail part of our identification

criteria. We do this for each inclusive jet multiplicity while checking for good agreement across many W/lepton distributions. This background chapter also includes our vertex correction procedure to correct for promotion. This latter work as well as our procedure for understanding the QCD/fake background for the muon channel is distinct to this analysis and represents an unique contribution.

Chapter 7 described our detector acceptance and various lepton, trigger, an event based efficiencies. Our acceptance calculation eliminates a potential in adding contributions of our signal MC and this thesis work also included the calculation of additional efficiencies due to additional cuts designed for this analysis.

In this analysis we measured several different systematics and methodically accounted for potential correlations as demonstrated in chapter 8. As was expected, the dominate systematics for most results was the jet energy scale (JES) systematic uncertainty. Indeed the trickiest systematics (JES, unfolding/hadron level correction, and $t\bar{t}$ background estimation) also involved fully accounting for bin-by-bin (e.g. jet p_T dependence) effects.

In the previous chapter, we have presented the measurement of several differential cross-sections, normalized cross-section shapes, and ratio observables for jet kinematics for 1-4 inclusive jets from events with a leptonic (electron and muon) decay of a W. These measurements were taken from the CDF detector at the Tevatron using $p\bar{p}$ collisions with center of mass energies of 1.96 TeV. The data compromises 2.8 fb^{-1} of data taking over the course of Run II. This measurement not only extended on previous W+jets work in the electron channel (see section 1.2) but included the muon channel results as well which are new for the Tevatron results.

Given our simple Alpgen MC theory comparison in chapter 9, it is difficult to make strong statements. With respect to the nth leading jet p_T and dijet mass, the theory prediction underestimates the data at higher momentum/mass for the sake of overestimation at the lower end. The dijet separation cross-section showed disagreement although this appears to be a known feature of the MC and a similar disagreement was likewise seen in the previous results (see figure 1.4 on page 85). There is no complimentary feature in the related $\Delta\eta$ distributions suggesting the issue involves the $\Delta\phi$ of the leading jet pair. The agreement between the electron and muon channel shapes is generally good and consistent although the absolute cross-sections are by definition different (muon cross-section results are systematically larger due to different reduce acceptances). There is a slight difference in the first leading jet p_T data/theory shapes but the difference is not resolvable at higher jet multiplicities. However, our basic jet multiplicity cross-section ratios (σ_{n+1}/σ_n and σ_n/σ_0) are distinguishable between both lepton channels.

During the course of this analysis, several innovated or improved procedures were developed. As previous noted, this includes a method for fitting background and signal shapes that are theory independent, a method for selecting our QCD background from events from data, and a procedure that corrects for the effect of promotion due to multiple interactions. We also carefully explored our detector acceptance, corrected our jet back to the hadron level, and accounted for systematics and the inter-correlation between systematic effects.

The importance of these results and indeed of other vector boson production in association with jets with that they can be used to test pQCD predictions and offer valuable

knowledge with respect to other processes such as $t\bar{t}$, Higgs, and new physics beyond the standard model.

References

[1] C. Quigg, *Gauge Theories of the Strong, Weak, and Electromagnetic Interactions*, Benjamin/Cummings, Menlo Park, California, 1983.

[2] D. Griffiths, *Introduction to Elementary Particles*, Wiley, New York, New York, 1987.

[3] C. A. Ronan, *The Natural History of the Universe*, Macmillan Publishing Company, New York, New York, p. 26-28.

[4] B. P. Roe, *Particle Physics at the New Millennium*, Springer, New York, New York, p. 246-281, 1996.

[5] K. Nakamura *et al.*. (Particle Data Group), J. Phys. G 37, 075021 (2010).

[6] J. C. Taylor, *Gauge Theories of Weak Interactions*, Cambridge University Press, Cambridge, 1976.

[7] M. E. Peskin and D. V. Schroeder, *An Introduction to Quantum Field Theory*, Westview Press, Boulder, Colorado, 1995.

[8] S. Weinberg, *The Quantum Theory of Fields* (Volume I), Cambridge University Press, Cambridge, 1995.

[9] R. P. Feynman, *QED: The Strange Theory of Light and Matter*, Princeton University Press, Princeton, New Jersey, 1985.

[10] R. D. Field, *Applications of Perturbative QCD*, Benjamin/Cummings, Menlo Park, California, 1989.

[11] A. Bassetto, M. Ciafaloni, G. Marchesini, and A. H. Mueller, Nucl. Phys. 207B, **189** (1982); A. H. Mueller, Phys. Lett. 104B, **161** (1981); Yu.L. Dokshitzer, V.A. Khoze, A.H. Mueller, and S.I. Troyan, *Basics of Perturbative QCD*, Editions Frontieres, (1991).

[12] B. Cooper, A. Messina, and D. Waters, CDF Internal Note **8046**.

[13] B. Cooper, A. Messina, and D. Waters, CDF Public Note **8381**.

[14] B. Cooper, Ph.D. thesis, University College London (2006); A. Messina, Ph.D. thesis, Universit'a di Roma La Sapienza (2004).

[15] T. Aaltonen *et al.* (CDF Collaboration), Phys. Rev. D 77, 011108(R) (2008), hep-ex/0711.4044.

[16] T. Aaltonen *et al.*, The CDF Collaboration, Phys. Rev. Lett. 102, 151801 (2009); Observation of the Production of a W Boson in Association with Single Charm at the Tevatron Public Analysis Web Page, http://www-cdf.fnal.gov/physics/new/qcd/wcharm2011/publicWc.html.

[17] CDF Public Results page for W+jets for 320 pb^{-1}, http://www-cdf.fnal.gov/physics/new/qcd/wjets_07/wjets.html.

[18] F. Abe *et al.*, Nucl. Instrum. Meth. A **271**, 387-403 (1988); CDF II Collaboration, FERMILAB-PUB-96/390-E (1996).

[19] A. Sill *et al.*, Nucl. Instrum. Meth. A **447**, 1 (2000).

[20] T. Affolder *et al.*, Nucl. Instrum. Meth. A **42586**, 249 (2004).

[21] D. Acosta *et al.*, Nucl. Instrum. Meth. A **518**, 605 (2004).

[22] L. Balka *et al.*, Nucl. Instrum. Meth. A **267**, 272 (1988).

[23] S. Bertolucci *et al.*, Nucl. Instrum. Meth. A **267**, 301 (1988).

[24] Y. Seiya *et al.*, Nucl. Instrum. Meth. A **480**, 524 (2002).

[25] D. Acosta *et al.*, Nucl. Instrum. Meth. A **461** 540 (2001).

[26] F. Abe *et al.*, Nucl. Instrum. Methods Phys. Res. A **271**, 387 (1985).

[27] CDF Top Quark Physics Group, http://www-cdf.fnal.gov/internal/physics/top/topnew.shtml.

[28] A tarball is a tar file or compressed tar file. With respect to this analysis, such files allow program executables, libraries, etc. to be moved easily to analysis computer farms.

[29] Top Code, http://www-cdf.fnal.gov/internal/physics/top/topcode.shtml; TopCode-Prescriptions.FarmsTarball (CDF internal webpage), http://www-cdf.fnal.gov/tiki/tiki-index.php?page=TopCodePrescriptions.FarmsTarball

[30] F. Rademakers and R. Brun, ROOT: An Object-Oriented Data Analysis Framework, Linux Journal, Issue 51, July (1998); ROOT webpage, http://root.cern.ch/.

[31] M. Martinez *et al.*, *GOOD RUN LIST v26 Page*, http://www-cdf.fnal.gov/internal/dqm/goodrun/v26/goodv26.html.

[32] Joint Physics Working Group, *Joint Physics Scale Factor Class*, http://www-cdf.fnal.gov/internal/physics/joint_physics/instructions/JPScaleFactor/index.html.

[33] Joint Physics Working Group, *PerfIDia*, http://ncdf70.fnal.gov:8001/PerfIDia/PerfIDia.html.

[34] Top Group Gen 6 MC Production, http://www-cdf.fnal.gov/internal/physics/top/RunIIMC/topmc6/index.shtml.

[35] M.L. Mangano, M. Moretti, F. Piccinini, R. Pittau, A. Polosa, JHEP 0307, (2003) 001, http://arxiv.org/ps/hep-ph/0206293; M. L. Mangano, M. Moretti, F. Piccinini, R. Pittau, and A. Polosa, *ALPGEN V2.13*, mlm.home.cern.ch/mlm/alpgen

[36] *Alpgen V2 validation for gen6*, http://www-cdf.fnal.gov/tiki/tiki-index.php?page=Alpgen+gen6.

[37] J. M. Campbell and R. K. Ellis, Phys. Rev. D **60**, 113006 (1999), http://arxiv.org/abs/hep-ph/9905386v2; D. Acosta *et al.* CDF Collaboration, Phys. Rev. Lett. **94**, 041803 (2005), http://arxiv.org/abs/hep-ex/0410008v2; U. Baur, T. Han and J. Ohnemus, Phys. Rev. D **57**, 2823 (1998).

[38] M. Cacciari, S. Frixione, M.L. Mangano, P. Nason, and G. Ridolfi, J. High Energy Phys. **04**, 068 (2004), http://arxiv.org/abs/hep-ph/0303085v1

[39] CDF Top Group, *CDF Top Quark Physics Public Results*, http://www-cdf.fnal.gov/physics/new/top/public_mass.html and http://www-cdf.fnal.gov/physics/new/top/public_xsection.html.

[40] D. Hare, E. Halkiadakis, and T. Spreitzer, CDF Internal Note **8614**; T. Spreitzer *et al.*, CDF Internal Note **7309**.

[41] U. Grundler, L. Lovas, and A. Taffard, CDF Internal Note **8618**; V. Martin, CDF Internal Note **7367**.

[42] CDF Run 2 Muon Detectors, http://www-cdfonline.fnal.gov/ops/cdf_muon/chambers.html.

[43] W. D. Dagenhart and D. Stentz, *Using CMX Muons*, CDF Internal Note **7989**.

[44] V. Martin, CDF Internal Note **7031**, Appendix B.2.

[45] K. Burkett, E. James, P. Beauchemin, and P. Savard, CDF Internal Note **8715**; K. Burkett *et al.*, CDF Internal Note **8722**; T. Aaltonen *et al.*, The CDF Collaboration, Phys. Rev. Lett. **101**, 181602 (2008) http://arxiv.org/abs/0807.3132v1.

[46] A. Sfyrla, CDF Internal Note **8989**; A. Annovi *et al.*, CDF Internal Note **9761**; A. Annovi *et al.*, CDF Internal Note **9807**.

[47] T. Aaltonen *et al.*, The CDF Collaboration, Phys. Rev. Lett. 100, 071801 (2008) http://arxiv.org/abs/0710.4112; V. Bartsch *et al.*, CDF Internal Note **8668**; Private correspondence with Emily Nurse.

[48] E. Lytken, A. Canepa, and D. Bortoletto, CDF Internal Note **8336**.

[49] This revelation was prompted by a study conducted by J. Strologas on the CMU efficiency between 7 and 3 cm; Private communication with John Strologas.

[50] Stubless muons are defined as tracks of energy deposition corresponding to a minimum ionizing particle and pointing to regions not covered by the muon detector; V. Martin, CDF Internal Note **7367**.

[51] Private correspondence with V. Martin.

[52] G. C. Blazey *et al.*, hep-ex/0005012; T. Aaltonen *et al.* CDF Collaboration, Phys. Rev. D **78**, 052006 (2008); A. Abulencia *et al.* CDF Collaboration, Phys. Rev. D 74, 071103(R) (2006); T. Affolder *et al.* (CDF Collaboration), Phys. Rev. D **64**, 032001 (2001).

[53] J. Strologas and S. Errede, CDF Internal Note **5877**; Also see [**54**]; Private correspondence with John Strologas.

[54] K. Bloom, CDF Internal Note **6559**.

[55] Jet Energy and Resolution Group, *Jet Energy Corrections*, http://www-cdf.fnal.gov/internal/physics/top/jets/corrections.html

[56] A. Bhatti *et al.*, Nucl. Instrum. Meth. A **566** 375-412 (2006).

[57] Jet Energy and Resolution Group, *Jet Energy Corrections – How to Apply them*, http://www-cdf.fnal.gov/internal/physics/top/jets/how-to-apply.html

[58] L. Nodulman, CDF Internal Note **6728**; H. S. Budd and W. K. Sakumoto, CDF Internal Note **6433**; B. Heinemann, CDF Internal Note **6406**; L. Nodulman, CDF Internal Note **6364**; *Jet Energy Corrections – Level 0*, http://www-cdf.fnal.gov/internal/physics/top/jets/level0.html.

[59] J. F. Arguin and B. Heinemann, CDF Internal Note **6239**.

[60] K. Hatakeyama and A. A. Bhatti, CDF Internal Note **7354**; A. A. Bhatti and K. Hatakeyama, CDF Internal Note **6854**.

[61] A. Bhatti and F. Canelli, CDF Internal Note **7450**; J. F. Arguin *et al.*, CDF Internal Note **6280**.

[62] J. F. Arguin and B. Heinemann, CDF Internal Note **6239**.

[63] J. F. Arguin *et al.*, CDF Internal Note **6565**.

[64] S. Pashapour and P. K. Sinervo, CDF Internal Note **7322**.

[65] F. Canelli and B. Heinemann, CDF Internal Note **7451**.

[66] Private correspondence with Kenichi Hatakeyama and Regis Lefevre via e-mail with Ben Kilminster and Jeannine Wagner.

[67] Private communication with Tom Junk.

[68] CDF Collaboration, Phys. Rev. Lett. **94** 091803 (2005), http://arxiv.org/abs/hep-ex/0406078v2; K. Copic, M. Schmitt, and V. Martin, CDF Internal Note **8195**.

[69] ROOT `TFractionFitter`, http://root.cern.ch/root/htmldoc/TFractionFitter.html.

[70] R. Barlow and C. Beeston, Comp. Phys. Comm. **77** 219-228 (1993); http://www.hep.man.ac.uk/~roger/hfrac.f.

[71] Lepton Working Group, http://www-cdf.fnal.gov/internal/physics/joint_physics/leptons/webpage.html.

[72] D. Hare, E. Halkiadakis, and T. Spreitzer, CDF Internal Note **8614**.

[73] Electron Trigger and ID efficiencies and Scale Factors in Gen 6, http://ncdf70.fnal.gov:8001/PerfIDia/HighElectronsID.

[74] U. Grundler, L. Lovas, and A. Taffard, CDF Internal Note **8618**.

[75] Muon Trigger, Reconstruction, and ID efficiencies and Scale Factors in Gen 6, http://ncdf70.fnal.gov:8001/PerfIDia/HighMuons.html.

[76] In collaboration with John Strologas.

[77] W. Sakumoto, CDF Internal Note **8318**; *Efficiency of the Z-vertex cut of 60 cm*, http://www-cdf.fnal.gov/internal/physics/joint_physics/instructions/zvertex-efficiency.html

[78] T. Affolder *et al.*, The CDF Collaboration, Phys. Rev. D **63**, 072003 (2001).

[79] Joint Physics Group, *PDF Uncertainties*, http://www-cdf.fnal.gov/internal/physics/joint_physics/instructions/PDFUncertainties/pdf.html

[80] We conform to the internal CDF nomenclature of CTEQ6M but technically we use the updated 6m PDFs which are denoted as CTEQ6.1M or CTEQ6_1M.

[81] D. Stump *et al.*, "Inclusive jet production, parton distributions, and the search for new physics", JHEP **0310**, 046 (2003); J. Pumplin *et al.*, "New generation of parton distributions with uncertainties from global QCD analysis", JHEP **0207**, 012 (2002); H. L. Lai *et al.* (CTEQ Collaboration), Eur. Phys. J. C **12**, 375 (2000).

[82] A. D. Martin *et al.*, Eur. Phys. J. C **14**, 133 (2000).

[83] K. Hagiwara *et al.*, Physical Review D66, 010001-1 (2002); PDG id table for fundamental particles, http://pdg.lbl.gov/mc_particle_id_contents.html.

[84] T. Affolder *et al.*, The CDF Collaboration, Phys. Rev. D **63**, 072003 (2001).

[85] S. Miller, Joint Physics PDF procedure, http://www-cdf.fnal.gov/internal/physics/joint_physics/pdfs/.

[86] O. Gonzalez and C. Rott, CDF Internal Note **7051**.

[87] D. H. Perkins, *Introduction to High Energy Physics*, 4th Edition, Addison-Wesley Menlo Park, California, p. 174 (2000).

[88] Literally, braking radiation; D. H. Perkins, *Introduction to High Energy Physics*, 4th Edition, Addison-Wesley Menlo Park, California, p. 354 (2000).

[89] *Useful Diagrams of Top Signals and Backgrounds*, http://www-d0.fnal.gov/Run2Physics/top/top_public_web_pages/top_feynman_diagrams.html

[90] A. Abulencia *et al.* (CDF Collaboration), Phys. Rev. D **73**, 032003 (2006).

[91] R. K. Ellis, K. Melnikov, and G. Zanderighi, Phys. Rev. D **80**, 094002 (2009); J. M. Campbell and R. K. Ellis, Phys. Rev. D **62** 114012 (2000).

[92] C. F. Berger *et al.*, Phys. Rev. Lett. **102**, 222001 (2009); C. F. Berger *et al.*, Phys. Rev. D **78**, 036003 (2008).

[93] D. Acosta *et al.* CDF Collaboration, Phys. Rev. Lett. **94**, 091803 (2005).

[94] T. Aaltonen *et al.* CDF Collaboration, Phys. Rev. D **79**, 011101(R) (2009); T. Aaltonen *et al.* CDF Collaboration, Phys. Rev. D **78**, 012002 (2008); Global Search for New Physics in 2.0 fb^{-1} of p-pbar Collisions at sqrt(s)=1.96 TeV, http://www-cdf.fnal.gov/physics/exotic/r2a/20080228.vista_sleuth/publicPage.html.

[95] See the discussion in [**12**] for BNLK NLL predictions.

APPENDIX

Cross-section Tables

This appendix gives the tabled version of the cross-section results presented in section 9. Each table includes the range (bin size) and cross-section for each cross-section histogram. The total and negative systematic error are included in the last pair of columns. For convenience we may used a simplified notation for the cross-section and the asymmetric error. Namely the cross-section will be σ and the total systematic noted by $\pm\Delta\sigma$. We will omit this notation for special ratio cross-sections like $r_{\Delta\eta}$ and σ_{n+1}/σ_n.

We also present the complimentary set of tables for the normalized cross-sections. The central value follows dividing by the appropriate inclusive jet multiplicity cross-section but the total systematic needs to be presented to track the relative improvement in our description and understanding of the shape. Note however, the values cited here are not the reduced cross-section values and thus represents a total cross-section defined with the nominal acceptance definition. The acceptance restricted reduced cross-sections can be obtained using 7.20 and equation 7.13 on 350 (see sections 7.4 and 9.1 for further details).

In table .1 we reproduce a similar mapping table as was presented before showing our systematic results (section 8.10 table 8.8). Here we give each cross-section observable (including normalized cross-sections and other cross-section ratios), the corresponding section where the cross-section was defined/introduced, and then the table and companion figure number for each channel (electrons then muons).

Cross-section Observable	Section	$W \to e\nu$ Table #	$W \to e\nu$ Figure #	$W \to \mu\nu$ Table #	$W \to \mu\nu$ Figure #
$\frac{\mathrm{d}\sigma}{\mathrm{d}n}$ †	9.3	.2	9.1	.3	9.2
$\frac{\mathrm{d}\sigma}{\mathrm{d}n}$	9.3	.4	9.3	.5	9.4
$\frac{\sigma_n}{\sigma_0}$	9.3	.6	9.5	.7	9.6
$\frac{\sigma_{n+1}}{\sigma_n}$	9.4	.8	9.7	.9	9.8
$\frac{\mathrm{d}\sigma}{\mathrm{d}p_T^{1st}}$	9.5	.10	9.9	.14	9.13
$\frac{\mathrm{d}\sigma}{\mathrm{d}p_T^{2nd}}$	9.5	.11	9.10	.15	9.14
$\frac{\mathrm{d}\sigma}{\mathrm{d}p_T^{3rd}}$	9.5	.12	9.11		9.15
$\frac{\mathrm{d}\sigma}{\mathrm{d}p_T^{4th}}$	9.5	.13	9.12	.17	9.16
$\frac{\mathrm{d}\sigma/\mathrm{d}p_T^{1st}}{\sigma_1}$	9.5	.18	9.17	.22	9.21
$\frac{\mathrm{d}\sigma/\mathrm{d}p_T^{2nd}}{\sigma_2}$	9.5	.19	9.18	.23	9.22
$\frac{\mathrm{d}\sigma/\mathrm{d}p_T^{3rd}}{\sigma_3}$	9.5	.20	9.19	.24	9.23
$\frac{\mathrm{d}\sigma/\mathrm{d}p_T^{4th}}{\sigma_4}$	9.5	.21	9.20	.25	9.24
$\frac{\mathrm{d}\sigma}{\mathrm{d}m_{jj}}$	9.7	.34	9.33	.35	9.34
$\frac{\mathrm{d}\sigma/\mathrm{d}m_{jj}}{\sigma_2}$	9.7	.36	9.35	.37	9.36
$\frac{\mathrm{d}\sigma}{\mathrm{d}R_{jj}}$	9.8	.38	9.37	.39	9.38
$\frac{\mathrm{d}\sigma/\mathrm{d}R_{jj}}{\sigma_2}$	9.8	.40	9.39	.41	9.40
$\frac{\mathrm{d}\sigma_2}{\mathrm{d}\Delta\eta}$	9.9	.42	9.43	.46	9.44
$\frac{\mathrm{d}\sigma_2/\mathrm{d}\Delta\eta}{\sigma 2}$	9.9	.44	9.45	.48	9.46
$\frac{\mathrm{d}\sigma_3}{\mathrm{d}\Delta\eta}$	9.9	.43	9.47	.47	9.48
$\frac{\mathrm{d}\sigma_3/\mathrm{d}\Delta\eta}{\sigma 3}$	9.9	.45	9.49	.49	9.50
$r_{\Delta\eta}$ (Eq. 9.6)	9.9	.50	9.51	.51	9.52

Table .1. The mapping of each cross-section table with its corresponding cross-section figure for each cross-section observable. †: The first jet multiplicity results are defined at the production level without reduce acceptance (default for all other observables).

$\geq n$ jets	$\sigma_n = \frac{\mathrm{d}\sigma}{\mathrm{d}n}$ (pb)
0	$2710 \pm 2 \,^{+71}_{-62} \pm 162$
1	$220 \pm 1 \,^{+29}_{-24} \pm 13$
2	$26.2 \pm 0.2 \,^{+5.9}_{-4.5} \pm 1.6$
3	$3.18 \pm 0.05 \,^{+1.02}_{-0.71} \pm 0.19$
4	$0.41 \pm 0.02 \,^{+0.26}_{-0.11} \pm 0.02$

Table .2. CDF Run II Preliminary. $W \to e\nu$ jet multiplicity *production* cross-section for 0-4 inclusive number of jets defined as $\sigma_n = \sigma(\mathrm{p\bar{p}} \to W + \geq n\mathrm{jets}) \times Br(W \to e\nu)$. Jets are defined with $p_T^{jet} > 20$ GeV/c and $|\eta^{jet}| < 2.0$. This is the production level cross-section version of table .4 and was shown in figure 9.1.

$\geq n$ jets	$\sigma_n = \frac{\mathrm{d}\sigma}{\mathrm{d}n}$ (pb)
0	$2720 \pm 3 \,^{+119}_{-104} \pm 163$
1	$271 \pm 1 \,^{+58}_{-17} \pm 16$
2	$35.6 \pm 0.2 \,^{+11.8}_{-3.8} \pm 2.1$
3	$4.68 \pm 0.08 \,^{+2.10}_{-0.69} \pm 0.28$
4	$0.69 \pm 0.03 \,^{+0.39}_{-0.15} \pm 0.04$

Table .3. CDF Run II Preliminary. $W \to \mu\nu$ jet multiplicity *production* cross-section for 0-4 inclusive number of jets defined as $\sigma_n = \sigma(\mathrm{p\bar{p}} \to W + \geq n\mathrm{jets}) \times Br(W \to \mu\nu)$. Jets are defined with $p_T^{jet} > 20$ GeV/c and $|\eta^{jet}| < 2.0$. This is the production level cross-section version of table .5 and was shown in figure 9.2.

$\geq n$ jets	$\sigma_n = \frac{\mathrm{d}\sigma}{\mathrm{d}n}$ (pb)
0	$1520 \pm 1.2 \,^{+79}_{-76} \pm 91$
1	$122 \pm 0.29 \,^{+17}_{-15} \pm 7.3$
2	$14.4 \pm 0.089 \,^{+3.3}_{-2.6} \pm 0.87$
3	$1.75 \pm 0.028 \,^{+0.57}_{-0.4} \pm 0.1$
4	$0.213 \pm 0.0093 \,^{+0.14}_{-0.059} \pm 0.013$

Table .4. CDF Run II Preliminary. $W \to e\nu$ jet multiplicity cross-section with $|\eta^e| < 1.1$, $p_T^e > 20$ GeV/c, and $M_T^W > 40$ GeV/c^2 for 0-4 inclusive number of jets. Jets are defined with $p_T^{jet} > 20$ GeV/c and $|\eta^{jet}| < 2.0$. The error is divided in to three respective parts: statistical, total systematic which is without the final luminosity systematic, and the luminosity systematic itself. This is a table version of plot 9.3 on page 421.

$\geq n$ jets	$\sigma_n = \frac{\mathrm{d}\sigma}{\mathrm{d}n}$ (pb)
0	$1480 \pm 1.4 \,^{+74}_{-69} \pm 89$
1	$147 \pm 0.39 \,^{+31}_{-11} \pm 8.8$
2	$19.2 \pm 0.13 \,^{+6.1}_{-2.1} \pm 1.2$
3	$2.49 \pm 0.045 \,^{+1.1}_{-0.38} \pm 0.15$
4	$0.36 \pm 0.016 \,^{+0.2}_{-0.08} \pm 0.022$

Table .5. CDF Run II Preliminary. $W \to \mu\nu$ jet multiplicity cross-section with $|\eta^\mu| < 1.1$, $p_T^\mu > 20$ GeV/c, and $M_T^W > 30$ GeV/c^2 for 0-4 inclusive number of jets. Jets are defined with $p_T^{jet} > 20$ GeV/c and $|\eta^{jet}| < 2.0$. The error is divided in to three respective parts: statistical, total systematic which is without the final luminosity systematic, and the luminosity systematic itself. This is a table version of plot 9.4 on page 421.

$\geq n$ jets	σ_n/σ_0
1	$0.0807 \pm 0.0002 \ ^{+0.0069}_{-0.0058}$
2	$0.00951 \pm 5.9{\times}10^{-5} \ ^{+0.0016}_{-0.0013}$
3	$0.00115 \pm 1.9{\times}10^{-5} \ ^{+0.0003}_{-0.00022}$
4	$0.00014 \pm 6.1{\times}10^{-6} \ ^{+7.8{\times}10^{-5}}_{-3.4{\times}10^{-5}}$

Table .6. CDF Run II Preliminary. $W \to e\nu$ jet multiplicity cross-section normalized to the total inclusive cross-section (σ_n/σ_0). The W cross-section is restricted to $|\eta^e| < 1.1$, $p_T^e > 20$ GeV/c, and $M_T^W > 40$ GeV/c^2 while jets are defined with $p_T^{jet} > 20$ GeV/c and $|\eta^{jet}| < 2.0$. The error is divided in to a statistical and total systematic uncertainty, respectively. This is a table version of plot 9.5 on page 422.

$\geq n$ jets	σ_n/σ_0
1	$0.0991 \pm 0.00027 \ ^{+0.015}_{-0.0027}$
2	$0.0129 \pm 8.8{\times}10^{-5} \ ^{+0.0033}_{-0.00088}$
3	$0.00168 \pm 3{\times}10^{-5} \ ^{+0.00062}_{-0.00019}$
4	$0.000243 \pm 1.1{\times}10^{-5} \ ^{+0.00012}_{-4.5{\times}10^{-5}}$

Table .7. CDF Run II Preliminary. $W \to \mu\nu$ jet multiplicity cross-section normalized to the total inclusive cross-section (σ_n/σ_0). The W cross-section is restricted to $|\eta^\mu| < 1.1$, $p_T^\mu > 20$ GeV/c, and $M_T^W > 30$ GeV/c^2 while jets are defined with $p_T^{jet} > 20$ GeV/c and $|\eta^{jet}| < 2.0$. The error is divided in to a statistical and total systematic uncertainty, respectively. This is a table version of plot 9.6 on page 422.

$\geq n$ jets	$\frac{\sigma_{n+1}}{\sigma_n}$
0	$0.081 \pm 0.0002\ ^{+0.010}_{-0.008}$
1	$0.118 \pm 0.0008\ ^{+0.009}_{-0.008}$
2	$0.121 \pm 0.0020\ ^{+0.010}_{-0.007}$
3	$0.122 \pm 0.0054\ ^{+0.029}_{-0.009}$

Table .8. CDF Run II Preliminary. $W \to e\nu$ jet multiplicity cross-section ratio (σ_{n+1}/σ_n) with n the number of inclusive jets. The W cross-section is restricted to $|\eta^e| < 1.1$, $p_T^e > 20$ GeV/c, and $M_T^W > 40$ GeV/c^2 while jets are defined with $p_T^{jet} > 20$ GeV/c and $|\eta^{jet}| < 2.0$. The error is divided in to a statistical and total systematic uncertainty, respectively. This is a table version of plot 9.7 on page 423.

$\geq n$ jets	$\frac{\sigma_{n+1}}{\sigma_n}$
0	$0.099 \pm 0.0003\ ^{+0.018}_{-0.005}$
1	$0.130 \pm 0.0009\ ^{+0.011}_{-0.006}$
2	$0.130 \pm 0.0024\ ^{+0.012}_{-0.005}$
3	$0.145 \pm 0.0067\ ^{+0.015}_{-0.012}$

Table .9. CDF Run II Preliminary. $W \to \mu\nu$ jet multiplicity ratio (σ_{n+1}/σ_n) with n the number of inclusive jets. The W cross-section is restricted to $|\eta^\mu| < 1.1$, $p_T^\mu > 20$ GeV/c, and $M_T^W > 30$ GeV/c^2 while jets are defined with $p_T^{jet} > 20$ GeV/c and $|\eta^{jet}| < 2.0$. The error is divided in to a statistical and total systematic uncertainty, respectively. This is a table version of plot 9.8 on page 424.

p_T range (GeV/c)	$d\sigma_1/dp_T^{1st}$ (pb/(GeV/c))
20-25	$7.63 \pm 0.03 \, {}^{+1}_{-1.1} \pm 0.46$
25-30	$4.97 \pm 0.025 \, {}^{+0.61}_{-0.7} \pm 0.3$
30-35	$3.3 \pm 0.021 \, {}^{+0.41}_{-0.39} \pm 0.2$
35-40	$2.29 \pm 0.018 \, {}^{+0.26}_{-0.31} \pm 0.14$
40-45	$1.62 \pm 0.016 \, {}^{+0.18}_{-0.2} \pm 0.097$
45-50	$1.15 \pm 0.014 \, {}^{+0.12}_{-0.13} \pm 0.069$
50-55	$0.88 \pm 0.012 \, {}^{+0.091}_{-0.1} \pm 0.053$
55-60	$0.654 \pm 0.01 \, {}^{+0.053}_{-0.066} \pm 0.039$
60-65	$0.491 \pm 0.0087 \, {}^{+0.045}_{-0.064} \pm 0.029$
65-70	$0.363 \pm 0.0079 \, {}^{+0.032}_{-0.031} \pm 0.022$
70-75	$0.301 \pm 0.007 \, {}^{+0.022}_{-0.035} \pm 0.018$
75-80	$0.22 \pm 0.0061 \, {}^{+0.014}_{-0.021} \pm 0.013$
80-85	$0.188 \pm 0.0057 \, {}^{+0.013}_{-0.021} \pm 0.011$
85-90	$0.143 \pm 0.0051 \, {}^{+0.012}_{-0.011} \pm 0.0086$
90-95	$0.125 \pm 0.0045 \, {}^{+0.015}_{-0.024} \pm 0.0075$
95-105	$0.075 \pm 0.0027 \, {}^{+0.0072}_{-0.011} \pm 0.0045$
105-120	$0.0475 \pm 0.0018 \, {}^{+0.0063}_{-0.0057} \pm 0.0028$
120-140	$0.024 \pm 0.00098 \, {}^{+0.002}_{-0.0048} \pm 0.0014$
140-175	$0.00793 \pm 0.00052 \, {}^{+0.0018}_{-0.0014} \pm 0.00048$
175-230	$0.00187 \pm 0.00018 \, {}^{+0.00026}_{-0.00029} \pm 0.00011$
230-430	$0.000147 \pm 2.8{\times}10^{-5} \, {}^{+2.3{\times}10^{-5}}_{-2.4{\times}10^{-5}} \pm 8.8{\times}10^{-6}$

Table .10. CDF Run II Preliminary. The leading jet p_T differential cross-section for $W \to e\nu + \geq 1$ inclusive jets. The W cross-section is restricted to $|\eta^e| < 1.1$, $p_T^e > 20\,\text{GeV/c}$, and $M_T^W > 40\,\text{GeV/c}^2$ while jets are defined with $p_T^{jet} > 20\,\text{GeV/c}$ and $|\eta^{jet}| < 2.0$. The error is divided in to three respective parts: statistical, total systematic which is without the final luminosity systematic, and the luminosity systematic itself. This is a table version of plot 9.9 on page 426.

p_T range (GeV/c)	$\mathrm{d}\sigma_2/\mathrm{d}p_T^{2\mathrm{nd}}$ (pb/(GeV/c))
20-25	$1.18 \pm 0.011 \; {}^{+0.29}_{-0.25} \pm 0.071$
25-30	$0.674 \pm 0.0086 \; {}^{+0.11}_{-0.14} \pm 0.04$
30-35	$0.361 \pm 0.0067 \; {}^{+0.053}_{-0.063} \pm 0.022$
35-40	$0.216 \pm 0.0052 \; {}^{+0.038}_{-0.028} \pm 0.013$
40-45	$0.15 \pm 0.0042 \; {}^{+0.017}_{-0.019} \pm 0.009$
45-50	$0.106 \pm 0.0036 \; {}^{+0.013}_{-0.023} \pm 0.0064$
50-55	$0.063 \pm 0.0031 \; {}^{+0.012}_{-0.0088} \pm 0.0038$
55-60	$0.0505 \pm 0.0025 \; {}^{+0.0055}_{-0.007} \pm 0.003$
60-65	$0.0358 \pm 0.0022 \; {}^{+0.0045}_{-0.0058} \pm 0.0021$
65-75	$0.0238 \pm 0.0013 \; {}^{+0.0018}_{-0.0033} \pm 0.0014$
75-85	$0.0173 \pm 0.00094 \; {}^{+0.0012}_{-0.0015} \pm 0.001$
85-100	$0.00866 \pm 0.00057 \; {}^{+0.0012}_{-0.0024} \pm 0.00052$
100-135	$0.00233 \pm 0.00024 \; {}^{+0.00026}_{-0.00018} \pm 0.00014$
135-260	$0.000341 \pm 4\times10^{-5} \; {}^{+3.2\times10^{-5}}_{-3.3\times10^{-5}} \pm 2\times10^{-5}$

Table .11. CDF Run II Preliminary. The second leading jet p_T differential cross-section for $W \to e\nu+ \geq 2$ inclusive jets. The W cross-section is restricted to $|\eta^e| < 1.1$, $p_T^e > 20$ GeV/c, and $M_T^W > 40$ GeV/c^2 while jets are defined with $p_T^{jet} > 20$ GeV/c and $|\eta^{jet}| < 2.0$. The error is divided in to three respective parts: statistical, total systematic which is without the final luminosity systematic, and the luminosity systematic itself. This is a table version of plot 9.10 on page 426.

p_T range (GeV/c)	$\mathrm{d}\sigma_3/\mathrm{d}p_T^{\mathrm{3rd}}$ (pb/(GeV/c))
20-25	$0.18 \pm 0.0039 \, ^{+0.059}_{-0.05} \pm 0.011$
25-30	$0.0802 \pm 0.0027 \, ^{+0.022}_{-0.018} \pm 0.0048$
30-35	$0.041 \pm 0.002 \, ^{+0.0086}_{-0.01} \pm 0.0025$
35-40	$0.0243 \pm 0.0016 \, ^{+0.0042}_{-0.0032} \pm 0.0015$
40-45	$0.017 \pm 0.0011 \, ^{+0.0029}_{-0.0065} \pm 0.001$
45-50	$0.009 \pm 0.00086 \, ^{+0.0021}_{-0.0034} \pm 0.00054$
50-70	$0.00291 \pm 0.00026 \, ^{+0.00086}_{-0.00056} \pm 0.00017$
70-170	$0.000147 \pm 2.8 \times 10^{-5} \, ^{+2.6 \times 10^{-5}}_{-1.8 \times 10^{-5}} \pm 8.8 \times 10^{-6}$

Table .12. CDF Run II Preliminary. The third leading jet p_T cross-section differential for $W \to e\nu + {\geq}3$ inclusive jets. The W cross-section is restricted to $|\eta^e| < 1.1$, $p_T^e > 20$ GeV/c, and $M_T^W > 40$ GeV/c^2 while jets are defined with $p_T^{jet} > 20$ GeV/c and $|\eta^{jet}| < 2.0$. The error is divided in to three respective parts: statistical, total systematic which is without the final luminosity systematic, and the luminosity systematic itself. This is a table version of plot 9.11 on page 427.

p_T range (GeV/c)	$\mathrm{d}\sigma_4/\mathrm{d}p_T^{\mathrm{4th}}$ (pb/(GeV/c))
20-25	$0.0259 \pm 0.0014 \, ^{+0.013}_{-0.0084} \pm 0.0016$
25-35	$0.00639 \pm 0.00055 \, ^{+0.005}_{-0.0028} \pm 0.00038$
35-50	$0.00221 \pm 0.00019 \, ^{+0.00061}_{-0.00095} \pm 0.00013$
50-90	$0.000104 \pm 3.8 \times 10^{-5} \, ^{+5.8 \times 10^{-5}}_{-8.4 \times 10^{-5}} \pm 6.2 \times 10^{-6}$

Table .13. CDF Run II Preliminary. The fourth leading jet p_T cross-section for $W \to e\nu + {\geq}4$ inclusive jets. The W cross-section is restricted to $|\eta^e| < 1.1$, $p_T^e > 20$ GeV/c, and $M_T^W > 40$ GeV/c^2 while jets are defined with $p_T^{jet} > 20$ GeV/c and $|\eta^{jet}| < 2.0$. The error is divided in to three respective parts: statistical, total systematic which is without the final luminosity systematic, and the luminosity systematic itself. This is a table version of plot 9.12 on page 427.

p_T range (GeV/c)	$\mathrm{d}\sigma_1/\mathrm{d}p_T^{\mathrm{1st}}$ (pb/(GeV/c))
20-25	$8.89 \pm 0.04\ ^{+1.4}_{-0.91} \pm 0.53$
25-30	$5.79 \pm 0.033\ ^{+0.98}_{-0.45} \pm 0.35$
30-35	$3.86 \pm 0.028\ ^{+0.76}_{-0.31} \pm 0.23$
35-40	$2.7 \pm 0.024\ ^{+0.5}_{-0.17} \pm 0.16$
40-45	$2.01 \pm 0.021\ ^{+0.38}_{-0.13} \pm 0.12$
45-50	$1.44 \pm 0.018\ ^{+0.31}_{-0.1} \pm 0.086$
50-55	$1.14 \pm 0.016\ ^{+0.21}_{-0.076} \pm 0.068$
55-60	$0.851 \pm 0.014\ ^{+0.19}_{-0.063} \pm 0.051$
60-65	$0.618 \pm 0.012\ ^{+0.14}_{-0.049} \pm 0.037$
65-70	$0.53 \pm 0.011\ ^{+0.079}_{-0.034} \pm 0.032$
70-75	$0.418 \pm 0.0096\ ^{+0.062}_{-0.027} \pm 0.025$
75-80	$0.317 \pm 0.0085\ ^{+0.057}_{-0.022} \pm 0.019$
80-85	$0.253 \pm 0.0078\ ^{+0.05}_{-0.021} \pm 0.015$
85-90	$0.21 \pm 0.0068\ ^{+0.025}_{-0.016} \pm 0.013$
90-95	$0.163 \pm 0.0061\ ^{+0.027}_{-0.017} \pm 0.0098$
95-105	$0.131 \pm 0.0037\ ^{+0.019}_{-0.0098} \pm 0.0078$
105-120	$0.0715 \pm 0.0024\ ^{+0.016}_{-0.0063} \pm 0.0043$
120-140	$0.0432 \pm 0.0014\ ^{+0.0055}_{-0.0029} \pm 0.0026$
140-175	$0.0165 \pm 0.00072\ ^{+0.0034}_{-0.0016} \pm 0.00099$
175-230	$0.00389 \pm 0.00027\ ^{+0.00086}_{-0.00038} \pm 0.00023$
230-430	$0.000387 \pm 4.2{\times}10^{-5}\ ^{+7.6{\times}10^{-5}}_{-5.1{\times}10^{-5}} \pm 2.3{\times}10^{-5}$

Table .14. CDF Run II Preliminary. The leading jet p_T cross-section for $W \to \mu\nu + \geq 1$ inclusive jet. The W cross-section is restricted to $|\eta^\mu| < 1.1$, $p_T^\mu > 20$ GeV/c, and $M_T^W > 30$ GeV/c^2 while jets are defined with $p_T^{jet} > 20$ GeV/c and $|\eta^{jet}| < 2.0$. The error is divided in to three respective parts: statistical, total systematic which is without the final luminosity systematic, and the luminosity systematic itself. This is a table version of plot 9.13 on page 428.

p_T range (GeV/c)	$\mathrm{d}\sigma_2/\mathrm{d}p_T^{\mathrm{2nd}}$ (pb/(GeV/c))
20-25	$1.55 \pm 0.016 \, ^{+0.48}_{-0.23} \pm 0.093$
25-30	$0.83 \pm 0.012 \, ^{+0.24}_{-0.097} \pm 0.05$
30-35	$0.493 \pm 0.0095 \, ^{+0.11}_{-0.05} \pm 0.03$
35-40	$0.318 \pm 0.0076 \, ^{+0.081}_{-0.033} \pm 0.019$
40-45	$0.198 \pm 0.006 \, ^{+0.044}_{-0.017} \pm 0.012$
45-50	$0.147 \pm 0.0052 \, ^{+0.031}_{-0.014} \pm 0.0088$
50-55	$0.113 \pm 0.0043 \, ^{+0.012}_{-0.0077} \pm 0.0068$
55-60	$0.0707 \pm 0.0034 \, ^{+0.014}_{-0.0069} \pm 0.0042$
60-65	$0.0524 \pm 0.0032 \, ^{+0.01}_{-0.0051} \pm 0.0031$
65-75	$0.0367 \pm 0.0018 \, ^{+0.0047}_{-0.0028} \pm 0.0022$
75-85	$0.0216 \pm 0.0013 \, ^{+0.0025}_{-0.0033} \pm 0.0013$
85-100	$0.0133 \pm 0.00086 \, ^{+0.0022}_{-0.0012} \pm 0.0008$
100-135	$0.00409 \pm 0.00032 \, ^{+0.00078}_{-0.00032} \pm 0.00025$
135-260	$0.000427 \pm 5.4{\times}10^{-5} \, ^{+0.00012}_{-5.3{\times}10^{-5}} \pm 2.6{\times}10^{-5}$

Table .15. CDF Run II Preliminary. The second leading jet p_T cross-section for $W \to \mu\nu + \geq 2$ inclusive jets. The W cross-section is restricted to $|\eta^\mu| <$ 1.1, $p_T^\mu > 20$ GeV/c, and $M_T^W > 30$ GeV/c^2 while jets are defined with $p_T^{jet} > 20$ GeV/c and $|\eta^{jet}| < 2.0$. The error is divided in to three respective parts: statistical, total systematic which is without the final luminosity systematic, and the luminosity systematic itself. This is a table version of plot 9.14 on page 428.

p_T range (GeV/c)	$\mathrm{d}\sigma_3/\mathrm{d}p_T^{\mathrm{3rd}}$ (pb/(GeV/c))
20-25	$0.244 \pm 0.006\ ^{+0.098}_{-0.048} \pm 0.015$
25-30	$0.123 \pm 0.0045\ ^{+0.046}_{-0.018} \pm 0.0074$
30-35	$0.0637 \pm 0.0032\ ^{+0.02}_{-0.0088} \pm 0.0038$
35-40	$0.0372 \pm 0.0024\ ^{+0.0081}_{-0.0061} \pm 0.0022$
40-45	$0.0203 \pm 0.0018\ ^{+0.011}_{-0.0051} \pm 0.0012$
45-50	$0.0113 \pm 0.0014\ ^{+0.0074}_{-0.0035} \pm 0.00068$
50-70	$0.0043 \pm 0.00042\ ^{+0.00071}_{-0.00083} \pm 0.00026$
70-170	$0.000226 \pm 4.3 \times 10^{-5}\ ^{+4.2 \times 10^{-5}}_{-3.8 \times 10^{-5}} \pm 1.4 \times 10^{-5}$

Table .16. CDF Run II Preliminary. The third leading jet p_T cross-section for $W \to \mu\nu+ \geq 3$ inclusive jets. The W cross-section is restricted to $|\eta^\mu| <$ 1.1, $p_T^\mu > 20$ GeV/c, and $M_T^W > 30$ GeV/c^2 while jets are defined with $p_T^{jet} > 20$ GeV/c and $|\eta^{jet}| < 2.0$. The error is divided in to three respective parts: statistical, total systematic which is without the final luminosity systematic, and the luminosity systematic itself. This is a table version of plot 9.15 on page 429.

p_T range (GeV/c)	$\mathrm{d}\sigma_4/\mathrm{d}p_T^{\mathrm{4th}}$ (pb/(GeV/c))
20-25	$0.0416 \pm 0.0024\ ^{+0.022}_{-0.013} \pm 0.0025$
25-35	$0.0128 \pm 0.001\ ^{+0.0066}_{-0.0043} \pm 0.00077$
35-50	$0.00236 \pm 0.00034\ ^{+0.00093}_{-0.0014} \pm 0.00014$
50-90	$0.000218 \pm 5.2 \times 10^{-5}\ ^{+7 \times 10^{-5}}_{-0.00011} \pm 1.3 \times 10^{-5}$

Table .17. CDF Run II Preliminary. The fourth leading jet p_T cross-section for $W \to \mu\nu+ \geq 4$ inclusive jets. The W cross-section is restricted to $|\eta^\mu| <$ 1.1, $p_T^\mu > 20$ GeV/c, and $M_T^W > 30$ GeV/c^2 while jets are defined with $p_T^{jet} > 20$ GeV/c and $|\eta^{jet}| < 2.0$. The error is divided in to three respective parts: statistical, total systematic which is without the final luminosity systematic, and the luminosity systematic itself. This is a table version of plot 9.16 on page 429.

p_T range (GeV/c)	$\frac{\mathrm{d}\sigma_1/\mathrm{d}p_T^{1st}}{\sigma_1}$ (c/GeV)
20-25	$0.0624 \pm 0.00024\ ^{+0.00055}_{-0.0014}$
25-30	$0.0406 \pm 0.00021\ ^{+0.00066}_{-0.001}$
30-35	$0.027 \pm 0.00018\ ^{+3.1\times10^{-5}}_{-0.00038}$
35-40	$0.0187 \pm 0.00015\ ^{+0.00032}_{-0.00049}$
40-45	$0.0133 \pm 0.00013\ ^{+2.7\times10^{-5}}_{-0.00036}$
45-50	$0.00942 \pm 0.00011\ ^{+8.4\times10^{-5}}_{-0.00027}$
50-55	$0.0072 \pm 9.9\times10^{-5}\ ^{+3.4\times10^{-5}}_{-0.00024}$
55-60	$0.00535 \pm 8.4\times10^{-5}\ ^{+0.00011}_{-0.00028}$
60-65	$0.00402 \pm 7.2\times10^{-5}\ ^{+4.7\times10^{-5}}_{-0.00018}$
65-70	$0.00297 \pm 6.5\times10^{-5}\ ^{+0.00012}_{-0.00014}$
70-75	$0.00246 \pm 5.8\times10^{-5}\ ^{+5.4\times10^{-6}}_{-0.00015}$
75-80	$0.0018 \pm 5\times10^{-5}\ ^{+4.3\times10^{-5}}_{-0.00012}$
80-85	$0.00154 \pm 4.7\times10^{-5}\ ^{+1.5\times10^{-5}}_{-9.5\times10^{-5}}$
85-90	$0.00117 \pm 4.2\times10^{-5}\ ^{+6\times10^{-5}}_{-5.8\times10^{-5}}$
90-95	$0.00102 \pm 3.7\times10^{-5}\ ^{+1.9\times10^{-5}}_{-8.7\times10^{-5}}$
95-105	$0.000613 \pm 2.2\times10^{-5}\ ^{+2.4\times10^{-5}}_{-2.5\times10^{-5}}$
105-120	$0.000388 \pm 1.5\times10^{-5}\ ^{+2.7\times10^{-7}}_{-3.4\times10^{-6}}$
120-140	$0.000196 \pm 8.1\times10^{-6}\ ^{+9.8\times10^{-6}}_{-1.8\times10^{-5}}$
140-175	$6.48\times10^{-5} \pm 4.2\times10^{-6}\ ^{+4.5\times10^{-6}}_{-3.9\times10^{-6}}$
175-230	$1.53\times10^{-5} \pm 1.5\times10^{-6}\ ^{+2.2\times10^{-8}}_{-6.1\times10^{-7}}$
230-430	$1.2\times10^{-6} \pm 2.3\times10^{-7}\ ^{+1.8\times10^{-8}}_{-5.8\times10^{-8}}$

Table .18. CDF Run II Preliminary. The leading jet p_T cross-section for $W \to e\nu+\ \geq 1$ inclusive jet normalized to the inclusive ≥ 1 jet multiplicity cross-section. The W cross-section is restricted to $|\eta^e| < 1.1$, $p_T^e > 20$ GeV/c, and $M_T^W > 40$ GeV/c^2 while jets are defined with $p_T^{jet} > 20$ GeV/c and $|\eta^{jet}| < 2.0$. The error is divided in to a statistical and total systematic uncertainty, respectively. This is a table version of plot 9.17 on page 430.

p_T range (GeV/c)	$\frac{\mathrm{d}\sigma_2/\mathrm{d}p_T^{\mathrm{2nd}}}{\sigma_2}$ (c/GeV)
20-25	$0.0819 \pm 0.0007\ ^{+0.0014}_{-0.0036}$
25-30	$0.0467 \pm 0.0006\ ^{+0.0015}_{-0.0022}$
30-35	$0.025 \pm 0.00047\ ^{+0.0001}_{-0.0016}$
35-40	$0.015 \pm 0.00036\ ^{+0.00086}_{-0.00064}$
40-45	$0.0104 \pm 0.0003\ ^{+0.00063}_{-0.00094}$
45-50	$0.00736 \pm 0.00025\ ^{+0.00036}_{-0.00061}$
50-55	$0.00437 \pm 0.00021\ ^{+0.0002}_{-0.00012}$
55-60	$0.0035 \pm 0.00018\ ^{+0.00017}_{-0.00034}$
60-65	$0.00248 \pm 0.00015\ ^{+4.2\times10^{-5}}_{-0.00021}$
65-75	$0.00165 \pm 8.9\times10^{-5}\ ^{+8.1\times10^{-5}}_{-0.0002}$
75-85	$0.0012 \pm 6.5\times10^{-5}\ ^{+0.00014}_{-0.00015}$
85-100	$0.0006 \pm 4\times10^{-5}\ ^{+4\times10^{-5}}_{-7.5\times10^{-5}}$
100-135	$0.000161 \pm 1.7\times10^{-5}\ ^{+1.9\times10^{-5}}_{-1.5\times10^{-5}}$
135-260	$2.36\times10^{-5} \pm 2.7\times10^{-6}\ ^{+2.3\times10^{-6}}_{-2.5\times10^{-6}}$

Table .19. CDF Run II Preliminary. The second leading jet p_T cross-section for $W \to e\nu +\ \geq 2$ inclusive jets normalized to the inclusive ≥ 2 jets multiplicity cross-section. The W cross-section is restricted to $|\eta^e| < 1.1$, $p_T^e > 20$ GeV/c, and $M_T^W > 40$ GeV/c^2 while jets are defined with $p_T^{jet} > 20$ GeV/c and $|\eta^{jet}| < 2.0$. The error is divided in to a statistical and total systematic uncertainty, respectively. This is a table version of plot 9.18 on page 431.

p_T range (GeV/c)	$\frac{\mathrm{d}\sigma_3/\mathrm{d}p_T^{3\mathrm{rd}}}{\sigma_3}$ (c/GeV)
20-25	$0.103 \pm 0.002\ ^{+1.6\times10^{-5}}_{-0.0064}$
25-30	$0.0459 \pm 0.0016\ ^{+0.00027}_{-0.0016}$
30-35	$0.0235 \pm 0.0012\ ^{+0.0006}_{-0.0021}$
35-40	$0.0139 \pm 0.0009\ ^{+0.0017}_{-0.0016}$
40-45	$0.00973 \pm 0.00066\ ^{+0.0011}_{-0.0019}$
45-50	$0.00514 \pm 0.0005\ ^{+0.00037}_{-0.00097}$
50-70	$0.00166 \pm 0.00015\ ^{+7.7\times10^{-5}}_{-4\times10^{-5}}$
70-170	$8.39\times10^{-5} \pm 1.6\times10^{-5}\ ^{+1.1\times10^{-5}}_{-9.5\times10^{-6}}$

Table .20. CDF Run II Preliminary. The third leading jet p_T cross-section for $W \to e\nu+ \geq 3$ inclusive jets normalized to the inclusive ≥ 3 jets multiplicity cross-section. The W cross-section is restricted to $|\eta^e| < 1.1$, $p_T^e > 20$ GeV/c, and $M_T^W > 40$ GeV/c^2 while jets are defined with $p_T^{jet} > 20$ GeV/c and $|\eta^{jet}| < 2.0$. The error is divided in to a statistical and total systematic uncertainty, respectively. This is a table version of plot 9.19 on page 431.

p_T range (GeV/c)	$\frac{\mathrm{d}\sigma_4/\mathrm{d}p_T^{4\mathrm{th}}}{\sigma_4}$ (c/GeV)
20-25	$0.122 \pm 0.0053\ ^{+0.0076}_{-0.0092}$
25-35	$0.03 \pm 0.0025\ ^{+0.0028}_{-0.0065}$
35-50	$0.0104 \pm 0.00094\ ^{+0.0022}_{-0.0023}$
50-90	$0.000489 \pm 0.00018\ ^{+2.4\times10^{-5}}_{-0.00036}$

Table .21. CDF Run II Preliminary. The fourth leading jet p_T cross-section for $W \to e\nu+ \geq 4$ inclusive jets normalized to the inclusive ≥ 4 jets multiplicity cross-section. The W cross-section is restricted to $|\eta^e| < 1.1$, $p_T^e > 20$ GeV/c, and $M_T^W > 40$ GeV/c^2 while jets are defined with $p_T^{jet} > 20$ GeV/c and $|\eta^{jet}| < 2.0$. The error is divided in to a statistical and total systematic uncertainty, respectively. This is a table version of plot 9.20 on page 432.

p_T range (GeV/c)	$\dfrac{\mathrm{d}\sigma_1/\mathrm{d}p_T^{\mathrm{1st}}}{\sigma_1}$ (c/GeV)
20-25	$0.0604 \pm 0.00027 \, ^{+0.002}_{-0.0027}$
25-30	$0.0394 \pm 0.00023 \, ^{+0.00027}_{-0.0014}$
30-35	$0.0263 \pm 0.00019 \, ^{+0.00026}_{-0.00035}$
35-40	$0.0184 \pm 0.00016 \, ^{+0.00015}_{-0.00044}$
40-45	$0.0137 \pm 0.00014 \, ^{+8.7\times10^{-5}}_{-0.00026}$
45-50	$0.00978 \pm 0.00012 \, ^{+2.4\times10^{-5}}_{-5.2\times10^{-6}}$
50-55	$0.00773 \pm 0.00011 \, ^{+4.2\times10^{-5}}_{-0.00016}$
55-60	$0.00579 \pm 9.5\times10^{-5} \, ^{+5.7\times10^{-5}}_{-1.5\times10^{-5}}$
60-65	$0.0042 \pm 8.3\times10^{-5} \, ^{+7.4\times10^{-5}}_{-3.6\times10^{-5}}$
65-70	$0.00361 \pm 7.5\times10^{-5} \, ^{+2.9\times10^{-5}}_{-0.00019}$
70-75	$0.00285 \pm 6.6\times10^{-5} \, ^{+2.5\times10^{-5}}_{-0.00015}$
75-80	$0.00215 \pm 5.8\times10^{-5} \, ^{+4.8\times10^{-6}}_{-6\times10^{-5}}$
80-85	$0.00172 \pm 5.3\times10^{-5} \, ^{+2\times10^{-5}}_{-2.1\times10^{-5}}$
85-90	$0.00143 \pm 4.6\times10^{-5} \, ^{+6.3\times10^{-6}}_{-0.00011}$
90-95	$0.00111 \pm 4.2\times10^{-5} \, ^{+3.7\times10^{-5}}_{-4.3\times10^{-5}}$
95-105	$0.000888 \pm 2.5\times10^{-5} \, ^{+3\times10^{-6}}_{-4.7\times10^{-5}}$
105-120	$0.000486 \pm 1.6\times10^{-5} \, ^{+5.5\times10^{-6}}_{-8.3\times10^{-6}}$
120-140	$0.000294 \pm 9.8\times10^{-6} \, ^{+1.3\times10^{-6}}_{-2.1\times10^{-5}}$
140-175	$0.000112 \pm 4.9\times10^{-6} \, ^{+6.4\times10^{-7}}_{-3\times10^{-6}}$
175-230	$2.65\times10^{-5} \pm 1.8\times10^{-6} \, ^{+1.6\times10^{-7}}_{-7.4\times10^{-7}}$
230-430	$2.63\times10^{-6} \pm 2.8\times10^{-7} \, ^{+3.7\times10^{-8}}_{-1.7\times10^{-7}}$

Table .22. CDF Run II Preliminary. The leading jet p_T cross-section for $W \to \mu\nu + \geq 1$ inclusive jet normalized to the inclusive ≥ 1 jet multiplicity cross-section. The W cross-section is restricted to $|\eta^\mu| < 1.1$, $p_T^\mu > 20$ GeV/c, and $M_T^W > 30$ GeV/c^2 while jets are defined with $p_T^{jet} > 20$ GeV/c and $|\eta^{jet}| < 2.0$. The error is divided in to a statistical and total systematic uncertainty, respectively. This is a table version of plot 9.21 on page 432.

p_T range (GeV/c)	$\frac{\mathrm{d}\sigma_2/\mathrm{d}p_T^{\mathrm{2nd}}}{\sigma_2}$ (c/GeV)
20-25	$0.0807 \pm 0.00078 \, ^{+0.00073}_{-0.0034}$
25-30	$0.0433 \pm 0.00065 \, ^{+0.00026}_{-0.0011}$
30-35	$0.0257 \pm 0.0005 \, ^{+0.00029}_{-0.0019}$
35-40	$0.0166 \pm 0.0004 \, ^{+0.00014}_{-0.0008}$
40-45	$0.0103 \pm 0.00032 \, ^{+0.00028}_{-0.00074}$
45-50	$0.00768 \pm 0.00027 \, ^{+0.00011}_{-0.00065}$
50-55	$0.00588 \pm 0.00023 \, ^{+0.00028}_{-0.00095}$
55-60	$0.00369 \pm 0.00018 \, ^{+5.8\times10^{-5}}_{-0.00032}$
60-65	$0.00273 \pm 0.00017 \, ^{+4.5\times10^{-5}}_{-0.00025}$
65-75	$0.00191 \pm 9.7\times10^{-5} \, ^{+7.6\times10^{-5}}_{-0.00028}$
75-85	$0.00113 \pm 7\times10^{-5} \, ^{+5.1\times10^{-5}}_{-0.00017}$
85-100	$0.000692 \pm 4.5\times10^{-5} \, ^{+1.9\times10^{-5}}_{-8\times10^{-5}}$
100-135	$0.000213 \pm 1.7\times10^{-5} \, ^{+7.9\times10^{-6}}_{-2.1\times10^{-5}}$
135-260	$2.23\times10^{-5} \pm 2.8\times10^{-6} \, ^{+3.4\times10^{-7}}_{-5\times10^{-7}}$

Table .23. CDF Run II Preliminary. The second leading jet p_T cross-section for $W \to \mu\nu + \geq 2$ inclusive jets normalized to the inclusive ≥ 2 jets multiplicity cross-section. The W cross-section is restricted to $|\eta^\mu| < 1.1$, $p_T^\mu > 20$ GeV/c, and $M_T^W > 30$ GeV/c^2 while jets are defined with $p_T^{jet} > 20$ GeV/c and $|\eta^{jet}| < 2.0$. The error is divided in to a statistical and total systematic uncertainty, respectively. This is a table version of plot 9.22 on page 433.

p_T range (GeV/c)	$\frac{\mathrm{d}\sigma_3/\mathrm{d}p_T^{3\mathrm{rd}}}{\sigma_3}$ (c/GeV)
20-25	$0.0979 \pm 0.0022 \, {}^{+0.0026}_{-0.0051}$
25-30	$0.0496 \pm 0.0018 \, {}^{+0.00026}_{-0.0024}$
30-35	$0.0256 \pm 0.0013 \, {}^{+0.00047}_{-0.0023}$
35-40	$0.015 \pm 0.00099 \, {}^{+0.00021}_{-0.0023}$
40-45	$0.00817 \pm 0.00073 \, {}^{+0.00063}_{-0.00094}$
45-50	$0.00456 \pm 0.00056 \, {}^{+0.00067}_{-0.00084}$
50-70	$0.00173 \pm 0.00017 \, {}^{+8.1\times10^{-5}}_{-0.00033}$
70-170	$9.08\times10^{-5} \pm 1.7\times10^{-5} \, {}^{+1.8\times10^{-6}}_{-1.6\times10^{-5}}$

Table .24. CDF Run II Preliminary. The third leading jet p_T cross-section for $W \to \mu\nu + \geq 3$ inclusive jets normalized to the inclusive ≥ 3 jets multiplcity cross-section. The W cross-section is restricted to $|\eta^\mu| < 1.1$, $p_T^\mu > 20$ GeV/c, and $M_T^W > 30$ GeV/c^2 while jets are defined with $p_T^{jet} > 20$ GeV/c and $|\eta^{jet}| < 2.0$. The error is divided in to a statistical and total systematic uncertainty, respectively. This is a table version of plot 9.23 on page 433.

p_T range (GeV/c)	$\frac{\mathrm{d}\sigma_4/\mathrm{d}p_T^{4\mathrm{th}}}{\sigma_4}$ (c/GeV)
20-25	$0.115 \pm 0.0056 \, {}^{+0.0023}_{-0.013}$
25-35	$0.0354 \pm 0.0027 \, {}^{+0.00096}_{-0.0053}$
35-50	$0.00656 \pm 0.00095 \, {}^{+0.0007}_{-0.0032}$
50-90	$0.000605 \pm 0.00015 \, {}^{+9.4\times10^{-5}}_{-0.0002}$

Table .25. CDF Run II Preliminary. The fourth leading jet p_T cross-section for $W \to \mu\nu + \geq 4$ inclusive jets normalized to the inclusive ≥ 4 jets multiplcity cross-section. The W cross-section is restricted to $|\eta^\mu| < 1.1$, $p_T^\mu > 20$ GeV/c, and $M_T^W > 30$ GeV/c^2 while jets are defined with $p_T^{jet} > 20$ GeV/c and $|\eta^{jet}| < 2.0$. The error is divided in to a statistical and total systematic uncertainty, respectively. This is a table version of plot 9.24 on page 434.

p_T range (GeV/c)	Data/Theory
20-25	$1.05 \pm 0.0041 \; ^{+0.14}_{-0.15}$
25-30	$1.05 \pm 0.0053 \; ^{+0.13}_{-0.15}$
30-35	$1.05 \pm 0.0067 \; ^{+0.13}_{-0.12}$
35-40	$1.03 \pm 0.0081 \; ^{+0.11}_{-0.14}$
40-45	$1.02 \pm 0.0098 \; ^{+0.11}_{-0.12}$
45-50	$0.984 \pm 0.012 \; ^{+0.11}_{-0.11}$
50-55	$1.01 \pm 0.014 \; ^{+0.1}_{-0.12}$
55-60	$1.02 \pm 0.016 \; ^{+0.083}_{-0.1}$
60-65	$1.05 \pm 0.019 \; ^{+0.096}_{-0.14}$
65-70	$0.977 \pm 0.021 \; ^{+0.085}_{-0.082}$
70-75	$1.05 \pm 0.025 \; ^{+0.077}_{-0.12}$
75-80	$0.994 \pm 0.028 \; ^{+0.065}_{-0.097}$
80-85	$1.04 \pm 0.032 \; ^{+0.074}_{-0.11}$
85-90	$0.988 \pm 0.035 \; ^{+0.084}_{-0.073}$
90-95	$1.09 \pm 0.04 \; ^{+0.13}_{-0.21}$
95-105	$0.931 \pm 0.033 \; ^{+0.089}_{-0.14}$
105-120	$0.921 \pm 0.035 \; ^{+0.12}_{-0.11}$
120-140	$1.05 \pm 0.043 \; ^{+0.089}_{-0.21}$
140-175	$0.849 \pm 0.055 \; ^{+0.19}_{-0.15}$
175-230	$0.958 \pm 0.093 \; ^{+0.13}_{-0.15}$
230-430	$0.869 \pm 0.17 \; ^{+0.14}_{-0.14}$

Table .26. CDF Run II Preliminary. The leading jet p_T cross-section data/theory ratio for $W \rightarrow e\nu + \geq 1$ inclusive jets. The theory prediction is taken from an Alpgen+Pythia MC. The W cross-section is restricted to $|\eta^e| < 1.1$, $p_T^e > 20$ GeV/c, and $M_T^W > 40$ GeV/c^2 while jets are defined with $p_T^{jet} > 20$ GeV/c and $|\eta^{jet}| < 2.0$. The error is divided in to a statistical and total systematic uncertainty, respectively. This is a table version of plot 9.25 on page 436.

p_T range (GeV/c)	Data/Theory
20-25	$1.05 \pm 0.0094 \ ^{+0.26}_{-0.22}$
25-30	$1.1 \pm 0.014 \ ^{+0.19}_{-0.23}$
30-35	$0.995 \pm 0.018 \ ^{+0.15}_{-0.17}$
35-40	$1.04 \pm 0.025 \ ^{+0.18}_{-0.13}$
40-45	$1.16 \pm 0.032 \ ^{+0.13}_{-0.15}$
45-50	$1.19 \pm 0.04 \ ^{+0.15}_{-0.26}$
50-55	$1.01 \pm 0.049 \ ^{+0.2}_{-0.14}$
55-60	$1.16 \pm 0.058 \ ^{+0.13}_{-0.16}$
60-65	$1.17 \pm 0.071 \ ^{+0.15}_{-0.19}$
65-75	$1.19 \pm 0.064 \ ^{+0.092}_{-0.16}$
75-85	$1.57 \pm 0.085 \ ^{+0.11}_{-0.13}$
85-100	$1.49 \pm 0.099 \ ^{+0.22}_{-0.42}$
100-135	$1.02 \pm 0.11 \ ^{+0.12}_{-0.08}$
135-260	$1.56 \pm 0.18 \ ^{+0.15}_{-0.15}$

Table .27. CDF Run II Preliminary. The second leading jet p_T cross-section data/theory for $W \rightarrow e\nu + \geq 2$ inclusive jets. The theory prediction is taken from an Alpgen+Pythia MC. The W cross-section is restricted to $|\eta^e| < 1.1$, $p_T^e > 20$ GeV/c, and $M_T^W > 40$ GeV/c^2 while jets are defined with $p_T^{jet} > 20$ GeV/c and $|\eta^{jet}| < 2.0$. The error is divided in to a statistical and total systematic uncertainty, respectively. This is a table version of plot 9.26 on page 436.

p_T range (GeV/c)	Data/Theory
20-25	$1.08 \pm 0.023\ ^{+0.35}_{-0.3}$
25-30	$1.11 \pm 0.038\ ^{+0.31}_{-0.25}$
30-35	$1.19 \pm 0.059\ ^{+0.25}_{-0.3}$
35-40	$1.3 \pm 0.083\ ^{+0.22}_{-0.17}$
40-45	$1.67 \pm 0.11\ ^{+0.29}_{-0.64}$
45-50	$1.55 \pm 0.15\ ^{+0.36}_{-0.58}$
50-70	$1.49 \pm 0.13\ ^{+0.44}_{-0.29}$
70-170	$1.49 \pm 0.28\ ^{+0.26}_{-0.19}$

Table .28. CDF Run II Preliminary. The third leading jet p_T cross-section data/theory for $W \to e\nu +\ \geq 3$ inclusive jets. The theory prediction is taken from an Alpgen+Pythia MC. The W cross-section is restricted to $|\eta^e| < 1.1$, $p_T^e > 20$ GeV/c, and $M_T^W > 40$ GeV/c^2 while jets are defined with $p_T^{jet} >$ 20 GeV/c and $|\eta^{jet}| < 2.0$. The error is divided in to a statistical and total systematic uncertainty, respectively. This is a table version of plot 9.27 on page 437.

p_T range (GeV/c)	Data/Theory
20-25	$1.11 \pm 0.058\ ^{+0.57}_{-0.36}$
25-35	$1.07 \pm 0.093\ ^{+0.85}_{-0.47}$
35-50	$2.38 \pm 0.2\ ^{+0.66}_{-1}$
50-90	$1.51 \pm 0.55\ ^{+0.84}_{-1.2}$

Table .29. CDF Run II Preliminary. The forth leading jet p_T cross-section data/theory for $W \to e\nu +\ \geq 4$ inclusive jets. The theory prediction is taken from an Alpgen+Pythia MC. The W cross-section is restricted to $|\eta^e| < 1.1$, $p_T^e > 20$ GeV/c, and $M_T^W > 40$ GeV/c^2 while jets are defined with $p_T^{jet} >$ 20 GeV/c and $|\eta^{jet}| < 2.0$. The error is divided in to a statistical and total systematic uncertainty, respectively. This is a table version of plot 9.28 on page 437.

p_T range (GeV/c)	Data/Theory
20-25	$0.977 \pm 0.0044\ ^{+0.16}_{-0.1}$
25-30	$0.982 \pm 0.0057\ ^{+0.17}_{-0.077}$
30-35	$0.958 \pm 0.0069\ ^{+0.19}_{-0.078}$
35-40	$0.97 \pm 0.0085\ ^{+0.18}_{-0.062}$
40-45	$0.993 \pm 0.01\ ^{+0.19}_{-0.066}$
45-50	$0.961 \pm 0.012\ ^{+0.2}_{-0.067}$
50-55	$0.998 \pm 0.014\ ^{+0.19}_{-0.067}$
55-60	$1 \pm 0.016\ ^{+0.22}_{-0.075}$
60-65	$0.933 \pm 0.018\ ^{+0.22}_{-0.075}$
65-70	$1.02 \pm 0.021\ ^{+0.15}_{-0.066}$
70-75	$1.05 \pm 0.024\ ^{+0.16}_{-0.068}$
75-80	$1.02 \pm 0.027\ ^{+0.18}_{-0.071}$
80-85	$1 \pm 0.031\ ^{+0.2}_{-0.083}$
85-90	$1.09 \pm 0.035\ ^{+0.13}_{-0.083}$
90-95	$1.07 \pm 0.04\ ^{+0.18}_{-0.11}$
95-105	$1.16 \pm 0.033\ ^{+0.17}_{-0.087}$
105-120	$1.05 \pm 0.035\ ^{+0.24}_{-0.092}$
120-140	$1.31 \pm 0.043\ ^{+0.17}_{-0.089}$
140-175	$1.18 \pm 0.051\ ^{+0.24}_{-0.12}$
175-230	$1.17 \pm 0.08\ ^{+0.26}_{-0.11}$
230-430	$1.55 \pm 0.17\ ^{+0.3}_{-0.2}$

Table .30. CDF Run II Preliminary. The leading jet p_T cross-section data/theory for $W \to \mu\nu+ \geq 1$ inclusive jets. The theory prediction is taken from an Alpgen+Pythia MC. The W cross-section is restricted to $|\eta^\mu| < 1.1$, $p_T^\mu > 20$ GeV/c, and $M_T^W > 30$ GeV/c^2 while jets are defined with $p_T^{jet} > 20$ GeV/c and $|\eta^{jet}| < 2.0$. The error is divided in to a statistical and total systematic uncertainty, respectively. This is a table version of plot 9.29 on page 438.

p_T range (GeV/c)	Data/Theory
20-25	$0.967 \pm 0.0098 \, ^{+0.3}_{-0.14}$
25-30	$0.944 \pm 0.014 \, ^{+0.27}_{-0.11}$
30-35	$0.978 \pm 0.019 \, ^{+0.22}_{-0.099}$
35-40	$1.04 \pm 0.025 \, ^{+0.27}_{-0.11}$
40-45	$1.04 \pm 0.032 \, ^{+0.23}_{-0.091}$
45-50	$1.14 \pm 0.04 \, ^{+0.24}_{-0.11}$
50-55	$1.27 \pm 0.049 \, ^{+0.14}_{-0.087}$
55-60	$1.22 \pm 0.059 \, ^{+0.25}_{-0.12}$
60-65	$1.14 \pm 0.07 \, ^{+0.23}_{-0.11}$
65-75	$1.25 \pm 0.063 \, ^{+0.16}_{-0.095}$
75-85	$1.36 \pm 0.085 \, ^{+0.16}_{-0.21}$
85-100	$1.48 \pm 0.095 \, ^{+0.25}_{-0.13}$
100-135	$1.36 \pm 0.11 \, ^{+0.26}_{-0.11}$
135-260	$1.4 \pm 0.18 \, ^{+0.4}_{-0.17}$

Table .31. CDF Run II Preliminary. The second leading jet p_T cross-section data/theory for $W \rightarrow \mu\nu + \geq 2$ inclusive jets. The theory prediction is taken from an Alpgen+Pythia MC. The W cross-section is restricted to $|\eta^{\mu}| <$ 1.1, $p_T^{\mu} > 20$ GeV/c, and $M_T^W > 30$ GeV/c^2 while jets are defined with $p_T^{jet} > 20$ GeV/c and $|\eta^{jet}| < 2.0$. The error is divided in to a statistical and total systematic uncertainty, respectively. This is a table version of plot 9.30 on page 438.

p_T range (GeV/c)	Data/Theory
20-25	$0.948 \pm 0.023\ ^{+0.38}_{-0.19}$
25-30	$1.05 \pm 0.038\ ^{+0.39}_{-0.16}$
30-35	$1.09 \pm 0.055\ ^{+0.34}_{-0.15}$
35-40	$1.22 \pm 0.079\ ^{+0.26}_{-0.2}$
40-45	$1.21 \pm 0.11\ ^{+0.67}_{-0.3}$
45-50	$1.18 \pm 0.15\ ^{+0.77}_{-0.37}$
50-70	$1.3 \pm 0.13\ ^{+0.22}_{-0.25}$
70-170	$1.43 \pm 0.27\ ^{+0.27}_{-0.24}$

Table .32. CDF Run II Preliminary. The third leading jet p_T cross-section data/theory for $W \to \mu\nu + \geq 3$ inclusive jets. The theory prediction is taken from an Alpgen+Pythia MC. The W cross-section is restricted to $|\eta^\mu| < 1.1$, $p_T^\mu > 20$ GeV/c, and $M_T^W > 30$ GeV/c^2 while jets are defined with $p_T^{jet} > 20$ GeV/c and $|\eta^{jet}| < 2.0$. The error is divided in to a statistical and total systematic uncertainty, respectively. This is a table version of plot 9.31 on page 439.

p_T range (GeV/c)	Data/Theory
20-25	$1.03 \pm 0.06\ ^{+0.55}_{-0.32}$
25-35	$1.18 \pm 0.092\ ^{+0.61}_{-0.4}$
35-50	$1.4 \pm 0.2\ ^{+0.55}_{-0.84}$
50-90	$2.23 \pm 0.53\ ^{+0.71}_{-1.1}$

Table .33. CDF Run II Preliminary. The forth leading jet p_T cross-section data/theory for $W \to \mu\nu + \geq 4$ inclusive jets. The theory prediction is taken from an Alpgen+Pythia MC. The W cross-section is restricted to $|\eta^\mu| < 1.1$, $p_T^\mu > 20$ GeV/c, and $M_T^W > 30$ GeV/c^2 while jets are defined with $p_T^{jet} > 20$ GeV/c and $|\eta^{jet}| < 2.0$. The error is divided in to a statistical and total systematic uncertainty, respectively. This is a table version of plot 9.32 on page 439.

m_{jj} range (GeV/c^2)	$\mathrm{d}\sigma_2/\mathrm{d}m_{jj}$ (pb/(GeV/c^2))
0-30	$0.0298 \pm 0.00078\ ^{+0.0085}_{-0.0064} \pm 0.0018$
30-45	$0.11 \pm 0.002\ ^{+0.029}_{-0.027} \pm 0.0066$
45-55	$0.166 \pm 0.0029\ ^{+0.039}_{-0.034} \pm 0.01$
55-65	$0.184 \pm 0.003\ ^{+0.034}_{-0.03} \pm 0.011$
65-75	$0.167 \pm 0.003\ ^{+0.03}_{-0.033} \pm 0.01$
75-85	$0.133 \pm 0.0027\ ^{+0.013}_{-0.018} \pm 0.008$
85-100	$0.111 \pm 0.002\ ^{+0.016}_{-0.019} \pm 0.0067$
100-120	$0.0699 \pm 0.0014\ ^{+0.013}_{-0.011} \pm 0.0042$
120-145	$0.043 \pm 0.00098\ ^{+0.0044}_{-0.0072} \pm 0.0026$
145-180	$0.022 \pm 0.00061\ ^{+0.0019}_{-0.0025} \pm 0.0013$
180-230	$0.0102 \pm 0.00035\ ^{+0.0014}_{-0.0018} \pm 0.00061$
230-325	$0.00323 \pm 0.00014\ ^{+0.00047}_{-0.00054} \pm 0.00019$
325-575	$0.000403 \pm 3\times10^{-5}\ ^{+2.7\times10^{-5}}_{-2.8\times10^{-5}} \pm 2.4\times10^{-5}$

Table .34. CDF Run II Preliminary. Dijet mass (m_{jj}) cross-section for $W \to e\nu + {\geq}2$ jets. The W cross-section is restricted to $|\eta^e| < 1.1$, $p_T^e > 20$ GeV/c, and $M_T^W > 40$ GeV/c^2 while jets are defined with $p_T^{jet} > 20$ GeV/c and $|\eta^{jet}| < 2.0$. The error is divided in to three respective parts: statistical, total systematic which is without the final luminosity systematic, and the luminosity systematic itself. This is a table version of plot 9.33 on page 440.

m_{jj} range (GeV/c^2)	$d\sigma_2/dm_{jj}$ (pb/(GeV/c^2))
0-30	$0.0421 \pm 0.0012 \, ^{+0.014}_{-0.0061} \pm 0.0025$
30-45	$0.156 \pm 0.003 \, ^{+0.048}_{-0.023} \pm 0.0094$
45-55	$0.224 \pm 0.0043 \, ^{+0.05}_{-0.031} \pm 0.013$
55-65	$0.238 \pm 0.0046 \, ^{+0.066}_{-0.032} \pm 0.014$
65-75	$0.201 \pm 0.0041 \, ^{+0.053}_{-0.023} \pm 0.012$
75-85	$0.176 \pm 0.0039 \, ^{+0.044}_{-0.023} \pm 0.011$
85-100	$0.133 \pm 0.0028 \, ^{+0.031}_{-0.012} \pm 0.008$
100-120	$0.0925 \pm 0.0019 \, ^{+0.023}_{-0.0096} \pm 0.0056$
120-145	$0.0606 \pm 0.0014 \, ^{+0.012}_{-0.0056} \pm 0.0036$
145-180	$0.0313 \pm 0.00086 \, ^{+0.0066}_{-0.0027} \pm 0.0019$
180-230	$0.0149 \pm 0.00049 \, ^{+0.0037}_{-0.0012} \pm 0.00089$
230-325	$0.00435 \pm 0.00019 \, ^{+0.00078}_{-0.00033} \pm 0.00026$
325-575	$0.000477 \pm 4.1{\times}10^{-5} \, ^{+0.00015}_{-4.7{\times}10^{-5}} \pm 2.9{\times}10^{-5}$

Table .35. CDF Run II Preliminary. Dijet mass (m_{jj}) cross-section for $W \to \mu\nu + \geq 2$ jets. The W cross-section is restricted to $|\eta^\mu| < 1.1$, $p_T^\mu > 20$ GeV/c, and $M_T^W > 30$ GeV/c^2 while jets are defined with $p_T^{jet} > 20$ GeV/c and $|\eta^{jet}| < 2.0$. The error is divided in to three respective parts: statistical, total systematic which is without the final luminosity systematic, and the luminosity systematic itself. This is a table version of plot 9.34 on page 441.

m_{jj} range (GeV/c^2)	$\frac{\mathrm{d}\sigma_2/\mathrm{d}m_{jj}}{\sigma_2}$ $(1/(\mathrm{GeV/c}^2))$
0-30	$0.00207 \pm 5.5{\times}10^{-5}\ ^{+0.0001}_{-9.8\times10^{-5}}$
30-45	$0.00763 \pm 0.00014\ ^{+0.00025}_{-0.00061}$
45-55	$0.0115 \pm 0.0002\ ^{+7.2\times10^{-5}}_{-0.00035}$
55-65	$0.0128 \pm 0.00022\ ^{+0.00021}_{-0.00045}$
65-75	$0.0116 \pm 0.00021\ ^{+0.00025}_{-0.00045}$
75-85	$0.00922 \pm 0.00019\ ^{+0.00043}_{-0.00096}$
85-100	$0.00772 \pm 0.00014\ ^{+9.3\times10^{-5}}_{-0.00053}$
100-120	$0.00485 \pm 9.8{\times}10^{-5}\ ^{+0.00016}_{-0.00018}$
120-145	$0.00298 \pm 6.9{\times}10^{-5}\ ^{+3.8\times10^{-5}}_{-0.0003}$
145-180	$0.00153 \pm 4.3{\times}10^{-5}\ ^{+0.00012}_{-0.00017}$
180-230	$0.00071 \pm 2.4{\times}10^{-5}\ ^{+4.8\times10^{-6}}_{-5.2\times10^{-5}}$
230-325	$0.000224 \pm 9.7{\times}10^{-6}\ ^{+3\times10^{-6}}_{-1.5\times10^{-5}}$
325-575	$2.79{\times}10^{-5} \pm 2.1{\times}10^{-6}\ ^{+3.7\times10^{-6}}_{-3.6\times10^{-6}}$

Table .36. CDF Run II Preliminary. Dijet mass (m_{jj}) cross-section normalized to the inclusive 2 jets cross-section for $W \to e\nu+\ \geq 2$ jets. The W cross-section is restricted to $|\eta^e| < 1.1$, $p_T^e > 20$ GeV/c, and $M_T^W > 40$ GeV/c^2 while jets are defined with $p_T^{jet} > 20$ GeV/c and $|\eta^{jet}| < 2.0$. The error is divided in to a statistical and total systematic uncertainty, respectively. This is a table version of plot 9.35 on page 441.

m_{jj} range (GeV/c^2)	$\frac{\mathrm{d}\sigma_2/\mathrm{d}m_{jj}}{\sigma_2}$ $(1/(\text{GeV/c}^2))$
0-30	$0.0022 \pm 6.3{\times}10^{-5} \; {}^{+3.4\times10^{-5}}_{-8\times10^{-5}}$
30-45	$0.00813 \pm 0.00016 \; {}^{+5.8\times10^{-5}}_{-0.00032}$
45-55	$0.0117 \pm 0.00023 \; {}^{+0.00033}_{-0.00086}$
55-65	$0.0124 \pm 0.00024 \; {}^{+0.0003}_{-0.0004}$
65-75	$0.0105 \pm 0.00022 \; {}^{+5.6\times10^{-5}}_{-0.00043}$
75-85	$0.00916 \pm 0.00021 \; {}^{+0.00018}_{-0.00048}$
85-100	$0.00696 \pm 0.00015 \; {}^{+0.00017}_{-0.00046}$
100-120	$0.00482 \pm 0.0001 \; {}^{+4.1\times10^{-5}}_{-0.00025}$
120-145	$0.00316 \pm 7.3{\times}10^{-5} \; {}^{+6.8\times10^{-5}}_{-0.00027}$
145-180	$0.00163 \pm 4.6{\times}10^{-5} \; {}^{+4.8\times10^{-5}}_{-0.00013}$
180-230	$0.000776 \pm 2.6{\times}10^{-5} \; {}^{+2.5\times10^{-5}}_{-4.1\times10^{-5}}$
230-325	$0.000227 \pm 1{\times}10^{-5} \; {}^{+9.2\times10^{-6}}_{-2.4\times10^{-5}}$
325-575	$2.49{\times}10^{-5} \pm 2.1{\times}10^{-6} \; {}^{+3.6\times10^{-7}}_{-2.7\times10^{-7}}$

Table .37. CDF Run II Preliminary. Dijet mass (m_{jj}) cross-section normalized to the inclusive 2 jets cross-section for $W \to \mu\nu+ \geq 2$ jets. The W cross-section is restricted to $|\eta^{\mu}| < 1.1$, $p_T^{\mu} > 20$ GeV/c, and $M_T^W > 30$ GeV/c^2 while jets are defined with $p_T^{jet} > 20$ GeV/c and $|\eta^{jet}| < 2.0$. The error is divided in to a statistical and total systematic uncertainty, respectively. This is a table version of plot 9.36 on page 442.

R_{jj} range	$\mathrm{d}\sigma_2/\mathrm{d}R_{jj}$ (pb)
0.4-0.6	$0.404 \pm 0.038 \,^{+0.11}_{-0.11} \pm 0.024$
0.6-0.8	$2.55 \pm 0.091 \,^{+0.76}_{-0.54} \pm 0.15$
0.8-1	$3.21 \pm 0.097 \,^{+0.95}_{-0.71} \pm 0.19$
1-1.2	$2.89 \pm 0.094 \,^{+0.7}_{-0.65} \pm 0.17$
1.2-1.4	$3 \pm 0.09 \,^{+0.76}_{-0.83} \pm 0.18$
1.4-1.6	$2.95 \pm 0.091 \,^{+0.92}_{-0.71} \pm 0.18$
1.6-1.8	$3.27 \pm 0.09 \,^{+0.74}_{-0.8} \pm 0.2$
1.8-2	$3.46 \pm 0.099 \,^{+0.97}_{-0.91} \pm 0.21$
2-2.2	$3.94 \pm 0.1 \,^{+0.92}_{-0.92} \pm 0.24$
2.2-2.4	$4.92 \pm 0.11 \,^{+0.99}_{-1} \pm 0.3$
2.4-2.6	$5.58 \pm 0.12 \,^{+0.97}_{-1} \pm 0.33$
2.6-2.8	$7.08 \pm 0.13 \,^{+0.88}_{-1.2} \pm 0.43$
2.8-3	$8.32 \pm 0.14 \,^{+1.3}_{-1.2} \pm 0.5$
3-3.2	$9.1 \pm 0.16 \,^{+1.4}_{-1.6} \pm 0.55$
3.2-3.4	$5.32 \pm 0.12 \,^{+0.68}_{-0.94} \pm 0.32$
3.4-3.6	$3.27 \pm 0.097 \,^{+0.72}_{-0.51} \pm 0.2$
3.6-3.8	$2.04 \pm 0.073 \,^{+0.37}_{-0.36} \pm 0.12$
3.8-4	$1.27 \pm 0.062 \,^{+0.25}_{-0.21} \pm 0.076$
4-4.2	$0.786 \pm 0.045 \,^{+0.1}_{-0.14} \pm 0.047$
4.2-4.4	$0.416 \pm 0.039 \,^{+0.098}_{-0.091} \pm 0.025$
4.4-4.6	$0.192 \pm 0.03 \,^{+0.058}_{-0.053} \pm 0.012$
4.6-4.8	$0.0951 \pm 0.02 \,^{+0.038}_{-0.019} \pm 0.0057$

Table .38. CDF Run II Preliminary. Dijet separation (R_{jj}) cross-section for $W \to e\nu + \geq 2$ jets. The W cross-section is restricted to $|\eta^e| < 1.1$, $p_T^e > 20$ GeV/c, and $M_T^W > 40$ GeV/c^2 while jets are defined with $p_T^{jet} > 20$ GeV/c and $|\eta^{jet}| < 2.0$. The error is divided in to three respective parts: statistical, total systematic which is without the final luminosity systematic, and the luminosity systematic itself. This is a table version of plot 9.37 on page 443.

R_{jj} range	$\mathrm{d}\sigma_2/\mathrm{d}R_{jj}$ (pb)
0.4-0.6	$0.724 \pm 0.054 \,^{+0.29}_{-0.14} \pm 0.043$
0.6-0.8	$3.9 \pm 0.13 \,^{+1.1}_{-0.54} \pm 0.23$
0.8-1	$4.92 \pm 0.15 \,^{+1.9}_{-0.66} \pm 0.3$
1-1.2	$4.29 \pm 0.14 \,^{+1.5}_{-0.56} \pm 0.26$
1.2-1.4	$4.03 \pm 0.13 \,^{+1.3}_{-0.46} \pm 0.24$
1.4-1.6	$4.32 \pm 0.13 \,^{+1.4}_{-0.61} \pm 0.26$
1.6-1.8	$4.51 \pm 0.14 \,^{+1.5}_{-0.69} \pm 0.27$
1.8-2	$5.04 \pm 0.15 \,^{+1.7}_{-0.74} \pm 0.3$
2-2.2	$5.75 \pm 0.16 \,^{+1.6}_{-0.75} \pm 0.34$
2.2-2.4	$6.5 \pm 0.16 \,^{+2}_{-0.72} \pm 0.39$
2.4-2.6	$7.34 \pm 0.17 \,^{+2.3}_{-0.79} \pm 0.44$
2.6-2.8	$9.46 \pm 0.18 \,^{+2.2}_{-1} \pm 0.57$
2.8-3	$10.5 \pm 0.2 \,^{+2.5}_{-1.1} \pm 0.63$
3-3.2	$11 \pm 0.23 \,^{+2.4}_{-1.2} \pm 0.66$
3.2-3.4	$6.29 \pm 0.17 \,^{+1.4}_{-0.75} \pm 0.38$
3.4-3.6	$4.05 \pm 0.14 \,^{+0.78}_{-0.47} \pm 0.24$
3.6-3.8	$2.37 \pm 0.12 \,^{+0.69}_{-0.29} \pm 0.14$
3.8-4	$1.53 \pm 0.084 \,^{+0.42}_{-0.25} \pm 0.092$
4-4.2	$0.835 \pm 0.06 \,^{+0.22}_{-0.15} \pm 0.05$
4.2-4.4	$0.477 \pm 0.051 \,^{+0.17}_{-0.063} \pm 0.029$
4.4-4.6	$0.233 \pm 0.032 \,^{+0.088}_{-0.029} \pm 0.014$
4.6-4.8	$0.12 \pm 0.026 \,^{+0.025}_{-0.046} \pm 0.0072$

Table .39. CDF Run II Preliminary. Dijet separation (R_{jj}) cross-section for $W \to \mu\nu + \geq 2$ jets. The W cross-section is restricted to $|\eta^\mu| < 1.1$, $p_T^\mu > 20$ GeV/c, and $M_T^W > 30$ GeV/c^2 while jets are defined with $p_T^{jet} > 20$ GeV/c and $|\eta^{jet}| < 2.0$. The error is divided in to three respective parts: statistical, total systematic which is without the final luminosity systematic, and the luminosity systematic itself. This is a table version of plot 9.38 on page 444.

R_{jj} range	$\frac{\mathrm{d}\sigma_2/\mathrm{d}R_{jj}}{\sigma_2}$
0.4-0.6	$0.028 \pm 0.0026\ ^{+0.00099}_{-0.0034}$
0.6-0.8	$0.177 \pm 0.0064\ ^{+0.01}_{-0.0074}$
0.8-1	$0.223 \pm 0.0068\ ^{+0.013}_{-0.012}$
1-1.2	$0.201 \pm 0.0066\ ^{+0.0024}_{-0.012}$
1.2-1.4	$0.208 \pm 0.0063\ ^{+0.0045}_{-0.026}$
1.4-1.6	$0.204 \pm 0.0064\ ^{+0.014}_{-0.016}$
1.6-1.8	$0.227 \pm 0.0063\ ^{+0.00019}_{-0.019}$
1.8-2	$0.24 \pm 0.007\ ^{+0.011}_{-0.025}$
2-2.2	$0.273 \pm 0.0072\ ^{+0.0015}_{-0.018}$
2.2-2.4	$0.341 \pm 0.0077\ ^{+0.007}_{-0.015}$
2.4-2.6	$0.387 \pm 0.0082\ ^{+0.0044}_{-0.017}$
2.6-2.8	$0.491 \pm 0.0094\ ^{+0.0054}_{-0.041}$
2.8-3	$0.577 \pm 0.0098\ ^{+0.02}_{-0.035}$
3-3.2	$0.631 \pm 0.011\ ^{+0.00082}_{-0.038}$
3.2-3.4	$0.369 \pm 0.0084\ ^{+0.00022}_{-0.03}$
3.4-3.6	$0.227 \pm 0.0068\ ^{+0.006}_{-0.0013}$
3.6-3.8	$0.141 \pm 0.0051\ ^{+1.8\times10^{-5}}_{-0.005}$
3.8-4	$0.0883 \pm 0.0043\ ^{+0.0017}_{-0.0019}$
4-4.2	$0.0545 \pm 0.0031\ ^{+8.6\times10^{-5}}_{-0.0042}$
4.2-4.4	$0.0288 \pm 0.0027\ ^{+0.00022}_{-0.0014}$
4.4-4.6	$0.0133 \pm 0.0021\ ^{+0.00081}_{-0.0016}$
4.6-4.8	$0.0066 \pm 0.0014\ ^{+0.00095}_{-0.00018}$

Table .40. CDF Run II Preliminary. Dijet separation (R_{jj}) cross-section normalized to the inclusive 2 jets cross-section for $W \to e\nu + \geq 2$ jets. The W cross-section is restricted to $|\eta^e| < 1.1$, $p_T^e > 20$ GeV/c, and $M_T^W > 40$ GeV/c^2 while jets are defined with $p_T^{jet} > 20$ GeV/c and $|\eta^{jet}| < 2.0$. The error is divided in to a statistical and total systematic uncertainty, respectively. This is a table version of plot 9.39 on page 444.

R_{jj} range	$\frac{\mathrm{d}\sigma_2/\mathrm{d}R_{jj}}{\sigma_2}$
0.4-0.6	$0.0378 \pm 0.0028\ ^{+0.0023}_{-0.0034}$
0.6-0.8	$0.203 \pm 0.0069\ ^{+0.0059}_{-0.0064}$
0.8-1	$0.256 \pm 0.0078\ ^{+0.012}_{-0.0068}$
1-1.2	$0.224 \pm 0.0073\ ^{+0.0041}_{-0.0045}$
1.2-1.4	$0.21 \pm 0.007\ ^{+0.00083}_{-0.0005}$
1.4-1.6	$0.225 \pm 0.0071\ ^{+0.0021}_{-0.0075}$
1.6-1.8	$0.235 \pm 0.0072\ ^{+0.002}_{-0.011}$
1.8-2	$0.263 \pm 0.0077\ ^{+0.0029}_{-0.01}$
2-2.2	$0.3 \pm 0.0082\ ^{+0.0062}_{-0.008}$
2.2-2.4	$0.339 \pm 0.0085\ ^{+8.1\times10^{-5}}_{-0.0034}$
2.4-2.6	$0.383 \pm 0.0091\ ^{+0.0014}_{-8.1\times10^{-5}}$
2.6-2.8	$0.493 \pm 0.0098\ ^{+0.00048}_{-0.032}$
2.8-3	$0.548 \pm 0.011\ ^{+0.0045}_{-0.033}$
3-3.2	$0.573 \pm 0.012\ ^{+0.0015}_{-0.044}$
3.2-3.4	$0.328 \pm 0.0092\ ^{+0.0028}_{-0.025}$
3.4-3.6	$0.211 \pm 0.0073\ ^{+0.00085}_{-0.02}$
3.6-3.8	$0.124 \pm 0.0061\ ^{+0.0017}_{-0.0026}$
3.8-4	$0.0797 \pm 0.0044\ ^{+0.0025}_{-0.0044}$
4-4.2	$0.0435 \pm 0.0031\ ^{+0.0017}_{-0.0031}$
4.2-4.4	$0.0249 \pm 0.0027\ ^{+0.00084}_{-0.0006}$
4.4-4.6	$0.0121 \pm 0.0017\ ^{+0.00056}_{-0.00016}$
4.6-4.8	$0.00625 \pm 0.0013\ ^{+0.00051}_{-0.0019}$

Table .41. CDF Run II Preliminary. Dijet separation (R_{jj}) cross-section normalized to the inclusive 2 jets cross-section for $W \to \mu\nu + \geq 2$ jets. The W cross-section is restricted to $|\eta^{\mu}| < 1.1$, $p_T^{\mu} > 20$ GeV/c, and $M_T^W > 30$ GeV/c^2 while jets are defined with $p_T^{jet} > 20$ GeV/c and $|\eta^{jet}| < 2.0$. The error is divided in to a statistical and total systematic uncertainty, respectively. This is a table version of plot 9.40 on page 445.

$\Delta\eta$ range	$d\sigma_2/d\Delta\eta$ (pb)
0-0.5	$7.06 \pm 0.092\ ^{+1.3}_{-1.2} \pm 0.42$
0.5-1	$7.73 \pm 0.095\ ^{+1.3}_{-1.3} \pm 0.46$
1-1.5	$5.49 \pm 0.076\ ^{+0.95}_{-1} \pm 0.33$
1.5-2	$4.67 \pm 0.067\ ^{+0.8}_{-0.94} \pm 0.28$
2-2.5	$2.6 \pm 0.051\ ^{+0.53}_{-0.44} \pm 0.16$
2.5-3	$1.39 \pm 0.034\ ^{+0.25}_{-0.28} \pm 0.084$
3-3.5	$0.556 \pm 0.021\ ^{+0.16}_{-0.11} \pm 0.033$
3.5-4	$0.0832 \pm 0.0067\ ^{+0.021}_{-0.022} \pm 0.005$

Table .42. CDF Run II Preliminary. Closest $\Delta\eta$ cross-section for $W \to e\nu+ \geq 2$ jets. The W cross-section is restricted to $|\eta^e| < 1.1$, $p_T^e > 20$ GeV/c, and $M_T^W > 40$ GeV/c^2 while jets are defined with $p_T^{jet} > 20$ GeV/c and $|\eta^{jet}| < 2.0$. The error is divided in to three respective parts: statistical, total systematic which is without the final luminosity systematic, and the luminosity systematic itself. This is a table version of plot 9.43 on page 448.

$\Delta\eta$ range	$\mathrm{d}\sigma_3/\mathrm{d}\Delta\eta$ (pb)
0-0.5	$0.186 \pm 0.015 \,^{+0.049}_{-0.054} \pm 0.011$
0.5-1	$0.717 \pm 0.027 \,^{+0.17}_{-0.2} \pm 0.043$
1-1.5	$0.8 \pm 0.028 \,^{+0.16}_{-0.16} \pm 0.048$
1.5-2	$0.858 \pm 0.027 \,^{+0.23}_{-0.2} \pm 0.051$
2-2.5	$0.508 \pm 0.021 \,^{+0.17}_{-0.11} \pm 0.03$
2.5-3	$0.404 \pm 0.017 \,^{+0.091}_{-0.1} \pm 0.024$
3-3.5	$0.174 \pm 0.011 \,^{+0.06}_{-0.04} \pm 0.01$
3.5-4	$0.0196 \pm 0.0028 \,^{+0.006}_{-0.0071} \pm 0.0012$

Table .43. CDF Run II Preliminary. Closest $\Delta\eta$ cross-section for $W \rightarrow e\nu + \geq 3$ jets. The W cross-section is restricted to $|\eta^e| < 1.1$, $p_T^e > 20$ GeV/c, and $M_T^W > 40$ GeV/c^2 while jets are defined with $p_T^{jet} > 20$ GeV/c and $|\eta^{jet}| < 2.0$. The error is divided in to three respective parts: statistical, total systematic which is without the final luminosity systematic, and the luminosity systematic itself. This is a table version of plot 9.47 on page 450.

$\Delta\eta$ range	$\dfrac{\mathrm{d}\sigma_2/\mathrm{d}\Delta\eta}{\sigma_2}$
0-0.5	$0.49 \pm 0.0064\ ^{+0.0019}_{-0.018}$
0.5-1	$0.536 \pm 0.0065\ ^{+0.0074}_{-0.026}$
1-1.5	$0.381 \pm 0.0054\ ^{+0.006}_{-0.017}$
1.5-2	$0.324 \pm 0.0048\ ^{+0.0092}_{-0.015}$
2-2.5	$0.181 \pm 0.0036\ ^{+0.0018}_{-0.0032}$
2.5-3	$0.0965 \pm 0.0024\ ^{+0.0029}_{-0.0035}$
3-3.5	$0.0386 \pm 0.0014\ ^{+0.0019}_{-0.00081}$
3.5-4	$0.00577 \pm 0.00047\ ^{+0.00012}_{-0.00061}$

Table .44. CDF Run II Preliminary. Closest $\Delta\eta$ cross-section normalized to the inclusive 2 jet cross-section for $W \to e\nu +\ \geq 2$ jets. The W cross-section is restricted to $|\eta^e| < 1.1$, $p_T^e > 20$ GeV/c, and $M_T^W > 40$ GeV/c^2 while jets are defined with $p_T^{jet} > 20$ GeV/c and $|\eta^{jet}| < 2.0$. The error is divided in to a statistical and total systematic uncertainty, respectively. This is a table version of plot 9.45 on page 449.

$\Delta\eta$ range	$\dfrac{\mathrm{d}\sigma_3/\mathrm{d}\Delta\eta}{\sigma_3}$
0-0.5	$0.106 \pm 0.0084 \ ^{+0.0051}_{-0.0082}$
0.5-1	$0.41 \pm 0.015 \ ^{+0.026}_{-0.028}$
1-1.5	$0.457 \pm 0.016 \ ^{+0.015}_{-0.043}$
1.5-2	$0.491 \pm 0.015 \ ^{+0.0058}_{-0.024}$
2-2.5	$0.29 \pm 0.012 \ ^{+0.003}_{-0.00025}$
2.5-3	$0.231 \pm 0.01 \ ^{+0.0076}_{-0.018}$
3-3.5	$0.0995 \pm 0.0066 \ ^{+0.0014}_{-0.00026}$
3.5-4	$0.0112 \pm 0.0016 \ ^{+0.00019}_{-0.002}$

Table .45. CDF Run II Preliminary. Closest $\Delta\eta$ cross-section normalized to the inclusive 3 jet cross-section for $W \to e\nu + \geq 3$ jets. The W cross-section is restricted to $|\eta^e| < 1.1$, $p_T^e > 20$ GeV/c, and $M_T^W > 40$ GeV/c^2 while jets are defined with $p_T^{jet} > 20$ GeV/c and $|\eta^{jet}| < 2.0$. The error is divided in to a statistical and total systematic uncertainty, respectively. This is a table version of plot 9.49 on page 451.

$\Delta\eta$ range	$\mathrm{d}\sigma_2/\mathrm{d}\Delta\eta$ (pb)
0-0.5	$9.99 \pm 0.14 \, ^{+2.5}_{-1.1} \pm 0.6$
0.5-1	$10.1 \pm 0.14 \, ^{+2.5}_{-1.1} \pm 0.6$
1-1.5	$8.04 \pm 0.11 \, ^{+1.8}_{-0.89} \pm 0.48$
1.5-2	$5.44 \pm 0.096 \, ^{+1.5}_{-0.65} \pm 0.33$
2-2.5	$3.12 \pm 0.069 \, ^{+0.92}_{-0.43} \pm 0.19$
2.5-3	$1.89 \pm 0.049 \, ^{+0.58}_{-0.26} \pm 0.11$
3-3.5	$0.644 \pm 0.027 \, ^{+0.23}_{-0.11} \pm 0.039$
3.5-4	$0.103 \pm 0.0075 \, ^{+0.053}_{-0.026} \pm 0.0062$

Table .46. CDF Run II Preliminary. Closest $\Delta\eta$ cross-section for $W \to \mu\nu+ \geq 2$ jets. The W cross-section is restricted to $|\eta^\mu| < 1.1$, $p_T^\mu > 20$ GeV/c, and $M_T^W > 30$ GeV/c^2 while jets are defined with $p_T^{jet} > 20$ GeV/c and $|\eta^{jet}| < 2.0$. The error is divided in to three respective parts: statistical, total systematic which is without the final luminosity systematic, and the luminosity systematic itself. This is a table version of plot 9.44 on page 449.

$\Delta\eta$ range	$d\sigma_3/d\Delta\eta$ (pb)
0-0.5	$0.289 \pm 0.024 \, ^{+0.074}_{-0.048} \pm 0.017$
0.5-1	$0.997 \pm 0.044 \, ^{+0.35}_{-0.15} \pm 0.06$
1-1.5	$1.29 \pm 0.045 \, ^{+0.41}_{-0.21} \pm 0.077$
1.5-2	$0.986 \pm 0.04 \, ^{+0.32}_{-0.18} \pm 0.059$
2-2.5	$0.779 \pm 0.034 \, ^{+0.33}_{-0.16} \pm 0.047$
2.5-3	$0.526 \pm 0.026 \, ^{+0.19}_{-0.093} \pm 0.032$
3-3.5	$0.271 \pm 0.016 \, ^{+0.11}_{-0.052} \pm 0.016$
3.5-4	$0.0327 \pm 0.0032 \, ^{+0.018}_{-0.011} \pm 0.002$

Table .47. CDF Run II Preliminary. Closest $\Delta\eta$ cross-section for $W \to \mu\nu+ \geq 3$ jets. The W cross-section is restricted to $|\eta^\mu| < 1.1$, $p_T^\mu > 20$ GeV/c, and $M_T^W > 30$ GeV/c^2 while jets are defined with $p_T^{jet} > 20$ GeV/c and $|\eta^{jet}| < 2.0$. The error is divided in to three respective parts: statistical, total systematic which is without the final luminosity systematic, and the luminosity systematic itself. This is a table version of plot 9.48 on page 451.

$\Delta\eta$ range	$\dfrac{\mathrm{d}\sigma_2/\mathrm{d}\Delta\eta}{\sigma_2}$
0-0.5	$0.521 \pm 0.0071 \; {}^{+0.0018}_{-0.028}$
0.5-1	$0.525 \pm 0.0071 \; {}^{+0.00083}_{-0.027}$
1-1.5	$0.419 \pm 0.006 \; {}^{+0.00018}_{-0.029}$
1.5-2	$0.283 \pm 0.0051 \; {}^{+0.0025}_{-0.011}$
2-2.5	$0.163 \pm 0.0037 \; {}^{+0.003}_{-0.0048}$
2.5-3	$0.0984 \pm 0.0026 \; {}^{+0.001}_{-0.0032}$
3-3.5	$0.0336 \pm 0.0014 \; {}^{+0.00088}_{-0.0023}$
3.5-4	$0.00536 \pm 0.00039 \; {}^{+0.00079}_{-0.00084}$

Table .48. CDF Run II Preliminary. Closest $\Delta\eta$ cross-section normalized to the inclusive 2 jets cross-section for $W \to \mu\nu+ \geq 2$ jets. The W cross-section is restricted to $|\eta^{\mu}| < 1.1$, $p_T^{\mu} > 20$ GeV/c, and $M_T^W > 30$ GeV/c^2 while jets are defined with $p_T^{jet} > 20$ GeV/c and $|\eta^{jet}| < 2.0$. The error is divided in to a statistical and total systematic uncertainty, respectively. This is a table version of plot 9.46 on page 450.

$\Delta\eta$ range	$\dfrac{\mathrm{d}\sigma_3/\mathrm{d}\Delta\eta}{\sigma_3}$
0-0.5	$0.116 \pm 0.0098 \; ^{+0.0017}_{-0.015}$
0.5-1	$0.401 \pm 0.018 \; ^{+0.0026}_{-0.024}$
1-1.5	$0.519 \pm 0.018 \; ^{+0.0056}_{-0.044}$
1.5-2	$0.396 \pm 0.016 \; ^{+0.016}_{-0.032}$
2-2.5	$0.313 \pm 0.014 \; ^{+0.0042}_{-0.017}$
2.5-3	$0.212 \pm 0.011 \; ^{+0.0057}_{-0.011}$
3-3.5	$0.109 \pm 0.0067 \; ^{+0.0022}_{-0.005}$
3.5-4	$0.0131 \pm 0.0013 \; ^{+0.00088}_{-0.0027}$

Table .49. CDF Run II Preliminary. Closest $\Delta\eta$ cross-section normalized to the inclusive 3 jets cross-section for $W \rightarrow \mu\nu + \geq 3$ jets. The W cross-section is restricted to $|\eta^{\mu}| < 1.1$, $p_T^{\mu} > 20$ GeV/c, and $M_T^W > 30$ GeV/c^2 while jets are defined with $p_T^{jet} > 20$ GeV/c and $|\eta^{jet}| < 2.0$. The error is divided in to a statistical and total systematic uncertainty, respectively. This is a table version of plot 9.50 on page 452.

$\Delta\eta$ range	$\dfrac{\mathrm{d}\sigma_3/\mathrm{d}\Delta\eta}{\mathrm{d}\sigma_2/\mathrm{d}\Delta\eta}$
0-0.5	$0.0263 \pm 0.0021\ ^{+0.0028}_{-0.0039}$
0.5-1	$0.0927 \pm 0.0035\ ^{+0.0077}_{-0.013}$
1-1.5	$0.146 \pm 0.0052\ ^{+0.011}_{-0.011}$
1.5-2	$0.184 \pm 0.006\ ^{+0.017}_{-0.012}$
2-2.5	$0.195 \pm 0.0086\ ^{+0.021}_{-0.013}$
2.5-3	$0.29 \pm 0.013\ ^{+0.014}_{-0.02}$
3-3.5	$0.313 \pm 0.022\ ^{+0.021}_{-0.022}$
3.5-4	$0.235 \pm 0.037\ ^{+0.016}_{-0.041}$

Table .50. CDF Run II Preliminary. Ratio of closest $\Delta\eta$ cross-section ($r_{\Delta\eta}$) for $W \to \mu\nu \geq 3$ and 2 jets as described in equation 9.6 on page 448. The W cross-section is restricted to $|\eta^e| < 1.1$, $p_T^e > 20$ GeV/c, and $M_T^W > 40$ GeV/c^2 while jets are defined with $p_T^{jet} > 20$ GeV/c and $|\eta^{jet}| < 2.0$. The error is divided in to a statistical and total systematic uncertainty, respectively. This is a table version of plot 9.51 on page 453.

$\Delta\eta$ range	$\dfrac{\mathrm{d}\sigma_3/\mathrm{d}\Delta\eta}{\mathrm{d}\sigma_2/\mathrm{d}\Delta\eta}$
0-0.5	$0.0289 \pm 0.0024 \,^{+0.0023}_{-0.0025}$
0.5-1	$0.0991 \pm 0.0044 \,^{+0.0096}_{-0.0073}$
1-1.5	$0.161 \pm 0.0058 \,^{+0.014}_{-0.011}$
1.5-2	$0.181 \pm 0.0076 \,^{+0.014}_{-0.016}$
2-2.5	$0.249 \pm 0.012 \,^{+0.025}_{-0.017}$
2.5-3	$0.279 \pm 0.015 \,^{+0.015}_{-0.012}$
3-3.5	$0.42 \pm 0.029 \,^{+0.015}_{-0.012}$
3.5-4	$0.318 \pm 0.036 \,^{+0.023}_{-0.034}$

Table .51. CDF Run II Preliminary. Ratio of closest $\Delta\eta$ cross-section $(r_{\Delta\eta})$ for $W \to \mu\nu \geq 3$ and 2 jets as described in equation 9.6 on page 448. The W cross-section is restricted to $|\eta^{\mu}| < 1.1$, $p_T^{\mu} > 20$ GeV/c, and $M_T^W > 30$ GeV/c^2 while jets are defined with $p_T^{jet} > 20$ GeV/c and $|\eta^{jet}| < 2.0$. The error is divided in to a statistical and total systematic uncertainty, respectively. This is a table version of plot 9.52 on page 453.